

# **THE EFFECT OF TURBULENCE ON BUBBLE-PARTICLE INTERACTION IN FLOTATION**

**A Thesis**

Submitted for the Award of the Degree of

**Doctor of Philosophy in Chemical Engineering**

By

**Ai Wang**

**B.E. (Mineral Processing Engineering)**



Discipline of Chemical Engineering  
School of Engineering  
College of Engineering, Science and Environment  
The University of Newcastle, NSW 2308  
AUSTRALIA

July, 2021

---

## **Statement of Originality**

I hereby certify that this thesis is my own work and contains no material previously published or written by another person. The thesis contains no material which has been accepted, or is being examined, for the award of any other degree or diploma in any university or other tertiary institution. I give consent to the final version of this thesis being made available worldwide when deposited in the University's Digital Repository, subject to the provision of the *Copyright Act* 1968.

(Signature)

**Ai Wang**

**31<sup>st</sup> July, 2021**

## **Acknowledgement of authorship**

I hereby certify that the work embodied in this thesis contains published paper/s/scholarly work of which I am a joint author. I have included as part of the thesis a written declaration endorsed in writing by my supervisor, attesting to my contribution to the joint publication/s/scholarly work.

By signing below, I confirm that Ai Wang contributed to the publication entitled “Development of a flotation recovery model with CFD predicted collision efficiency” as the first author. Part of the results presented in Chapter 4 and 6 of her thesis are extracted from this publication.

Signature:

Subhasish Mitra

Ai Wang

## Acknowledgement

In 2017 I started my PhD journey with a heart yearning to peek through the mist for where my research would take me. Along the way came countless hardships in which the resilience and bravery are fostered with all the generous help. The end of the PhD journey is a time to recall the help I received, without which my spiritual soil would be barren, and my research creek would be dry.

It is the small things that bring about big changes. This journey, although formally started in 2017, was initiated in 2015 when Prof. Geoffrey Evans was giving the course-Two-phase flow - in China University of Mining and Technology. The way Prof. Geoffrey approached a problem was so lucid and elegant that I couldn't help wondering where the difficulty of the problem initially lay. Besides this, the blackboard full of the schematics, equations and predictions brought me to a world where it is difficult to withdraw from after tasting the science of deduction. After he generously agreed to supervise me in Australia, these two elements of his guidance - the clarity and the deduction –helped me in my times of need. I can't thank him enough for planting the interest of modelling nature in my early research life and sharpening my questions in a gentle and insightful way.

For the countless times I walked into the office of my supervisor Dr Subhasish Mitra, “Speaking mathematically and meticulously” is his criterion I tried to live up to. These two adverbs become the passports of this journey which renders me enormous confidence and changes my identity from an outsider to a researcher with scales to measure the world. Indeed, these two principals have been applied beyond writing to file hierarchy on computers, to the documenting of simulations and experiments, and finally to the fundamental thinking patterns. Similar to these two principals, Dr Subhasish’s many other philosophical beliefs have been applied to my overall personal development, such as prioritizing the lab works, (namely what the nature does), taking ownership of things, and critical discussions. His 24/7 support has always been my source of strength among the ups and downs over the last four years.

I would also like to thank my co-supervisor Associate Professor Elham Doroodchi for always being aware of the applications of the fundamental research to the industry, and Dr Roberto Moreno-Atanasio for the insights into the surface chemistry, and how to write clearly. Their constructive criticisms and valuable advice kept me afloat throughout the course of this journey. Their engaging discussions helped me quickly grasp the focus of the research.

I wish to thank all my research group members on level 3 of NIER building—Pavel (Mohammad Hoque), Guichao, Linhan, Deside, Tuyen, Sagar, Dilruba, Fahim, Hamed, Vahid, Chuanzhen, Chunfu and Raju, for providing the warm and supportive environment. From them I obtained numerous tips regarding mathematics, computation, engineering, and time management. Special acknowledgement goes to Pavel for his detailed corrections of my first publication and generous assistance in the laboratory, and to Linhan for his interest in sharing how to install the open-source software. Many thanks to the staff of the Chemical Engineering Discipline and NIER precinct – Con for his help in installing the softwares (Matlab and Ansys); Neil for his ordering of experimental materials, and Zoe for her help in photocopying and printing.

I would like to mention my previous supervisors – Jiongtian Liu, Yijun Cao and Xiaokang Yan in CUMT, Xuzhou, China. This PhD journey would never be initiated without their paving the way for the study of hydrodynamics in flotation and their encouragement on my overseas study.

I would also like to acknowledge the postgraduate scholarship received from the University of Newcastle, Australia and the China Scholarship Council (CSC), China to carry out this research. In addition, I wish to acknowledge the funding support from the Australian Research Council for the ARC Centre of Excellence for Enabling Eco-Efficient Beneficiation of Minerals.

Finally, I deeply appreciate my family, especially my parents for their endless attempt to stand in my shoes and enlighten me with how hopeless situations can be perceived positively. Although they themselves are bearing the foreign feeling of having a daughter remotely across the sea for years, they chose to look on the brighter side of things. The optimism and resilience they conveyed are the driving forces for me to face the challenges.

*Ai Wang*

*Newcastle, Australia*

*July 2021*

## Abstract

Mineral separation based on flotation is a complex multiphase multi-step physico-chemical process. In a given flotation system, efficient physical contact between the bubbles and particles is the first step to successful recovery of valuable minerals. Several models are reported in the literature to estimate the efficiency of this physical contact process based on an idealised flow field to simply the problem. Nevertheless, presence of turbulence in any practical flotation system inevitably renders such phase interactions as a stochastic process introducing a distribution of collision efficiency as a function of local flow conditions. This research study aimed to contribute to this less explored area of flotation by investigating the mechanistic effect of turbulence on bubble-particle interactions with specific objectives to quantify collision efficiency distribution; change in bubble rise velocity due to hydrophobic particle attachment to bubble surface and their effect on the overall recovery.

Firstly, the effect of turbulence on collision efficiency was numerically studied for a single-bubble-multiple particles system under typical flotation conditions comprising bubble diameter  $d_B \sim 1$  mm; bubble Reynolds number  $Re_B \sim 230$ ; particle diameter  $d_P \sim 30$  to  $100 \mu\text{m}$ ; and turbulence intensity  $Ti \sim 4\% - 20\%$ . A theoretical model was developed to estimate bubble-particle collision efficiency incorporating the turbulent dispersion behaviour assuming homogeneous turbulence condition. Also developed was an Eulerian-Lagrangian CFD modelling framework incorporating a large eddy simulation (LES) turbulence model and two-way coupling between the particles and fluid through drag and buoyancy force exchange and the random walk model for momentum exchange between particles and surrounding eddies. The CFD model showed chaotic trajectories of particles in the turbulent flow field and produced a distribution of the collision efficiency parameter depending on the local flow conditions. It was noted that particles injected along the bubble centre line had the highest probability for collision. Both the theoretical model and CFD model had comparable prediction for lower turbulence intensity cases ( $<7\%$ ), however a deviation was apparent in the higher turbulence intensity cases.

Secondly, the developed CFD model was applied to simulate the interaction behaviour between a bubble and a particle swarm for a range of solid concentrations ( $\sim 0.39 - 6.16$  vol %) with the same range of turbulence intensity value. The maximum collision efficiency along the injecting radius decreased with the increasing solid concentration as more particles were

dispersed away from the bubble centre at high solid concentrations. In general, the overall collision efficiency was noted to decrease with increasing solid concentration due to the greater lateral dispersion of particles. An optimal turbulence intensity of  $\sim 7\%$  was obtained corresponding to maximum overall collision efficiency. Turbulence intensity however was found to have no significant effect on averaged local solid concentration.

Thirdly, the decrease in bubble rise velocity due to collection of hydrophobic particles at the interface was quantified experimentally. Highspeed imaging was performed to determine the rise velocity of millimetric size particle-laden bubbles ( $d_B \sim 2.76$  to  $3.34$  mm) with bubble surface loading (BSL) varying from 0 to 0.6 both in the absence and presence of surfactant. An image processing methodology was developed to quantify the bubble surface loading as bubble rises. Bubble rise velocity was observed to decrease with bubble surface loading, but this declining trend was less steep in the presence of surfactant. In absence of surfactant, bubble surface loading contributed significantly to surface immobility. A correction factor to Schiller-Naumann drag coefficient model was proposed accounting for the bubble surface loading.

To obtain a more realistic estimation of collision efficiency, earlier developed CFD model was extended to multi-bubble-particles system. The predicted collision efficiency was higher than that in single-bubble domain and the optimal collision efficiency occurred at turbulence intensity  $\sim 20\%$  compared to  $\sim 7\%$  found earlier in single-bubble case. A novel flotation recovery model based on first-order kinetics was finally proposed which included the CFD model predicted collision efficiency and the developed drag correction factor model for particle-laden bubbles. In this recovery model, a maximum bubble surface loading of 0.142 was determined by fitting the model-predicted bubble velocity with available experimental data. With this maximum bubble surface loading constraint, the recovery model predicted two distinct regimes - a loading regime in the early flotation period and a saturated regime wherein the bubble loading capability was entirely exhausted. The model predicted recovery value was compared to a laboratory scale coal flotation test and reasonable agreement was obtained.

# Table of Contents

<b>Chapter 1. Introduction .....</b>	<b>1</b>
1.1. Background of the study.....	1
1.2. Problem statement .....	5
1.3. Research objectives .....	6
1.4. Organization of the thesis.....	7
<b>Chapter 2. Literature Review .....</b>	<b>10</b>
2.1. Flotation recovery model.....	10
2.2. Modelling of bubble-particle collision .....	13
2.2.1. Bubble-particle collision in the absence of turbulent flow .....	13
2.2.2. Bubble-particle collision in the presence of turbulent flow .....	27
2.3. Bubble surface loading (BSL).....	38
2.3.1. Bubble loading method in stagnant liquid and flowing liquid.....	39
2.3.2. Measurement of the bubble surface loading .....	41
2.3.3. Maximum bubble surface loading.....	49
2.3.4. The terminal rise velocity of particle-laden bubbles.....	51
2.4. Knowledge gap .....	54
2.5. Research scope .....	55
<b>Chapter 3. Effect of turbulence dispersion on bubble-particle collision efficiency in single-bubble system .....</b>	<b>56</b>
3.1. Introduction .....	56
3.2. Critical distance for particle injection above a stationary bubble .....	58
3.3. Theoretical modelling: Turbulence dispersion.....	61
3.3.1. Horizontal displacement of particles due to mean flow.....	62
3.3.2. Horizontal displacement of particles due to fluctuating flow .....	64
3.3.3. Collision efficiency .....	65
3.4. CFD modelling .....	66
3.5. Results and discussion.....	73
3.5.1. Model validation .....	73
3.5.2. Turbulence dispersion (TD) model and CFD model: comparison of collision efficiency.....	77
3.5.3. Particle dispersion .....	83

3.6. Conclusion .....	91
<b>Chapter 4. The effect of solid concentrations on bubble-particle collision efficiency in single-bubble system .....</b>	<b>93</b>
4.1. Introduction .....	93
4.2. CFD modelling methodology .....	94
4.3. Data analysis.....	96
4.3.1. Determination of particle volumetric concentration around the bubble .....	96
4.3.2. Particle tracking method of determining collision efficiency along radius ...	97
4.3.3. Overall collision efficiency .....	98
4.4. Results and discussion.....	100
4.4.1. Flow pattern and particle movement.....	100
4.4.2. Particles collision number and local solid concentration .....	104
4.4.3. Turbulent collision efficiency .....	108
4.5. Conclusion.....	112
<b>Chapter 5. Effect of bubble surface loading on bubble rising velocity .....</b>	<b>114</b>
5.1. Introduction .....	114
5.2. Experimental methodology .....	116
5.2.1. Materials.....	116
5.2.2. Method.....	118
5.2.3. Data processing .....	120
5.3. Results and discussion.....	127
5.3.1. Bubble rising behaviour .....	127
5.3.2. Bubble rise velocity and drag coefficient.....	135
5.4. Conclusion.....	143
<b>Chapter 6. Development of a flotation recovery model.....</b>	<b>145</b>
6.1. Introduction .....	145
6.2. Multi-bubble flotation system .....	147
6.2.1. Modelling method .....	147
6.2.2. Data analysis .....	149
6.2.3. Modelling results.....	151
6.3. Flotation recovery model.....	155
6.4. Results and discussion.....	162
6.4.1. Bubble surface loading and predicted recovery in a batch flotation cell ....	162
6.4.2. Recovery in a semi-batch flotation cell.....	169

6.5. Conclusion .....	173
<b>Chapter 7. Conclusions and recommendations.....</b>	<b>175</b>
7.1. Summary of the work .....	175
7.2. Recommended future work .....	180
<b>References.....</b>	<b>182</b>
<b>Appendix A – Turbulent eddy sizes .....</b>	<b>197</b>
<b>Appendix B – Inlet turbulence intensity levels in single-bubble domain.....</b>	<b>199</b>
<b>Appendix C - Surface area of an ellipsoidal cap .....</b>	<b>201</b>

# List of Figures

<b>Fig. 1.1.</b> Schematic sketch of the bubble-particle interaction in a mechanical flotation cell: (a) a flotation cell; (b) hydrophobicisation of mineral particles; (c) three sub-processes of bubble-particle interactions; and (d) particle recovery in froth layer. ....	2
<b>Fig. 2.1.</b> Bubble-particle collision regimes (not to scale) based on bubble diameter, particle size and particle density (Nguyen and Schulze, 2004). ....	13
<b>Fig. 2.2.</b> Schematic of bubble-particle collision with grazing trajectories of particles in laminar flow. ....	14
<b>Fig. 2.3.</b> Schematic of bubble-particle collision scenarios in turbulent flow: 1) The velocity of bubble (blue circle) and particle (red circle) are dependent on the eddy and collision occurs in the same eddy; 2) the velocity of bubble and particle (black circles) are independent on the eddy and particles migrate to another eddy to collide with the bubble (Nguyen et al., 2016). ....	32
<b>Fig. 2.4.</b> Schematic of the four types of particle loading onto a bubble: (a) monolayer loading; (b) multilayer loading; (c) loading of particle clusters; (d) loading of particles-small-bubbles clusters ....	38
<b>Fig. 2.5.</b> Schematic of bubble loading method in the stagnant liquid: (a) Bubble Pick-up method (Wimmers and Fortuin, 1988); (b) Top-loading method (Gallegos-Acevedo et al., 2006); (c) suspension loading method (Xia et al., 2018). ....	40
<b>Fig. 2.6.</b> Schematic of experimental set up to determine the bubble surface loading in flowing liquid: (a) particle-laden bubble rising in flotation column (Bradshaw and Connor, 1996); (b) particle-laden bubble held stationary while slurry flowing downwards (Vinke et al., 1993). ....	41
<b>Fig. 2.7.</b> Optical method of measuring bubble surface loading: (a) Schematic of angle measurement of the particle-laden bubble (Huang et al., 2011); (b) Curving fitting of the particle-laden bubble pendant (Wang et al., 2019a). ....	43
<b>Fig. 2.8.</b> Direct method of measuring bubble surface loading: (a) Measurement of bubble diameter and (b) Bubble surface loading sampler. (Ostadrahimi et al., 2019). ....	44
<b>Fig. 2.9.</b> Schematic of different parameter to represent bubble surface loading. ....	45
<b>Fig. 3.1.</b> Schematic of the distortion of streamline around the bubble. ....	59
<b>Fig. 3.2.</b> The normalized distance between the bubble centre and height where onset of streamline distortion occurs as a function of bubble Reynolds number. ....	61

<b>Fig. 3.3.</b> Decomposition of the particle position into the mean flow and the fluctuating flow: (a) in low turbulence intensity case; (b) in high turbulence intensity case. The symbols are: ● Initial position of the particle; ○ the critical position when particle just touches the bubble; and ⊖ the two-extreme boundaries of the final position of the particle. ....	62
<b>Fig. 3.4.</b> Computational domain and boundary conditions.....	66
<b>Fig. 3.5.</b> Bubble drag coefficient vs number of cells for $Re_B \sim 230$ , $R_B \sim 500 \mu\text{m}$ . ....	67
<b>Fig. 3.6.</b> The change of collision efficiency with number of particles for turbulence intensity $Ti \sim 4\%$ and particle diameter $d_P \sim 60 \mu\text{m}$ at bubble Reynolds number $Re_B \sim 230$ . 73	
<b>Fig. 3.7.</b> Comparison of collision efficiency predicted by Turbulence Dispersion model with the literature (Dai et al., 2000) as a function of particle size. The Weber-Paddock collision model for both mobile bubble surface and immobile bubble surface, denoted by the subscripts $m$ and $im$ were included ( $d_B \sim 0.77 \text{ mm}$ , $U_B \sim 0.316 \text{ m/s}$ , $\rho_p \sim 2650 \text{ kg/m}^3$ , $\rho_j \sim 1000 \text{ kg/m}^3$ , $\mu_L \sim 0.001 \text{ kg.m}^{-1}\text{s}^{-1}$ ). ....	74
<b>Fig. 3.8.</b> Validation of DPM model in the absence of turbulence for $d_B \sim 1 \text{ mm}$ : (a) bubble drag coefficient vs. bubble Reynolds number and (b) collision efficiency vs. particle radius at $Re_B \sim 230$ . The symbols are: ○ Schiller Naumann drag model ( <i>Schiller and Naumann, 1933</i> ); □ Yoon-Luttrell ( <i>Yoon and Luttrell, 1989</i> ) model; * Weber Paddock model ( <i>Weber and Paddock, 1983</i> ) and ● DPM model (present study). ....	76
<b>Fig. 3.9.</b> Comparison of collision efficiency $E_c$ over the initial releasing radius $R_i/R_B$ in various particle size cases predicted by the turbulence dispersion (TD) model and CFD model at: a) $Ti \sim 4\%$ ; b) $Ti \sim 20\%$ . ....	78
<b>Fig. 3.10.</b> Collision efficiency $E_c$ vs the normalized initial releasing radius $R_i/R_B$ : a) $d_P \sim 30 \mu\text{m}$ ; b) $d_P \sim 60 \mu\text{m}$ ; c) $d_P \sim 100 \mu\text{m}$ . – ⊖ denotes the grazing radius beyond which particles released would not collide in flow of the same bubble Reynolds number and particle diameter in the absence of turbulence.....	81
<b>Fig. 3.11.</b> Normalized 90%-collision radius $R_{90\%}/R_B$ vs turbulence intensity $Ti \sim 4\%$ to 20% for three different particle diameters. ....	83
<b>Fig. 3.12.</b> Energy dissipation rate contours of (a) $Ti \sim 4\%$ and (b) $Ti \sim 20\%$ on the centre plane $y = 0 \text{ mm}$ at different time instants. ....	85
<b>Fig. 3.13.</b> Average energy dissipation rate in flow direction from the inlet for different inlet turbulence intensities. ....	86

<b>Fig. 3.14.</b> Particle trajectories for different turbulence intensities at $R_i/R_B = 0.232$ (up) and 1.000 (down) for $d_P \sim 60 \mu\text{m}$ . For illustration purpose 8 particles are presented in each case.....	87
<b>Fig. 3.15.</b> The temporal horizontal displacement ( $s = \sqrt{x_p^2 + y_p^2}$ ) of particle trajectories from the bubble vertical centre axis for different turbulence intensities and particle sizes. Particles were released at $R_i/R_B = 0.232$ at time = 0 s.....	88
<b>Fig. 3.16.</b> Spatial evolution of particle velocity (a) and inertial force (b) in horizontal direction under different particle diameters and turbulence intensities for particle released at $R_i/R_B \sim 0.232$ .....	90
<b>Fig. 4.1.</b> 3D Computation domain used for simulation with sectional view of the mesh around bubble.....	95
<b>Fig. 4.2.</b> Schematic of counting particle concentration in virtual shells around the bubble and tracking individual particles from the releasing bins above.....	97
<b>Fig. 4.3.</b> Definition of the normalized equivalent critical radius $K_1 (R_C/R_B)$ , (left side: Actual probability of collision; right side: the equivalent probability of collision) .....	99
<b>Fig. 4.4.</b> Interaction of particles with fluid at $Re_B \sim 230$ for $Ti \sim 0\%$ to 20% at (a) $C_{P,i} \sim 0.39 \text{ vol\%}$ ; (b) $C_{P,i} \sim 3.08 \text{ vol\%}$ . Vortex was marked by Q criterion = 1. Particle locations were extracted at 0.0107 s after the first injection.....	101
<b>Fig. 4.5.</b> Particle radial velocity as a function of turbulence intensity at $Re_B \sim 230$ for different injecting solid concentration at 0.0112 s after the first injection.....	102
<b>Fig. 4.6.</b> Interaction of particle with fluid at $Re_B \sim 230$ for (a) $Ti \sim 4\%$ , $C_{P,i} \sim 0.77 \text{ vol\%}$ ; (b) $Ti \sim 20\%$ , $C_{P,i} \sim 0.77 \text{ vol\%}$ . Flow field was marked by streamline, and for demonstration of the evolution of single particle trajectory, only the positions of 4 particles (size exaggerated for illustration purpose) from the particle swarm are shown.....	104
<b>Fig. 4.7.</b> The cumulative number of particle-bubble collisions vs time ( $R_{i,cyl} \sim 3R_B$ ; $Ti \sim 4\%$ and $C_{P,i} \sim 3.08 \text{ vol\%}$ ). ....	105
<b>Fig. 4.8.</b> The number of particles that collide against the bubble per time unit vs $R_{i,cyl}/R_B$ ratio for three different solid concentrations $C_{P,i}$ : a) $Ti \sim 4\%$ ; b) $Ti \sim 20\%$ .....	106
<b>Fig. 4.9.</b> Solid concentration vs $R_{s,j}/R_B$ ratio at 0.0132 s after the first injection of particles: (a) $Ti \sim 4\%$ , $C_{P,i} \sim 0.77 \text{ vol\%}$ ; (b) $Ti \sim 4\%$ , $C_{P,i} \sim 1.54 \text{ vol\%}$ ; (c) $Ti \sim 4\%$ , $C_{P,i} \sim 3.08 \text{ vol\%}$ ; (d) $Ti \sim 20\%$ , $C_{P,i} \sim 0.77 \text{ vol\%}$ ; (e) $Ti \sim 20\%$ , $C_{P,i} \sim 1.54 \text{ vol\%}$ ; (f) $Ti \sim 20\%$ , $C_{P,i} \sim 3.08 \text{ vol\%}$ .....	107

<b>Fig. 4.10.</b> The injected and collided particle number vs $R_{bin,i}/R_B$ ratio. ( $Ti \sim 4\%$ ; $C_{P,i} \sim 3.08$ vol% and $R_{i,cyl}/R_B \sim 5.0$ ).....	109
<b>Fig. 4.11.</b> Collision efficiency vs $R_{bin,i}/R_B$ ratio for $C_{P,i} \sim 0.77\% - 3.08$ vol% at (a) $Ti \sim 4\%$ ; (b) $Ti \sim 20\%$ .....	110
<b>Fig. 4.12.</b> Change of turbulent collision efficiency vs solid concentration around the bubble for different turbulence intensity values. .....	111
<b>Fig. 5.1.</b> Variation of contact angle with the concentration of hydrophobic agent ...	117
<b>Fig. 5.2.</b> Schematic diagram of the experimental setup for determining bubble rising behaviour.....	118
<b>Fig. 5.3.</b> Schematic of the experimental setup for vortex identification.....	120
<b>Fig. 5.4.</b> Image processing algorithm applied to determine the bubble surface loading of a rising particle-laden bubble: (step 1) high-speed image; (step 2) Boundary marking; (step 3) Identification of the loading section and reconstruction of the bubble surface.....	122
<b>Fig. 5.5.</b> Determining the two loading points: (a) two loading points marked on the bubble (b) enlarged zoom-in angle of the determined loading points; (c) the critical angle as a function of the distance in pixels. ....	123
<b>Fig. 5.6.</b> Image processing algorithm applied to determine the bubble surface loading of the particle-laden bubble pendant: (a) Surface reconstruction of the clean pendant; (b) Loading section identification and surface reconstruction of the particle-laden pendant. ....	125
<b>Fig. 5.7.</b> Image processing algorithm to mark the bubble from the PIV raw images	126
<b>Fig. 5.8.</b> High speed visualizations of particle-laden bubble ( $d_B \sim 2.76$ mm) in 20% of CMC of SDS solution for different initial surface loading level: (a) 0.00; (b) 0.14; (c) 0.40; (d) 0.77.....	128
<b>Fig. 5.9.</b> Variation of trajectory for a particle-laden bubble in (a) 20% of CMC of SDS, $d_B \sim 2.76$ mm; and (b) pure water, $d_B \sim 2.76$ mm for a range of initial bubble surface loading 0.00 – 0.94.....	129
<b>Fig. 5.10.</b> Variation of aspect ratio for particle-laden bubble in (a) 20% of CMC of SDS, $d_B \sim 2.76$ mm; and (b) pure water, $d_B \sim 2.76$ mm for a range of initial bubble surface loading 0.00 – 0.94.....	130
<b>Fig. 5.11.</b> Evolution of instantaneous bubble surface loading in (a) 20% of CMC of SDS, $d_B \sim 2.76$ mm; and (b) pure water, $d_B \sim 2.76$ mm for a range of initial bubble surface loading 0.00 – 0.94.....	131
<b>Fig. 5.12.</b> Schematic of the critical loading angle. .....	133

<b>Fig. 5.13.</b> Contours of vorticity around the rising bubble ( $d_B \sim 2.70$ mm, $Re_B \sim 775$ ) in pure water at different time instances after the bubble detach from the needle at $t = 0$ ms. Filled circle represents the marked bubble. Colour bar represents the vorticity value. ....	135
<b>Fig. 5.14.</b> Instantaneous velocity of particle-laden bubble vs different bubble surface levels in (a) 20% of CMC of SDS, $d_B \sim 2.76$ mm; (b) pure water, $d_B \sim 2.76$ mm.....	136
<b>Fig. 5.15.</b> Terminal velocity of particle-laden bubble as a function of bubble surface level for two bubble size in different solutions.....	138
<b>Fig. 5.16.</b> Bubble shape vs surface loading in pure water and 20% of CMC of SDS surfactant.....	139
<b>Fig. 5.17.</b> The drag coefficient of particle-laden bubble as a function of bubble surface level for two bubble size in different solutions.....	140
<b>Fig. 5.18.</b> The correction factor as a function of bubble surface loading level in (a) 20% of CMC of SDS, $d_B \sim 2.76$ mm; and (b) pure water, $d_B \sim 2.76$ mm for a range of initial bubble surface loading 0.00 – 0.94.....	142
<b>Fig. 6.1.</b> (a) 3D computational domain and boundary conditions and (b) the top view of nine - bubble arrangement. .....	148
<b>Fig. 6.2.</b> Sectional view of the poly-hexacore meshing in the plane of (a) $z \sim 4$ mm and (b) middle plane $y \sim 0$ mm.....	149
<b>Fig. 6.3.</b> Schematic of tracking individual particles from releasing bins in the presence of multiple bubbles: (a) top view; (b) side view of Plane A-A.....	150
<b>Fig. 6.4.</b> Collision efficiency with the central bubble and the surrounding bubbles vs $R_{bin,i} / R_B$ ratio for particle injecting concentration $C_{P,i} \sim 3.08\%$ at (a) $Ti \sim 0\%$ ; (b) $Ti \sim 4\%$ ; (c) $Ti \sim 20\%$ .....	152
<b>Fig. 6.5.</b> Comparison of collision efficiency in (a) single-bubble system and (b) multi-bubble system for different turbulence intensities and solid concentrationa.....	154
<b>Fig. 6.6.</b> Comparison of flow field in (a) single-bubble domain and (b) multi-bubble domain at $Ti \sim 20\%$ (Up: instantaneous velocity field; Down: flow streamline). .....	155
<b>Fig. 6.7.</b> Schematic of bubble-particle interaction process in the pulp phase. ....	156
<b>Fig. 6.8.</b> Comparison of bubble solid loading, $BSL$ and bubble rise velocity, $U_B$ with Huang et al (2011) for solid concentration $\epsilon_S \sim 0.69\%$ . Here $H_{B,trav}$ represents the distance travelled by the bubble over time.....	164
<b>Fig. 6.9.</b> Temporal evolution of a) Bubble velocity $U_B$ and bubble surface loading $BSL$ ; and b) Recovery $R$ , calculated from the collision efficiency in both single-bubble (SB) and	

multi-bubble (MB) domain, for three different solid concentrations (at $\epsilon_G \sim 10\%$ , $Ti \sim 0\%$ ). .....	166
<b>Fig. 6.10.</b> Temporal evolution of a) Bubble velocity $U_B$ and bubble surface loading $BSL$ ; and b) Recovery $R$ , at $\epsilon_G \sim 10\%$ and $\epsilon_S \sim 0.44\%$ for three different solid concentrations. $U_B$ , $BSL$ and $R$ were calculated from the collision efficiency in multi-bubble (MB) domain.....	168
<b>Fig. 6.11.</b> Recovery profile for five different solid concentrations at $Ti \sim 0\%$ in a semi-batch flotation process. R was calculated from the collision efficiency in both single-bubble (SB) and multi-bubble (MB) domain.....	170
<b>Fig. 6.12.</b> Model predicted recovery calculated using collision efficiency determined for a) single-bubble cases and b) multi-bubble cases, under different turbulence for $\epsilon_S \sim 1.83\%$ in a semi-batch flotation process for different turbulence intensities. ....	171
<b>Fig. 6.13.</b> Comparison of model predicted recovery with Yang et al (2018), solid concentration $\epsilon_S \sim 6.90\%$ , gas volume fraction $\epsilon_G \sim 2.10\%$ . ....	172
<b>Fig. A.1.</b> Autocorrelation function at plane $y = 0$ for different turbulence intensity.....	197
<b>Fig. B.1.</b> Temporal evolution of spatial-averaged RMS velocity on the inlet for different turbulence intensity levels.....	200
<b>Fig. C.1.</b> Schematic of the ellipsoidal cap.....	201
<b>Fig. C.2.</b> X-Z plane of the ellipsoid.....	202

## List of Tables

<b>Table 2.1.</b> Collision efficiency models in the absence of turbulent flow .....	22
<b>Table 2.2.</b> Comparative summary of turbulence consideration in numerical modelling of flotation.....	30
<b>Table 2.3.</b> A summary of turbulence intensity range in studies of bubble-particle collision.....	36
<b>Table 2.4.</b> Models of turbulent collision efficiency .....	37
<b>Table 2.5.</b> The conversion of BSL from original parameters (angles, particle number etc.) into the ratio of the surface area occupied by particles to the whole bubble surface area. ....	46
<b>Table 2.6.</b> Previous studies on measuring bubble surface loading.....	47
<b>Table 2.7.</b> A summary of models for maximum bubble surface loading.....	50
<b>Table 3.1.</b> Governing equations of the CFD model .....	68
<b>Table 3.2.</b> Summary of the operating conditions and numerical scheme used in simulations .....	71
<b>Table 4.1.</b> A summary of input phase parameters of CFD model, boundary conditions and numerical scheme.....	96
<b>Table 4.2.</b> Summary of the ratio of particle diameter to the integral length scale of the flow for turbulence intensity 4% - 20%. ....	103
<b>Table 4.3.</b> Average local concentration in the virtual shell of radius $R_{s,j} \sim 1.4R_B$ to $2.8R_B$ . ....	108
<b>Table 5.1.</b> A summary of bubble size and surface mobility in pure water / SDS solution .....	116
<b>Table 5.2.</b> Fitting parameters in the bubble rise velocity correlation.....	138
<b>Table 6.1.</b> Physical properties and operating conditions used in the model prediction .....	163
<b>Table 6.2.</b> Input phase parameters of the recovery model .....	165
<b>Table 6.3.</b> Input phase parameters for the model prediction .....	172
<b>Table A.1.</b> Summary of length scales for different turbulent intensity .....	198

## List of publications

Peer reviewed journal papers:

1. Ai Wang, Mohammad Mainul Hoque, Roberto Moreno-Atanasio, Geoffrey Evans, Subhasish Mitra, Development of a flotation recovery model with CFD predicted collision efficiency, *Minerals Engineering*, 159, 2020, 106615.
2. Ai Wang, Mohammad Mainul Hoque, Roberto Moreno-Atanasio, Elham Doroodchi, Geoffrey Evans, Subhasish Mitra, Effect of bubble surface loading on bubble rising velocity, *Minerals Engineering*, 2021 (under review).

Peer reviewed conference papers:

1. Ai Wang, Mohammad Mainul Hoque, Linhan Ge, Geoffrey Evans, Subhasish Mitra, Effects of turbulence on bubble-particle collision in flotation: A LES-Lagrange approach, *XXIX International Mineral Processing Congress (IMPC), Moscow, Russia, 17<sup>th</sup> Sep. – 21<sup>st</sup> Sep., 2018*.
2. Ai Wang, Subhasish Mitra, Mohammad Mainul Hoque, Roberto Moreno-Atanasio, Geoffrey Evans, A novel flotation recovery model that includes CFD-computed turbulence intensity on particle-bubble collision efficiency, *Flotation 19, Cape Town, South Africa, 11<sup>st</sup> Nov.– 14<sup>th</sup> Nov., 2019*.

# Nomenclature

$a, b$	semi-minor, semi-major axis	(m)
$A_{cross,B}$	the cross-sectional area of bubble	(m <sup>2</sup> )
$a_p, b_p$	particle coefficient of the correlation coefficient $A_p$	(-)
$A_p$	correlation coefficient	(-)
$AR$	aspect ratio	(-)
$b_m$	machine acceleration	(m/s <sup>2</sup> )
$BSL$	bubble surface loading	(-)
$BSL_{crit}$	critical bubble surface loading	(-)
$BSL_{initial}$	initial bubble surface loading of the bubble pendant	(-)
$BSL_{max}$	maximum bubble surface loading	(-)
$C_d$	bubble drag coefficient	(-)
$C_{D,BP}$	drag coefficient of the particle-laden bubble	(-)
$CMC$	Critical Micelle Concentration	(-)
$C_p(\Delta t)$	average number concentration of particles	(/m <sup>3</sup> )
$C_{p,sB,j}$	solid volumetric concentration of the virtual shell $j$ around the bubble	(vol %)
$C_{p,i}$	particle injection concentration	(vol %)
$C(r_{auto})$	autocorrelation function	(-)
$d_B, d_p$	bubble/particle diameter	(m)
$E_A$	attachment efficiency	(-)
$E_c$	collision efficiency	(-)
$E_{ci}$	collision efficiency at the releasing radius $R_i$	(-)
$E_{ct,i}$	collision efficiency of each bin in turbulent environment	(-)
$E_D$	detachment efficiency	(-)
$F_d$	Particle drag force	(N)
$F_{p,r}$	Particle inertial force in horizontal direction	(μN)
$g$	gravitational constant	(m/s <sup>2</sup> )
$H_B$	the vertical distance between bubble centre and particle initial position	(m)
$H_{B,trav}$	travelling distance of bubbles	(m)

$H_{B,\text{onset}}$	the vertical distance between bubble centre and particle initial position at the onset of streamline distortion	(m)
$k$	flotation rate constant	(/s)
$K_l$	normalized equivalent critical radius	(-)
$l$	Integral length scale of fluid	(mm)
$M$	the total number of virtual shells	(-)
$m_p$	the mass of a single particle	(kg)
$N$	the total number of bins	(-)
$N_c, N_t$	actual collision number, the total amount of released particles along each circle	(-)
$N_{\text{collision},i}$	the number of collided particles in bin $i$	(-)
$N_{\text{injected},i}$	the number of injected particles in bin $i$	(-)
$N_p$	the number of particles remained in the pulp	(-)
$N_{P,\text{collision}}$	the number of collided particles	(-)
$N_{P,\text{encountered}}(\Delta t)$	the number of particles encountered by the bubble during $\Delta t$	(-)
$N_{P,i}$	the number of particles inside the injection virtual cylinder of radius $R_i$	(-)
$N_{P,j}$	the number of particles in virtual shell $j$	
$N_{P,\text{recovered}}(T)$	the total number of particles recovered after time $T$	(-)
$N_{sB,S}$	the number of particles within the pulp surrounding the single bubble	(-)
$Q$	Q-criterion	( $s^{-2}$ )
$r$	the radial displacement of flow, normalized by bubble radius	(-)
$r_{\text{auto}}$	the difference in the two locations for calculation of autocorrelation function	(m)
$R(t)$	flotation recovery	(-)
$R_B, R_p$	bubble, particle radius	(m)
$R_{B,P,m}$	distance between particle centre axis and bubble centre axis	(m)
$R_{\text{bin},i}$	radius of bin inside the virtual cylinder	(m)
$R_c$	radius of particle grazing trajectory	(m)
$R_i$	radius of releasing circle	(m)
$R_{i,\text{cyl}}$	radius of the injecting virtual cylinder	(m)
$r_o$	the initial horizontal displacement of flow, normalized by bubble radius	(-)

$r_{onset}$	the critical radial displacement of flow at the onset of (-) streamline distortion, normalized by bubble radius	(-)
$R_{s,j}$	radius of virtual shell around the bubble	(m)
$R_{90\%}$	90%-collision radius	(m)
$S$	Strain rate	(s <sup>-1</sup> )
$r'$	the sum of bubble and particle radius normalized by bubble radius	(-)
$S_{bubble}$	the surface area of the bubble	(m <sup>2</sup> )
$S_{cap}$	The surface area of the ellipsoidal cap which is occupied by particles	(m <sup>2</sup> )
$SDS$	Sodium Dodecyl Sulfate	(-)
$S_{loading}$	the area of the bubble surface occupied by particles	(m <sup>2</sup> )
$S_{pendant}$	the surface area of the initial bubble pendant	(m <sup>2</sup> )
$S_{x,mean}$	horizontal displacement of particle due to the mean flow	(m)
$S_{x,fluc}$	horizontal displacement of particle due to the fluctuating flow	(m)
$T,t$	time	(s)
$Ti$	turbulence intensity	(%)
$t_{tot}$	the total time for particle to travel to the height of the bubble equator	(s)
$T_{wakeshed}$	period of wake shedding for the bubble	(s)
$u_B$	terminal velocity of bubble	(m/s)
$U_B$	bubble slip velocity	(m/s)
$u_{BP}$	terminal velocity of the particle-laden bubble	(m/s)
$U_{B\_initial}$	initial bubble rise velocity	(m/s)
$u_{f,rms}$	the RMS velocity of fluid	(m/s)
$\mathbf{u}_i$	the instantaneous velocity of fluid	(m/s)
$\overline{\mathbf{u}}_i$	the mean velocity of fluid	(m/s)
$\dot{\mathbf{u}}_i$	the fluctuating velocity of fluid	(m/s)
$\mathbf{u}_P$	particle velocity	(m/s)
$u_{P,r}$	the horizontal velocity components of particles	(m/s)
	$u_{P,r} = \sqrt{u_{P,x}^2 + u_{P,y}^2}$	
$u_{P,rms}$	the RMS velocity of particle	(m/s)
$u_{P,rms,x-}$	the RMS velocity of particle in $x$ - direction	(m/s)
$u_{P,rms,x}$	the RMS velocity of particle in $x$ direction	(m/s)

$u_{P,x}, u_{P,y}$	the particle velocity in $x$ and $y$ direction	(m/s)
$U_r, U_\theta$	the radial velocity and the tangential velocity of the flow, (-) normalized by bubble velocity	(-)
$U_{r,onset}, U_{\theta,onset}$	the radial velocity and the tangential velocity of the flow at the onset of streamline distortion, normalized by bubble velocity	(-)
$U_{x,onset}$	flow velocity in $x$ direction at the onset of streamline distortion, normalized by bubble velocity	(-)
$u_{rms}$	Root-mean-square velocity	(m/s)
$u'$	Fluctuating velocity	(m/s)
$V_{cross,B}$	the volume of pulp swept by the moving bubble	(m <sup>2</sup> )
$V_G$	the volume of bubble	(m <sup>3</sup> )
$V_{pulp}$	the volume of the associated pulp surrounding the bubble	(m <sup>3</sup> )
$V_{sB,G}$	the volume of a single bubble	(m <sup>3</sup> )
$V_{sB,pulp}$	the volume of pulp surrounding the single bubble	(m <sup>3</sup> )
$V_S$	solid volume	(m <sup>3</sup> )
$V_L$	liquid volume	(m <sup>3</sup> )
$V_{sB,S}$	volume of solid within the pulp surrounding the single bubble	(m <sup>3</sup> )
$V_{sp}$	the volume of a single particle	(m <sup>3</sup> )
$V_T$	the total volume including the single bubble and its surrounding pulp	(m <sup>3</sup> )
$x, y, z$	the coordinates in $x, y$ and $z$ direction, respectively	(m)
$x_{l,i}, y_{l,i}$	coordinates of edge points of the particle-laden bubble	(m)
$y_{B,i}$	y coordinate of the centre of the particle-laden bubble	(m)
$Z_{BP}$	collision frequency	(s <sup>-1</sup> )

### Greek letters

$\alpha_p$	correction factor of drag coefficient	(-)
$\gamma$	the Euler–Mascheroni constant	(-)
$\Delta t$	time interval	(s)
$\varepsilon$	energy dissipation rate	(m <sup>2</sup> /s <sup>3</sup> )
$\epsilon$	volume fraction	(-)
$\zeta$	random number of the Gaussian distribution	(-)
$\eta$	Kolmogorov length scale	(m)
$\theta$	the polar angle of the flow	(rad)
$\theta_{con}$	contact angle	(deg)

$\theta_l$	the angle of loading identification	(deg)
$\theta_o$	the initial angle displacement of the flow	(rad)
$\theta_{onset}$	the polar angle of the flow at the onset of streamline distortion	(rad)
$\theta_{polar}$	polar angle	(deg)
$\theta_{crit}$	critical loading angle	(deg)
$\lambda$	Taylor length scale	(m)
$\mu$	liquid dynamic viscosity	(kg.m <sup>-1</sup> s <sup>-1</sup> )
$\nu$	liquid kinematic viscosity	(m <sup>2</sup> /s)
$\rho$	density	(kg/m <sup>3</sup> )
$\sigma$	surface tension	(N/m)
$\tau_l$	the integral time scale of eddy	(s)
$\phi$	packing factor of particles on bubble surface	(-)
$\psi$	stream function	(-)
$\Omega$	Vorticity	(s <sup>-1</sup> )

### Dimensionless letters

$Ga$	Galileo number
$Re$	Reynolds number
$St$	Stokes number

### Subscript

$B$	Bubble
$P$	Particle
$BP$	Particle-laden bubble
$G$	Gas
$L$	Liquid
$S$	Solid
$pulp$	Pulp (solid + liquid)

# Chapter 1. Introduction

---

***“Mathematics is the tool specially suited for dealing with abstract concepts of any kind and there is no limit to its power in this field.”***

**-Paul Dirac**

## Chapter summary

This chapter provides a background of the bubble-particle interaction mechanism which remains central to the mineral flotation. A brief description of the flotation process is provided with focus on the three sub-process: bubble-particle collision, attachment, and detachment. Specific knowledge gaps in the mechanism of turbulent collision and the rising behaviour of particle-laden bubbles are identified which lead to problem definition of this research work. Finally, the specific objectives of the present research work are presented, followed by the organization of the thesis.

### 1.1. Background of the study

Froth flotation is the most preferred beneficiation technology in mineral processing industry deployed globally. In Australia alone, mineral processing constitutes ~15% of the gross domestic product (GDP) (*Minerals Council of Australia, 2017*). Froth flotation technology has been utilised over a century for the processing of base metals and coal particles in the size range from ~ 20 to 500  $\mu\text{m}$  (Schulze, 1977; Mehta and Ityokumbul, 2003). Specifically, column flotation is applied for particles of finer size (~ 20 to 150  $\mu\text{m}$ , Chegeni et al., 2016; Sarhan et al., 2018) while a larger size range particles (- 500  $\mu\text{m}$ , Schulze, 1977) are separated in conventional mechanical flotation cells. The flotation process works on the principle of selective separation of the desired minerals (hydrophobic) from the gangue particles (hydrophilic) in the presence of a carrier phase (air bubbles). In-depth understanding of bubble-particle interaction is the key to successful separation of desired minerals from gangue materials in flotation.

An example of the flotation process is presented in **Fig. 1.1** to illustrate the significance of bubble-particle interactions. First the slurry is preconditioned by adding a collector chemical (hydrophobic agent) which preferentially adsorbs on the surface of the ore particles (**Fig. 1.1b**) to enhance hydrophobicity of the ore particles. After the slurry is fed to the flotation cell, the high-speed (700 – 1300 rpm) impeller is turned on to keep particles suspended in slurry and to disperse air into small bubbles (diameter, 0.5 mm – 1.0 mm). The spinning impeller inevitably produces turbulent flow, resulting in high collision rate between bubbles and particles in the mixing/aeration zone. After the collision, the hydrophobic ore particles are attached to the bubble surface (**Fig. 1.1c**). The particle-laden bubbles then rise into the separation zone wherein the flow becomes less turbulent. The gangue particles previously entrained in the wake of bubbles settle to the lower part of the flotation cell and are discharged as tailings. The particle-laden bubbles further rise into the concentration zone and become a part of the froth (**Fig. 1.1d**) to be collected as concentrate.

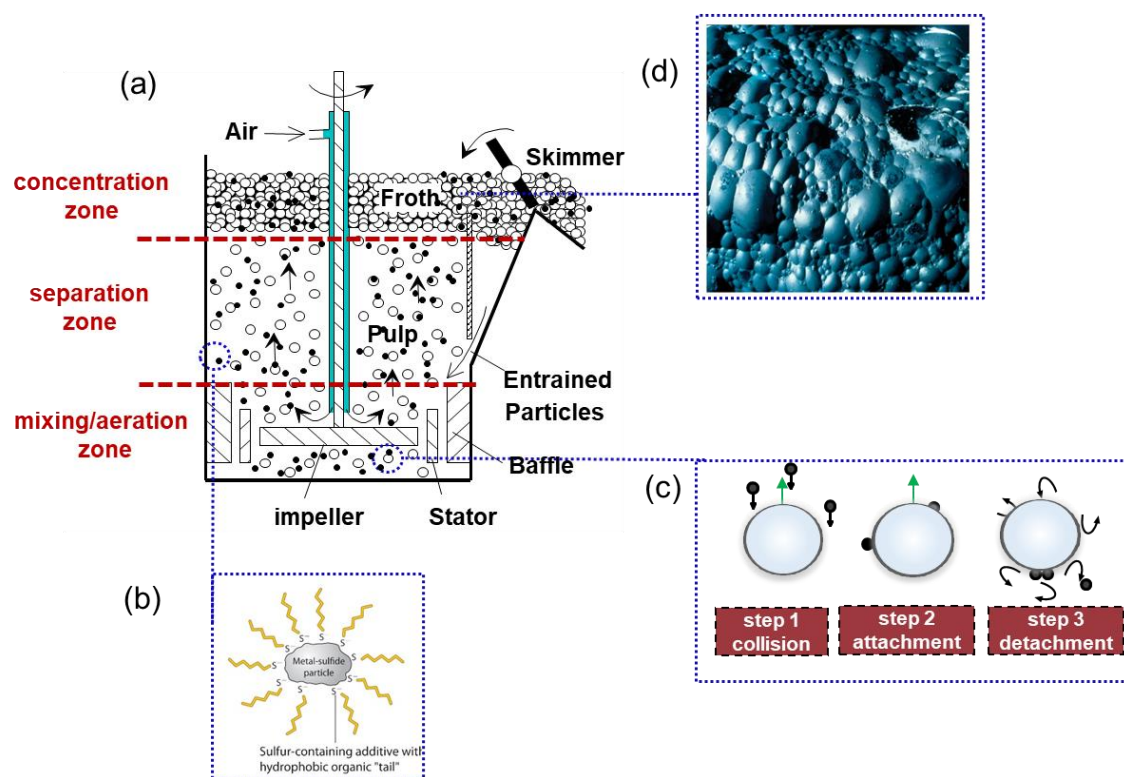


**Fig. 1.1.** Schematic sketch of the bubble-particle interaction in a mechanical flotation cell: (a) a flotation cell; (b) hydrophobicisation of mineral particles; (c) three sub-processes of bubble-particle interactions; and (d) particle recovery in froth layer.

Although flotation is a complex physico-chemical process, it can be simplified into three sub-processes: bubble-particle collision, particles attachment to bubble surface, and particles

detachment from bubble surface (**Fig. 1.1c**). Referring to **Fig. 1.1a**, it could be readily realised that the first step is hydrodynamically dominated which relies on the system flow to facilitate sufficient bubble-particle contacts. The kinetic energy of the turbulent flow in the vicinity of the impeller is dissipated and the energy is transferred to smaller turbulent eddies. Eddies in the universal equilibrium range which are of comparable sizes to the bubble and particles contribute to the fluctuating motion of particles relative to bubbles and lead to bubble-particle collision.

Once a particle collides with a bubble, in the second step, various surface forces i.e. hydrophobic, electrical double layer and van der Waals force contribute to attachment of a particle to bubble interface resulting in draining of the intervening liquid film. Once a three-phase contact line is established, attractive capillary force keeps a particle attached to bubble interface which counterbalances the particle gravity, pressure force (bubble internal pressure, hydrostatic head and fluid pressure) and drag force. In step three, during rise of a bubble-particle aggregate to the froth zone above, some particles may detach from the bubble interface due to continuous interaction with the surrounding flow field. It is important that detachment of particles at the third step be kept at a minimum by suitably tailoring the flow field to maximise the desired mineral recovery.

Clearly, successful operation of flotation depends significantly on the hydrodynamic condition that increases bubble-particle collision (step 1) and decreases bubble-particle detachment (step 3). Industrial flotation devices are often designed based on the heuristics due to lack of appropriate physical models which incurs excessive design margin hence capital cost. From a fundamental research point of view, it is desired that all the substeps of flotation process are known with a better clarity to enable a more first-order-principle based design that has potential to decrease equipment cost.

It is well acknowledged that the bubble-particle collision efficiency in a turbulent flow field is higher than that in the absence of turbulence (Jameson, 2010; Sahbaz et al., 2012; Wang et al., 2017b). To maximize the bubble-particle collisions, flotation cells such as Jameson flotation cell (Sahbaz et al., 2012) and Concorde cell (Jameson, 2010) typically have high-turbulent regions to enhance bubble-particle collisions. For example, the Concorde flotation cell features a choke region to accelerate the speed of slurry to that of sound to generate high turbulence level (Jameson, 2010). As a result, the recovery was boosted by 20% compared to the typical overall plant recovery. Similarly, the application of vortex generator in flotation

column increases the turbulent energy dissipation rate resulting in  $\sim 10\%$  higher recovery compared to a system without a vortex generator (Wang et al., 2017b).

The bubble-particle collision phenomenon in turbulent flow has been primarily investigated based on numerical simulations (Nadeem et al., 2006; Wan et al., 2020; Islam and Nguyen, 2020). In the absence of any direct experimental measurement which understandably is difficult to perform in the complex multiphase flotation system, numerical simulations provide detailed physical information of the system. One of the numerical challenges, however, is to generate an appropriate turbulence condition which resembles a practical flow field (Montorfano et al., 2013). Relatively fewer efforts have been devoted to strengthening the understanding of the bubble-particle collision mechanism in turbulent flow.

Recovery of collected minerals depends on the available buoyancy force of bubbles to reach the froth phase. Uribe-Salas et al. (2003) reports that in the extreme flow conditions (downward slurry more than 0.74 cm/s at solid concentrations 25% - 35%) the bubble surface can be fully loaded with particles, leading to the descending of particle-laden bubbles. As a result of the descending bubbles, the loaded particles on bubble surface were discharged into the tailings rather than collected as concentrates. A limited number of experimental studies were devoted to quantifying the effect of bubble surface loading level on the bubble rising velocity. Eskanlou, et al. (2018a) analysed the rising behaviour of particle-laden bubbles using shadowgraphy imaging technique and found that the velocity of a fully loaded bubble reduced by  $\sim 20\%$  compared to a bare bubble. Furthermore, Wang et al. (2019a, b) quantified the velocity reduction of particle-laden bubbles in the presence of surfactant and proposed a drag coefficient modification factor to include the effect of bubble surface loading (BSL) and the diameters of the loaded particles.

Macroscale empirical and semi-empirical models of the flotation process without considering the bubble-particle collision have been developed by some researchers (Gorain et al., 1995; Amini et al., 2017). These empirical models are suitable for the design and operation of flotation cells, however, their predictive capability is limited outside the domain of the original experiments (Liu and Schwarz, 2009a). Research related to various microscale bubble-particle collision processes occurring in flotation has been considered only under some ideal flow assumptions, for example, quiescent fluid environment (Sherrell, 2004) which is markedly different from practical systems.

## 1.2. Problem statement

In a practical flotation cell there exists a non-uniform distribution of turbulence intensity throughout. For example, high turbulence level exists in the vicinity of impeller and a lower turbulence level exists towards the froth layer away from the impeller. Such spatial distribution of turbulence intensity significantly affects the bubble-particle collision efficiency locally. It is noted that early modelling work in this area however utilized only ideal flow conditions into the collision efficiency models without accounting for turbulence directly (Koh and Schwarz, 2003; Shahbazi et al., 2010).

All reported collision efficiency models are based on a single bubble-particle system. A considerable number of experimental and numerical studies of bubble-particle collision were devoted to analyzing the trajectory of single particle (Nguyen and Schulze, 2004; Nadeem et al., 2006; Islam and Nguyen, 2020). However, in practical flotation system, solid concentration could be as high as  $\sim 25\%$  which can affect the bubble-particle collision efficiency derived this way. The numerical results of Ge et al. (2020) indicated that collision efficiency is a function of solid concentration and bubble Reynolds number in the absence of turbulence. However, there are no reported studies addressing such effect of solid concentration on bubble-particle collision efficiency in turbulent flow.

For successful recovery to occur, particle-laden bubbles need to reach the froth phase. This however is limited by the particle loading on bubbles as bubble buoyancy is compromised at higher surface loading. The rising behaviour of a bubble loaded with particles is therefore another important aspect in flotation research (Uribe-Salas et al., 2003; Huang et al., 2011; Eskanlou et al., 2018a; Wang et al., 2019a, b). Most recovery models however use rise velocity of bare bubbles without accounting for surface loading level (Jameson et al., 1977; Yoon and Mao, 1996). Such assumption may lead to bias of the recovery prediction from the experimental results.

Kinetic models are powerful mathematical tools to include both the turbulent bubble-particle collision and the rising velocity of particle-laden bubbles in the prediction of particle

recovery. A detailed review of the current research status of bubble-particle interaction in modelling the particle recovery is presented in Chapter 2 (Section 2.1). The existing kinetic models only considered collision efficiency in absence of turbulence and only assume the superficial velocity of gas as the rising velocity of bubble without considering the effect of bubble surface loading (Jameson et al., 1977; Yoon and Mao, 1996; Ngo-Cong et al., 2018). A kinetic model which includes the turbulent collision efficiency, and the evolution of the dynamic bubble rising velocity as bubbles load more particles over time, is required to obtain more realistic prediction of recovery in flotation. Recently, Wang et al. (2019a) quantified the reduction in bubble rise velocity due to varied degree of surface loading. However, a significant knowledge gap remains in understanding the dynamics of particle-laden bubble, role of surfactant and how bubble rise velocity and drag coefficient is correlated with bubble surface loading.

### 1.3. Research objectives

This study aims to broaden the physical understanding of the bubble-particle interaction mechanism in turbulent flow. It is realised that several parameters such as turbulence intensity, solid concentration, turbulent dispersion of particles, and bubble surface loading govern the bubble-particle interaction mechanism which in turn affects the final product recovery. Following research objectives were set to quantify these parameters using a combination of numerical and experimental techniques:

1. develop a theoretical model to quantify the effect of turbulence dispersion on the bubble-particle collision efficiency.
2. develop an Eulerian-Lagrangian computational fluid dynamics (CFD) modelling framework including turbulence to simulate the effect of turbulence dispersion of particles on the collision efficiency and compare with the theoretical model prediction in (1).
3. quantify the effect of solid concentration on collision efficiency at different turbulence levels using the CFD model in (2).
4. propose a drag coefficient model for millimetric size bubbles accounting for the effect of bubble surface loading in the absence and presence of surfactant.

5. extend the CFD model in (2) by incorporating multiple bubbles and quantify collision efficiency.
6. develop a first-order flotation model to predict product recovery incorporating the CFD model predicted collision efficiency in (5), solid concentration and bubble surface loading.

#### **1.4. Organization of the thesis**

The structure of this thesis is organized as follows:

In Chapter 2, a comprehensive literature review is provided to address the research background of the problem. A review of the current research status of the bubble-particle interaction in modelling the particle recovery in flotation system is provided to identify the need to investigate interaction mechanism. Next, a review on theoretical modelling, experimental and numerical studies of the bubble-particle collision in laminar flow and in turbulent flow are separately addressed. Finally, studies on the bubble surface loading behaviour are reviewed which include the loading method in stagnant and flowing liquid, the measurement of the bubble surface loading, the range of maximum bubble surface loading in flowing condition and more importantly, the terminal velocity of the particle-laden bubble.

In Chapter 3, the effect of turbulence dispersion on collision efficiency for different particle size and turbulence intensity is investigated. First, the critical distance for the onset of streamline distortion above the bubble is examined over intermediate Reynolds number range typically occurred in flotation. Applying this distance, a theoretical turbulence dispersion model is developed. Also developed is an Eulerian-Lagrangian computational fluid dynamics (CFD) model to predict the collision efficiency and its prediction is compared with the theoretical model. The CFD model performs better in capturing the effect of turbulence dispersion on bubble-particle collision behaviour. The CFD predicted energy dissipation rates and particle trajectories at different turbulence intensities are investigated. The inertia force of particles passing the bubble is analysed. Research objectives 1 and 2 are addressed in this chapter.

In Chapter 4, the effect of solid concentration on collision efficiency in turbulent flow is examined using the developed CFD model in Chapter 3. The interaction between particles

and the fluid is first examined by quantifying distribution of particle in the surrounding vortex, and by the trajectory of particles in the particle swarm at different turbulence intensities. A quasi-steady collision rate regime is then determined by examining the slope of the cumulative particle collision number over time. The effect of different initial releasing radius of the particle swarm is analysed by plotting the collision rate in this quasi-steady regime for different particle concentration. The evolution of local averaged particle concentration in the vicinity of bubble for different turbulence intensities is also examined. The distribution of collision efficiency along the particle injecting radius under different solid concentrations and turbulence intensity is quantified, based on which the overall collision efficiency is examined. Research objective 3 is addressed in this chapter.

In Chapter 5, the rising behaviour of particle-laden bubbles with different bubble surface loading (BSL) level in the absence and presence of surfactant is investigated using high-speed imaging technique. An experimental methodology is developed to obtain the desirable BSL in a controlled manner. An algorithm of quantifying the bubble surface loading is developed. The temporal evolution of apparent BSL on the bubble surface as the particle-laden bubble ascends is studied. A critical BSL below which the expansion of the loaded particles on the bubble surface would occur is calculated and compared with the experimental outcome. In addition, the oscillation period of instantaneous bubble surface loading for low initial BSL in pure water is observed and compared with the reported vortex shedding period for bubble/droplet in literature. The flow separation and vortex shedding around the bare bubble is experimentally confirmed using Particle Image Velocimetry (PIV). Finally, in the presence and absence of surfactant, a correction factor is separately modelled to include the effect of BSLS on the drag coefficient of the particle-laden bubble. Research objective 4 is addressed in this chapter.

In Chapter 6, the effect of turbulent collision efficiency, solid concentration, and bubble surface loading on recovery is investigated. First, the collision efficiency in the presence of multiple bubbles in turbulent flow is numerically examined and the predicted overall collision efficiency is compared with that in the single-bubble system. A theoretical flotation recovery model is then proposed which incorporated the CFD-predicted collision efficiency in Chapters 4 and 6, together with the correction factor of drag coefficient based on bubble surface loading. A maximum bubble surface loading is determined by fitting the model-predicted bubble velocity with available experimental data. With this maximum bubble surface loading

constraint, the regimes of bubble velocity and recovery in batch flotation are identified for different solid concentrations and turbulence intensities. The recovery model is then modified for semi-batch flotation system and optimal turbulence intensity is examined. Finally, the model predicted recovery is compared with that of a lab-scale coal flotation test. Research objectives 5 and 6 are addressed in this chapter.

In Chapter 7, a summary of findings and conclusions drawn in this study is presented, together with the recommendations for future works.

In Appendix A, the length scales of turbulent eddies in the single-bubble flotation domain described in Chapter 3 are quantified.

In Appendix B, the capability of CFD model (developed in Chapter 3) to generate predefined turbulence intensities at the inlet boundary is validated.

In Appendix C, the surface area of an ellipsoidal cap is calculated to determine the bubble surface loading level in Chapter 5.

# Chapter 2. Literature Review

---

In this chapter, firstly the previous studies on the first-order recovery model in flotation are briefly reviewed to identify the current understanding level of bubble-particle collision in turbulent flow and the effect of surface loading level on the bubble rising velocity. Secondly, the bubble-particle collision in laminar is reviewed, followed by discussion on the collision mechanisms. Emphasis is placed on the statistical approach in modelling turbulent flow and the turbulent collision efficiency. The experimental and numerical studies of the collision behaviour in turbulent flow are also discussed. Finally, a comprehensive review of the bubble surface loading (BSL), including the loading method, BSL quantification and the effect of BSL on the rise velocity of bubble-particle aggregate is presented.

## 2.1. Flotation recovery model

Similar to the multi-component chemical reactions wherein the kinetics involve interactions between the molecules, flotation process also involves interactions between the fluid, bubbles and particles. Although a complex process, without loss of generality, flotation process can be conveniently described by an analogous kinetic model reflecting the fact that in a semi-batch system, rate of change in particle concentration is proportional to particle concentration, leading to the following form of kinetic model (Zuniga, 1935):

$$\frac{dN}{dt} = -kN^n \quad (2.1)$$

where the kinetic constant  $k$  is given as

$$k = ZE_c E_a (1 - E_d) \quad (2.2)$$

where  $N$  is the number of particles remained in the flotation domain,  $t$  is the time,  $k$  is the flotation rate constant,  $Z$  is collision frequency.  $E_c$ ,  $E_a$  and  $E_d$  are the collision efficiency, attachment efficiency and detachment efficiency, respectively.  $n$  describes the order of the kinetic model.

For flotation of single ores or dilute slurry,  $n$  is usually observed to be unity. Assuming first-order flotation kinetics, the recovery of particle in flotation can be determined by integrating Eq. (2.1) over time

$$R = 1 - e^{-kt} \quad (2.3)$$

It can be noted from Eq. (2.3) that the recovery can be characterised by the flotation rate constant which is sensitive to the collision frequency and collision efficiency as shown in Eq. (2.2).

Depending on the flow conditions, the flotation rate constant can be approached in different ways (Yoon and Mao, 1996; Duan et al., 2003; Jameson et al., 1977; Koh and Schwarz, 2006). In the absence of turbulence, Jameson, et al. (1977) developed the model of flotation rate constant in flotation cells by assuming zero detachment of particles:

$$k = 1.5 \frac{G_{fr} h}{d_B V_{cell}} E_c E_a \quad (2.4)$$

where  $G_{fr}$  is the air flow rate;  $h$  is the height of the flotation cell;  $d_B$  is the bubble diameter and  $V_{cell}$  is the volume of the flotation cell. Similarly, Yoon and Mao (1996) developed a model of flotation rate constant for continuous generation of single bubbles in a flotation column:

$$k = \frac{3U_B}{4R_B} E_c E_a (1 - E_d) \quad (2.5)$$

where  $U_B$  is the superficial velocity of air which is defined as the volumetric air flow rate divided by the cross-sectional area of the column.

In these models of flotation rate constant in laminar flow, it can be noted that the collision frequency is directly related to the superficial velocity of air. However, in the real flotation system, it is the bubble rising velocity that governs the interaction between bubbles and particles. The bubble rising velocity does not necessarily equal the superficial velocity. Besides, as the bubble surface is loaded with more particles, its rising velocity can be significantly impacted by the level of surface loading (Wang et al., 2019a). Therefore, as the bubble loads more particles, the flotation rate constant over time is a dynamic process evolving with the gradually impacted bubble velocity. However, theoretical kinetic models are most limited to the fixed bubble velocity and fewer efforts have been devoted to strengthening the understanding of such dynamic evolution with varying bubble velocity.

In the presence of turbulence, flow is composed of multi-scale eddies, causing the stochastic movement of bubbles and particles. The flotation rate constant model in turbulent flow becomes a function of the root-mean-square (RMS) fluctuating velocity of bubbles and

particles. Duan et al. (2003) extended the model of Jameson et al. (1977) to include the turbulence effect on the flotation rate constant by adding the root-mean-square velocity term of bubbles. This theoretical model assumed that when the bubble diameter is much larger than the particle diameter, the RMS fluctuating velocity of particles can be neglected. Therefore, the model is expressed as:

$$k = 2.39 \frac{G_{fr}}{d_B V_{cell}} \left[ \frac{0.33 \varepsilon^{4/9} d_B^{7/9}}{\nu^{1/3}} \left( \frac{\Delta \rho_B}{\rho_L} \right)^{2/3} \frac{1}{U_B} \right] E_c E_a (1 - E_d) \quad (2.6)$$

where  $G_{fr}$  is the air flow rate;  $V_{cell}$  is the volume of the flotation cell;  $\varepsilon$  is the energy dissipation rate;  $\nu$  is the kinematic viscosity;  $\Delta \rho_B$  is the difference between the bubble and fluid densities and  $U_B$  is the bubble rising velocity. Nguyen and Schulze (2004) included the RMS fluctuating velocity of particles into the flotation rate constant model:

$$k = \pi (R_p + R_B)^2 (V_s + U_B) N_B f \left[ \frac{\sqrt{U_B'^2 + U_P'^2}}{V_s + U_B} \right] E_c E_a (1 - E_d) \quad (2.7)$$

where  $\overline{U'_B}$  and  $\overline{U'_P}$  are the root-mean-square fluctuating velocity of bubble and particle, respectively,  $V_s$  is the particle settling velocity,  $N_B$  is the bubble number concentration. Koh and Schwarz (2006) further differentiated collision mechanisms base on the particle size by using the collision frequency models of Abrahamson (1975) and Saffman and Turner (1956). For particles of diameter smaller than Taylor length scale, the model is expressed as:

$$k = \sqrt{\frac{8\pi}{15}} N_B \left( \frac{d_p + d_B}{2} \right)^3 \left( \frac{\varepsilon}{\nu} \right)^{0.5} E_c E_a (1 - E_d) \quad (2.8)$$

In comparison, for particles of diameter larger than Taylor length scale, the model is:

$$k = 5 N_B \left( \frac{d_p + d_B}{2} \right)^2 \left( \overline{U'_P}^2 + \overline{U'_B}^2 \right)^{1/2} E_c E_a (1 - E_d) \quad (2.9)$$

Eq. (2.8) - (2.9) were applied in the mass source term in the balance equations of particles to determine the mass transfer of particles from the slurry to the bubble surface in the numerical simulation of flotation cells. The predicted rate constant qualitatively agreed with the reported data from the literature. Similarly, Karimi et al. (2014a) applied the rate constant model of Duan et al. (2003) to the mass source term of particles continuity equation in the Computational Fluid Dynamics (CFD) modelling of flotation cells to determine the effect of impeller speed

and gas flow rate etc. on the flotation rate constant. The numerical predictions agreed quantitatively with the experiments.

One of the key parameters in the flotation rate constant is the bubble-particle collision efficiency which is directly governed by the local flow conditions. In the next section, different mechanisms of bubble-particle collision efficiency in the absence and presence of turbulent flow are reviewed.

## 2.2. Modelling of bubble-particle collision

### 2.2.1. Bubble-particle collision in the absence of turbulent flow

Depending on particle inertia, bubble size and bubble surface mobility, bubble-particle collision in the absence of turbulence may be governed by several mechanisms: a) Brownian collision; b) collision by interception; c) collision by inertial impact; and d) collision by gravity. Brownian collision is caused by molecular diffusion of submicron particles, which are much smaller than the size range of particles featured in flotation. Hence, the Brownian collision is not dealt in this review. The regime map for these mechanisms is presented in **Fig. 2.1**. It is noteworthy mentioning that the boundary between each mechanism is not fully understood and bubble-particle collisions may be subject to several mechanisms at the same time.

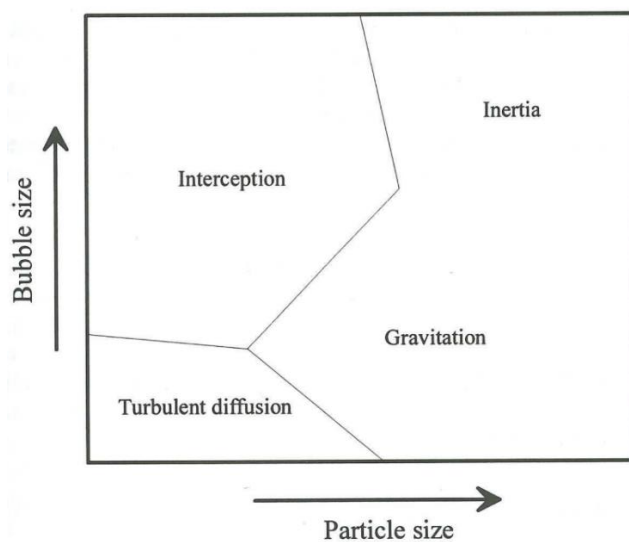


**Fig. 2.1.** Bubble-particle collision regimes (not to scale) based on bubble diameter, particle size and particle density (Nguyen and Schulze, 2004).

A convenient way to describe the parameters of bubble-particle collision is to use dimensionless numbers, such as the Bubble Reynolds number ( $Re_B$ ), Particle Stokes number ( $St$ ) and Galileo number ( $Ga$ ). These three dimensionless numbers represent the flow field around the bubble, how close the particles follow the fluid streamline, and the interplay between the gravity and viscous force, respectively. These three numbers are described below:

$$Re_B = \frac{2R_B U_B \rho_L}{\mu_L} \quad (2.10)$$

$$St = \frac{2\rho_p U_B R_p^2}{9R_B \mu_L} \quad (2.11)$$

$$Ga = \frac{8(R_B + R_p)^3 g(\rho_p - \rho_L) \rho_L}{\mu_L^2} \quad (2.12)$$

where  $R_B$  and  $R_p$  are the bubble and particle radii, respectively,  $U_B$  is the bubble slip velocity,  $\rho_L$  and  $\rho_p$  are the liquid and particle densities,  $\mu_L$  is the dynamic viscosity of the liquid.

The bubble-particle collision can be quantified by collision efficiency, which is defined by the ratio of the number of particles collided with a bubble to the total number of particles in the path swept by the bubble. In the absence of turbulence, the trajectory of a particle is deterministic, and a grazing trajectory exists where the particle, initially located at the injecting radius  $R_c$ , just touches the bubble, as shown in **Fig. 2.2**. Only particles initially located within the critical radius  $R_c$  will collide with the bubble.

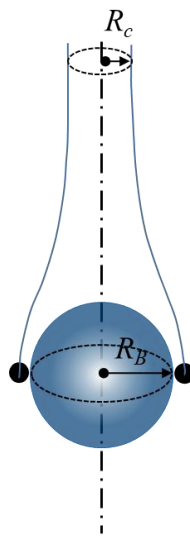


**Fig. 2.2.** Schematic of bubble-particle collision with grazing trajectories of particles in laminar flow.

The collision efficiency can therefore be described as the ratio of the area inscribed by the critical radius  $R_c$  to the area inscribed by the bubble radius  $R_B$ , namely:

$$E_c = \frac{R_c^2}{R_B^2} \quad (2.13)$$

It is clear that calculation of the critical radius  $R_c$  of the grazing trajectory is essential to determine the collision efficiency. Depending on the collision mechanism, the critical radius can be calculated differently. A brief description of the three collision mechanisms and the determination of collision efficiency for each mechanism are provided below.

### **2.2.1.1. Interceptional collision**

If the particle inertia can be neglected i.e. if the particle Stokes number is negligible, it can be assumed that the particle centre follows fluid streamline closely. Therefore, the grazing trajectory of the particle is equivalent to the grazing fluid streamlines. Interceptional collision is due to the compression of fluid streamline passing the bubble, causing the particle to make contact with the bubble. To quantify the collision efficiency, the critical radius  $R_c$  is determined from the grazing fluid streamline. Depending on the bubble Reynolds number  $Re_B$ , the flow condition can be classified into three categories: Stokes flow, for  $Re_B$  much less than unity; potential flow, for very large  $Re_B$ ; and intermediate flow, for  $Re_B$  between the two extremes. Among them, analytical solutions of streamlines for Stokes flow and potential flow exist (Yoon and Luttrell, 1989). However, the flow conditions in flotation usually fall into the category of intermediate flow, for which only empirical expression or numerical simulation of streamlines are available (Yoon and Luttrell, 1989).

### **2.2.1.2. Inertial collision**

If the particle Stokes number is larger than 0.08 (Levin, 1961), particles start to deviate from the curved streamline around and continue along a straight path. The grazing trajectory concept, used in examining collision by interception, still applies to the inertial collision. The critical radius of the grazing trajectory is determined by exploring the initial releasing radius of trajectory until the particle contacts the bubble surface. The inertial force of a particle can have either a negative or positive effect on the inertial collision efficiency (Dai et al., 1998).

### **2.2.1.3. Gravitational collision**

The trajectory of a particle may also deviate from the streamline under the influence of gravity. Such deviation increases with either the Galileo number or the scaled particle settling velocity i.e., the particle free-settling velocity normalized by the bubble slip velocity. Dobby and Finch (1987) noted that “Gravitational collision alone is hypothetical; it would occur for particles having a finite settling velocity but zero dimension”. The gravitational collision mechanism usually occurs together with the inertial collision mechanism, and significantly contributes to the bubble-particle collision for particles down to 1  $\mu\text{m}$  in size (Nguyen and Schulze, 2004).

### **2.2.1.4. Previous studies on collision efficiency modelling**

A significant number of studies (Langmuir and Blodgett, 1946; Sutherland, 1948; Gaudin, 1957; Weber and Paddock, 1983; Dobby and Finch, 1987; Yoon and Luttrell, 1989; Dai et al., 1998; Nguyen and Schulze, 2004; Firouzi et al. 2011; Verrelli et al., 2011; Gao, et al., 2017; Hassanzadeh, et al., 2018; Li et al., 2020) were conducted to quantify the collision efficiency analytically, experimentally, and numerically.

#### ***2.2.1.4.1. Analytical studies***

The analytical model of collision efficiency can be obtained under simple flow conditions such as Stokes flow or potential flow through simplification of particle properties. Extensive analytical studies are reported to examine the governing factor of collision.

Among early efforts to analytically model the collision efficiency, Sutherland (1948) developed an efficiency model for collision due to interception by calculating the grazing streamline. Particles were assumed as inertia-free and the streamline function was based on the Ramsey (1935) equation for potential flow. Similarly, Gaudin (1957) applied the Stokes stream functions and reported a collision efficiency model for inertia-free particles in the Stokes flow regime.

In the intermediate flow regime where bubble Reynolds number is between Stokes flow and potential flow, there is a lack of analytical stream function because neither the fluid viscous force nor fluid inertial force dominate. Yoon and Luttrell (1989) approximated an empirical stream function based on reported data in the literature and used this function to develop an efficiency model for collision due to interception in the intermediate flow regime. The

predictions of this model agreed well with flotation test results. As typical flotation falls into the intermediate flow regime, the model developed by Yoon and Luttrell was extensively used in modelling the recovery in both flotation cells and columns (Koh and Schwarz, 2006; Koh and Smith, 2011).

The three collision efficiency models described above were developed based on the assumption that the collision angle was 90°; namely, collision can occur on the whole upper half of the bubble. However, Weber and Paddock (1983) argued that for collision by interception, the collision angle for a spherical bubble and particles is less than 90°, and can be calculated when the radial flow velocity on the bubble surface is zero. By assuming Stokes flow and analysing the momentum equation for the particle, Weber and Paddock calculated the collision angle as a function of the Galileo number  $Ga$ , bubble Reynolds number  $Re_B$  and the particle-bubble radius ratio under the condition  $Ga \ll 9Re_B$ . An interceptional-gravitational collision efficiency model for bubble Reynolds numbers up to 300 was developed by Weber and Paddock (1983).

Nguyen and Kmet (1992) argued that the assumption of  $Ga \ll 9Re_B$  in Weber and Paddock model (1983) only holds true for very light fine particles. Nguyen and Kmet's mathematical model of collision angle removed this assumption and included the effect of hindered settling. Based on the determined collision angle, Nguyen and Kmet proposed an efficiency model of collision-by-interception, combined with collision-by-gravity, in the counter-current flow regime. Good agreement between the experimental values and theoretical predictions were obtained.

Collision by inertial impact is relatively important for coarse and/or heavy particles. Langmuir and Blodgett (1946) developed an inertial collision efficiency model for particle Stokes numbers  $St$  larger than 0.7. Good agreement between the model prediction and the experimental results was achieved. Noting that even weak inertial forces may significantly affect the particle velocity on the bubble surface, Dai et al. (1998) simplified the liquid velocity around the bubble in potential flow regime and proposed an analytical model of collision efficiency - the Generalized Sutherland Equation (GSE) for mobile bubble surfaces. The negative and positive effects of the particle inertia on the collision efficiency were also identified. The GSE model was experimentally validated with minimal deviation for particle Stokes numbers up to 0.27 and particle diameters between 7  $\mu\text{m}$  and 60  $\mu\text{m}$ . Nguyen et al. (2006) also obtained good agreement between GSE model and numerical predictions for

ultrafine particles ( $<10\text{ }\mu\text{m}$  in diameter). However, a significant deviation of GSE model was observed for particle diameter larger than  $50\text{ }\mu\text{m}$ . Additionally, as the particle size increases, the collision angle predicted by the numerical results reduced to a minimum at a certain particle size before the angle increased, unlike the monotonous decreasing trend predicted by GSE model.

While majority of the analytical studies on the bubble-particle collision efficiency focused on spherical particles, there are limited studies which examined the non-spherical particles (Sokovnin et al., 2014; Hassas et al., 2016). Hassas et al. (2016) argued that the trajectory of arbitrary-shaped particles is difficult to predict. Such uncertainty is because the shape and orientation of the particle may affect the drag force, leading to a non-linear settling path (Nguyen and Schulze, 2004). Sokovnin et al. (2014) developed analytical models of collision efficiency for rod-like and disk-like particles in Stokes and Levich regimes. The order of magnitude of the collision efficiency predicted by the models Sokovnin proposed agreed well with the experimental data.

#### ***2.2.1.4.2. Experimental studies***

Experimental studies of collision efficiency can be classified into direct and indirect methods (Nguyen and Schulze, 2004). In the indirect methods, flotation tests are conducted with strong hydrophobic particles where the attachment efficiency and detachment efficiency are considered as unity and zero respectively. Based on first-order kinetics, the collision efficiency can be calculated directly from recovery determined by the tests. In the direct methods, particles are released above a single bubble. The collision efficiency can be determined by finding the grazing trajectory of particles. Experimental investigations using the direct method, however, is limitedly reported due to the smallness of particles which is difficult to capture using optical method.

Experimental investigations (Nguyen and Evans, 2004a; Verrelli et al., 2011; Li et al., 2020) were conducted for the influence of short-range hydrodynamic forces on the trajectory of particles when passing around the bubble. Nguyen and Evans (2004a) quantitatively measured the trajectory of a particle on the surface of a bubble in pure water. The experimental data agreed well with the predictions of the short-range hydrodynamic forces model which they earlier proposed (Nguyen and Evans, 2004b). Verrelli compared the observed trajectories and velocity of particles in pure water with the model proposed by Nguyen and Schulze (2004) and

found that the experimental results of particle movement are closer to the predictions based on mobile surface assumption.

In both the experiments of Nguyen and Evans (2004) and Verrelli et al. (2011), the bubble was held stationary and particles were released from above the bubble. The collision behaviour in rising bubble cases were reported by Li et al. (2020). The trajectories of falling hydrophobic ballotini when colliding or passing a rising bubble deviate considerably from the cases of a stationary bubble superimposed with liquid velocity. Therefore, Li et al. (2020) argued that it is important to consider the real flow condition when modelling the bubble-particle collision.

#### **2.2.1.4.3. Numerical studies**

Numerical examination of the collision efficiency involves modelling the movement of particles in the liquid around a bubble. This modelling can be broadly divided into the Eulerian-Eulerian method, which considers dispersed particle phase as continuous phase, and the Eulerian-Lagrangian method, which considers particles as a discrete phase and tracks the trajectory of each particle. From Section 2.2.1.1 – 2.2.1.3, it is clear that examination of bubble-particle collision efficiency requires tracking the trajectory of each particle. As such, most computational studies in this area applies the Eulerian-Lagrangian method. Additionally, the bubble in the numerical exploring of the collision efficiency is usually considered as undeformable except for rather limited studies (Wierink, 2012). The consideration of rigid bubbles is because for the flotation-sized bubble ( $\sim 1$  mm), the internal air circulation of the bubble is damped in the presence of surfactant on the bubble surface.

The collision angle and collision efficiency can be affected by the short-range hydrodynamic forces which particles were subject to when approaching a bubble. Firouzi et al. (2011) compared the numerical results of the particle momentum equation when the short-range hydrodynamic forces were included and excluded for particles of diameters up to 100  $\mu\text{m}$  and densities in the range of 1300 – 7000  $\text{kg}/\text{m}^3$ . The effect of short-range hydrodynamic forces was found to be significant for light particles (density 1300  $\text{kg}/\text{m}^3$ ) with diameters greater than 40  $\mu\text{m}$  in the absence of surfactant. Liu and Schwarz (2009a) confirmed that the short-range hydrodynamic forces have negligible effect on small particles (diameter  $\leq 30$   $\mu\text{m}$ ). Huang et al. (2012) further found that for small particle Stokes numbers ( $St \sim 0.003$ ) in the

range of  $Re_B \sim 1 - 100$ , the collision efficiencies numerically calculated were insensitive to the short-range hydrodynamic forces for a fully contaminated bubble.

The level of surface mobility significantly affects the flow field in the vicinity of a bubble, further complicating the modelling of collision efficiency (Huang et al., 2012; Legendre e al., 2009). Sarrot et al. (2005) applied direct numerical simulations based on the JADIM code to simulate the flow field around the bubble in a three-dimensional model at  $Re_B \sim 0.01 - 1000$ . The spherical cap model was included in the modelling framework to examine the effect of surface contamination levels on collision efficiency. Boundary conditions on the bubble surface were differentiated between the clean and contaminated region. In the clean region of the bubble surface, the normal velocity and tangential stress were considered zero, whereas in the contaminated region, the no-slip condition was applied to represent the retarded surface. Particles were assumed to be inertia-free. Results of the numerical study revealed that the collision efficiency is dependent on the level of surface contamination, the bubble Reynolds number and the ratio of particle to bubble radius  $d_p / d_B$  or  $(d_p / d_B)^2$ , with the exponent depending on a threshold value. Later, Legendre et al. (2009) established a correlation between the threshold value and the surface contamination together with the bubble Reynolds number.

Huang et al. (2012) extended the work of Sarrot et al. (2005) and Legendre e al. (2009) to include the effect of particle inertia on the collision efficiency using direct numerical simulations for  $Re_B \sim 1 - 100$ ,  $d_p / d_B \sim 0.001 - 0.02$  and particle Stokes number  $St \sim .001 - 1$ . A theoretical model of collision efficiency which included the effect of surface contamination levels was proposed. Large particle Stokes numbers were found to positively affect the collision efficiency because these particles deviate away from the streamline when approaching the bubble surface. On the other hand, small particle Stokes numbers negatively affect the collision efficiency because particles are pulled away from the bubble surface under the influence of centrifugal force exerted on the particle by the tangential liquid velocity. It was also found that a critical surface contamination level exists below this level the collision position between the particle and the bubble is on the mobile surface region, while above this level, the collision position may occur in either the mobile or immobile region on the bubble surface.

The effect of an acoustic field on the bubble-particle collision efficiency was numerically examined by Yasmin et al. (2019) using a one-way coupled 3D numerical model,

which consists of the Rayleigh-Plesset equation for oscillatory bubble motion combined with DEM approach to model particle motion in the presence of an acoustic field (Bond number 0.01 – 0.5). The collision efficiency was improved in both below and above the resonance frequency. Impact regimes were presented with the Bond number and frequency or oscillation amplitude ratio as coordinates. The transition boundaries between the collision and non-collision regimes were quantified. Also identified in this study was the further need to expand the modelling framework to include the effect of shape oscillation mode on bubble-particle collision.

Due to the smallness of particles in flotation, the effect of particle concentration on the bubble-particle collision efficiency is often assumed to be negligible. Therefore, most numerical studies examined the trajectory of a single particle (Nadeem et al, 2006; Huang et al., 2012; Li et al., 2019). However, limited studies (Nguyen and Kmet, 1992; Ge et al., 2020) indeed reported the effect of particles concentration on collision efficiency. Ge et al. (2020) developed a two-way coupled modelling framework, Computational Fluid Dynamics – Discrete Element Method (CFD-DEM), using the open-source software CFDEM. A particle swarm, with solid concentrations in the range of ~ 0.01 – 0.25, was released above the bubble (bubble Reynolds number  $Re_B \sim 50 - 200$ , particle density  $7000 \text{ kg/m}^3$  and diameter  $30 \mu\text{m}$ ). The results indicated that the effect of solid concentration on collision efficiency depends on the bubble Reynolds number. For lower  $Re_B (\leq 150)$ , the increase of solid concentration caused a more lateral expansion of the particle swarm, leading to decreased collision efficiency. For higher  $Re_B (> 150)$ , collision efficiency was insensitive to solid concentration because the inertial collision was dominant.

Following this brief review, a summary of collision efficiency models, either analytical or empirical, is presented in **Table 2.1**.

**Table 2.1.** Collision efficiency models in the absence of turbulent flow

Authors	Collision Models	Type of collision mechanism	Comments
Langmuir and Blodgett (1946)	$E_{c,p} = \left( \frac{St}{St + 0.5} \right)^2$ ( Potential flow) $E_{c,st} = \left( 1 + \frac{3}{4} \frac{\ln(2St)}{St - St_{crit}} \right)^{-2}$ ( Stokes flow) $E_c = \frac{P_{c,p} + (Re_B / 60)E_{c,st}}{1 + Re_B / 60}$	Inertial	$St_{crit}$ equals 1.2 and is the critical particle Stokes number below which bubble-particle inertial collision is zero. $E_{c,st}$ is valid when $St > St_{crit}$ ;
Sutherland (1948)	$E_c = 3R_p / R_B$	Interception	Suitable for potential flow;
Gaudin (1957)	$E_c = \frac{3}{2} (R_p / R_B)^2$	Interception	Suitable for Stokes flow;
Flint and Howarth (1971)	$E_c = \frac{V_s}{V_s + U_B}$	Interception	Suitable for $St$ less than 0.1 at which inertial force is neglected. Validated for $St$ in the range of 0.001 and 0.1.
Reay and Ratcliff (1973)	$E_c = \frac{V_s}{V_s + U_B} (1 + \frac{R_p}{R_B})^2 \sin \theta_c$ $\theta_c = 85.0 - 2.50 \log Re_B$ (for $0.1 < Re_B < 1$ ) $\theta_c = 85.5 - 12.49 \log Re_B$ (for $1 < Re_B < 20$ ) $\theta_c = 78.1 - 7.37 \log Re_B$ (for $20 < Re_B < 400$ )	Interception	Suitable for $St < 0.1$ ; Collision angle has been fitted into a function of $Re_B$ , an improvement over the previous interception models which consider the collision angle as uniformly $90^\circ$
Reay and Ratcliff (1973)	$E_c = m(R_p / R_B)^n$ ( $n > 1$ )	Interception	Suitable for Stokes flow and when both bubble and particle size are very fine ( $R_p < 20 \mu\text{m}$ , $R_B < 100 \mu\text{m}$ ).

Anfruns and Kitchener (1977)	$E_c = \frac{(1+R_p/R_B)^2}{1+V_s/U_B} \left[ v_p/v_b + \frac{2\psi_c}{(1+R_p/R_B)^2} \right]$	Interception	Suitable for Stokes flow; Particle drag force and inertial force were neglected.
Weber and Paddock (1983)	$E_c = \left[ 1 + \frac{2}{1 + (37/\text{Re}_B)^{0.85}} \right] R_p/R_B \quad (\text{mobile bubble surface, } \text{Re}_B < 200)$ $E_c = 1.5 \left[ 1 + \frac{(3/16)\text{Re}_B}{1 + 0.249\text{Re}_B^{0.56}} \right] (R_p/R_B)^2 \quad (\text{immobile bubble surface, } 200 < \text{Re}_B < 300)$	Interception + gravity	Suitable for intermediate flow
Dobby and Finch (1987)	1. Low particle inertia, $St < 0.1$ $E_{co} = E_{c,g} + E_{c,i}$ $E_{c,g} = \frac{V_s}{V_s + U_B} (1 + \frac{R_p}{R_B})^2 \sin \theta_c$ $E_{c,i} = 1.5 \left[ 1 + \frac{(3/16)\text{Re}_B}{1 + 0.249\text{Re}_B^{0.56}} \right] (R_p/R_B)^2$ 2. Intermediate particle inertia, $0.1 < St < 0.8$ $E_c = E_{co} (1.627 \text{Re}_B^{0.06} St^{0.54} (V_s/U_B)^{-0.16})$ $(\text{Re}_B^{0.06} St^{0.54} V_s/U_B^{-0.16} > 0.614, 20 < \text{Re}_B < 300, V_s/U_B < 0.25)$	Combination of interception and inertial	Suitable for intermediate flow; Considered the subrange of particle inertia; Collision angle as a function of $\text{Re}_B$ was taken into account.
Yoon and Luttrell (1989)	$E_c = \left( \frac{R_p}{R_B} \right)^2 \left( \frac{3}{2} + \frac{4\text{Re}_B^{0.72}}{15} \right) \quad (\text{Intermediate flow})$	Interception	Suitable for intermediate flow; Collision angle was considered as uniformly $90^\circ$ Experimentally validated up to $\text{Re}_B \sim 100$ .
Schulze (1989)	The interception effect: (when $R_p/R_B \leq 1/\xi$ ) $E_{c,i} = 1.5 (R_p/R_B)^2 \left[ 1 + \frac{(3/16)\text{Re}_B}{1 + 0.249\text{Re}_B^{0.56}} \right]$	Interception and inertial	

---


$$\xi = 1.5 \left[ 1 + \frac{(3/16) \text{Re}_B}{1 + 0.249 \text{Re}_B^{0.56}} \right] \left( \frac{1}{\sin \theta_c} \right)$$

The gravitational effect:

$$E_{c,g} = \sin^2 \theta_c (1 + R_p / R_B)^2 V_s / U_B$$

The inertial effect:

$$E_{c,in} = \left( \frac{1}{1 + V_s / U_B} \right) (1 + R_p / R_B)^2 \left( \frac{St}{St + a} \right)^b$$

The overall collision efficiency:

$$E_c = E_{c,i} + E_{c,g} + [1 - \frac{E_{c,i}}{(1 + R_p / R_B)^2}] E_{c,in}$$

Schulze (1989)	$E_c = \frac{(St)^c - d}{(St)^c + e}$	Inertial	Suitable for intermediate flow; c, d, e are a function of $\text{Re}_B$ ; interceptional force was not considered.
----------------	---------------------------------------	----------	--

Nguyen and Kmet (1992)	$E_c = \frac{U_B}{U_B + V_s} \left( \frac{R_p}{R_B} \right)^2 (1.5 + \frac{9 \text{Re}_B}{32(1 + 0.249 \text{Re}_B^{0.56})})$ $+ g(\text{Re}_B) \frac{Ga}{18 \text{Re}} (1 - \alpha_s)^{4.86}$ $g(\text{Re}_B) = 0.9983 + 1.084e - 3 \log(\text{Re}_B) + 2.129e - 4 \log^2(\text{Re}_B) - 3.997e - 4 \log^3(\text{Re}_B)$	Interception	The collision angle was assumed as 90°;
------------------------	---	--------------	---

---

---

Dai et al. (1998)

$$E_c = E_{c,su} \sin^2 \theta_t \exp \left\{ 3K \left[ \cos \theta_t \left( \ln \frac{3}{E_{c,su}} - 1.8 \right) - \frac{2 + \cos^3 \theta_t - 3 \cos \theta_t}{2E_{c,su} \sin^2 \theta_t} \right] \right\}$$

Combination of interception and inertial

$$K = \frac{2v_b(\rho_p - \rho_l)R_p^2}{9\eta R_b}$$

$$E_{c,su} = 3 \frac{R_p}{R_b}$$

$$\theta_t = \arcsin \{ 2\beta (\sqrt{1+\beta^2} - \beta) \}^{0.5}$$

$$\beta = \frac{3f\eta}{U_b(\rho_p - \rho_l)R_p}$$

Nguyen and Schulze (2004)

The gravitational effect:

$$E_c = \frac{V_s}{U_b + V_s}$$

The interception effect:

$$E_c = \frac{2f(R)}{27(1+V_s/U_b)Y^2} \left\{ \sqrt{X^2 + 3Y^2} - X \right\} \left\{ \sqrt{X^2 + 3Y^2} + 2X \right\}^2$$

The combined gravitational and interception effect:

$$E_c = \frac{2f(R)}{27(1+V_s/U_b)Y} \left\{ \sqrt{(X+h)^2 + 3Y^2} - (X+h) \right\} \\ \left\{ \sqrt{(X+h)^2 + 3Y^2} + 2(X+h) \right\}^2$$

The encounter by gravity, interception and inertia simultaneously at low St:

$$E_c = f(R) \frac{(X+h)\sin^2 \varphi_{co} - C_1 X^2 \frac{\cos^3 \varphi_{co} - 3 \cos \varphi_{co} + 2}{3}}{1+v_s} + O(St^{1.5})$$


---

Suitable for potential flow;  
Collision angles was considered as a function of  $Re_B$ .

Combination of interception and inertial

The collision angle was assumed as 90°

---

Sarrot et al. (2005)

$$E_c = \frac{R_p}{R_B} \frac{15 + 3 \text{Re}_B^{3/4}}{15 + \text{Re}_B} \quad (\text{for mobile bubble surface})$$

Interception

Direct numerical simulation was used;  
Bubbles with a variety of surface mobility  
were analysed.

$$E_c = 1.5 \left( \frac{R_p}{R_B} \right)^2 \left( 1 + \frac{\text{Re}_B^{2/3}}{5} \right) \quad (\text{for immobile bubble surface})$$

Sokovnin et al. (2014)

$$E_{c,L}^{rod} = 4.90\delta'^2 - 3.25\delta'^3$$

Interception

Particle size is much smaller than bubble size,  
particle density is close to fluid density;  
Considered the shape of particle on collision  
efficiency;  
Particle inertia was neglected.

$$E_{c,St}^{rod} = 0.30\delta'^2 + 5.65\delta'^3$$

$$E_{c,L}^{disk} = 4.58\delta'^2 - 3.00\delta'^3 \quad (\text{for non-spherical particles})$$

$$E_{c,St}^{disk} = 0.28\delta'^2 + 5.48\delta'^3$$

$$\delta' = l_p / r_B$$

---

## 2.2.2. Bubble-particle collision in the presence of turbulent flow

As shown in the previous section, bubble-particle collision behaviour in the absence of turbulence has been extensively investigated. However, the flow in flotation system is usually made turbulent by impellers or jet-pumps to disperse air into small bubbles, to keep the suspension of solid particles, and more importantly, to enhance bubble-particle collision. Although the mechanistic understanding of the collision behaviour in the absence of turbulence provides a background knowledge of the bubble-particle collision in turbulent flow, the collision mechanism in turbulent flow is profoundly different and will be discussed in detail in the subsequent sections.

### 2.2.2.1. Fundamentals of turbulence

An important characteristic of turbulence is that the fluid velocity is stochastic, varying both spatially and temporally. Such a stochastic feature is because turbulent flow is composed of multi-scale eddies. First, the large energy-containing eddies are strongly influenced by the flow geometry and provide the main kinetic energy for transportation. These eddies are unstable and can easily break up into smaller eddies. In this way, the kinetic energy of the larger eddies cascades to smaller eddies. Secondly, the viscous subrange eddies characterize the smallest eddies at the end of the energy cascade. Eddies in this range are universal and independent of the geometry of flow. Viscous force in this range dominates the inertial force and kinetic energy of these eddies are dissipated into thermal energy. Finally, the inertial subrange eddies are between the sizes of large energy-containing eddies and viscous subrange eddies. The viscous effect in this range is negligible (Nguyen and Schulze, 2004; Pope, 2000).

From a statistical point of view, a turbulent flow field can be considered as a superimposition of the fluctuating velocity components on the mean velocity. Despite its stochastic feature, the velocity of the turbulent flow under fully developed state remains statistically steady. To characterize the turbulence level, a dimensionless number “Turbulence intensity” can be defined as the ratio of root-mean-square fluctuating velocity  $u_{rms}$  to the mean velocity of the flow  $\bar{u}$  as follows:

$$Ti = \frac{u_{rms}}{\bar{u}} \quad (2.14)$$

Other parameters to characterise turbulent flow are turbulent kinetic energy  $k_{tur}$  and turbulent energy dissipation rate  $\varepsilon$ :

$$k_{tur} = \frac{1}{2} \left( \overline{(\dot{u}_x)^2} + \overline{(\dot{u}_y)^2} + \overline{(\dot{u}_z)^2} \right) \quad (2.15)$$

$$\varepsilon = -\frac{dk_{tur}}{dt} \quad (2.16)$$

where  $\dot{u}_x$ ,  $\dot{u}_y$ ,  $\dot{u}_z$  are the fluctuating velocity in  $x$ ,  $y$  and  $z$  direction, respectively.

### 2.2.2.2. Numerical modelling of turbulence

The need for numerical modelling of turbulence originates from the difficulty of optically capturing the random and rapid moment of turbulent flow and the dispersed phases - bubbles and particles. Numerical modelling of the carrier phase – turbulent flow - provides insight into the governing factors of bubble-particles interaction. Depending on the treatment of smaller-scale eddies motions, turbulence models fall into three categories: Direct Numerical Simulation (DNS), Large Eddy Simulation (LES) and Reynolds-Averaged Navier-Stokes (RANS).

The DNS method is the most straightforward approach as it resolves all length and time scales of eddies. However, the computational cost of DNS increases as the cube of Reynolds number  $Re$  and hence DNS is intractable for high  $Re$  flow. In the RANS method, an average value is applied to divide the flow into mean and fluctuating parts. The motion of eddies is represented by the turbulent kinetic energy which is related to the fluctuating velocity. Despite the low computational cost and extensive application in engineering, the RANS method does not resolve turbulence and its accuracy of modelling the interaction between micrometric particles and small-scales eddies in flotation is rather limited.

The LES method directly solves the larger-scale turbulent eddies of which the velocity is above the filtered velocity and models the motion of smaller eddies below the filtered velocity. The computational cost of LES approach lies between DNS and RANS because the computational domain size and time do not need to be discretised into small scales for small eddies. Another advantage of the LES method is that it is more reliable than the RANS due to its capability of resolving larger-scale eddies (Pope, 2000).

A brief chronological literature summary of numerical modelling of turbulence in flotation is presented in **Table 2.2**. It is apparent that limited studies applied the DNS method in modelling turbulence (Wan et al., 2020). It can also be observed that a majority of turbulence modelling in the single-bubble domain or flotation cells applied the RANS method due to its low computational cost. Koh and Schwarz (2003) performed RANS-based computational modelling of flotation cell and examined the bubble-particle collision rate using the simulated local turbulence velocity. The predicted trend of collision increasing with turbulence dissipation rate is consistent with Wan et al. (2020). Sahbaz et al. (2012) quantified the turbulence intensity map in a Jameson flotation cell based on RANS-modelled turbulence. The maximum floatable particle size was estimated based on the numerically determined energy dissipation rate in the cell. Islam and Nguyen (2020) quantified the interaction between a bubble and multiple particles by modelling turbulent flow using RANS method and modelling the dispersion of particles using the random walk method. Islam found that collision due to turbulence can surpass the gravity-drive collision. Despite the extensive use of the RANS in flotation, the numerical predictions of the collision between small bubble and particles in the surrounding turbulent eddies are not experimentally validated.

Limited study of modelling turbulence in flotation using LES method is indeed reported by Wang et al. (2017a), as shown in **Table 2.2**. The predicted energy dissipation rate and vorticity were used in calculating the bubble-particle detachment efficiency and good agreement between the model predictions and the theoretical efficiency was achieved, suggesting that LES model is capable of modelling the turbulent eddies and their interaction with bubble and particles.

**Table 2.2.** Comparative summary of turbulence consideration in numerical modelling of flotation

Authors	System	Model type	Turbulence model	Particle dispersion model
Koh and Schwarz (2003)	flotation cell	3D, ASM	RANS	-
Nadeem et al. (2006)	single-bubble domain	2D, E-L	RANS, k- $\epsilon$	Not considered
Kostoglou et al. (2007)	flotation cell	3D, mixture	RANS, k- $\omega$	Not considered
Liu and Schwarz (2009a)	single-bubble domain	3D, E-L	RANS, sst	G-I
Mirgaux et al., (2009)	flotation cell	3D, E-L	RANS	Not considered
Troshko and Zdravistch (2009)	slurry bubble column	3D, E-E	RANS, k- $\epsilon$	Not considered
Sahbaz, et al., (2012)	flotation column	3D, Single phase	RANS, k- $\epsilon$	-
Karimi, et al., (2014a)	slurry bubble column	3D, E-E	RANS, k- $\epsilon$	Not considered
Wang et al., (2015)	flotation column	3D, Single phase	RANS, RSM	-
Wang et al., (2017a)	water channel	2D, Single phase	LES	-
Wang et al., (2017b)	Pipe flow unit in flotation column	3D, Single phase	RANS, k- $\epsilon$	-
Sarhan et al., (2018)	slurry bubble column	3D, E-E	RANS, k- $\epsilon$	Not considered
Wan et al., (2020)	slurry bubble column	3D, E-L	DNS	-
Islam and Nguyen (2020)	single-bubble domain	2D, E-L	RANS, k- $\epsilon$	random walk model
Bhutani et al., (2020)	slurry bubble column	3D, E-E (with population balance)	RANS, k- $\epsilon$	Not considered
Li et al., (2021)	single-bubble domain	3D, E-L	constant eddy viscosity	random walk model

### 2.2.2.3. Bubble-particle collision in turbulence

The interaction between bubble, particle and turbulent eddies strongly depends on the size of the dispersed phase and the length of eddies. It is commonly believed that there exists a critical eddy size of the interaction mechanism between particles and eddies. Particles smaller than this critical eddy size are mainly influenced by the viscous subrange eddies, while particles larger than it are influenced by the inertial subrange (Koh and Schwarz, 2006; Nguyen and Schulze, 2004; Liu and Schwarz, 2009a). However, there is limited understanding of such critical eddy size. Nguyen and Schulze (2004) considered that fine particles of size larger than ten times of the Kolmogorov (the smallest eddy size in the viscous subrange) length scale are mainly affected by the inertial subrange. However, Koh and Schwarz (2009) determined the critical eddy size as when particle relaxation time equals the characteristic time of fluctuating velocity over the eddy integral length.

The importance of the critical eddy size is because it affects the correlation between the movement of particles and the turbulent flow. Small particles follow the eddy motion closely and their fluctuating velocity are dependent on the fluid fluctuating velocity. Therefore, the collision may occur due to turbulence shear, turbulence acceleration, or gravity within the same eddy (see the particle in red and bubble in blue in **Fig. 2.3**). For larger particles and/or more vigorous turbulent flow, the fluctuating velocity are uncorrelated with the fluid velocity. As a result, particles may migrate from eddy to eddy and collide with the bubble (see the particles and bubble in black in **Fig. 2.3**).

Early studies of the bubble-particle collision behaviour focused on the collision frequency (Koh and Schwarz, 2006), an alternative name for collision kernel (Abrahamson, 1975; Ngo-Cong, D., 2018) defined as the number of collisions per unit liquid volume per unit time divided by the number concentration of bubbles and particles (Koh and Schwarz, 2006). Saffman, and Turner (1956) proposed a theoretical model of collision frequency for the particle velocity dependent on the fluid motion. Later, Abrahamson (1975) developed a collision frequency model for dispersed independent of the eddies. These two models by Saffman and Turner (1956) and Abrahamson (1975) were widely applied in quantifying the collision frequency in flotation cells/columns (Koh et al., 2009; Karimi et al., 2014a, b).

The two collision frequency models developed by Saffman and Turner (1956) and Abrahamson (1975) suit low and high turbulence intensity cases respectively. Kostoglou et al. (2006) developed a more general collision frequency model to account for the medium

turbulence intensity. Kostoglou et al. (2007) further considered the collision frequency as the sum of three terms – a) collision due to the buoyant motion a bubble, b) collision due to the gravitational motion of a particle and c) collision due to turbulence. Recently, the collision frequency was also numerically investigated using Direct Numerical Simulations (Wan et al., 2020). Comprehensive reviews of the collision frequency of bubble and particles in flotation were reported by Nguyen et al. (2016) and Kostoglou et al. (2020).

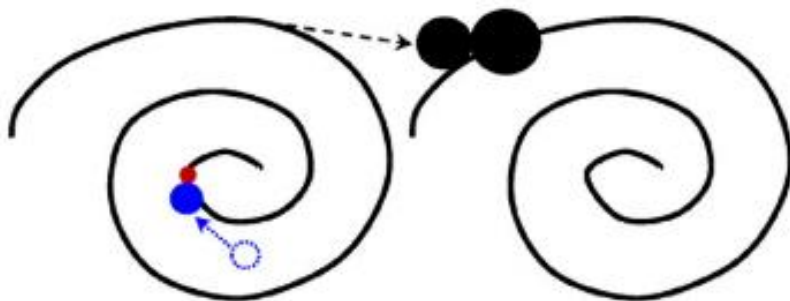


**Fig. 2.3.** Schematic of bubble-particle collision scenarios in turbulent flow: 1) The velocity of bubble (blue circle) and particle (red circle) are dependent on the eddy and collision occurs in the same eddy; 2) the velocity of bubble and particle (black circles) are independent on the eddy and particles migrate to another eddy to collide with the bubble (Nguyen et al., 2016).

Compared with the extensively studied collision frequency, research on how the trajectories of particles develop with turbulence level is still very limited, leading to the difficulty in quantifying the turbulent collision efficiency of bubble and particles (Kostoglou et al., 2020). Studies related to the bubble-particle collision efficiency will be discussed in the subsequent section.

#### 2.2.2.4. Previous studies on turbulent collision efficiency

Unlike the extensive studies of bubble-particle collision efficiency in the absence of turbulence as described in Section 2.2.1.4, investigations of collisions in turbulent flow are rather limited and can be classified into experimental (Brady et al., 2006; Shahbazi et al., 2010;

Meng, et al., 2016; Darabi et al., 2019; Sommer et al., 2020) and numerical studies (Liu and Schwarz, 2009a; Wan et al., 2020).

#### ***2.2.2.4.1. Experimental studies***

Quantification of the root-mean-square (RMS) fluctuating velocity of the dispersed phases (bubbles and particles) is key in determining the bubble-particle collision. Theoretical RMS velocity models are related to both liquid viscosity and turbulent dissipation rate based on the assumption of homogeneous and isotropic turbulence (Levins and Glastonbury, 1972; Abrahamson, 1975; Leipe and Mockel, 1976; Lee and Erickson, 1987). Among the theoretical models, the Leipe and Mockel model (1976) is the most commonly used one in examining the bubble-particle collision when particle inertia effect can not be ignored (Koh and Schwarz, 2006; Koh and Smith, 2011; Karimi et al., 2014a,b; Ngo-Cong, et al., 2018). Brady et al. (2006) experimentally quantified the RMS velocity of particles and bubbles using Particle Image Velocimetry (PIV) and compared the results with the theoretical models. The model of Leipe and Mockel (1976) was in good agreement with the experimental data with negligible deviation.

The distribution of collision efficiency in flotation cells can be determined experimentally by utilizing only ideal flow conditions into the collision efficiency models without accounting for turbulence directly. The measurement of turbulent conditions in flotation cells/columns are reviewed by Meng et al. (2016). Applying this method, Shahbazi et al. (2010) proposed a two-dimensional regime map of collision efficiency with air flow rate and impeller speed as coordinates. With the increase of impeller speed (the increase of turbulence level) the bubble-particle collision efficiency increased. This finding is consistent with the numerical observation of Koh and Schwarz (2003) in a CSIRO flotation cell.

The method of determining the bubble-particle collision efficiency by Shahbazi et al. (2010) was also applied in the experimental work of Darabi et al. (2019) in a Denver flotation cell. Darabi et al. found that the collision frequency in the turbulent zone can be more than 10 times that in the relatively quiescent zone. By comparing the collision efficiency of different mechanisms such as gravity, inertia, interception and turbulence, it was found that coarse particles ( $212 \mu\text{m} < d_p < 300 \mu\text{m}$ ) were mainly affected by the inertial, gravitational and interceptional mechanism. In comparison, fine particles ( $d_p < 38 \mu\text{m}$ ) were mainly influenced by turbulent collision. This laminar-model based method of determining collision efficiency,

although can provide guidance to the industrial flotation process, does not reflect the mechanism of bubble-particles collision in turbulent flow.

Experimental investigation of particle trajectory around the bubble provides physical insight into turbulent collision mechanism and can be used to validate theoretical models of turbulent collision. However, studies in this field are rather limited due to the difficulty in capturing the small-scale eddies and random movement of particles and bubbles in turbulent flow. Sommer et al. (2020) experimentally investigated the trajectories of particles passing a stationary bubble under various turbulence intensities in high particle concentrations ( $\sim 0.22\%$ ) using Positron Emission Particle Tracking (PEPT) method. The deviation in particle trajectory and residence time were observed to be significantly influenced by the turbulence intensity level. In their studies, the tracer particle was made of three parts: the radioactive core part, the adhesive layer which facilitated the coating, and the coating layer to resemble the surface chemistry of the targeted mineral.

The difference in the trajectories of hydrophobic and hydrophilic particles in turbulent flow in a mechanical cell was experimentally examined by Cole et al. (2022) using PEPT method. Although the collision between bubble and particles in turbulent flow was not directly observed, the PEPT results show hydrophobic particles have the highest occupancy in the froth region which plausibly was a result of collision and attachment with the bubble. In comparison the hydrophilic particles which only have limited occupancy in the froth region tend to move downwards into the vessel and have highest occupancy in the region below the impeller.

#### **2.2.2.4.2. Numerical studies**

Extensive studies of bubble-particle collision in flotation cells were quantified by utilizing the numerically obtained flotation conditions to collision efficiency models without accounting for turbulence (Koh and Schwarz, 2006; Koh and Smith, 2011; Karimi et al., 2014a,b). In comparison, only a limited number of studies quantified the bubble-particle collision by examining the particle trajectories. Liu and Schwarz (2009a) numerically investigated the collision efficiency between single bubble and multiple particles in turbulent flow based on the Eulerian-Lagrangian method. The bubble-particle turbulent Reynolds numbers were calculated based on the turbulence kinetic energy of the contributing eddies and plotted as the dependant variable of the collision efficiency. It was observed that a critical turbulent Reynolds number of 100 existed below which turbulence had a positive effect on the

collision efficiency because particles released far from the bubble centre migrated to the bubble surface. Above this critical value, turbulence had a negative effect presumably because more particles were dispersed away from the bubble.

In reality, the flotation system in reality contains multiple bubbles to increase the bubble surface area flux. Therefore, the collision behaviour in the presence of multiple bubbles and multiple particles in turbulent flow is of more realistic meaning. Wan et al. (2020) studied the effect of homogeneous and isotropic turbulence on the collision between monosized particles and multiple millimetric size bubbles ( $d_B \sim 190 - 300 \mu\text{m}$ ) using DNS method. They found that the radial relative velocity between particles and bubbles increased with the increase of turbulence dissipation rate, leading to increased collision between bubbles and particles. However, due to the complexity of the interaction between turbulent flow and the dispersed phase, the bubbles and particles in Wan's study were randomly relocated after collision which does not occur in real flow. Besides, in Wan's study both the dispersed phases (particles and bubbles) were point particles which does not hold in flow of higher turbulence intensity where eddies may be smaller than the dimensions of dispersed phases (Yao, et al., 2021).

The monosized particles assumption used by Liu and Schwarz (2009a) and Wan et al. (2020) is an ideal case. In a real flotation system, the particle phase consists of a range of particle sizes. A hybrid finite element-control volume framework coupled with population balance model was developed by Bhutani et al. (2016) and was later applied to model the interaction between polysized particles and bubbles in turbulent flow (Bhutani et al., 2020). The bubble loading which is a result of collision and attachment was found to increase with increased particle size. Bhutani et al. (2020) also found that monosized simulation tend to overpredict the collision and attachment rate compared to the polysized simulation.

Focusing on the effect of particle inertia on turbulent collision efficiency, Islam and Nguyen (2020) numerically examined the collision behaviour of particles with bubbles of both mobile and immobile surface in a two-dimensional domain ( $R_B \sim 1 \text{ mm}$ ,  $Re_B \sim 10 - 400$ ,  $R_P \sim 5 - 25 \mu\text{m}$ ) using Eulerian-Lagrangian method. The trajectory of individual particle was tracked to determine the collision with the bubble and the overall collision efficiency was considered to be a linear addition of laminar collision efficiency and turbulent model by Levich (1962). In general, the CFD predictions agreed well with the overall collision efficiency for lighter particles and low bubble Reynolds numbers at turbulence intensities larger than 5%.

Recently, a theoretical model of bubble-particle collision efficiency in turbulent flow was also developed by Ngo-Cong et al. (2018) based on homogeneous isotropic assumption of turbulence. In their study, depending on the density of particles, the effect of the difference between particle diameter and Kolmogorov length scale, as well as the interplay of turbulence shear, turbulence acceleration and gravity on the bubble-particle collisions were examined. The turbulent collision efficiency was observed to intensify with the increase of turbulence dissipation and exceeded unity, suggesting that for the given phase properties, turbulent collision efficiency is larger than the laminar collision efficiency.

The effect of both large-scale turbulence (eddies much larger than bubble size) and small-scale turbulence (eddies much smaller than bubble size) on collision efficiency was numerically studied in Li et al. (2021). Based on the assumption that eddies larger than bubble size could accelerate the bubble velocity relative to the slurry, they found the collision efficiency increases with the increase in energy contained in large-scale eddies. While simulating small eddies, they assumed that turbulence was generated externally to the local environment around the bubble. They therefore adopted a zero-equation turbulence model with fixed turbulence kinetic energy and energy dissipation rate as inputs to solve the turbulent flow field. The energy contained in small-scale turbulence was found to have greater positive effect on collision efficiency for fine particles ( $d_P \leq 31 \mu\text{m}$ ) than for coarse particles ( $d_P \geq 74 \mu\text{m}$ ).

Following this review, the range of the turbulence intensity in the studies of bubble-particle collision in turbulent flow is presented in **Table 2.3**. Also summarized are the models of turbulent collision efficiency listed in **Table 2.4**. It can be concluded that the effect of turbulence on bubble-particle collision is not fully understood.

**Table 2.3.** A summary of turbulence intensity range in studies of bubble-particle collision

Authors	System	Range of turbulence intensity
Nadeem et al. (2006)	Single bubble – multiple particles, inlet turbulence, $d_B \sim 1.0 - 1.5 \text{ mm}$ , $Re_B \sim 107 - 254$ , $d_P \sim 10 - 80 \mu\text{m}$	10%
Sahbaz et al. (2012)	Jameson flotation cell, inlet velocity of air and water $\sim 1.4 \text{ m/s}$ .	0 - 23%
Sommer et al. (2020)	Single bubble – multiple particles, grid generated isotropic turbulence, $d_B \sim 2.5 \text{ mm}$ , $Re_B \sim 450$ , $d_P \sim 200 - 400 \mu\text{m}$	5% - 15%
Islam and Nguyen (2020)	Single bubble – multiple particles, inlet turbulence, $d_B \sim 2.0 \text{ mm}$ , $Re_B \sim 10 - 400$ , $d_P \sim 5 - 25 \mu\text{m}$	2% - 9%

**Table 2.4.** Models of turbulent collision efficiency

Authors	Collision models	Type of collision mechanism	Comments
Levich (1962)	$E_c = 8.05 \frac{\rho_L}{\rho_P - \rho_L} \frac{\lambda_K}{R_B + R_P}$	Turbulent	Collision by turbulent diffusion, applicable for aerosol system.
Ngo-Cong et al. (2018)	$E_c = 0.92 \left[ \frac{2.07 \frac{\epsilon^{8/9} R_B^{14/9}}{\nu^{2/3}} \left( \frac{\rho_f - \rho_B}{\rho_f} \right)^{4/3} + \frac{4 R_p^6 \epsilon^2}{6075 \nu^4} \left( \frac{\rho_P - \rho_L}{\rho_L} \right)^2}{-2 B_{u_f, rms}^2 + A_B R_B^2 \frac{\epsilon}{3\nu} + A_p R_p^2 \frac{\epsilon}{3\nu} + 2 B R_B R_p \frac{\epsilon}{3\nu}} \right]^{0.5}$	Turbulent	defined as the ratio of collision frequency to the ideal rate of collision
Islam and Nguyen (2020) For mobile bubble surface:	$E_c = \left( R - R^2 \right) \frac{\left( X + \frac{v_s}{R - R^2} \right) \sin^2 \theta_C - C_p X^2 \frac{\cos^3 \theta_C - 3 \cos \theta_C + 2}{3}}{1 + v_s} + 8.05 \frac{\rho_L}{\rho_P - \rho_L} \frac{\eta}{R_B + R_P}$	Combination of gravity, interception, inertia and turbulent	The overall collision efficiency was obtained by adding the encounter efficiencies in laminar flow and that in turbulence flow.
For immobile bubble surface:	$E_c = \frac{R^2}{1 + v_s} \left[ \left( X + \frac{v_s}{R^2} \right) + Y \cos \theta_C \right] \sin^2 \theta_C + \frac{v_s}{1 + v_s} \sin^2 \theta_C + 8.05 \frac{\rho_L}{\rho_P - \rho_L} \frac{\eta}{R_B + R_P}$		

### 2.3. Bubble surface loading (BSL)

Apart from collision efficiency, another important parameter in determining the particle recovery is the bubble surface loading. Bubble surface loading can be defined as the fraction of the bubble surface area occupied by the loaded particles to the total surface area of the bubble (Sarkar et al., 2011; Wang et al., 2019a, b).

The loading of particles onto the bubble surface may result in four major outcomes (Omota et al., 2006a): (a) monolayer loading (**Fig. 2.4a**) which occurs when particle-particle cohesion forces are negligible compared to the weight of a single particles; (b) multilayer loading (**Fig. 2.4b**) which occurs when the particle-particle cohesion forces exceed the particle weight; (c) loading of particle clusters (**Fig. 2.4c**) which occurs when the particle-particle cohesion forces further increase but the weight of the cluster is still smaller than the adhesion force between particle and bubble. Further increase of particle-particle cohesion forces may lead to larger particle cluster which is unable to adhere to a bubble; and (d) the loading of particles-small-bubbles cluster (**Fig. 2.4d**) which occurs when small bubbles of comparable size to the particles are present. This section of review is restricted to the monolayer loading.

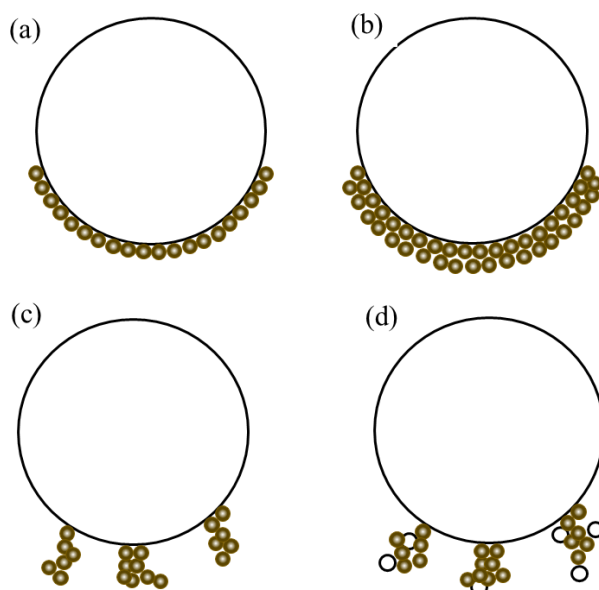


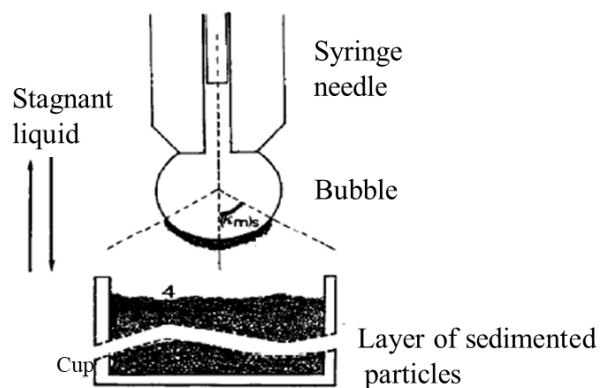
**Fig. 2.4.** Schematic of the four types of particle loading onto a bubble: (a) monolayer loading; (b) multilayer loading; (c) loading of particle clusters; (d) loading of particles-small-bubbles clusters

### **2.3.1. Bubble loading method in stagnant liquid and flowing liquid**

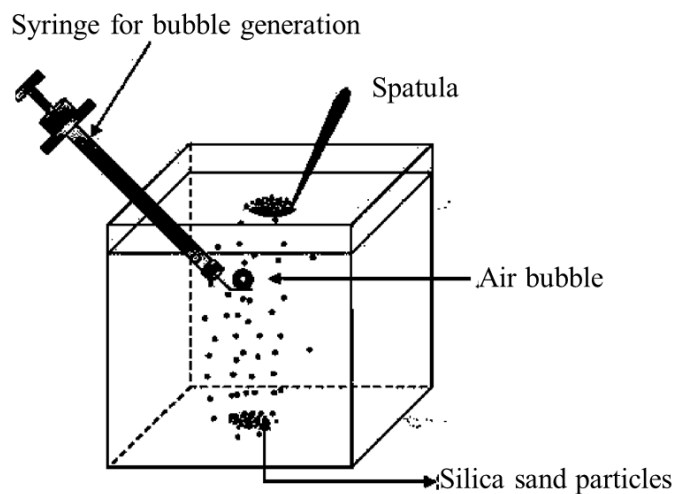
In stagnant liquid, particles can be loaded either by moving the bubble towards stationary particles (Bubble Pick-up Method, Wimmers and Fortuin, 1988; Vinke et al., 1991a), or by releasing particles above the bubble (Top-loading Method, Gallegos-Acevedo et al., 2006; Eskanlou et al., 2018a), or by settling of particles from suspension onto the bubble (suspension loading method, Xia et al., 2018; Wang et al. 2019a).

The Bubble Pick-up Method (BPU, **Fig. 2.5a**) developed by Lee (1969), is used to quantify the maximum bubble surface loading (Wimmers and Fortuin, 1988). In this method, both the particles and the syringe used to generate bubbles are completely immersed in the stagnant liquid. The bubble is moved down until immersed in particles to allow particles to be loaded onto bubble surface. Although the BPU method allows precise control of the bubble movement, it can not be applied to particles of high contact angle. This is because these particles can be tightly adhered to each other, making the surface of the particle layer impenetrable by the bubble. In the Top-loading method (**Fig. 2.5b**), the bubble is generated through a syringe needle and kept stationary. Particles released by spatula penetrate the free gas-liquid surface and settle onto the bubble surface by gravity. This method can be applied to load the bubble surface to a desirable level in order to examine the effect of bubble surface loading on the bubble velocity (Eskanlou et al., 2018a) or to investigate the particle-particle arrangement pattern in the loading region (Gallegos-Acevedo et al., 2006). In the suspension loading method (**Fig. 2.5c**), the magnetic stirrer in the tank is turned on to ensure that particles in the suspension can be loaded onto the surface of bubble on the nozzle tip. The stirrer is turned off once the surface loading reaches the required level. Because the suspension is conditioned prior to start of the loading procedure, particles of higher contact angle can be used in the suspension loading method. However, this method can not be used to load small bubbles due to the difficulty of these bubbles remaining stationary on a nozzle tip in stagnant liquid (Oguz and Prosperetti, 1993).

(a)



(b)



(c)

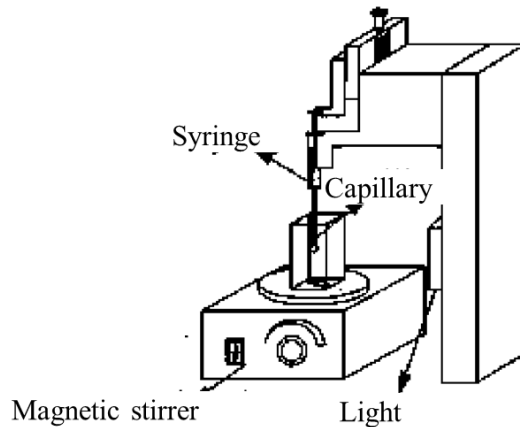


**Fig. 2.5.** Schematic of bubble loading method in the stagnant liquid: (a) Bubble Pick-up method (Wimmers and Fortuin, 1988); (b) Top-loading method (Gallegos-Acevedo et al., 2006); (c) suspension loading method (Xia et al., 2018).

In flowing liquid, a bubble can be loaded with particles while rising through the flotation columns (**Fig. 2.6a**). The particle-laden bubbles are then deflected off the cone into the particle collector. This method reveals the bubble surface loading in actual flotation conditions and is adopted by many researchers (Bradshaw and Connor, 1996; Huang et al., 2011; Chegeni et al., 2016). Alternatively, the bubble can be loaded using the earlier mentioned BPU method and then held stationary in the flowing liquid (**Fig. 2.6b**). The flow enters the tank through the inlet and ascends to the top of the tank wherein the flow is then deflected downwards toward the stationary bubble. The transparent system enables the bubble surface loading to be captured by a camera. The bubble surface loading is observed to reduce with increasing downward liquid velocity (Vinke et al., 1993).

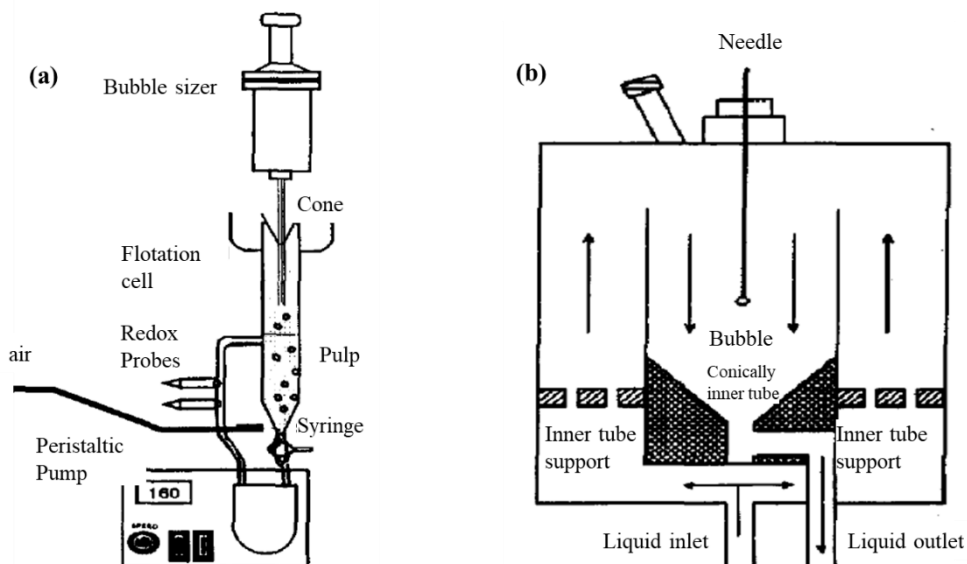


**Fig. 2.6.** Schematic of experimental set up to determine the bubble surface loading in flowing liquid: (a) particle-laden bubble rising in flotation column (Bradshaw and Connor, 1996); (b) particle-laden bubble held stationary while slurry flowing downwards (Vinke et al., 1993).

### 2.3.2. Measurement of the bubble surface loading

#### 2.3.2.1. Optical method

In the optical method, the particle-laden bubble is directly captured by a high-speed camera (Huang et al., 2011). The bubble is assumed as spherical, as shown in **Fig. 2.7a** and the clean angle  $\theta_{clean}$ , defined as the angle between the vertical axis of the bubble and the position

vector from the bubble centre to the highest loaded particle, can be measured from the captured image. Applying the measured clean angle, the bubble surface loading can be calculated below (Wimmers and Fortuin, 1988):

$$BSL = \frac{1 + \cos \theta_{clean}}{2} \quad (2.17)$$

Optical method can also be applied to detect the level of bubble surface loading of a particle-laden bubble pendant (Wang et al., 2019a), as shown in **Fig. 2.7b**. The bubble surface of the pendant can be fitted to the pendant drop model (Yang, et al., 2017, Wang. et al., 2019). The area for the bubble pendant surface and the loading surface is calculated by numerically integrating the area enclosed via rotating the pendant curve AB and LB, respectively. The bubble surface loading can be calculated as the ratio of the surface area occupied by particles to the whole surface area of the bubble.

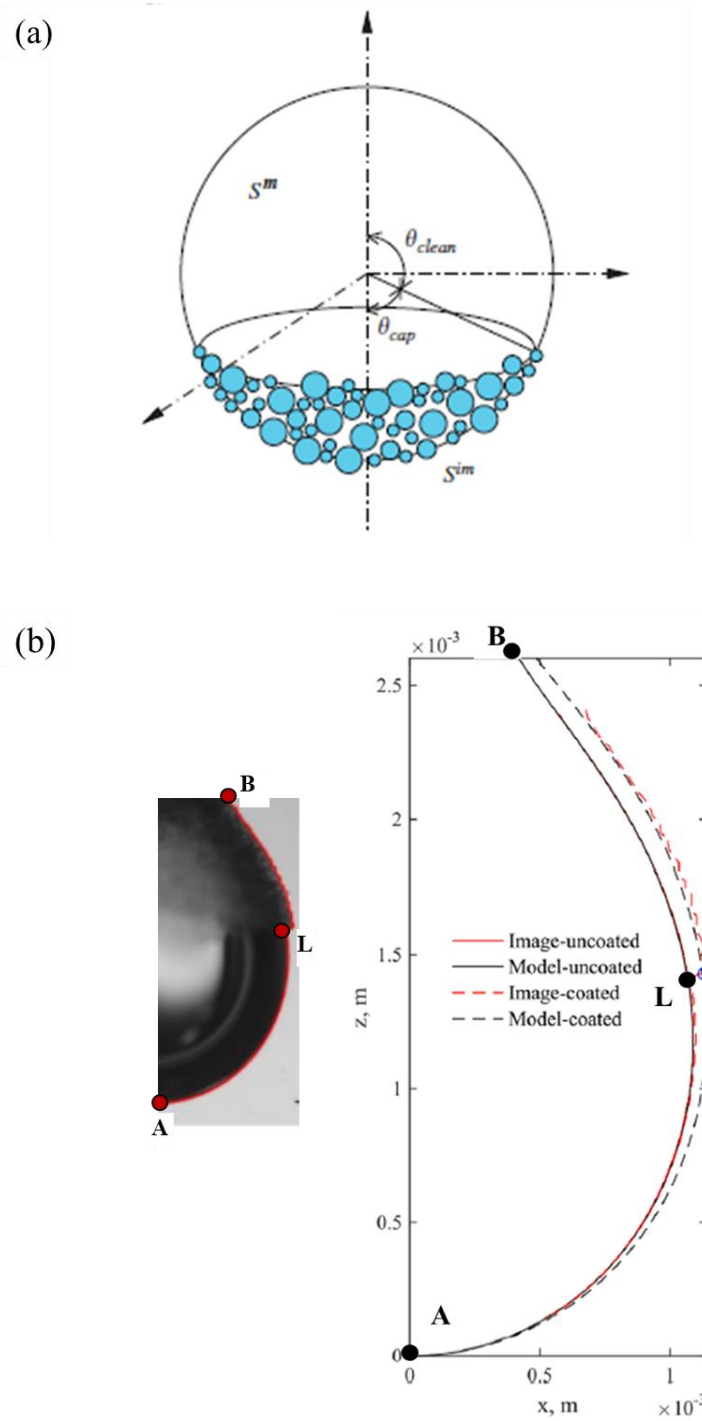


**Fig. 2.7.** Optical method of measuring bubble surface loading: (a) Schematic of angle measurement of the particle-laden bubble (Huang et al., 2011); (b) Curving fitting of the particle-laden bubble pendant (Wang et al., 2019a).

### 2.3.2.2. BSL sampler method

To identify the bubble surface loading level in an opaque flotation cell/column, the BSL sampler can be used wherein particle-laden bubbles in the flotation system continuously enter

the sampling point (Fig. 2.8) and rise through the sampling tube into the collection tank. The loaded bubbles then break up at the top of the collection tank, displacing water out of the collection tank. The volume of the displaced water can be measured by the decreased height of the free gas-liquid surface in the collection tank and the cross-sectional area of the tank. The detached particles from the laden bubble settle to the bottom of the tank and are collected later to measure their weight.

If the bubble diameter is  $d_B$ , the displaced volume of water is  $V$ , and the mass of the collected particles is  $m_p$ . The bubble surface loading is expressed as:

$$BSL = \frac{m_p d_B}{4d_p \rho_p V} \quad (2.18)$$

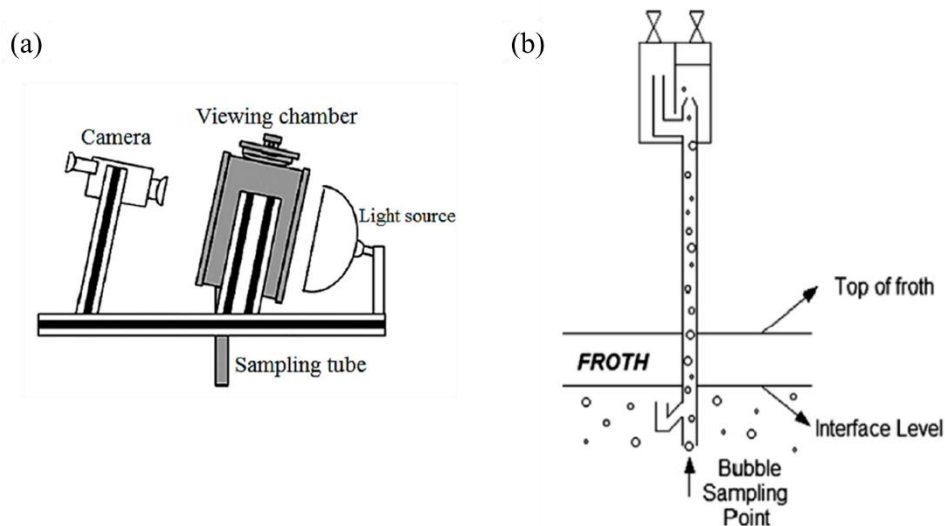


**Fig. 2.8.** Direct method of measuring bubble surface loading: (a) Measurement of bubble diameter and (b) Bubble surface loading sampler. (Ostadrahimi et al., 2019).

### 2.3.2.3. Acoustic method

The acoustic method is based on the theory that the acoustic resonance frequency of a bubble decreases with the increase of the mass of the loaded particles on the bubble surface. Therefore, by quantifying the change in bubble resonance frequency before and after particles are loaded, the bubble surface loading can be determined (Zhang et al., 2012). One advantage of the acoustic method of measuring BSL is its capability in the opaque flotation system. However, the acoustic method does not account for the effect of gas volumetric fraction on the

resonance frequency of a particle-laden bubble in flotation. Such lack of consideration may lead to the bias of predictions from the real BSL value.

Using the BSL measurement methods described in this section, extensive studies (Gallegos-Aceredo et al., 2006; Omota et al., 2006a; Huang et al., 2011; Wang et al., 2019b) were conducted to understand the bubble surface loading behaviour. The reported surface loading, however, was quantified using different parameters which can be classified into four categories, as shown in **Fig. 2.9**: 1) the loading angle,  $\theta_{1,load}$  (deg), between the bubble vertical axial and the upmost particle in the loading region; 2) the loading angle,  $\theta_{2,load}$  (deg), which is the supplementary angle of  $\theta_{1,load}$ ; 3) the number of loaded particles per bubble,  $n_{load}$  and 4) the weight of particles loaded per unit bubble surface area,  $\dot{m}_{load}$  (mg/mm<sup>2</sup>).

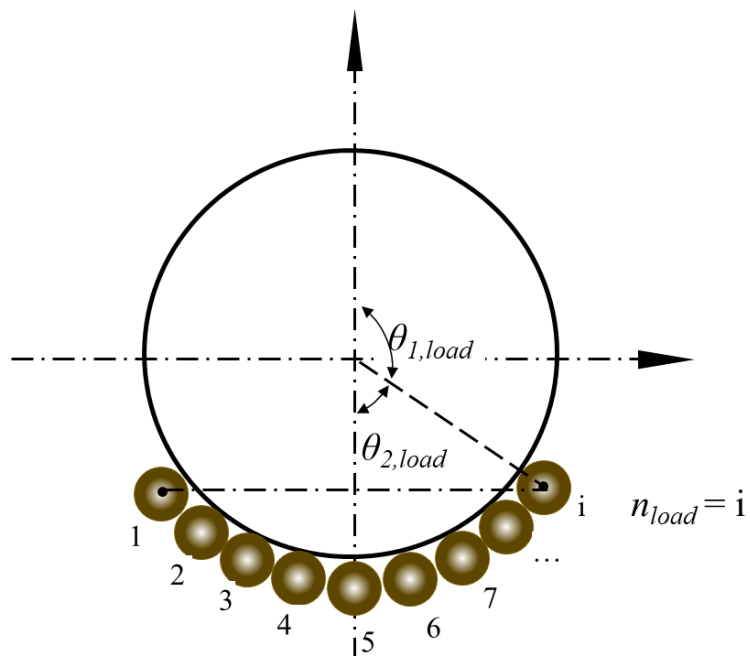


**Fig. 2.9.** Schematic of different parameter to represent bubble surface loading.

The variety of quantifying parameters makes it difficult to directly compare the BSL levels in literature. Therefore, the reported BSLs which were quantified using different parameters are converted in this review into the ratio of the surface area of the bubble occupied by the loaded particles to the total surface area of the bubble. The mathematics of the conversion is illustrated in **Table 2.5**.

**Table 2.5.** The conversion of BSL from original parameters (angles, particle number etc.) into the ratio of the surface area occupied by particles to the whole bubble surface area.

Original parameters	Converted BSL
$\theta_{1,load}$ , deg	$BSL = \frac{\cos(\theta_{1,load}\pi/180) + 1}{2}, -$
$\theta_{2,load}$ , deg	$BSL = \frac{\cos(\pi - \theta_{2,load}\pi/180) + 1}{2}, -$
$n_{load}$ , number of particles per bubble	$BSL = \frac{n_{load} R_p^2}{4R_B^2 \phi_p}, -$
$\dot{m}_{load}$ , mg/mm <sup>2</sup>	$BSL = \frac{3\dot{m}_{load}}{4\rho_p R_p \phi_p}, -$

A chronological literature survey of the studies of bubble surface loading is presented in **Table 2.6** wherein the original parameters to represent the bubble surface loading are converted into the dimensionless unit using the mathematics in **Table 2.5**.

**Table 2.6.** Previous studies on measuring bubble surface loading

Reference	System	Measurement method	Original parameters	Converted BSL in dimensionless unit
Wimmers and Fortuin (1988)	bubble pick-up apparatus ( $R_B \sim 0.2 - 0.4$ mm, $R_P \sim 5 - 10$ $\mu\text{m}$ , $\rho_P \sim 1800 - 4527$ kg/m $^3$ )	Optical	$\theta_{2,load} \sim 0 - 90$ , deg	0 - 0.50, -
Vinke et al.(1991a)	bubble pick-up apparatus, contact angle $\theta_c \sim 5$ deg ( $R_B \sim 0.35 - 0.55$ mm, $R_P \sim 8 - 38$ $\mu\text{m}$ , $\rho_P \sim 2280 - 4370$ kg/m $^3$ )	Optical	$\theta_{2,load} \sim 0 - 117$ , deg	0 - 0.73, -
Falutsu, et al. (1992)	flotation column	BSL sampler	0 - 0.072, g/ml air	-
Bradshaw and Connor (1996)	flotation cell ( $R_B \sim 0.62$ mm, $R_P \sim 19 - 75$ $\mu\text{m}$ , $\rho_P \sim 5040$ kg/m $^3$ )	BSL sampler	$n_{load} \sim 25 - 1281$ 0 - 0.14, -	0 - 0.14, -
Uribe-Salas et al. (2003)	Bubble loaded while rising in downward slurry in flotation column, slurry velocity > 0.7 cm/s, solid concentrations ~ 15 - 35% ( $R_P \sim 95$ $\mu\text{m}$ , $\rho_P \sim 2650$ kg/m $^3$ )	Optical	BSL ~1.00, -	1.00, -
Seaman et al. (2004)	In flotation cell or column, solid is a mixture of Mgo, galena, sphalerite, pyrite and gangue	BSL sampler	31g/L	-
Omota, et al. (2006a)	Analytical modelling of BSL for bubble pick-up method ( $R_B \sim 0.5$ mm, $R_P \sim 100$ $\mu\text{m}$ , $\rho_P \sim 1374$ kg/m $^3$ )	Optical	$\theta_{2,load} = 0 - 180$ , deg	0-0.50, -
Omota, et al. (2006b)	bubble pick-up apparatus, contact angle $\theta_c \sim 5$ deg ( $R_B \sim 0.182 - 0.6$ mm, $R_P \sim 11 - 22$ $\mu\text{m}$ )	Optical	$\theta_{2,load} = 0 - 180$ , deg	0-0.50, -
Gallegos-Acevedo et al. (2006)	Stationary bubble loaded by particles feed from top before rising ( $R_B \sim 1.05 - 2.50$ mm, $R_P \sim 95$ $\mu\text{m}$ , $\rho_P \sim 2560$ kg/m $^3$ )	Optical	BSL ~1.00, -	1.00, -
Koh and Schwarz (2008)	Numerical simulations of particle recovery based on three sub-process, solid concentration ~ 4% ( $R_B \sim 1.00$ mm, $R_P \sim 5 - 100$ $\mu\text{m}$ , $\rho_P \sim 2600$ kg/m $^3$ )	Numerical modelling	BSL ~0.20, -	0.20
Huang et al. (2011)	Bubble loaded while rising through stationary pulp, contact angle $\theta_c \sim 44$ deg ( $R_B \sim 0.30 - 0.58$ mm, $R_P \sim 11$ $\mu\text{m}$ , $\rho_P \sim 2650$ kg/m $^3$ )	BSL sampler	$\theta_{1,load} \sim 0 - 137$ , deg	0 - 0.11 for $R_B \sim 0.5$ mm, 0 - 0.41 for $R_B \sim 0.3$ mm.

Sarkar et al. (2011)	In flotation cell, contact angle $\theta_c \sim 59$ deg solid concentrations ~ 5% - 20% ( $R_B \sim 0.021$ mm, $R_P \sim 1.55 - 7.35$ $\mu\text{m}$ , $\rho_P \sim 2650$ $\text{kg}/\text{m}^3$ )	BSL sampler	0 – 0.35, -	0 – 0.35, -
Zhang et al. (2012)	Stationary bubble loaded by particles feed from top ( $R_B \sim 0.55$ , 0.89 mm, $R_P \sim 57.5$ $\mu\text{m}$ , $\rho_P \sim 2200$ $\text{kg}/\text{m}^3$ )	Acoustic	$\theta_{2,load} \sim 0 - 90$ , deg	0 – 0.5, -
Spencer, et al. (2012)	In flotation cell, solid concentrations 4 – 12% ( $R_B \sim 0.27 - 0.36$ mm, $R_P \sim 150$ $\mu\text{m}$ , $\rho_P \sim 2200$ $\text{kg}/\text{m}^3$ )	Acoustic	BSL ~0.80, -	0.80, -
Chegeni, et al. (2016)	In flotation column, solid concentrations 10% ( $R_B \sim 0.8 - 2.0$ mm, $R_P \sim 31.5 - 75.0$ $\mu\text{m}$ , $\rho_P \sim 2500$ $\text{kg}/\text{m}^3$ )	BSL sampler	$\dot{m}_{load} \sim 0.0188 - 0.0434$ $\text{mg}/\text{mm}^2$	0.06 – 0.19, -
Eskanlou et al. (2018a)	Stationary bubble loaded by particles feed from top ( $R_B \sim 1.3 - 2.0$ mm, $R_P \sim 75 - 150$ $\mu\text{m}$ , $\rho_P \sim 2650$ $\text{kg}/\text{m}^3$ )	Optical	BSL ~0, 1.00, -	0, 1.00, -
Eskanlou et al. (2018b, 2019)	Bubble loaded while rising in flotation column contact angle $\theta_c \sim 12 - 80$ deg ( $R_B \sim 0.45 - 0.9$ mm, $R_P \sim 31.5 - 150$ $\mu\text{m}$ , $\rho_P \sim 2500 - 6960$ $\text{kg}/\text{m}^3$ )	BSL sampler	$\dot{m}_{load} \sim 0.0027 - 0.0043$ , $\text{mg}/\text{mm}^2$	0.03 – 0.31, -
Ostadrahimi, et al. (2019)	In flotation cell ( $R_B \sim 0.36 - 0.98$ mm, $R_P \sim 40 - 54$ $\mu\text{m}$ , $\rho_P \sim 3940$ $\text{kg}/\text{m}^3$ )	BSL sampler	$\dot{m}_{load} \sim 0.0027 - 0.0043$ , $\text{mg}/\text{mm}^2$	0.03, -
Wang et al. (2019a)	Stationary bubble loaded by the settling of previously magnetic bar –stirred particles ( $R_B \sim 1.45$ mm, $R_P \sim 32$ $\mu\text{m}$ , $\rho_P \sim 2650$ $\text{kg}/\text{m}^3$ )	Optical	BSL ~0 - 0.60, -	0 – 0.60, -
Wang et al. (2019b)	Stationary bubble loaded by the settling of previously magnetic bar –stirred particles ( $R_B \sim 1.45$ mm, $R_P \sim 32 - 133$ $\mu\text{m}$ , $\rho_P \sim 2650$ $\text{kg}/\text{m}^3$ )	Optical	BSL ~0 – 0.60, -	0 – 0.60

### 2.3.3. Maximum bubble surface loading

In flotation, it is desirable to maximize the bubble surface loading to achieve better recovery of particles. Hence, it is of interest to examine the theory of the maximum bubble surface loading ( $BSL_{max}$ ) in both stagnant and flowing conditions. For a stationary bubble with monolayer loading of particles in stagnant liquid, the maximum bubble surface loading is obtained when the total force exerted on the lowest particles in the loading region reaches zero (Omota et al., 2006a, b; Eskinlou et al., 2019). This is because the lowest particle is subject to the maximum cohesive forces exerted by all layers of particles above it (Omota et al., 2006a, b).

Forces on the lowest particle include: a) the gravity  $F_g = \frac{4}{3}\pi R_p^3 \rho_p g$ ; b) the buoyance force  $F_b = \frac{\pi}{3} R_p^3 \rho_L g (1 - \cos \alpha)^2 (2 + \cos \alpha)$ ; c) the capillary force  $F_c = 2\pi R_p \sigma \sin \alpha \sin(\alpha + \theta_{con})$ ; d) the capillary pressure introduced force  $F_\sigma = \pi R_p^2 (\sin^2 \alpha) \left( \frac{2\sigma}{R_B} - 2R_B \rho_L g \right)$ ; and e) the cohesive force which is a function of contact angle, the number of particles in the monolayer, the modified particle Bond number and the ratio of the particle radius to the bubble radius (Vinke et al., 1991a). for a stationary particle-laden bubble in stagnant liquid, the drag force of loaded particles equals zero. The maximum  $BSL_{max}$  can be calculated based on the following force balance:

$$F_b + F_c - F_g - F_\sigma - F_{coh} = 0 \quad (2.19)$$

In flowing conditions, it is necessary to include the drag force exerted by the flow around the bubble onto the particles in the group of detaching force. In the case of flowing liquid, the maximum bubble surface loading is often less than the  $BSL_{max}$  for a stationary particle-laden bubble in stagnant liquid (Vinke et al., 1993) because of the additional drag force. Despite the importance of the drag force in determining  $BSL_{max}$ , the drag force applied to loaded particles is still not fully understood.

Depending on different treatment of cohesive force and drag force, the models for maximum bubble surface loading  $BSL_{\max}$  can be different, as listed in **Table 2.7**.

**Table 2.7.** A summary of models for maximum bubble surface loading

Authors	System	Models	Comments
Wimmers and Fortuin (1988)	Stationary state	$BSL_{\max} = \frac{1}{2} - \frac{Bo_P}{3 \sin^2(\theta_{con}/2)}$ $Bo_P = \frac{R_p^2 g (\rho_p - \rho_L)}{\sigma}$	the cohesive force and capillary pressure introduced force ignored
Wimmers and Fortuin (1988)	In flowing liquid	$BSL_{\max} = \frac{1}{2} - \frac{Bo_P(1+a)}{3 \sin^2(\theta/2)}$ $a = \frac{\rho_L d_B}{4 d_p (\rho_p - \rho_L)}$	the drag force of a single bubble was simplified as the buoyancy force. $a$ is a dimensionless modification factor.
Vinke et al. (1991a)	Stationary state	$2 \arccos(1 - 2 BSL_{\max}) - \sin(2 \arccos(1 - 2 BSL_{\max}))$ $= \frac{8}{\pi} \frac{\lambda_{BP}}{1 + \lambda_{BP}} \left( \frac{3/8 \theta^2}{(1 + \lambda_{BP}) Bo_P} - 1 \right)$	$\lambda_{BP}$ is the ratio between particle radius and bubble radius. smaller porosity
Omota et al. (2006a)	Stationary state	$\sin^2 \frac{\theta}{2} = \phi \frac{(\rho_p - \rho_L) g R_p (R_p + R_b)}{\sigma}$ $(BSL_{\max} - \sin(BSL_{\max}) \cos(BSL_{\max}))$	cohesive force and packing factor included

A series of studies reported the maximum bubble surface loading value in flotation cells/columns. Bradshaw and Connor (1996) showed that the average range of bubble surface loading in flotation column was  $0 \sim 0.14$  for bubble diameters  $\sim 1.2$  mm. This range is similar to the  $0 \sim 0.19$  value range for bubble diameters  $\sim 0.8 - 2.0$  mm reported by Chegeni et al. (2016), as well as the  $0 \sim 0.20$  value range for bubble diameter  $\sim 1.0$  mm reported by Koh and Schwarz (2008). However, the maximum bubble surface loading in a flotation vessel seems to increase with the decrease of bubble size. For example, Huang et al. (2011) found that for bubble diameters  $\sim 0.3$  mm, the range of BSL can be as high as 0.41. Similarly, Sarkar et al. (2011) reported BSL range of  $0 \sim 0.35$  for bubble diameter  $\sim 0.041$  mm.

### 2.3.4. The terminal rise velocity of particle-laden bubbles

Quantifying the effect of the bubble surface loading on the rising velocity of a particle-laden bubble is critical to predict the recovery of particles. The loaded particles significantly change physicochemical properties of a particle-laden bubble, such as the density (Uribe-Salas et al., 2003), the shape and the surface rigidity (Wang et al., 2019a). These changes reduce the bubble velocity, therefore affect the particle recovery.

Uribe-Salas et al. (2003) experimentally demonstrated the descending of fully loaded particle-laden bubbles in a flotation column with downward flow. They reported that once the velocity of the downward slurry exceeded 0.74 cm/s, the gas volumetric fraction in the vicinity of the tailing outlet at the bottom of a flotation column was four times that at the top of the column. From this observation, they concluded that because the density of particle-laden bubble is higher than water, the particle-laden bubble descended at a velocity higher than the downward slurry. In addition, it was observed that further increase of the solid concentration (> 25%) and the velocity of the downward slurry completely suppressed the movement of rising bubbles.

Sarkar et al. (2011) modelled the velocity of the particle-laden bubble based on the force balance. They assumed the Stokes flow condition and computed the drag coefficient  $C_{D,BP}$  as follows:

$$C_{D,BP} = \frac{24\mu_{pulp}}{\rho_{pulp}U_{BP}d_{BP}} \quad (2.20)$$

where  $\mu_{pulp}$  is the pulp viscosity,  $\rho_{pulp}$  is the pulp density,  $d_{BP}$  is the diameter of particle-laden bubble and is considered as the projected area of the particle-laden bubble in the bubble rising direction:

$$d_{BP} = (d_B + d_P)\sin\theta_c + d_P \quad (2.21)$$

where  $\theta_c$  is equivalent to the loading angle  $\theta_{2,load}$ , as shown in **Fig. 2.9**. Based on the force balance, the terminal velocity of the particle-laden bubble was calculated as:

$$U_{BP} = \frac{g}{18\mu_{pulp}d_{BP}}(d_B^3(\rho_{BP} - \rho_G) + N_P d_P^3(\rho_{BP} - \rho_S)) \quad (2.22)$$

Sarkar et al. (2011) only considered the parameters such as the weight of loaded particles, the diameter of the particle-laden bubble in the Stokes drag model in Eq. (2.20). The change in the drag force due to the modified surface mobility of particle-laden bubbles was not considered.

Huang et al. (2011) experimentally examined the velocity reduction of particle-laden bubbles in pure water. They found that to predict such velocity reduction, both the weight of the loaded particles and the modified drag force of particle-laden bubble due to loaded particles have to be considered in the force balance. Huang et al. argued that the change in the surface mobility due to the loaded particles can be used as an analogy with the change in surface immobility due to the contamination of the surfactant on bubble surface. Hence, the drag coefficient as a function of the surface loading level can be related to the drag coefficient for immobile surface and for mobile surface, as shown in Eq. (2.23) (Sadhala and Johnson, 2006).

$$\frac{C_d(\theta_{clean}) - C_d^m}{C_d^{im} - C_d^m} = \frac{1}{2\pi}(2(\pi - \theta_{clean}) + \sin \theta_{clean} + \sin 2\theta_{clean} - \frac{1}{3}\sin 3\theta_{clean}) \quad (2.23)$$

where  $\theta_{clean}$  is equivalent to the loading angle  $\theta_{load}$ ,  $C_d^m$  is the drag coefficient for mobile bubble surface and can be expressed as:

$$C_d^m = \frac{16}{Re_B} \left( 1 + \frac{Re_B}{8 + (Re_B + 3.315 Re_B^{0.5})} \right) \quad (2.24)$$

$C_d^{im}$  in Eq. (2.23) is the drag coefficient for immobile bubble surface and can be calculated as:

$$C_d^{im} = \frac{24}{Re_B} (1 + 0.15 Re_B^{0.687}) \quad (2.25)$$

The predicted terminal velocity of a particle-laden bubble agreed well with the experimental results. Eqs. (2.23) -(2.25) can only be used in pure water because in the presence of surfactant, both the loading region and bare region on the bubble surface can be immobile.

Eskanlou et al. (2019) considered that the terminal velocity of the particle-laden bubble is equal to the slip velocity of bubble in multiphase flow developed by Nguyen and Schulze (2004):

$$U_{BP} = \frac{gd_B^2 F(\alpha_L)(\rho_L - \rho_{pulp})}{18\mu(1+0.15\text{Re}_{BP}^{0.687})} \quad (2.26)$$

where  $F(\alpha_L)$  is a function of liquid holdup  $\alpha_L$  and expressed as follows:

$$F(\alpha_L) = (1 - \alpha_L)^{m-1} \quad (2.27)$$

where  $m$  is a function of bubble Reynolds number.  $\text{Re}_{BP}$  in Eq. (2.26) is the loaded bubble Reynolds number, expressed as:

$$\text{Re}_{BP} = \frac{d_{BP} U_{BP} \rho_L \alpha_L}{\mu_{sl}} \quad (2.28)$$

Compared to Sarkar's model (2011) which assumed Stokes flow regime, Eskanlou's model calculated the drag coefficient in intermediate flow regime typical in flotation by including the correction factor  $1 + 0.15 \text{Re}_{BP}^{0.687}$ . In addition, the inclusion of the effect of liquid holdup on the bubble velocity is one step close to the practical flotation condition. However, the change in surface rigidity of a particle-laden bubble was still not considered in the drag model.

Eskanlou et al. (2018) experimentally quantified the behaviour of a fully loaded bubble in the presence of surfactant. They found that the loaded particles attached to the bubble surface prevents deformation of the bubble surface leading to a more spherical shape compared to a bare bubble. The spherical shape, in turn, led to a relatively straight vertical trajectory without any zigzag. The reduction in the velocity of the fully loaded bubble was ~20% compared to bare bubble.

Wang et al. (2019a) quantified the velocity reduction of particle-laden bubbles with various levels of bubble surface loading. Their study confirmed the finding of Eskanlou et al. (2019) that the particle-laden bubble is more spherical when loaded with particles. A drag modification factor  $\eta_P$  was termed to include the effect of BSL level on the drag coefficient. Based on the Schiller-Naumann model, the modified drag coefficient of the particle-laden bubble was expressed as:

$$C_{D,BP} = (1 + \eta_P) \eta_B \frac{24}{\text{Re}_{BP}} (1 + 0.15 \text{Re}_{BP}^{0.687}) \quad (2.29)$$

The drag modification factor  $\eta_p$  can be calculated from the force balance and was found to increase with BSL level, suggesting that the particle-laden bubble with higher BSL is subject to larger resisting drag force. Although a correlation between  $\eta_p$  and BSL was not proposed, Wang's work is the first experimental quantification of the drag coefficient over various bubble surface levels.

The influence of particle size on the behaviour of rising particle-laden bubbles was investigated by Wang et al. (2019b). It was observed that the rising velocity of particle-laden bubbles decreases with the increasing particle size. Analysis of the drag modification factor  $\eta_p$  as a function of particle diameter presented a non-linear trend: for the fully loaded bubble, as the bubble diameter increased from 92  $\mu\text{m}$  to 125  $\mu\text{m}$ ,  $\eta_p$  increases by 3.74%; but as the bubble diameter increased from 125  $\mu\text{m}$  to 157  $\mu\text{m}$   $\eta_p$  is boosted by 14.41%. It was concluded that the velocity reduction of a particle-laden bubble is greatly affected by the drag force when bubbles are loaded with coarser particles.

## 2.4. Knowledge gap

A thorough literature review of the effect of turbulence on the bubble-particle interaction in flotation identified the following knowledge gaps:

- (1) Bubble-particle collision interactions in the existing literature have been largely studied based on ideal flow field. Effect of turbulence on the bubble-particle collision efficiency is still not fully understood which is attributed to an apparent lack of any appropriate representation of the complex turbulent flow field and limited knowledge of associated particle dispersion.
- (2) Earlier studies on the modelling of bubble-particle collision interactions are entirely based on a single bubble-particle system. For a better description of the collision efficiency parameter in a typical flotation environment, a statistical representation is deemed appropriate in a multibubble-particle system which needs to account for volume fraction of bubble and particles.
- (3) Successful recovery of particles depends on the rise velocity of particle-laden bubbles reaching the froth layer. Existing studies on the rising dynamics of a

particle-laden bubble are noted to be rather limited. Besides, quantification of rising velocity of particle-laden bubbles is limited to pure water in the absence of any surface contaminant e.g., surfactant. Also, limited studies are reported on the bubble drag coefficient correlated to surface loading in the presence of surfactant which closely represents bubble dynamics in a typical flotation environment.

- (4) The existing recovery models are mostly limited to bubble-particle collision efficiency derived under ideal flow conditions. Also, most the models include only constant bubble rise velocity without accounting for transient variation in bubble surface loading.

## 2.5. Research scope

This chapter aimed at describing the theoretical modelling of the recovery in flotation; the critical review of the bubble-particle collision in both laminar and turbulent flow; and the effect of bubble surface loading on bubble rising behaviour. While each of these areas is a broad field of research in its own right, a general background was however deemed indispensable to present a physical picture of the research problem. In the subsequent chapters and appendices, studies are presented based on the body of knowledge presented in Chapter 2 to address the research objectives laid out in Section 1.3.

# **Chapter 3. Effect of turbulence dispersion on bubble-particle collision efficiency in single-bubble system**

---

## **3.1. Introduction**

It is widely established that physical contacts or collisions between bubbles and particles governs the recovery in a typical flotation system (Nguyen and Schulze, 2004; Jameson, 2010). The trajectory of a particle approaching a bubble is important in determining a collision outcome which depends on the characteristics of surrounding flow field. In an ideal flow field either laminar (viscosity dominated) or potential (negligible viscosity effect), particle trajectory is deterministic and has been extensively studied leading to proposition of various collision models. An excellent review of these models can be found in Dai et al. (2000).

However, in practical flotation systems, flow field is far from ideal due to complex phase interactions and background turbulence. Sahbaz et al.(2012) and Meng et al. (2014) showed that turbulence intensity (defined as the ratio of root-mean-squared fluctuating velocity to the mean velocity component of the flow field) in a Jameson cell or stirred tank flotation cell can reach up to ~23%. In a turbulent flow environment, particles gain kinetic energy from the multi-scale eddies around them. Consequently, particle trajectory fluctuates and deviates significantly from the flow streamline which has been experimentally observed in Sommer et al. (2020). Such interactions between particles and turbulent eddies are referred to as turbulence dispersion which contributes significantly to successful collisions and consequently recovery of particles (Wang et al., 2017b).

Particle recovery in flotation system can be attributed to two separate parameters – bubble-particle collision frequency ( $Z_{PB}$ ) and corresponding collision efficiency ( $E_c$ ) (Koh and Schwarz, 2006). The collision frequency  $Z_{PB}$  represents the number of events where the path of bubble and particle crosses (Nguyen and Schulze, 2004). Saffman and Turner (1956) proposed a collision frequency model accounting for particle acceleration by utilizing energy dissipation rate and liquid viscosity. Arguing that the particle velocity is independent of eddy

velocity when its relaxation time is larger than the integral time scale of eddy, Abrahamson (1975) put forth a threshold particle diameter and determined the collision frequency of cross-eddy collision for particles beyond the threshold. The collision frequency models by Saffman and Turner (1956) and Abrahamson (1975) have been extensively applied in predicting recovery in flotation process (Duan et al., 2003; Koh and Smith, 2011; Karimi et al., 2014a, b).

The collision efficiency parameter  $E_c$  is determined as the ratio of actual to ideal rate of particles encountering the bubble (Nguyen and Schulze, 2004). Compared to the well-developed collision frequency models, there is a limited knowledge of the effect of turbulence dispersion on collision efficiency  $E_c$ . Shahbazi et al. (2010) experimentally determined the bubble-particle collision efficiency in a flotation cell by applying the measured bubble Reynolds number into the collision efficiency models developed in the absence of turbulence. The predicted trends that collision efficiency increases with turbulence level agreed with the data reported by Wang et al. (2017b). However, such laminar flow model based method ignores the properties of turbulence flow. Realizing the necessity of examining the trajectory of particles directly in turbulent flow to determine the turbulent collision efficiency, Nadeem et al. (2006) conducted numerical simulations in single-bubble-multiple-particles system by introducing turbulence at the inlet. Their study, however, ignored the dispersion of particles caused by the fluctuating velocity from surrounding eddies and therefore shows similar trend to the predictions of collision efficiency models based on the absence of turbulence.

Relatively fewer studies on collision efficiency in turbulent flow indeed included the turbulence dispersion (Liu and Schwarz, 2009a; Ngo-Cong et al., 2018; Islam and Nguyen, 2020). Liu and Schwarz (2009a) assumed that only eddies of size between the Kolmogorov scale and the bubble size affect the collision efficiency. They included the particle tracking approach in their numerical simulations and noted that collision efficiency generally increased with energy dissipation rate. Such increasing trend was consistent with the analytical prediction by Ngo-Cong et al. (2018). Turbulence dispersion was also incorporated in the numerical simulations by Islam and Nguyen (2020) through the “random walk model”. The predicted collision efficiency agreed well with the sum of the collision efficiency developed by Nguyen and Schulze (2004) in the absence of turbulence and the collision efficiency developed by Levich (1962) in the presence of turbulence. However, the predicted collision efficiency by Islam and Nguyen (2020) was found to decrease with the turbulence intensity level in contrast

to the increasing trend reported by Liu and Schwarz (2009a) and Ngo-Cong et al. (2018). It is apparent that due to the complicated nature of turbulence, there is still no consensus in how the turbulence dispersion affects the collision efficiency.

This chapter aimed at determining the effect of turbulence dispersion on collision efficiency. The specific objective was to develop a simple theoretical model of collision efficiency accounting for the effect of turbulence dispersion through fluctuating velocity component of both particle and fluid phase and compare the model prediction with a developed Eulerian-Lagrangian computational fluid dynamics (CFD) model. This chapter is organized as follows: Section 2 examines the critical distance for streamline distortion in the presence of bubble as an input parameter to the following two developed models. Section 3 presents the development of the theoretical turbulence dispersion model of collision efficiency; Section 4 illustrates the development of the Eulerian – Lagrangian CFD model; and Section 5 presents the validation of the developed theoretical and numerical models and the capability of both models to predict the effect of turbulence dispersion on collision efficiency was compared. Finally, the dispersion behaviour of particles in turbulent flow was investigated.

### 3.2. Critical distance for particle injection above a stationary bubble

In the numerical modelling, a stationary bubble was considered with a downward liquid flow field set at the bubble slip velocity to determine the collision efficiency (Yoon, et al., 1989; Nadeem et al., 2006; Islam and Nguyen, 2020). It is noteworthy mentioning that one determining factor of collision efficiency is the ideal rate of particles that encounter a bubble if particles approach the bubble axially along the direction of flow (Nguyen and Schulze, 2004). Therefore, it is necessary to ascertain that particles released above the bubble were initially positioned at a location where the streamlines were not distorted in the presence of bubble (Yoon, et al., 1989). This section examines this critical upstream distance which can be used both in the theoretical turbulence dispersion model (Section 3.3) and CFD model (Section 3.4).

**Fig. 3.1** presents the schematic of the fluid streamlines above a stationary bubble. It was assumed that the onset of distortion of streamline around the bubble occurs at a critical height  $H_{B,\text{onset}}$  which can be calculated from the critical radial distance  $r_{\text{onset}}$  and polar angle  $\theta_{\text{onset}}$ , as shown in the following equation:

$$H_{B,\text{onset}} / R_B = r_{\text{onset}} \cos \theta_{\text{onset}} \quad (3.1)$$

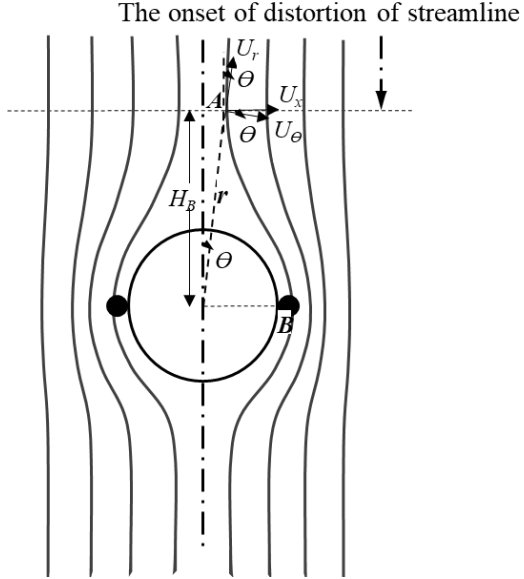


**Fig. 3.1.** Schematic of the distortion of streamline around the bubble.

To determine  $r_{\text{onset}}$  and  $\theta_{\text{onset}}$ , we define that the onset of the distortion occurs when the velocity in x direction  $U_{x,\text{onset}}$  normalized by the inlet velocity  $U_B$  reaches 1%, namely:

$$U_{x,\text{onset}} = 1\% \quad (3.2)$$

The flow velocity in x direction  $U_{x,\text{onset}}$  in Cartesian coordinate system can be converted from the radial velocity  $U_{r,\text{onset}}$  normalized by the inlet velocity  $U_B$  and tangential velocity  $U_{\theta,\text{onset}}$  normalized by the inlet velocity  $U_B$ , in a spherical coordinate system as follows:

$$U_{x,\text{onset}} = U_{r,\text{onset}} \sin \theta_{\text{onset}} + U_{\theta,\text{onset}} \cos \theta_{\text{onset}} \quad (3.3)$$

The flow radial velocity  $U_{r,\text{onset}}$  in Eq. (3.3) can be calculated as follows (Clift, et al., 1978):

$$U_{r,\text{onset}} = -\frac{1}{r_{\text{onset}}^2 \sin \theta_{\text{onset}}} \left. \frac{\partial \psi}{\partial \theta} \right|_{r_{\text{onset}}, \theta_{\text{onset}}} \quad (3.4)$$

where the stream function  $\psi$  normalized by  $U_B R_B^2$  can be calculated from the model proposed by Yoon, et al. (1989) at intermediate Reynolds number range - typically occurred in flotation, as shown in the following equation:

$$\psi = \sin^2 \theta \left( \frac{1}{2} r^2 - \frac{3}{4} r + \frac{1}{4r} + \frac{\text{Re}_B^{0.72}}{15} \left( \frac{1}{r^2} - \frac{1}{r} + r - 1 \right) \right) \quad (3.5)$$

Based on Eq. (3.5), the derivative of stream function with respect to the polar angle  $\theta$  can be calculated as follows:

$$\frac{\partial \psi}{\partial \theta} = 2 \sin \theta \cos \theta \left( \frac{1}{2} r^2 - \frac{3}{4} r + \frac{1}{4r} + \frac{\text{Re}_B^{0.72}}{15} \left( \frac{1}{r^2} - \frac{1}{r} + r - 1 \right) \right) \quad (3.6)$$

The tangential velocity  $U_{\theta, onset}$  in Eq. (3.3) can be calculated as follows:

$$U_{\theta, onset} = \frac{1}{r_{onset} \sin \theta_{onset}} \frac{\partial \psi}{\partial r} \Big|_{r_{onset}, \theta_{onset}} \quad (3.7)$$

where the derivative of stream function with respect to the radial distance  $r$  can be calculated as follows:

$$\frac{\partial \psi}{\partial r} = 2 \sin^2 \theta \left( r - \frac{3}{4} - \frac{1}{4r^2} + \frac{\text{Re}_B^{0.72}}{15} \left( -\frac{2}{r^3} + \frac{1}{r^2} + 1 \right) \right) \quad (3.8)$$

Another relationship between the critical radial distance  $r_{onset}$  and polar angle  $\theta_{onset}$  is necessary to solve Eq. (3.2). It is noted that at position B (see **Fig. 3.1**) where the particle just grazes the bubble surface, the stream function  $\psi$  of the grazing streamline is the same as at position A and can be calculated as:

$$\psi \Big|_{r_{onset}, \theta_{onset}} = \sin^2 90^\circ \left( \frac{1}{2} r'^2 - \frac{3}{4} r' + \frac{1}{4r'} + \frac{\text{Re}_B^{0.72}}{15} \left( \frac{1}{r'^2} - \frac{1}{r'} + r' - 1 \right) \right) \quad (3.9)$$

where  $r' = (R_B + R_p) / R_B$  and the largest particle radius 50  $\mu\text{m}$  examined in this chapter is used as the particle radius  $R_p$ .

The normalized critical height  $H_{B,\text{onset}} / R_B$  calculated using Eqs. (3.1) - (3.9) is presented in **Fig. 3.2** and is observed to follow a power law dependency on the bubble Reynolds number in the functional form of  $H_{B,\text{onset}} = 6.0 \text{Re}_B^{-0.13}$  ( $R^2 = 0.99$ ). Such a decreasing trend suggests that the streamline distortion occurs closer to the bubble for larger  $\text{Re}_B$  due to the increased inertia of fluid particles. It is also noted that  $H_{B,\text{onset}}$  is less than  $4R_B$  for the typical range of bubble Reynolds number in flotation, 20-300 (Dobby and Finch, 1987). Therefore, it is recommended that the stationary bubble be centred at  $4R_B$ , namely 2.0 mm, below the inlet boundary to avoid the distortion of streamlines.

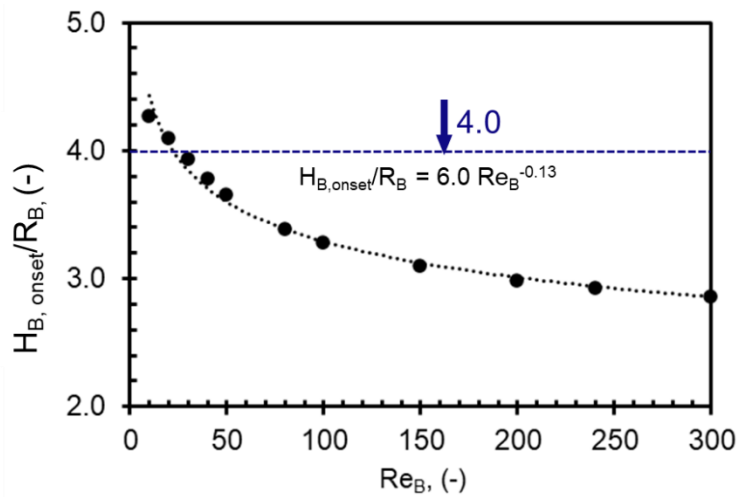


**Fig. 3.2.** The normalized distance between the bubble centre and height where onset of streamline distortion occurs as a function of bubble Reynolds number.

### 3.3. Theoretical modelling: Turbulence dispersion

Following the determination of the critical distance for distortion of streamlines, a modelling approach for quantifying collision efficiency is presented in this section. It is assumed that the turbulent flow in the vicinity of a bubble is homogeneous and isotropic. Let us consider the case of a stationary bubble with turbulent flow sweeping past the bubble in the downward direction as shown in **Fig. 3.3**.

For a particle released at a radius  $R_i$  from the bubble vertical centre axis in an isotropic turbulent flow (see **Fig. 3.3a**), its trajectory is affected by both mean velocity and the fluctuating velocity component of the flow field (Nguyen, et al. 2016). As a result, on the

bubble equator the final horizontal position of particle is the superimposition of the horizontal displacement due to mean flow,  $S_{x,mean}$ , and that due to the fluctuating flow,  $S_{x,fluc}$ , as shown in **Fig. 3.3**. The collision efficiency can be determined based on  $S_{x,mean}$  and  $S_{x,fluc}$  which is discussed in the next section.

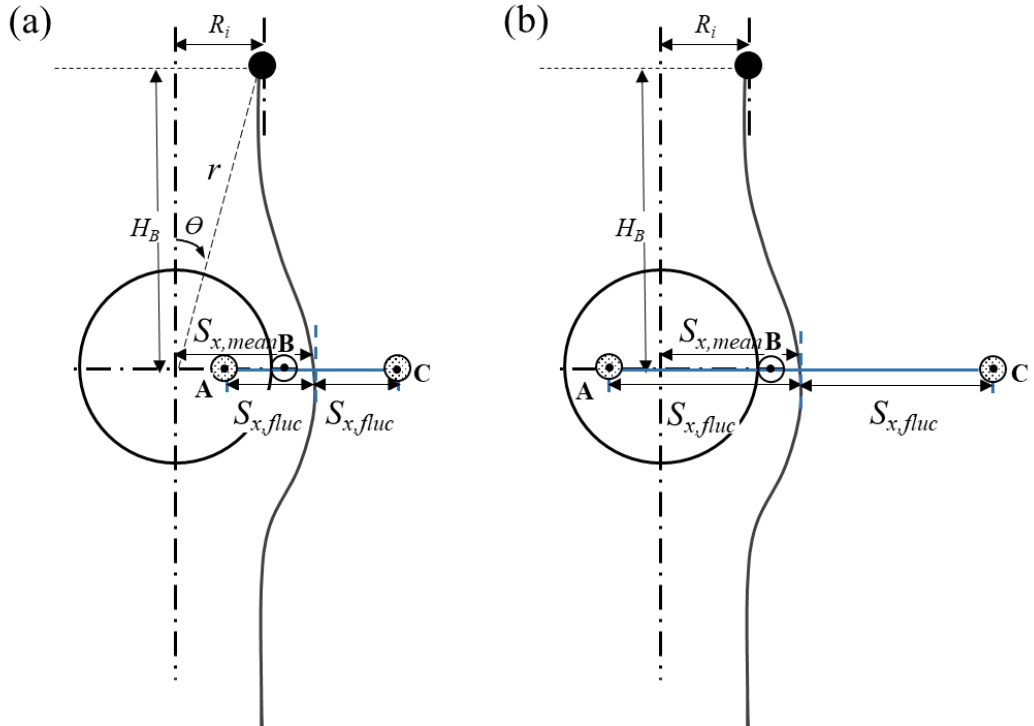


**Fig. 3.3.** Decomposition of the particle position into the mean flow and the fluctuating flow:  
 (a) in low turbulence intensity case; (b) in high turbulence intensity case. The symbols are: ● Initial position of the particle; ○ the critical position when particle just touches the bubble; and ⊙ the two-extreme boundaries of the final position of the particle.

### 3.3.1. Horizontal displacement of particles due to mean flow

Assuming that particle inertia is negligible, the horizontal displacement of a particle due to mean flow can be obtained by integrating the mean flow velocity (in absence of the fluctuating component) over a specified time interval as follows:

$$S_{x,mean} = \int_0^{t_{tot}} U_r U_B \sin \theta dt \quad (3.10)$$

where the normalized radial velocity  $U_r$  of flow can be calculated using the following equation:

$$U_r = -\frac{1}{r^2 \sin \theta} \frac{\partial \psi}{\partial \theta} \quad (3.11)$$

The time taken by a particle to travel the height of  $H_B$  and reach the level of the bubble equator is used as the total integration time in Eq. (3.10). The radial distance  $r$  and the polar angle  $\theta$  during the integration can be calculated as follows:

$$dr = U_r dt \quad (3.12)$$

$$d\theta = \frac{U_\theta}{r} dt \quad (3.13)$$

where the tangential velocity  $U_\theta$  is calculated:

$$U_\theta = \frac{1}{r \sin \theta} \frac{\partial \psi}{\partial r} \quad (3.14)$$

Two initial conditions - polar angle and the radial distance are needed to solve Eq. (3.10) which are given as:

$$\theta_o = \tan^{-1} \frac{R_i}{H_B} \quad (3.15)$$

$$r_o = \frac{R_i}{\sin \theta_o R_B} \quad (3.16)$$

Eqs. (3.10) - (3.16) were used together to determine the particle horizontal displacement due to mean flow.

### 3.3.2. Horizontal displacement of particles due to fluctuating flow

The particle displacement due to fluctuating flow field as shown in **Fig. 3.3** can be expressed as:

$$S_{x,fluc} = \int_0^{H_B/U_B} u_{P,rms,x} dt \quad (3.17)$$

The total integration time period of the particle arriving at the bubble equator level in Eq. (3.17) can be simplified as  $H_B / U_B$ .

Assuming an isotropic and homogeneous turbulent flow field, the root-mean-square velocity of the particle in one direction of x-axis (see **Fig. 3.3**) can be calculated as follows:

$$u_{P,rms,x-}^2 = \frac{1}{2} u_{P,rms,x}^2 \quad (3.18)$$

$$u_{P,rms,x}^2 = \frac{1}{3} u_{P,rms}^2 \quad (3.19)$$

The root-mean-square velocity of the dispersed particles in turbulence,  $u_{P,rms}$ , is determined as (Yuu, 1984):

$$u_{P,rms} = A_P^{0.5} u_{f,rms} \quad (3.20)$$

where  $u_{f,rms}$  is the root-mean-square velocity of fluid.

The correlation coefficient  $A_P$  is a function of particle properties and can be written as:

$$A_P = \frac{a_P \tau_l + b_P^2}{a_P \tau_l + 1} \quad (3.21)$$

where the integral time scale,  $\tau_l$ , can be calculated as the ratio of the turbulence integral length scale to the root-mean-square velocity of flow, as shown in the following equation:

$$\tau_l = \frac{l}{u_{f,rms}} \quad (3.22)$$

According to Yuu (1984) and Ngo-Cong et al. (2018), the coefficient  $a_p$  and  $b_p$  in Eq. (3.21) can be calculated by:

$$a_p = \frac{36\mu}{d_p^2(2\rho_p + \rho_f)} \quad (3.23)$$

$$b_p = \frac{3\rho_f}{(2\rho_p + \rho_f)} \quad (3.24)$$

where  $\mu$  is the dynamic viscosity,  $d_p$  is the particle diameter,  $\rho_p$  is particle density and  $\rho_f$  is the liquid density. Eqs. (3.17) - (3.24) are used together to determine the particle displacement due to fluctuating flow field.

### 3.3.3. Collision efficiency

Following the determination of the particle horizontal displacement due to the mean flow  $S_{x,mean}$  and the fluctuating flow component  $S_{x,fluc}$ , the collision efficiency parameter is determined in this section. Depending on the turbulence intensity  $Ti$ , particles released on one side of the bubble may collide with the bubble on the same side (at low  $Ti$ , see **Fig. 3.3a**), or may go over the bubble vertical axis and collide with the bubble on the other side (at high  $Ti$ , see **Fig. 3.3b**). In the range of all possible final positions  $AC \sim 2S_{x,fluc}$ , particles which fall into the range of AB collide with the bubble (B denotes the position at particles just collide with the bubble). In this sense, the collision efficiency for particles released at radius  $R_i$  and height  $H_B$  from a bubble in turbulent flow can be defined as:

$$E_c = \frac{|AB|}{|AC|} = \frac{|(R_B + R_p) - (S_{x,mean} - S_{x,fluc})|}{2S_{x,fluc}} \quad (3.25)$$

### 3.4. CFD modelling

A 3D CFD model including continuity, momentum, the large eddy simulation (LES) turbulence model and discrete phase method (DPM) approach was developed using the finite volume method based commercial solver ANSYS (v19.2) platform to determine bubble-particle collision behaviour. The relevant governing equations are summarized in **Table 3.1**. **Fig. 3.4** presents the dimensions of 3D computational domain ( $5 \text{ mm} \times 5 \text{ mm} \times 6 \text{ mm}$ ) and boundary conditions.

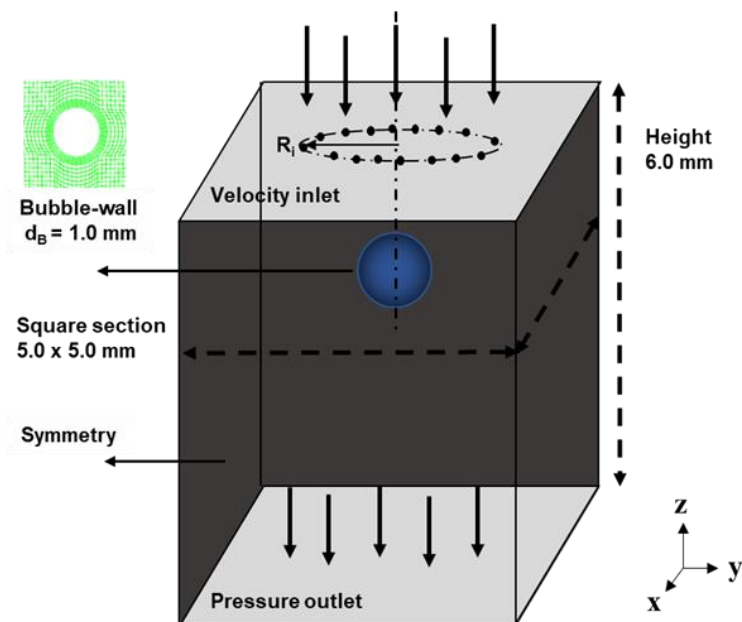


**Fig. 3.4.** Computational domain and boundary conditions.

A hexahedral mesh was generated using ICEM CFD meshing tool. A mesh independence test was also carried out based on five different mesh sizes. **Fig. 3.5** shows computation of bubble drag coefficient for the conditions:  $Re_B \sim 230$  and  $R_B \sim 500 \mu\text{m}$ . It is clearly seen that as the mesh cell number exceeds 238,072, the bubble drag coefficient becomes almost invariant of the mesh density. Based on this test result, the rest of the simulations were performed with this mesh size.

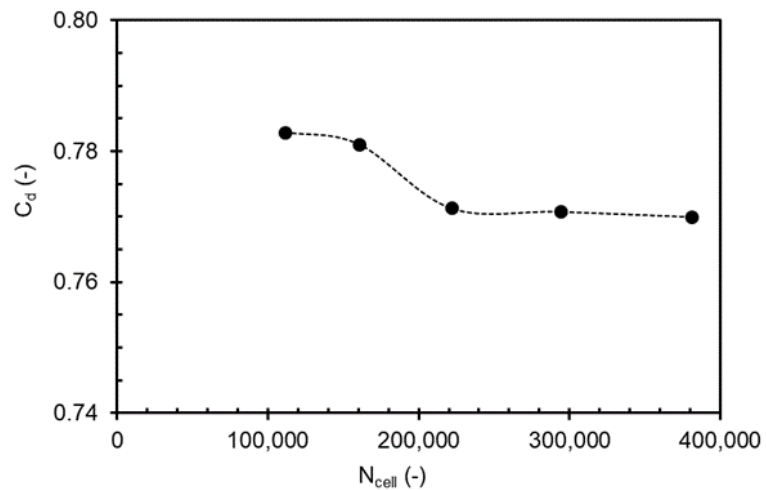


**Fig. 3.5.** Bubble drag coefficient vs number of cells for  $Re_B \sim 230$ ,  $R_B \sim 500 \mu\text{m}$ .

**Table 3.1.** Governing equations of the CFD model

LES velocity decomposition	$u_i = \bar{u}_i + u'_i$	
Continuity equation	$\frac{\partial \rho}{\partial t} + \frac{\partial}{\partial x_i}(\rho \bar{u}_i) = 0$	$\rho$ is density; $\bar{u}_i$ is filtered velocity;
Momentum equation	$\frac{\partial \rho \bar{u}_i}{\partial t} + \frac{\partial}{\partial x_j}(\rho \bar{u}_i \bar{u}_j) = -\frac{\partial \bar{p}}{\partial x_i} + 2 \frac{\partial}{\partial x_j}[\mu(\bar{S}_{ij})] - \frac{\partial}{\partial x_j}(\tau_{ij}) + f'_p$ $\bar{S}_{ij} = \frac{1}{2} \left( \frac{\partial \bar{u}_i}{\partial x_j} + \frac{\partial \bar{u}_j}{\partial x_i} \right)$ $\tau_{ij} = \rho \bar{u}_i \bar{u}_j - \rho \bar{u}_i \bar{u}_j$	$\bar{p}$ is filtered pressure; $f'_p$ is the sum of particle-fluid forces in control volume; $\mu$ is molecular viscosity; $\bar{S}_{ij}$ is the resolved scale strain rate tensor and $\tau_{ij}$ is the unknown subgrid-scale (SGS) stress tensor.
Subgrid-scale (SGS) stress tensor	$\tau_{ij} - \frac{1}{3} \tau_{kk} \delta_{ij} = -2 \mu_t \bar{S}_{ij}$ $\mu_t = C_k \Delta k^{0.5}$	$\tau_{kk}$ is the isotropic part of the subgrid-scale stress, $k$ is turbulence kinetic energy.
Fourier inlet fluctuating velocity generator	$u'(x) = 2 \sum_{n=1}^N \hat{u}^n \cos(\kappa^n \cdot x + \psi^n) \sigma^n$	$\hat{u}^n$ , $\psi^n$ and $\sigma^n$ are the amplitude, phase and direction of Fourier mode n. n is fix at 100. $\sigma^n$ and $\kappa^n$ should be orthogonal to maintain the continuity.
Particle trajectory	$m_p \frac{du_p}{dt} = F_d + F_g + F_l + F_{vm}$	$m_p$ = particle mass, $u_p$ = particle velocity, $F_d$ = drag force, $F_g$ = gravity force, $F_l$ = lift force, $F_{vm}$ = virtual mass force.

In order to gain a more accurate velocity distribution around the bubble, the mesh size refinement around the bubble was restricted to 30  $\mu\text{m}$  to meet the DPM simulation requirements (particle size  $\leq$  cell size). Besides, to model the boundary layer on the bubble surface, size of the first cell layer was also found to be 30  $\mu\text{m}$  to meet the  $y^+ = 1$  requirement in the LES model (ANSYS; Schlichting, 1979). Away from the bubble interface, mesh size was kept 83  $\mu\text{m}$ .

Another consideration to determine the computational mesh size was the theoretical eddy sizes. The relative motion between bubbles and particles which leads to collision are strongly affected by eddies in the inertial subrange (Nguyen and Schulze, 2004; Liu and Schwarz, 2009a), Taylor microscale (smallest eddy length in the inertial subrange) needs to be resolved. Three principal eddy sizes i.e. integral length scale, Taylor microscale and Kolmogorov scale which are often used to characterise the turbulent energy spectrum are summarized in **Table A.1** in Appendix A. Kolmogorov scale being the smallest length scale was possible to resolve only for the lower turbulence intensity case ( $Ti \sim 4\%$ ), but could not be resolved for the higher turbulence intensity case ( $Ti \sim 20\%$ ) due to the particle size limitation within the DPM modelling framework stated earlier.

A rigid stationary bubble was placed 2.0 mm below the inlet boundary while liquid flow enters the inlet at a mean slip velocity of 0.23 m/s. This modelling approach has been applied in a significant number of studies (Nadeem, et al., 2006; Li et al., 2019; Ge et al., 2020; Islam et al., 2020;). The approach also reduces the gas-liquid two-phase flow simulation into single-phase (liquid) flow simulation with lower computational cost and enables to resolve the boundary layer on bubble surface. This approach is suitable for modelling bubbles with diameter up to 1.0 mm because the shape deformation can be considered negligible in this bubble size regime (Clift et al., 1978). It should be noted that EDLVO forces were not applied between bubble and particles therefore attachment of particles onto the bubble was not accounted. Additionally, because the bubble was set stationary, the influence of particle collisions on bubble movement was not accounted. The bubble surface was set as no-slip wall condition to simulate the immobile surface condition which prevails in a typical flotation environment due to the presence of surfactant.

This distance between the bubble centre and the inlet boundary 2.0 mm was determined in Section 3.2 to ensure that liquid flow at the inlet was not distorted in the presence of the bubble. The mean liquid 0.23 m/s in the direction of gravity (-z), with the corresponding bubble Reynolds number being 230 which represents an intermediate flow regime. Boundary condition at the outlet was set to atmospheric pressure. The four sides of the domain were assigned to symmetry (free slip) condition.

The Large Eddy Simulation (LES) approach with Smagorinsky-Lilly Subgrid-Scale model (SGS) was used to simulate the turbulent flow. The LES approach was reported to be capable of modelling turbulent flows more accurately than the Reynolds averaged Navier Stokes (RANS) family models but at lower computational expense than the Direct Numerical Simulation (DNS) method (Pope, 2000). Four turbulence intensity  $Ti$  levels, -4%, 7%, 11% and 20% were used with the integral length scales for each case set equal to the bubble diameter of  $1 \times 10^{-3}$  m. These  $Ti$  levels are within the range reported by Sahbaz et al.(2012) and Meng et al. (2014) in flotation system. The Spectral Synthesizer method (Montorfano et al., 2013) was applied at the inlet to generate fluctuating velocity based on the pre-set turbulence intensity level. The generated turbulence intensity at the inlet by this method was quantified in Appendix B and indeed agreed with the predefined one. A summary of the operating conditions is presented in **Table 3.2**.

**Table 3.2.** Summary of the operating conditions and numerical scheme used in simulations

Phase			
Water	Density	998.2 kg/m <sup>3</sup>	
	Viscosity	1×10 <sup>-6</sup> m <sup>2</sup> /s	
	Turbulence intensity level	4%, 7%, 11%, 20%	
	Integral length scale	1×10 <sup>-3</sup> m	
Particle	Density	1200 kg/m <sup>3</sup>	
	Diameter	30, 60, 100 μm	
	Release radius, R <sub>v</sub> /R <sub>B</sub>	0, 0.116, 0.232, 0.506, 0.750, 1.000, 1.500,	
	Number of total released particles	1000	
Bubble	Diameter	1000 μm	
	Reynolds number	230	
Numerical scheme			
Discretisation schemes		Second-order upwind bounded central differencing scheme	(momentum), (pressure)
Gradient/derivative calculations		Least-squares cell-based gradient method	
Pressure-velocity coupling		SIMPLE algorithm	
Time step size		10 <sup>-4</sup> s	
Residuals for convergence		10 <sup>-3</sup>	

The dispersion of particles, which is governed by the interaction of a particle with surrounding eddies, was predicted by integrating the particle trajectory equation in **Table 3.1** over a time scale that is lesser of the eddy lifetime and the particle eddy crossing time (ANSYS).

The drag force  $F_d$  on particles was calculated as:

$$F_d = m_p \frac{9C_d \mu \text{Re}_p}{48 \rho_p R_p^2} (\bar{u}_i + \dot{u}_i - u_p) \quad (3.26)$$

The momentum exchange due to the mean fluid velocity was modelled by calculating the drag coefficient  $C_d$  using the following Spherical drag law (Morsi and Alexander, 1972):

$$C_d = a_1 + \frac{a_2}{\text{Re}_p} + \frac{a_3}{\text{Re}_p^2}$$

$$a_1, a_2, a_3 = \begin{cases} 0, 24, 0 & (0 < \text{Re}_p < 0.1) \\ 3.690, 22.73, 0.0903 & (0.1 < \text{Re}_p < 1) \\ 1.222, 29.1667, -3.8889 & (1 < \text{Re}_p < 10) \\ 0.6167, 46.50, -116.67 & (10 < \text{Re}_p < 100) \\ 0.3644, 98.33, -2778 & (100 < \text{Re}_p < 1000) \end{cases} \quad (3.27)$$

The Morsi and Alexander drag law was chosen for covering a large range of particle Reynolds numbers which may occur in turbulent flow due to the interaction of particles with different length scales of eddies. The momentum exchange due to the fluctuating fluid velocity was modelled by calculating the fluctuating fluid velocity  $\dot{u}_i$  using the random walk model (Ziff et al., 2009), also known as the “eddy lifetime model”:

$$\dot{u}_i = 1.49 \zeta \sqrt{\varepsilon \tau_l} \quad (3.28)$$

where  $\zeta$  is a random number of the Gaussian distribution,  $\varepsilon$  is the energy dissipation rate and  $\tau_l$  is the eddy integral lifetime.

Simulations were conducted for three different particle diameters- 30, 60 and 100  $\mu\text{m}$ , respectively. To avoid the overlap of particles, the number of particles contained in each “parcel”, the basic unit utilized by the DPM method was set to one. Also, the number of particles initially released from a circular injection domain as shown in **Fig. 3.4** was set to avoid any overlap of particles. For example, the number of particles initially released from the circle of radius  $0.506 R_B$  was 40 for  $d_P = 30 \mu\text{m}$  and 12 for  $d_P = 100 \mu\text{m}$ . The time interval between each successive release of particles was set to  $5 \times 10^{-3} \text{ s}$ .

The collision efficiency  $E_c$  is defined as the ratio of the number of particles colliding with bubble  $N_c$  to the total released number of particles  $N_t$  along the circle above the bubble as given in (Moreno-Atanasio et al., 2016):

$$E_c = N_c / N_t \quad (3.29)$$

To determine the actual collision number  $N_c$ , the particle coordinates data were obtained from the simulations and processed by an in-house MATLAB code. A collision was accounted when the distance between the centre of particle and bubble was equal to or less than the sum of particle and bubble radius, as shown in the following equation:

$$(x_p - x_b)^2 + (y_p - y_b)^2 + (z_p - z_b)^2 \leq (R_p + R_b)^2 \quad (3.30)$$

where  $x_p$ ,  $y_p$  and  $z_p$  are the coordinates of the particle centre;  $x_b$ ,  $y_b$  and  $z_b$  are the coordinates of the bubble centre. To ensure that the collision efficiency is statistically stable,

separate sets of simulations were conducted with different number particles  $N_t$  in the circular injection domain. **Fig. 3.6** illustrates the independence test of collision efficiency over  $N_t$ . It was clearly

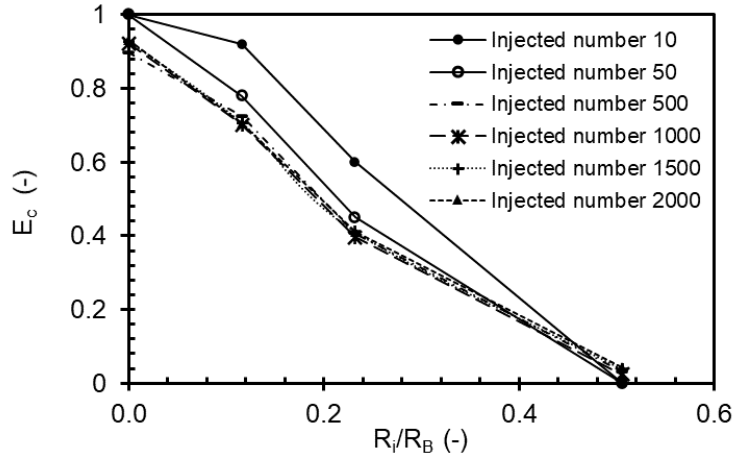


**Fig. 3.6.** The change of collision efficiency with number of particles for turbulence intensity  $Ti \sim 4\%$  and particle diameter  $d_p \sim 60 \mu\text{m}$  at bubble Reynolds number  $Re_B \sim 230$ .

observed that as the number of the total released particles reach 1000, the collision efficiency becomes invariant of the released particle number. As a result, the value of the total released number of particles  $N_t$  was set at 1000 for all subsequent computational runs.

### 3.5. Results and discussion

#### 3.5.1. Model validation

The collision efficiency predicted by the turbulence dispersion model for different particle sizes ( $d_p \sim 5$  to  $60 \mu\text{m}$ ) and turbulence intensities ( $Ti \sim 4\%$  to  $20\%$ ) was plotted against the well-known collision efficiency models (Langmuir and Blodgett, 1946; Sutherland, 1948; Flint and Howarth, 1971; Weber and Paddock, 1983; Schulze, 1989; Yoon, R.H., Luttrell, 1989; Nguyen and Kmet, 1992; Dai et al., 2000), as shown in **Fig. 3.7**. It can be noted that at lower turbulence intensity  $\sim 4\%$ , the collision efficiency  $E_c$  is close to the prediction of Yoon-Luttrell,

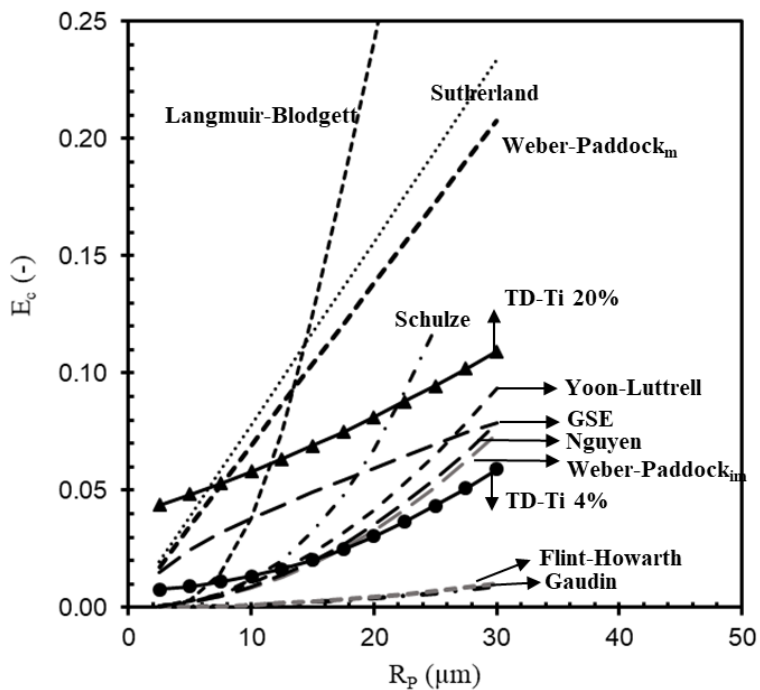


**Fig. 3.7.** Comparison of collision efficiency predicted by Turbulence Dispersion model with the literature (Dai et al., 2000) as a function of particle size. The Weber-Paddock collision model for both mobile bubble surface and immobile bubble surface, denoted by the subscripts  $m$  and  $im$  were included ( $d_B \sim 0.77$  mm,  $U_B \sim 0.316$  m/s,  $\rho_p \sim 2650$  kg/m $^3$ ,  $\rho_f \sim 1000$  kg/m $^3$ ,  $\mu_L \sim 0.001$  kg.m $^{-1}$ s $^{-1}$ ).

Weber- Paddock model (immobile bubble surface), Nguyen model and the GSE model. In comparison, the Langmuir-Blodgett (L-B) model, Sutherland model and Weber – Paddock (W-P) based on mobile surface assumption significantly overestimate the collision efficiency. This is because the L-B model is suitable for particle Stokes number  $St$  larger than 0.7, a threshold higher than the maximum  $St \sim 0.44$  examined in **Fig. 3.7**. The Sutherland model was developed for potential flow which is close to the flow condition in the presence of mobile-surface bubble. The critical thickness for the rupture of the liquid film between bubble and particles increased for mobile bubble surface case, leading to enhanced collision efficiency (Schulze, 1992; Liu and Schwarz, 2009b). Such enhancement was confirmed in **Fig. 3.7** where both the Sutherland model and mobile-bubble-surface based W-P model resulted in larger collision efficiency. On the other hand, the Flint-Howarth (F-H) model and Gaudin

significantly underestimate the collision efficiency because these two models were developed in Stokes flow regime and hence only suit to bubble size smaller than  $\sim 0.1$  mm, a value much smaller than the examined bubble size of 0.77 mm in **Fig. 3.7**. However, as turbulence intensity increased from  $T_i \sim 4\%$  to  $\sim 20\%$ , only collision efficiency  $E_c$  predicted by the turbulence dispersion (TD) model increased as other models in **Fig. 3.7** do not include any turbulence-related parameters.

To demonstrate the capability of the 3D CFD model developed in the present study, it was first validated by comparing its prediction of drag coefficient of a spherical object (rigid bubble in this case) with the well-known Schiller Naumann (S-N) model (1933). **Fig. 3.8a** compares the CFD model predicted drag coefficient ( $C_d$ ) of a rigid bubble ( $d_B = 1$  mm) as a function of bubble Reynolds number ( $Re_B = 60$  to  $400$ ) with the S-N model. The predicted drag coefficient decreases with increasing Reynolds number which can be conveniently described by a power law fit ( $R^2 \geq 0.98$ ). Clearly, the CFD model predicted  $C_d$  values provide an excellent agreement with the S-N drag model producing deviations less than 10%.

As a next set of validation, the collision efficiency computed by the CFD model was compared with the well-known Yoon-Luttrell and Weber model for a  $Re_B \sim 230$  case (see **Fig. 3.8b**). Yoon-Luttrell model computes collision efficiency as a function of  $Re_B$  and is commonly used in estimating bubble-particle interaction (Koh and Smith, 2011). On the other hand, Weber model includes the effect of gravitational force and collision angles (Weber and Paddock, 1983; Dobby and Finch, 1987).

The simulations were carried out for particle size ranging from  $\sim 15$  to  $45$   $\mu\text{m}$ . Particle trajectory was computed from the force balance model (**Table 3.1**) and a collision was defined when the difference between the particle and bubble centres was computed to be less than the sum of particle and bubble radius. It is noted that collision efficiency increases with particle radius, a trend which holds true for all the three models. The present CFD model provides a reasonable agreement with the Weber model with deviation in the range from  $\sim 1\%$  to  $47\%$ . In comparison, the Yoon-Luttrell model overestimates the collision efficiency with deviation in the range from  $\sim 8\%$  to  $58\%$ . The Yoon-Luttrell model is validated for bubble Reynolds number  $Re_B$  in the range up to 100 and assumes that collision occur evenly on the whole upper hemisphere of bubble and hence the collision angle is fixed as  $90^\circ$ . In contrast, the collision

angle in Weber model is calculated based on stream function and particle trajectory and found to be less than 90°. Such shrinking of collision angle is also consistent with other reported studies (Dai et al., 1998; Woo, 1971).

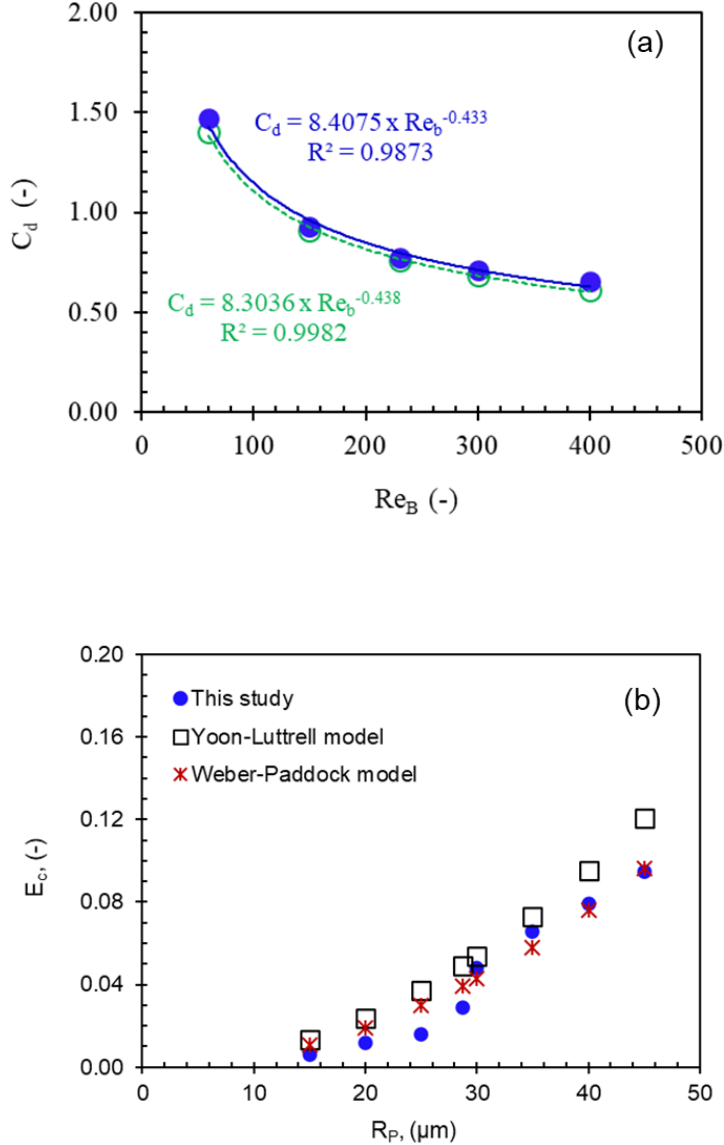


**Fig. 3.8.** Validation of DPM model in the absence of turbulence for  $d_B \sim 1$  mm: (a) bubble drag coefficient vs. bubble Reynolds number and (b) collision efficiency vs. particle radius at  $Re_B \sim 230$ . The symbols are: ○ Schiller Naumann drag model ([Schiller and Naumann, 1933](#)); □ Yoon-Luttrell ([Yoon and Luttrell, 1989](#)) model; \* Weber Paddock model ([Weber and Paddock, 1983](#)) and ● DPM model (present study).

### 3.5.2. Turbulence dispersion (TD) model and CFD model: comparison of collision efficiency

**Fig. 3.9** compares the collision efficiency predicted by the turbulence dispersion (TD) model using Eq. (3.25) and the CFD model using Eq. (3.29) along each releasing circle for different particle size ( $d_P \sim 30$  to  $100 \mu\text{m}$ ) at different turbulence intensity levels ( $T_i \sim 4\%$  to  $20\%$ ). The phase parameters listed in **Table 3.2** were applied in the turbulence dispersion model. The integral length scales for turbulent flow determined in the CFD model, 0.294 mm, 0.312 mm, 0.356 mm and 0.448 mm for the corresponding turbulence intensities of 4%, 7%, 11% and 20%, respectively (see Appendix A). These values were applied in Eq. (3.22) to calculate the collision efficiency from the TD model.

In the lower turbulence intensity case ( $T_i \sim 4\%$ , **Fig. 3.9a**), the TD model predicted a probability distribution of collision efficiency with particles released closer to the bubble featuring higher collision efficiency for the larger size particles. Such a trend closely agreed with the CFD model predictions. For example, the TD model predicted collision efficiency above the bubble centre ( $R_i/R_B \sim 0$ ) is 1.0 which agreed well ( $\sim 14.7\%$  deviation) with the CFD model. It is noteworthy mentioning that the probability distribution of collision efficiency along the initial radial releasing direction was also reported by Liu and Schwarz (2009a) for bubble Reynolds number  $\sim 100$  in the cases of different turbulence energy dissipation rates.

The observed probabilistic distribution of the collision efficiency parameter is attributed to the stochastic movement of particles due to the interactions with the surrounding eddies. However, it can be observed that the collision efficiency close to the central axis of the bubble ( $R_i/R_B \sim 0$  to  $0.1$ ) was overestimated by the TD model compared to the CFD model for the smaller size particles i.e.  $d_P \sim 30 \mu\text{m}$  and  $60 \mu\text{m}$ . Such differences could be attributed to the assumption of simplistic treatment of turbulence in the TD model wherein fluctuating velocity components remain position independent as opposed to the CFD model which had a comprehensive treatment of turbulence in a resolved manner and accounted for position dependent fluctuating velocities. Consequently in the CFD model, a considerable number of injected particles were predicted to be dispersed away from the bubble causing reduction in the collision efficiency.

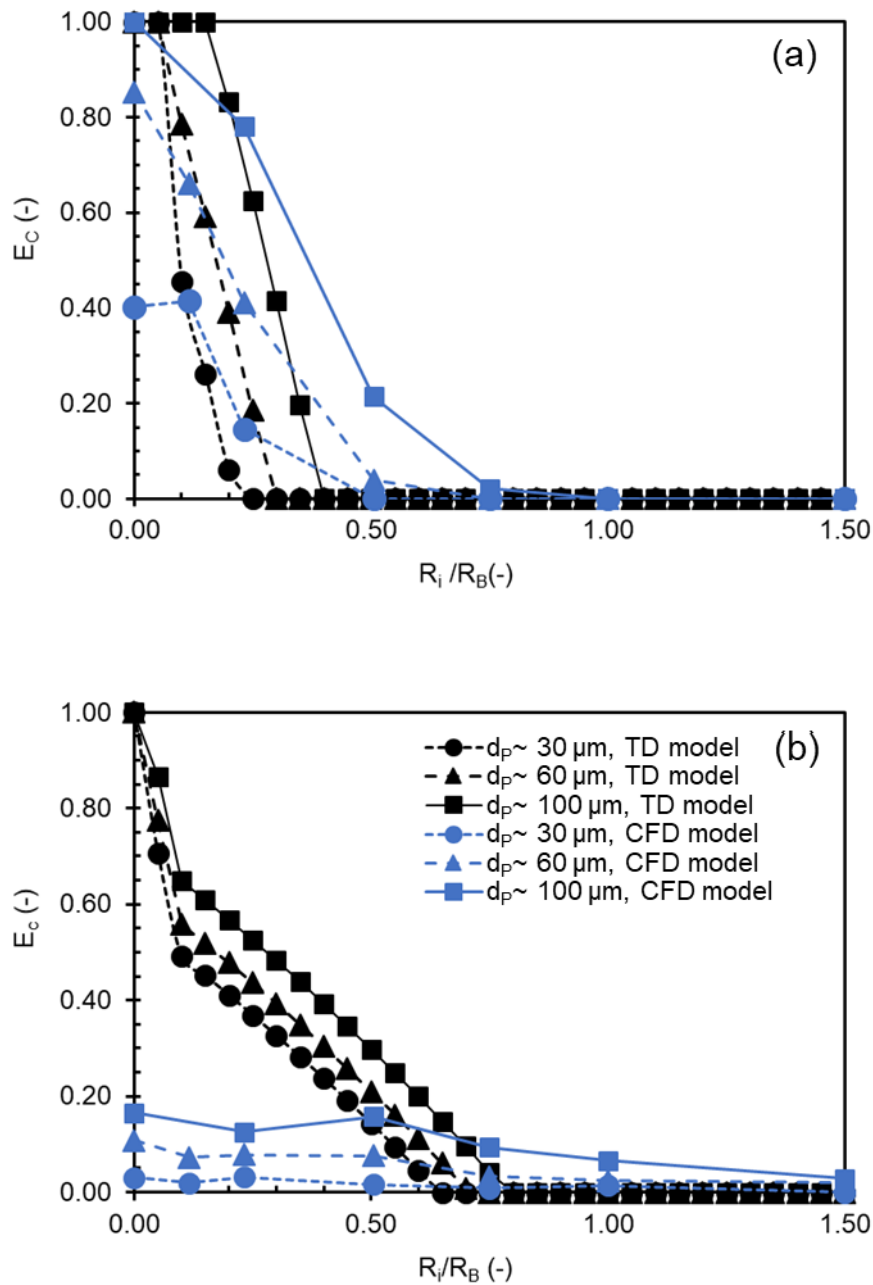
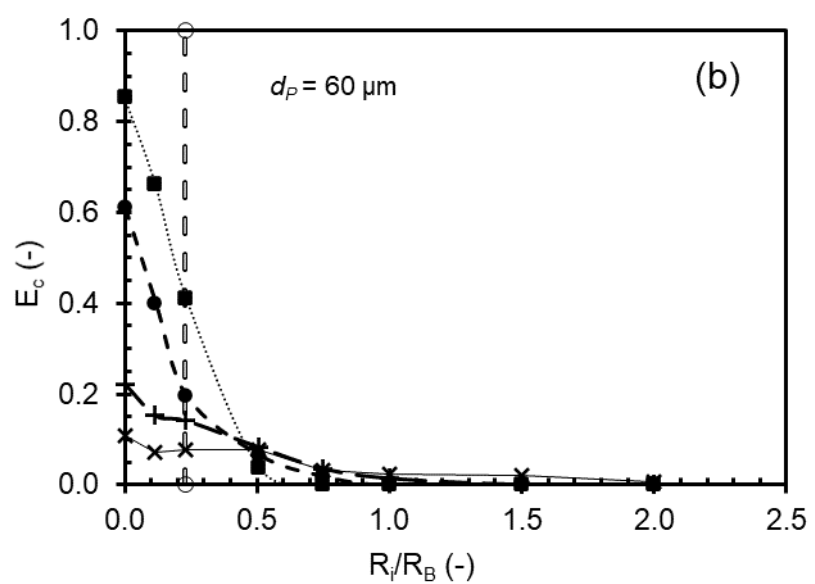
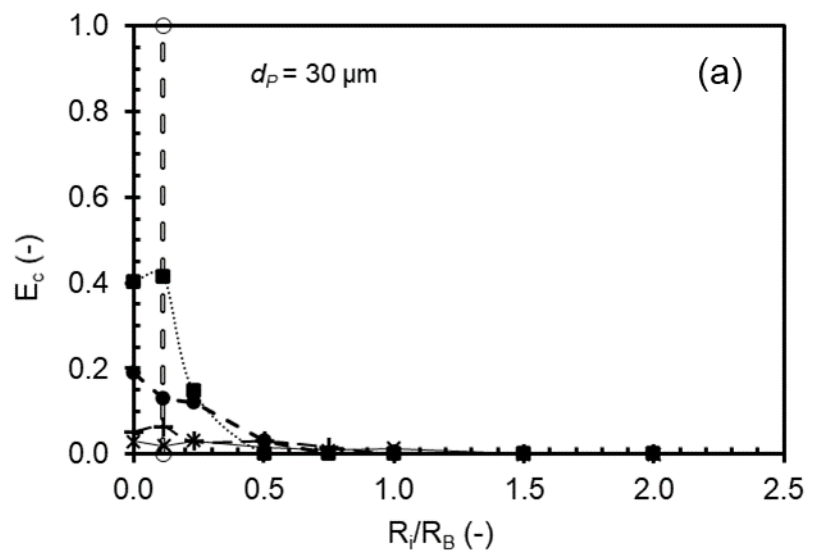


**Fig. 3.9.** Comparison of collision efficiency  $E_c$  over the initial releasing radius  $R_i/R_B$  in various particle size cases predicted by the turbulence dispersion (TD) model and CFD model at: a)  $Ti \sim 4\%$ ; b)  $Ti \sim 20\%$ .

In the higher turbulence intensity case ( $Ti \sim 20\%$ , **Fig. 3.9b**), both models predicted decreasing trend of collision efficiency with decreasing particle diameter. However, in all

particle diameter cases, the TD model overestimated the collision efficiency for all particle releasing positions. Apparently, difference in the predictions of these two modelling approaches increased as the turbulence intensity was increased. Such overestimation of collision efficiency at higher turbulence intensity can be attributed to the simplified correlation of momentum exchange between particles and surrounding turbulent eddies presented in Eq. (3.20) of the TD model. This correlation was based on the statistically averaged behaviour of particle and fluid phase in a single-bubble flotation domain without considering the local energy dissipation rate and integral lifetime of the eddies. In contrast, the random walk model (Ziff et al., 2009) which was applied in the CFD model, accounts for the localized momentum exchange for the particle dispersion by including these two turbulence properties as shown in Eq. (3.28) and provides a more realistic estimate of the turbulence dispersion in predicting bubble-particle collision phenomenon.

The observed difference between the two models at high turbulence intensity level presented in **Fig. 3.9** inevitably brings focus to the distribution of collision efficiency predicted by the CFD model. **Fig. 3.10** illustrates the CFD model predictions for a range of turbulence intensities ( $Ti \sim 0\% \text{ to } 20\%$ ) for different particle diameters ( $d_p \sim 30 \text{ to } 100 \mu\text{m}$ ). At  $Ti \sim 0\%$  in which represents an ideal flow situation flow, the collision efficiency shows a binary outcome between 0 and 1 wherein particles initially released within the grazing radius collided with the bubble and particles released outside missed the collision. As the particle diameter increases from  $30 \mu\text{m}$  to  $100 \mu\text{m}$ , the grazing radius  $R_C/R_B$  increases from  $0.112 \text{ mm}$ ,  $0.230 \text{ mm}$  to  $0.378 \text{ mm}$ . Such binary distribution was reported by various researchers (Weber and Paddock, 1983; Dai, et al., 2000; Nguyen and Schulze, 2004) and is the basic feature of bubble-particle collision in laminar flow.



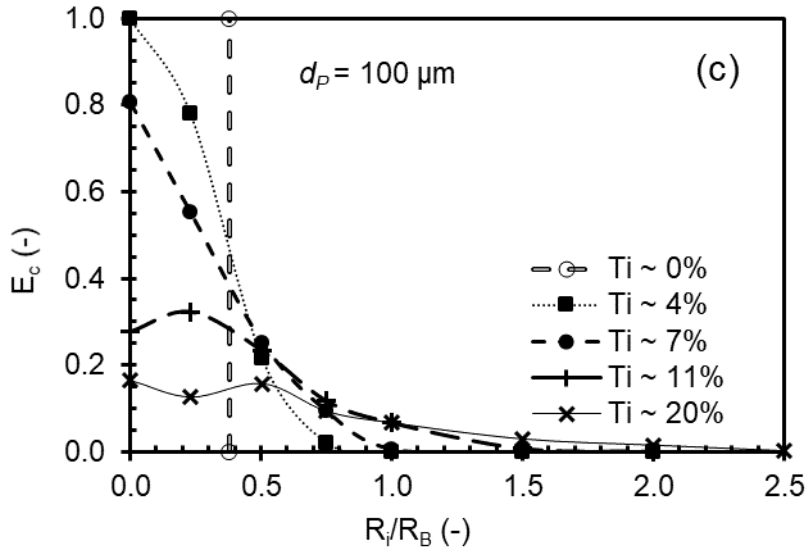


**Fig. 3.10.** Collision efficiency  $E_c$  vs the normalized initial releasing radius  $R_i/R_B$ : a)  $d_P \sim 30 \mu\text{m}$ ; b)  $d_P \sim 60 \mu\text{m}$ ; c)  $d_P \sim 100 \mu\text{m}$ .  $\ominus$  denotes the grazing radius beyond which particles released would not collide in flow of the same bubble Reynolds number and particle diameter in the absence of turbulence.

As the turbulence intensity increases from 4% to 20%, the collision efficiency increases with the increasing particle diameter due to interceptional and inertia effect. In all particle diameters cases,  $E_c$  illustrated a probability distribution with the maximum collision efficiency occurring along the central axis above the centre of the bubble. Furthermore, it can be observed from the gradually flattening feature of the curve, the standard deviation of the  $E_c$  probability distribution increased with increase in turbulence intensity. This behaviour is attributed to the dominant effect of random fluctuating flow velocity over the mean flow velocity on the collision efficiency. Besides, in the presence of turbulence, particles released outside the grazing radius  $R_g/R_B$  in laminar flow case, also have a chance to collide with the bubble, confirming the hypothesis of Nguyen and Schulze (2004) that the grazing radius does not exist in turbulent flow.

**Fig. 3.10** also shows the collision efficiency distribution gradually reduced to zero with increase in the initial releasing radius. It was of interest to examine the zero-collision radius and its dependency on the turbulence intensity. However, considering the probability distribution of collision efficiency, it is more statistically meaningful to examine the effective initial releasing radius within which the collision number reaches 90% of the total collision

number, namely 90%-collision radius. The sum of the number of actual collisions  $N_c$  occurred due to the release of particles along the releasing radius can be calculated as follows:

$$N_c = \sum_{i=2}^N \left( \pi \left( \frac{R_i}{R_B} \right)^2 E_{c1} + \left( \left( \frac{R_i}{R_B} \right)^2 - \left( \frac{R_{i-1}}{R_B} \right)^2 \right) E_{ci} \right) \quad (3.31)$$

where  $E_{ci}$  is the collision efficiency at the initial releasing radius  $R_i$ .

To gain more accurate collision number, the range of  $R_i/R_B \sim 0$  to 2.5 was discretised into 100 intervals with the collision efficiency  $E_{ci}$  at each interval being interpolated from the model predicted  $E_c$  curve. Applying Eq. (3.31), the 90%-collision radius can be obtained where the integration of the right side of the equation equals 90%  $N_c$ .

**Fig. 3.11** presents the normalized 90%-collision radius  $R_{90\%}/R_B$  predicted by both TD model and CFD model, as a function of turbulence intensity for three different particle diameters ( $d_P \sim 30$  to  $100 \mu\text{m}$ ). It can be noted that in both models  $R_{90\%}/R_B$  increased with the turbulence intensity level and particle diameter. For example, the prediction of TD model at  $d_P \sim 30 \mu\text{m}$ , at  $Ti \sim 20\%$  was 0.50 at  $R_o/R_B = 0.25$ , 2.5 times of that at  $Ti \sim 4\%$ . It is noted that the energy-containing integral length scale of eddies at  $Ti \sim 20\%$  is 0.448 mm, 1.5 times of 0.294 mm at  $Ti \sim 4\%$ . Therefore, this increasing trend of  $R_{90\%}/R_B$  with  $Ti$  is because particles in higher turbulence intensity flow are subject to larger size integral eddies and can travel further away from the initial releasing location. Besides, similar to the prediction of collision efficiency by

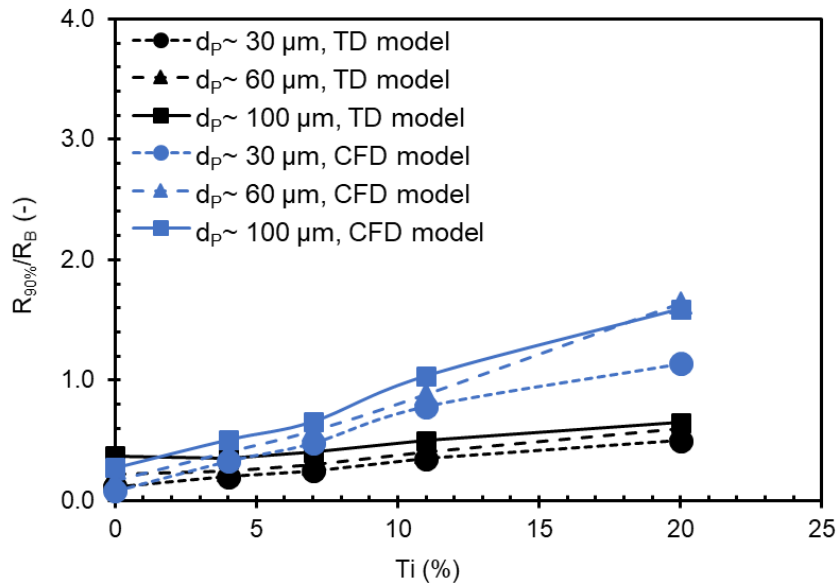


**Fig. 3.11.** Normalized 90%-collision radius  $R_{90\%}/R_B$  vs turbulence intensity  $Ti \sim 4\%$  to  $20\%$  for three different particle diameters.

the two models in **Fig. 3.9**, it is apparent that in lower turbulence intensity cases ( $Ti \leq 7\%$ ), predicted  $R_{90\%}/R_B$  ratio by TD model is close to  $\sim 0.5$  -  $1$  times of the CFD model prediction, while significant deviation can be observed in higher turbulence intensity cases ( $Ti > 7\%$ ).

Based on **Fig. 3.9** and **Fig. 3.11**, it can be concluded that for lower turbulence intensity  $Ti$  ( $\leq 7\%$ ), the TD model is able to provide satisfactory turbulent collision efficiency. However, at higher  $Ti$  ( $> 7\%$ ), due to the statistically averaged momentum exchange between eddies and particles in TD model, the random walk model (RWM) method applied in CFD model performs better compared to the TD model.

### 3.5.3. Particle dispersion

As the carrier phase, turbulent flow field plays an important role in the particle dispersion behaviour. **Fig. 3.12a-b** presents the temporal evolution of energy dissipation rate predicted by the CFD model in different turbulence intensity cases in the absence of particles. In both  $Ti$  cases, it can be noted that the energy dissipation rate  $\varepsilon$  reached the maximum ( $\sim 1.0 \text{ m}^2/\text{s}^3$ ) at bubble surface, suggesting that the particles in the vicinity of bubble surface may be

subject to higher turbulence levels. The energy dissipation rate then gradually reduced in the downstream of the bubble and local maximum value occurred on both sides of the bubble vertical axis due to the trailing vortex behind the bubble.

As turbulence intensity was increased, the energy dissipation rate  $\varepsilon$  at the inlet increased from approximately zero in  $Ti \sim 4\%$  case to  $\sim 1.0$  in  $Ti \sim 20\%$  at  $t \sim 1.35$  s. The high  $\varepsilon$  at the inlet caused the  $\varepsilon$  in the upstream of the bubble to be unevenly distributed with local maximum value  $\sim 0.2$ , indicating that particles released above the bubble encountered more chaotic turbulence flow when approaching the bubble. Also observed in **Fig. 3.12** is the rapid changing of the trailing vortex structure in  $Ti \sim 20\%$  case. Unlike the constantly attached vortex in lower  $Ti$  case, **Fig. 3.12** clearly shows in higher  $Ti$  ( $\sim 20\%$ ) case vortex shedding occurred in the downstream of the bubble. Such shear layer instability is governed by the boundary layer separation around the bubble (Thompson and Hourigan, 2005) and is positively correlated to the flow velocity at the edge of the boundary layer (Bloor, 1964). With the increase of  $Ti$ , the fluctuating velocity in the vicinity of the bubble including the edge of the boundary layer, also increased, leading to the vortex shedding.

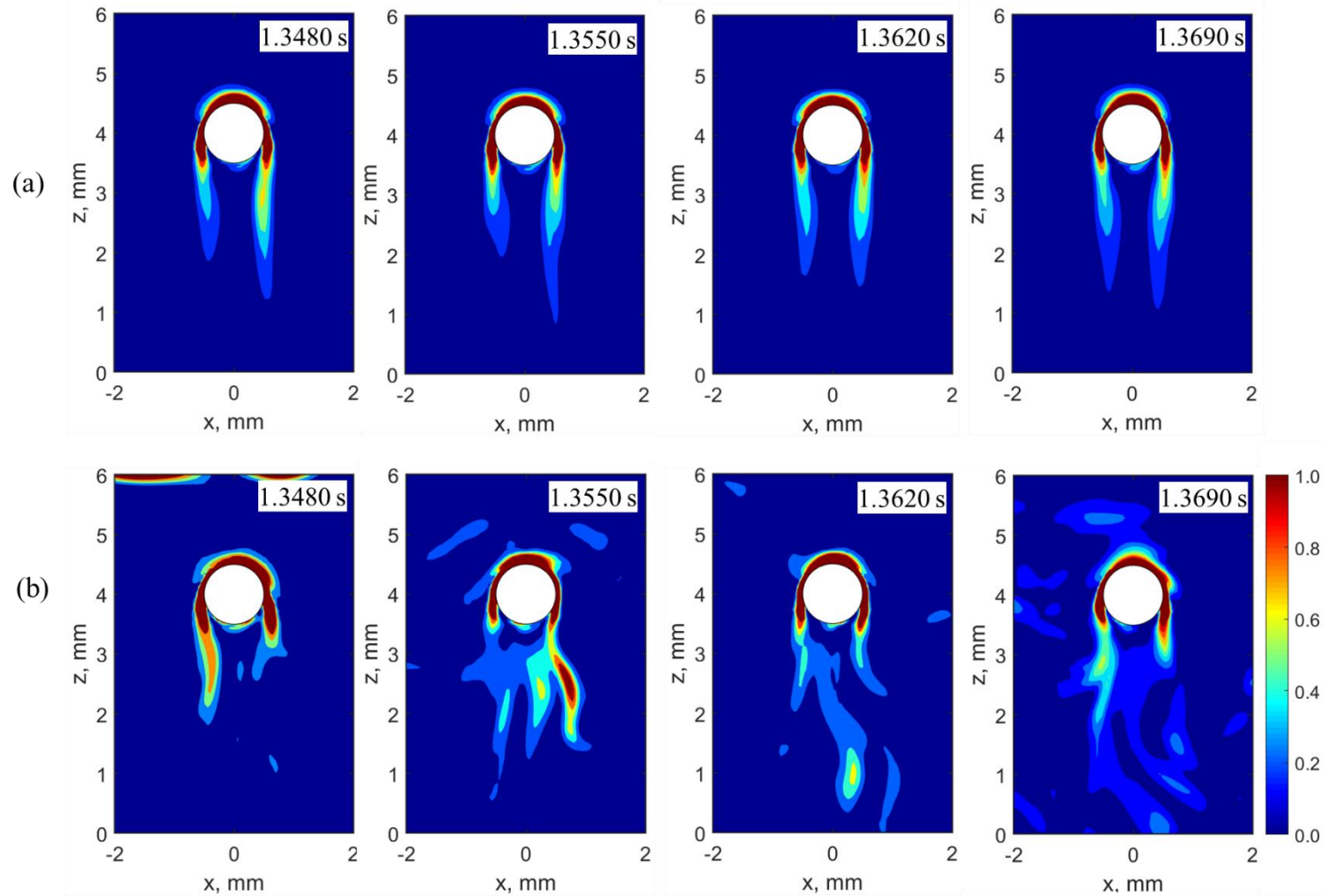


**Fig. 3.12.** Energy dissipation rate contours of (a)  $Ti \sim 4\%$  and (b)  $Ti \sim 20\%$  on the centre plane  $y = 0$  mm at different time instants.

**Fig. 3.13** compares the average energy dissipation rate  $\varepsilon$  along the flow direction at  $t \sim 1.3480$ s in the single-bubble domain for different turbulence intensities. It can be observed that the average energy dissipation rate initially decreased as the turbulence decayed. At  $\sim 1$  mm away from the bubble centre, the energy dissipation rate increased due to the turbulence augmentation caused by the bubble. The maximum  $\varepsilon$  occurred at the bubble centre plane in all  $Ti$  cases. With the increase of turbulence intensity, the energy dissipation rate increased. Especially at the bubble centre, the  $\varepsilon$  at  $Ti \sim 20\%$  case was 3 times at  $Ti \sim 4\%$ .

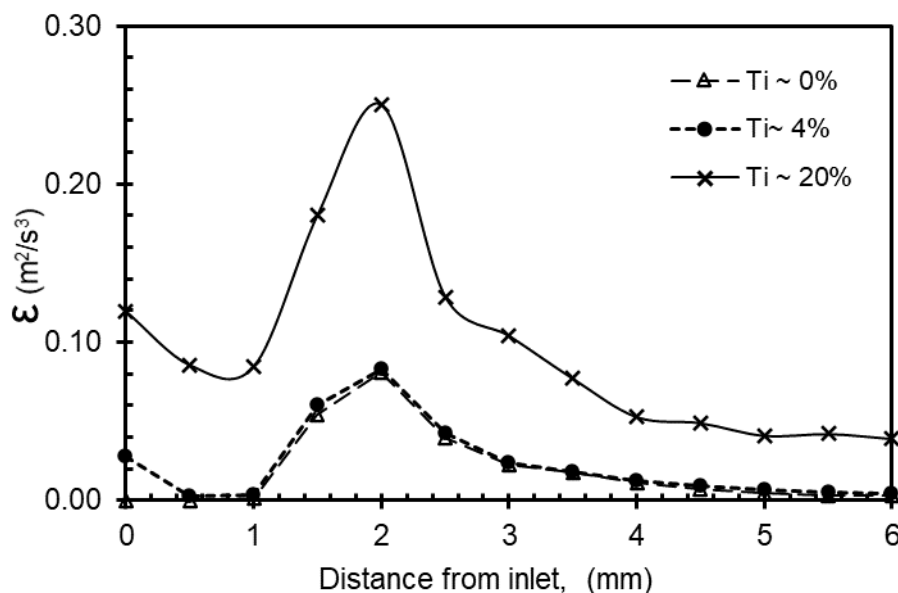


**Fig. 3.13.** Average energy dissipation rate in flow direction from the inlet for different inlet turbulence intensities.

The effect of turbulence dispersion on bubble-particle collision efficiency is reflected on the particle trajectory when particles approach the bubble. **Fig. 3.14** presents the CFD model predicted trajectories of particles released at different initial positions and two different turbulence intensity levels ( $Ti \sim 4\%$  and  $20\%$ ). At lower turbulence intensity ( $Ti \sim 4\%$  in **Fig. 3.14a** and **Fig. 3.14c**) particles injected at the same releasing radial location, generally exhibited only slight deviation in their trajectory. Considering the low energy dissipation rate presented in the upstream of the bubble as shown in **Fig. 3.12** and **Fig. 3.13**, the nearly deterministic nature of the particle trajectories suggests the dominant effect of mean flow over fluctuating flow components.

In contrast to the lower  $Ti$  case, in higher  $Ti$  case ( $Ti \sim 20\%$ , **Fig. 3.14b** and **Fig. 3.14d**) the trajectories of particles were observed to be more chaotic compared to the lower  $Ti$  cases. For example, some particles released on the right side of the bubble central axis migrated over the bubble centre plane (**Fig. 3.14b**). This chaotic behaviour can be attributed to the chaotic eddies in the upstream of the bubble as suggested in **Fig. 3.12**. With the increase of the turbulence intensity, the fluctuating flow components dominates the particle trajectory when is increased. In particular, the chaotic behaviour of particles also explains the apparent increase in 90%-collision radius with the increased turbulence intensity. As shown in **Fig. 3.14c** and **Fig. 3.14d**, particles released far away from the bubble ( $R_i/R_B \sim 1.000$ ) remained farther apart from the bubble at  $Ti \sim 4\%$  but approached the bubble at higher turbulence intensity ( $Ti \sim 20\%$ ) due to the increased fluctuating flow component.

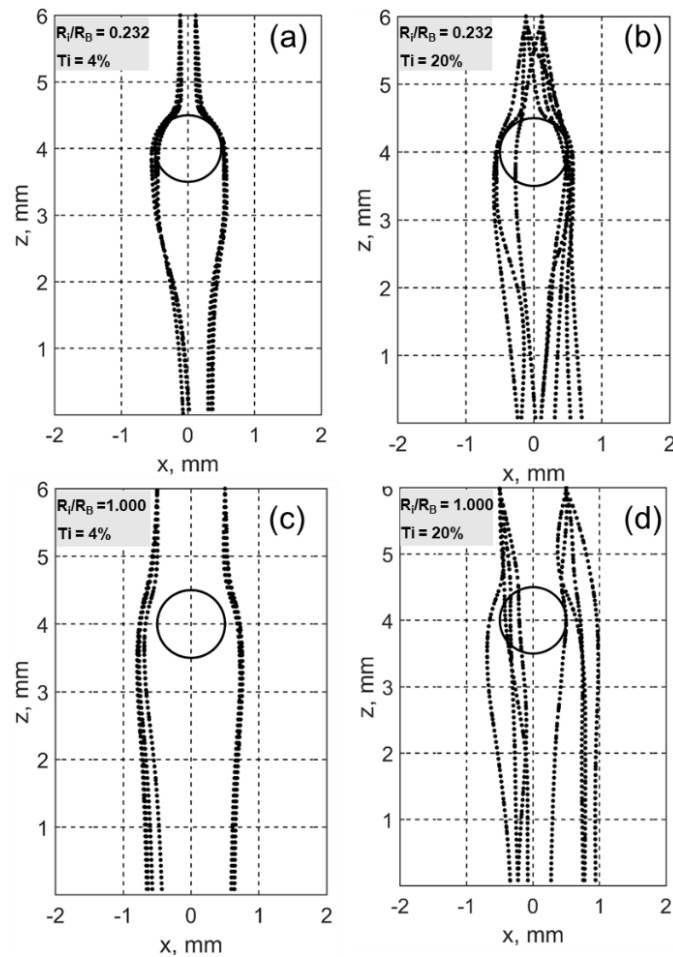


**Fig. 3.14.** Particle trajectories for different turbulence intensities at  $R_i/R_B = 0.232$  (up) and 1.000 (down) for  $d_P \sim 60 \mu\text{m}$ . For illustration purpose 8 particles are presented in each case.

The streamlines for a given bubble Reynolds number in the absence of turbulence are deterministic. Investigation of the deviation of particle trajectories from the deterministic streamline at the currently examined  $Re_B \sim 230$  gains insight into the particle dispersion behaviour in turbulent flow. The horizontal displacement ( $\sqrt{x_p^2 + y_p^2}$ ) for particles from the bubble vertical centre axis are quantified in **Fig. 3.15** wherein all particles were initially released at the same location  $R_i/R_B \sim 0.232$ . The particle Stokes number ( $\rho_p U_B d_p^2 / (9\mu_L d_B)$ ) for  $d_p \sim 30 \mu\text{m}$  in the CFD model is 0.0276, much smaller than the critical Stokes number 0.08 reported by Levin (1961). Consequently the inertial deposition of particles with  $d_p \sim 30 \mu\text{m}$  on bubble surface is negligible and the horizontal displacement of  $d_p \sim 30 \mu\text{m}$  at  $Ti \sim 0\%$  can be used to represent the corresponding horizontal displacement of the deterministic streamline. In the absence of turbulence, the horizontal displacement increased with increasing particle size, suggesting that larger particles are influenced by negative inertial effect by being dispersed away from the flow streamline. As turbulence intensity increased, the horizontal displacement for all particles cases also increased due to the increased particle kinetic energy obtained from the surrounding eddies.

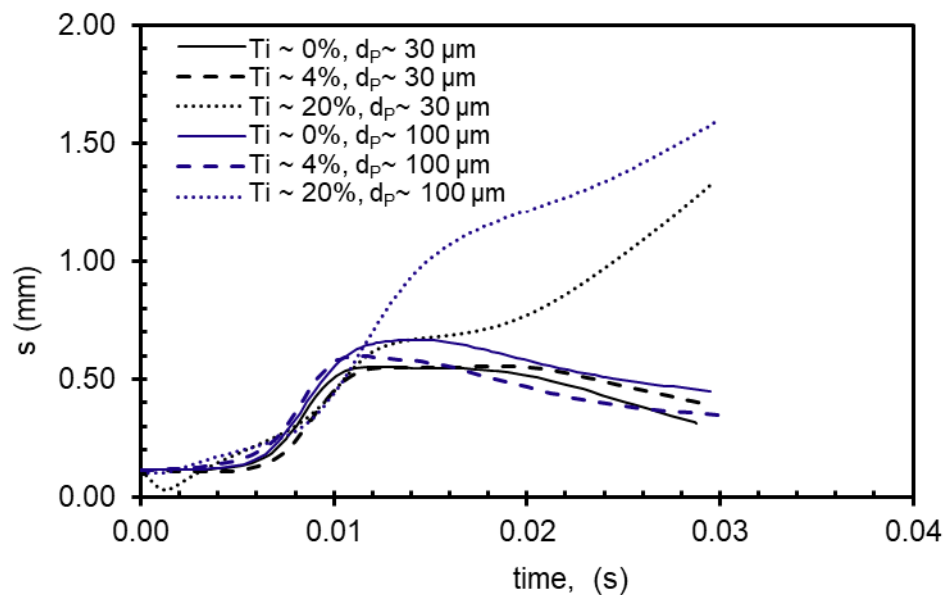


**Fig. 3.15.** The temporal horizontal displacement ( $s = \sqrt{x_p^2 + y_p^2}$ ) of particle trajectories from the bubble vertical centre axis for different turbulence intensities and particle sizes. Particles were released at  $R_i/R_B = 0.232$  at time = 0 s.

Inertial force is a decisive factor in governing the trajectory of a particle when it approaches the bubble (Li, et al., 2020). **Fig. 3.16** illustrates CFD model predicted spatial variation in particle horizontal velocity component  $u_{P,r}$  and inertial force  $F_{P,r}$ , for different size particle ( $d_p \sim 30, 60$  and  $100 \mu\text{m}$ ) released at radial location  $R_i/R_B \sim 0.232$  in different turbulence intensity cases. The horizontal velocity component  $u_{P,r}$  was determined as follows:

$$u_{P,r} = \sqrt{u_{P,x}^2 + u_{P,y}^2} \quad (3.32)$$

where  $u_{P,x}$  and  $u_{P,y}$  are particle velocity in  $x$  and  $y$  direction respectively.

As shown in **Fig. 3.16a**, three distinct regimes – R1, R2 and R3 could be identified to mark the spatial variations in the particle horizontal velocity. Of the three regimes, regime R1 (from the inlet location,  $z = 0.006 \text{ m}$  to the bubble north pole,  $z = 0.0045 \text{ m}$ ) is the most important one as collision efficiency is significantly affected by the particle dynamics in the flow field above the bubble (Nguyen and Schulze, 2004). As  $Ti$  is increased from 4% to 20%, it can be observed that both the magnitude and oscillation level of  $u_{p,r}$  increase due to the increased inertial force (**Fig. 3.16b**). Furthermore, for a given  $Ti$  as particle diameter is increased, the horizontal velocity of particles also increases due to the increased inertia.

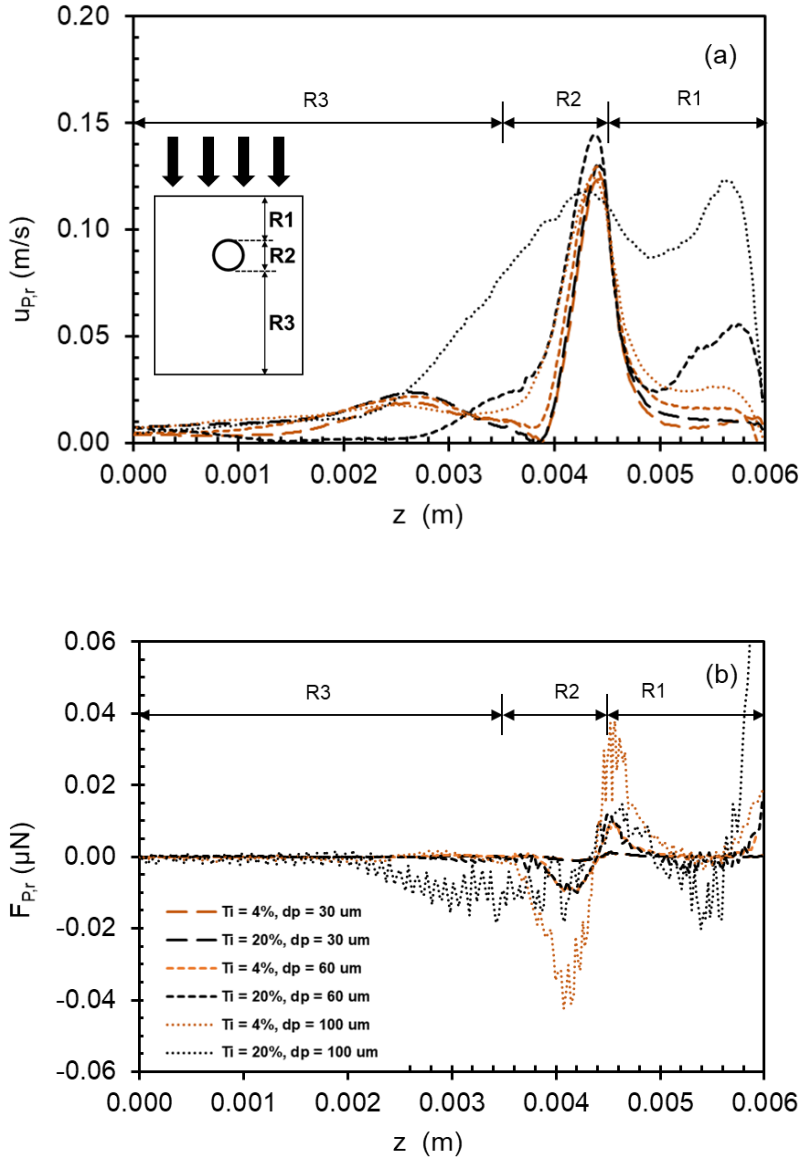


**Fig. 3.16.** Spatial evolution of particle velocity (a) and inertial force (b) in horizontal direction under different particle diameters and turbulence intensities for particle released at  $R_i/R_B \sim 0.232$ .

Regime R2 spans from the bubble north pole ( $z = 0.0045$  m) to the bubble south pole ( $z = 0.0035$  m), with both the velocity and inertial force exhibiting non-linear dependency on the travelling distance due to the distortion of flow streamlines around the bubble. It can also be noted that closer to the bubble equator location ( $z = 0.0040$  m), for the smallest particle case ( $d_p \sim 30\text{ }\mu\text{m}$ ) both the horizontal velocity and the inertial force approach zero value at low turbulence intensity ( $Ti \sim 4\%$ ). However, at increased turbulence intensity, both the horizontal

velocity and inertial force increase at the bubble equator location for higher particle diameter cases which suggest interactions of eddies and particles leading to momentum transfer to particles and corresponding deflection in particle trajectories.

Regime R3 is defined as an escaping stage and spans from the bubble south pole ( $z = 0.0035$  m) to the domain outlet ( $z = 0.000$  m). It features a relatively flat slope for both the velocity and inertial forces. In this regime, all the inertial force profiles collapse on a single line and approach zero value towards the outlet which is in good agreement with the experimental observations of Li et al. (2020). Farther away from bubble, distortion of the flow streamlines due to the presence of bubble becomes relatively insignificant and consequently the horizontal drag force component caused by the distortion, gradually approaches zero (Li et al., 2020).

### 3.6. Conclusion

In this study, the collision of particles with a bubble in flow with different levels of turbulence intensity ( $Ti \sim 4$  to 20%) was computationally studied.

The critical distance of the onset of streamline distortion above the bubble followed a power law dependency on bubble Reynolds number, suggesting that the streamline distortion occurs closer to the bubble for larger bubble Reynolds number due to the increased inertia of fluid particles. A value of 4.0 for the critical distance was found suitable to avoid the streamline distortion at the inlet over the typical range of bubble Reynolds number in flotation.

A theoretical turbulence dispersion (TD) model accounting for the effect of both mean flow and fluctuating flow was developed and compared with an Eulerian – Lagrangian CFD model to predict collision efficiency. In lower turbulence intensity cases ( $Ti \leq 7\%$ ), the turbulence dispersion model agreed well with the CFD model, however, in higher turbulence intensity cases ( $Ti > 7\%$ ), the TD model was found to overestimate the collision efficiency. This bias in the TD model can be attributed to the simplified correlation of momentum exchange between particles and eddies. The random walk model (RWM) method applied in CFD model is more robust and preferred to the theoretical TD model in capturing the effect of turbulence dispersion on bubble-particle collision behaviour.

The CFD predicted energy dissipation rates increased with the increasing turbulence intensity. Particle trajectory in different turbulence intensity cases shows that at lower  $Ti$  when the mean flow dominates the fluctuating flow, the particle trajectory exhibits relatively more deterministic pattern with slight deviations. However, in higher  $Ti$  cases, chaotic movements across the upper bubble part were observed as particles obtained more kinetic energy from the surrounding eddies. Force analysis showed that before arriving at the bubble north pole, larger particles in higher  $Ti$  cases illustrated higher horizontal velocity due to inertial effect. Farther downstream of the bubble, the horizontal velocity and inertial force for all particle sizes and turbulence intensity cases collapsed onto a single curve due to weaker effect of the bubble.

The comparison between theoretical turbulence dispersion model and CFD model which was based on random walk momentum exchange model demonstrated the ability of the developed CFD model to determine the effect of turbulence dispersion on bubble-particle collision efficiency in turbulent flow.

# **Chapter 4. The effect of solid concentrations on bubble-particle collision efficiency in single-bubble system**

---

## **4.1. Introduction**

Theoretically, bubble-particle collision efficiency is defined as the ratio of the number of particles making physical contact with a bubble to the total number of particles approaching the bubble from a distance (Nguyen and Schulze, 2004). Due to the difficulties of tracking the number of particles colliding with a bubble, the majority of studies that focused on the collision efficiency applies the “grazing trajectory” method to determine the collision efficiency (Dobby and Finch, 1987; Yoon and Luttrell, 1989), as shown in Section 2.2. Particles included inside the volume enclosed by the grazing trajectory collided with the bubble. The grazing trajectory can be determined by trial – and – error by releasing a single particle at varying radial distances above the bubble. However, the grazing trajectory method assumes that the behaviour of an individual particle is not affected by the presence of other particles. Therefore, the trajectory of a single particle released at a certain radial distance above the bubble is representative of all particles released at the same radial distance regardless of the solid concentration. In reality, the solid concentration can modify the viscosity of the suspension, causing a change in drag force exerted on particles from the fluid (Nguyen and Schulze, 2004). Therefore, the particle movement may vary in different solid concentration cases (Nguyen and Kmet, 1992; Nitsche et al., 1997).

In the absence of turbulence, relatively fewer studies indeed reported on the effect of solid concentration on bubble-particle collision efficiency. Nguyen and Kmet (1992) included the effect of solid concentration on the particle settling velocity into the calculation of collision efficiency in Stokes flow. However, the effect of solid concentration on collision efficiency was not explicitly reported. Recently, Ge et al. (2020) numerically quantified the collision efficiency by releasing a particle swarm (solid concentrations  $\sim 0.01 - 0.25$ ) above a stationary bubble in various bubble Reynolds numbers  $Re_B$  ( $\sim 50 - 200$ ). At higher  $Re_B$  ( $> 150$ ) collision

efficiency was found to be insensitive to solid concentration because the particle swarm was rendered high kinetic energy when approaching the bubble and did not have sufficient time to deform in lateral direction. In contrast, at lower  $Re_B$  ( $\leq 150$ ), the particle swarm expanded in lateral direction as the solid concentration increased, causing the decrease of collision efficiency.

In turbulent flow, a particle swarm is subject not only to the acceleration or deformation due to the mean fluid velocity (Ge et al., 2020), but also to the phenomenon “preferential concentration” - the accumulation of dense particles in specific regions (Eaton and Fessle, 1994). Wan et al. (2020) numerically confirmed this phenomenon by observing that particles of Stokes number around unity migrated from the eddy core to the edges of the eddy. In Wan’s studies, the preferential concentration did not reduce the collision rate between bubbles and particles in turbulent flow. However, the effect of preferential concentration on the turbulence collision efficiency was not examined. Until now, there is a lack of fundamental understanding of the influence of solid concentration on turbulent collision efficiency.

This chapter aims to examine the effect of solid concentration on bubble-particle collision efficiency in turbulent flow. This chapter is organized in the following manner: Section 2 illustrates the methodology of the CFD model; Section 3 presents the algorithm of analysing the local solid concentration and collision efficiency; Section 4 examines the interaction between particles and fluid under different solid concentrations; the local solid concentrations around the bubble; and the distribution of turbulent collision efficiency in bubble radial direction. Finally, the overall turbulent collision efficiency as a function of the local solid concentration under different turbulence intensity levels was examined.

## 4.2. CFD modelling methodology

The Eulerian-Lagrangian 3D CFD modelling framework comprising continuity, momentum, large eddy simulation (LES) turbulence model and discrete phase method (DPM) developed in Chapter 3 was applied in this chapter. In addition, the simulation geometry, meshing and boundary conditions were the same as those used in Chapter 3. To examine the effect of solid concentration on the turbulent collision efficiency, a particle swarm in a virtual

cylinder of radius  $R_i$  with different solid concentrations was injected at a height of  $R_B$  above the bubble surface, as shown in **Fig. 4.1**.

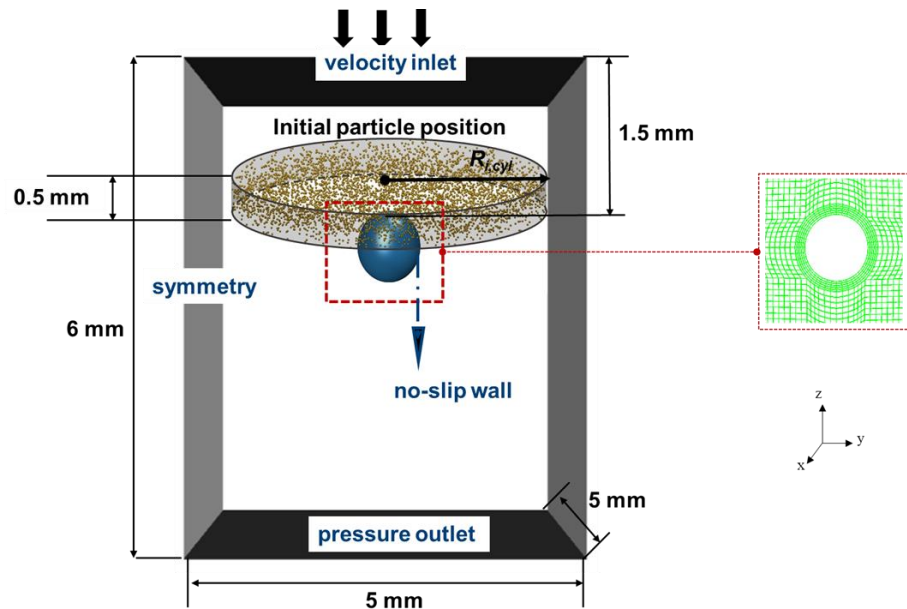


**Fig. 4.1.** 3D Computation domain used for simulation with sectional view of the mesh around bubble.

Five particle injections were performed with a time interval of 0.0024 s between each injection to ensure that there was neither a gap nor an overlap over time for the injected particles. The bubble was surrounded by particle-laden pulp at 0.0107 s after the first injection and therefore particle coordinates were extracted at this time for concentration examination. The virtual cylinders radii  $R_{i,cyl}$  were varied in the range of 2.5-5.0 $R_B$  to explore whether the concentration was affected by the initial injecting volume. A MATLAB code was written to generate a random particle distribution in each of these virtual volumes. For each simulation run, five different values of particle volumetric concentration,  $C_{P,i}$ ,  $\sim 0.39\%, 0.77\%, 1.54\%, 3.08\%$  and  $6.16\%$  were considered. A summary of phase parameters and boundary conditions are listed in **Table 4.1** where phase parameters are within the range specified in the reference.

**Table 4.1.** A summary of input phase parameters of CFD model, boundary conditions and numerical scheme

Phase parameters	Bubble radius, $R_B$ : 500 $\mu\text{m}$ (Koh and Schwarz, 2006); Particle radius, $R_P$ : 15 $\mu\text{m}$ (Ahmed and Jameson, 1985); Particle density, $\rho_P$ : 1200 $\text{kg/m}^3$ (Gharai and Venugopal, 2015).
Boundary conditions	Top boundary: velocity inlet, 0.23 m/s, turbulence intensities $T_i$ : 0%, 4%, 7%, 11% and 20%. Side boundaries: symmetry, free slip condition. Bottom boundary: pressure outlet (1 atm.). Bubble surface: no-slip wall condition.
Discretisation schemes	Second-order upwind (momentum), bounded central differencing scheme (pressure)
Gradient/derivative calculations	Least-squares cell-based gradient method
Pressure-velocity coupling	SIMPLE algorithm
Residual	$10^{-3}$
Time step size (flow and particle injection)	$10^{-4}$ s

### 4.3. Data analysis

#### 4.3.1. Determination of particle volumetric concentration around the bubble

To quantify the particle concentration distribution around the bubble,  $C_{P,sB,j}$ , the space between the bubble surface and a virtual shell of  $5R_B$  around the bubble was divided into  $M$  number of virtual shells ( $j=1$  to  $M$ ,  $M=15$ ). Each pair of neighbouring shells had a radial difference of  $0.33R_B$  (see **Fig. 4.2**). The particle concentration distribution around the bubble,  $C_{P,sB,j}$  was determined by the following equation:

$$C_{P,sB,j} = \frac{N_{P,j}}{\frac{4}{3}\pi(R_{s,j}^3 - R_B^3)}; (j=1) \quad (4.1)$$

$$C_{P,sB,j} = \frac{N_{P,j}}{\frac{4}{3}\pi(R_{s,j+1}^3 - R_{s,j}^3)}; (1 < j \leq 15) \quad (4.2)$$

where  $N_{P,j}$  is the number of particles in virtual shell  $j$ ,  $R_{s,j}$  is the radius of virtual shell  $j$ .

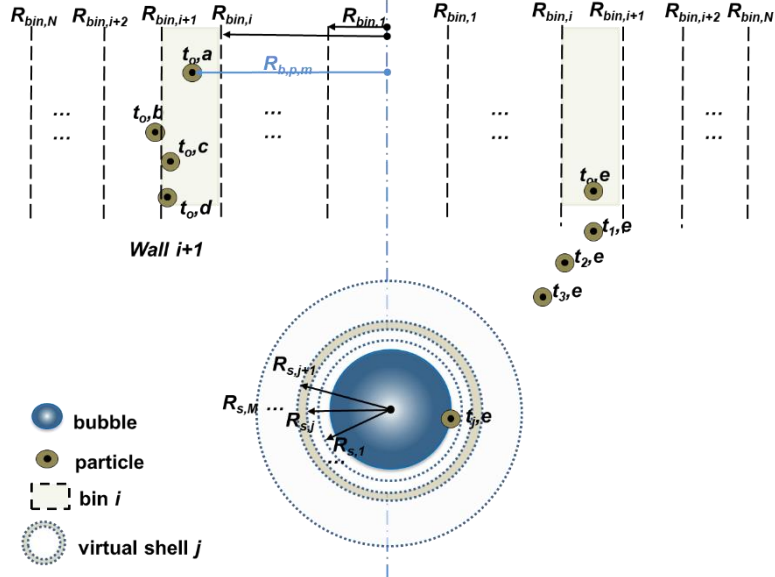


**Fig. 4.2.** Schematic of counting particle concentration in virtual shells around the bubble and tracking individual particles from the releasing bins above.

### 4.3.2. Particle tracking method of determining collision efficiency along radius

To calculate the total number of injected particles that finally collide with the bubble over a simulation runtime, the position coordinates of each particle were tracked. A criterion was defined to determine a bubble-particle collision event as follows:

$$(x_{P,m} - x_B)^2 + (y_{P,m} - y_B)^2 + (z_{P,m} - z_B)^2 \leq (R_{P,m} + R_B)^2 \quad (4.3)$$

where  $x_{P,m}$ ,  $y_{P,m}$  and  $z_{P,m}$  are the coordinates of the particle examined in  $x$ ,  $y$ , and  $z$  direction.  $x_B$ ,  $y_B$  and  $z_B$  are the coordinates of the bubble centre.  $R_{P,m}$  and  $R_B$  are radius of a particle and the bubble, respectively.

In a turbulent environment, particles follow random trajectories and it is intuitive that a collision efficiency probability distribution will exist along the radial direction from the

bubble surface. To quantify this, the CFD model predicted particle position data were analysed using a separate MATLAB code. Those particles which undergo a collision interaction with the bubble, were classified into  $N$  number of virtual bins ( $i = 1$  to  $N$ ,  $N=7$ ) in the particle release volume above the bubble. The virtual bins were located at an increasing distance along the radial direction with reference to bubble axis. The particle releasing volume in **Fig. 4.2** illustrates this bins division method. The  $i^{\text{th}}$  bin has radius  $R_{\text{bin},i+1}$  and all bins are equally spaced.

$$R_{\text{bin},i+2} - R_{\text{bin},i+1} = R_{\text{bin},i+1} - R_{\text{bin},i} \quad (4.4)$$

where  $R_{\text{bin},i}$  and  $R_{\text{bin},i+2}$  are the radius of neighbouring bin.

At  $t = 0$ , particles are placed into  $i^{\text{th}}$  bin using the following criteria:

$$R_{\text{bin},i+1} - R_{B,P,m} \geq 0 \quad (4.5)$$

$$R_{\text{bin},i} - R_{B,P,m} < 0 \quad (4.6)$$

where  $R_{B,P,m}$  is the distance between particle centre axis and bubble centre axis.

For an illustration, let us assume that at the initial time, particle  $a$  in **Fig. 4.2** is located in the  $i^{\text{th}}$  bin. Meanwhile, particle  $b$  is located at the virtual surface boundary between the  $i^{\text{th}}$  and  $i+1^{\text{th}}$  bin. Since its centre lies in the  $i+1^{\text{th}}$  bin, it is therefore counted in this bin. Particle  $c$  and  $d$  belong to the  $i^{\text{th}}$  bin since its centre remains in this bin. The number of particles initially injected in each bin,  $N_{\text{injected},i}$  can thus be determined. After a collision occurs, then the corresponding particle's position can be determined by tracking its initial position (**Fig. 4.2**, particle  $e$ ). Therefore, the total number of particles in each bin undergoing collisions,  $N_{\text{collision},i}$  can be determined and corresponding collision efficiency in each bin,  $E_{ct,i}$  can be determined by the following equation:

$$E_{ct,i} = N_{\text{collision},i} / N_{\text{injected},i} \quad (4.7)$$

### 4.3.3. Overall collision efficiency

The probability distribution of collision efficiency calculated in Section 4.3.2 was used to determine the overall collision efficiency, as shown schematically in **Fig. 4.3**.

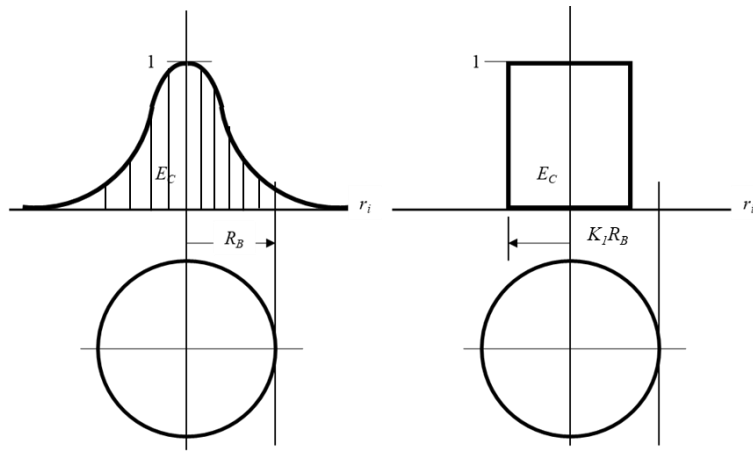


**Fig. 4.3.** Definition of the normalized equivalent critical radius  $K_1 (R_C/R_B)$ , (left side: Actual probability of collision; right side: the equivalent probability of collision)

The left-hand side of the figure shows the efficiency (probability) curve generated by the tracking of many particles from their initial radial positions. The right-hand side of the figure shows the same data, whereby the volume under the curve is the maintained, but bounded within a cylindrical volume with vertical axis fixed at  $E_C$  equal to one, and radius equal to some multiple,  $K_1$ , of the bubble radius,  $R_B$ .  $K_1$  is termed as “normalized equivalent critical radius” ( $R_C/R_B$ ). Essentially,  $K_1 R_B$  is equivalent to  $R_C$ , but with a broader definition in allowing not all particles within the injection radius colliding with the bubble, and that not all particles outside this radius not colliding with the bubble. The parameter  $K_1$  was calculated by equating the number of possible collisions in the particle grazing volume above the bubble to the sum of the number of actual collisions occurred due to release of particles from the virtual bins as follows:

$$R_B \pi (K_1 R_B)^2 E_{co} = \sum_{i=2}^N (R_B \pi R_{bin,1}^2 E_{ct,1} + R_B \pi (R_{bin,i}^2 - R_{bin,i-1}^2) E_{ct,i}) \quad (i > 1) \quad (4.8)$$

Substituting  $K_1 R_B$  for  $R_C$  into the definition of collision efficiency:

$$E_{ct} = (R_C / R_B)^2 \quad (4.9)$$

where  $R_C$  is the critical grazing radius within which a particle approaching the bubble will make a physical contact with the bubble, gives:

$$E_{ct} \equiv K_1^2 \quad (4.10)$$

where  $K_1$  will be a function of the system conditions, including velocity fluctuations, solid concentration, and particle, bubble and liquid properties.

## 4.4. Results and discussion

### 4.4.1. Flow pattern and particle movement

The effect of the fluid phase turbulence on bubble-particle collision behaviour is analysed in this section. **Fig. 4.4a-b** shows the CFD-predicted vortex structure around the bubble at the plane  $y \sim 0$  mm under different solid concentrations for  $Ti \sim 0\% - 20\%$  at 0.0112 s after the first injection of particles. The vortex boundary was marked by the Q criterion (Jeong and Hussain, 2006) which denotes the relative dominance of rotational strain on shear strain. The Q-criterion was calculated as follows:

$$Q = \frac{1}{2}(\Omega^2 - S^2) \quad (4.11)$$

where the vorticity  $\Omega$  can be calculated as:

$$\Omega = \left( \frac{\partial u_i}{\partial x_j} - \frac{\partial u_j}{\partial x_i} \right) \quad (4.12)$$

where  $u_i$  and  $u_j$  are the flow velocity. The strain rate  $S$  can be calculated as:

$$S = \frac{1}{2} \left( \frac{\partial u_i}{\partial x_j} + \frac{\partial u_j}{\partial x_i} \right) \quad (4.13)$$

It is apparent that at  $Ti \sim 0$  vortex remained attached to the bubble rear surface which is consistent with the earlier reported observations by Vallée et al. (2018) that vortex shedding around a stationary rigid sphere does not occur up to a Reynolds number of 270.

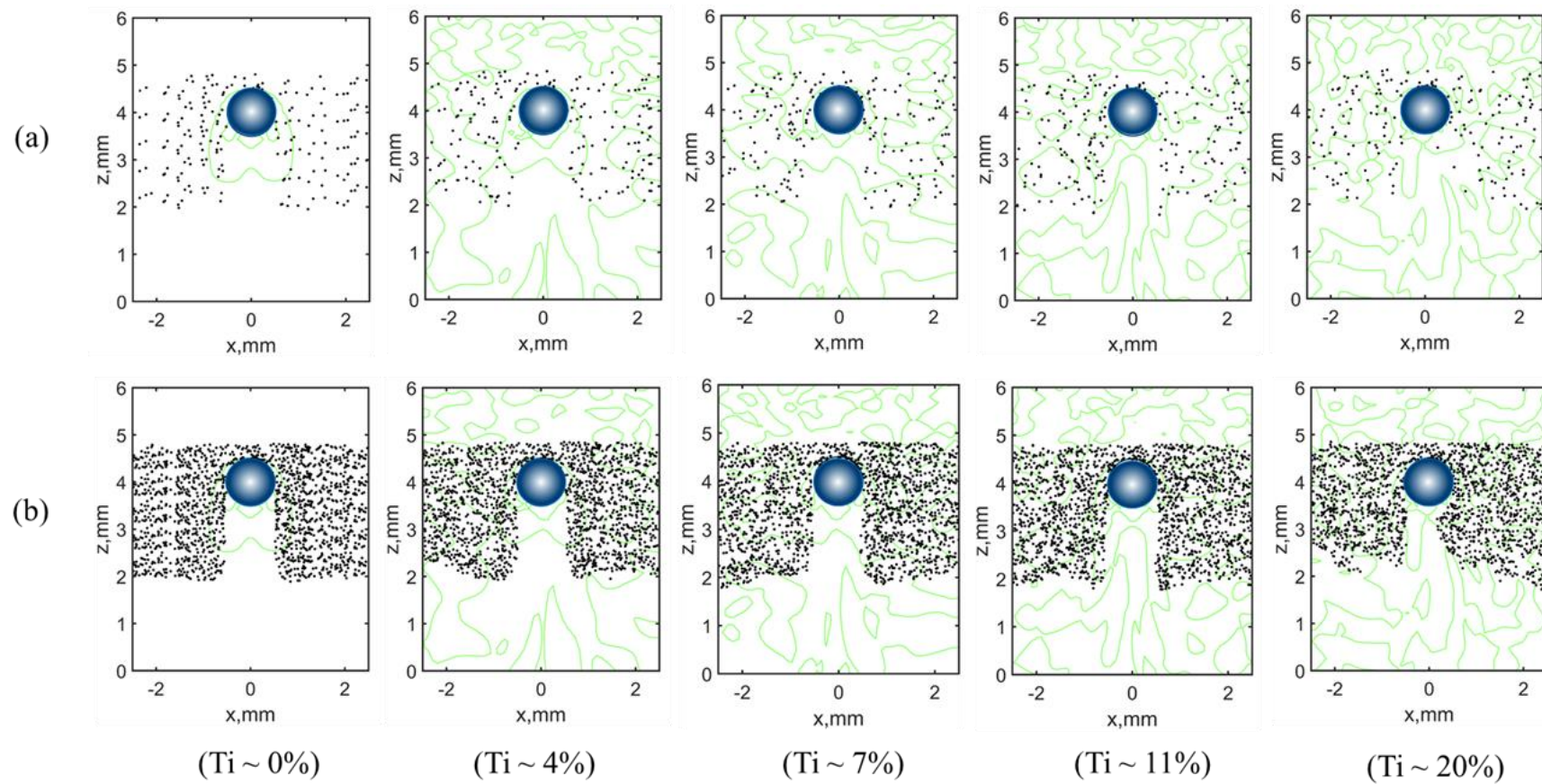


**Fig. 4.4.** Interaction of particles with fluid at  $Re_B \sim 230$  for  $Ti \sim 0\%$  to  $20\%$  at (a)  $C_{P,i} \sim 0.39$  vol %; (b)  $C_{P,i} \sim 3.08$  vol %. Vortex was marked by Q criterion = 1. Particle locations were extracted at 0.0107 s after the first injection.

For low solid concentration cases ( $C_{P,i} \sim 0.39\%$ , **Fig. 4.4a**), particles tended to accumulate on the edge of vortex due to the inertia, as the turbulence intensity  $Ti$  increased from 4% to 20%. This accumulation is consistent with the numerical observations of Wan et al (2020). Such preferential concentration suggested that once particles are injected into the turbulent flow field, the trajectories of particles are subject to the turbulence intensity level which in turn, alter the local solid concentration.

For high solid concentration cases ( $C_{P,i} \sim 3.08\%$ , **Fig. 4.4b**), the preferential concentration that occurred in low solid concentration was not obvious due to the large number of particles. However, with the increase of solid concentration, Ge et al. (2020) numerically reported an increase in lateral dispersion of the particle swarm as the particle swarm approached the bubble in laminar flow. Similarly, for low turbulence intensity levels (<7%) in this study **Fig. 4.5** shows that the averaged radial velocity for particles in the virtual injecting cylinder above the bubble increased with solid concentration. For high turbulence intensity ( $\geq 7\%$ ), however, the particle

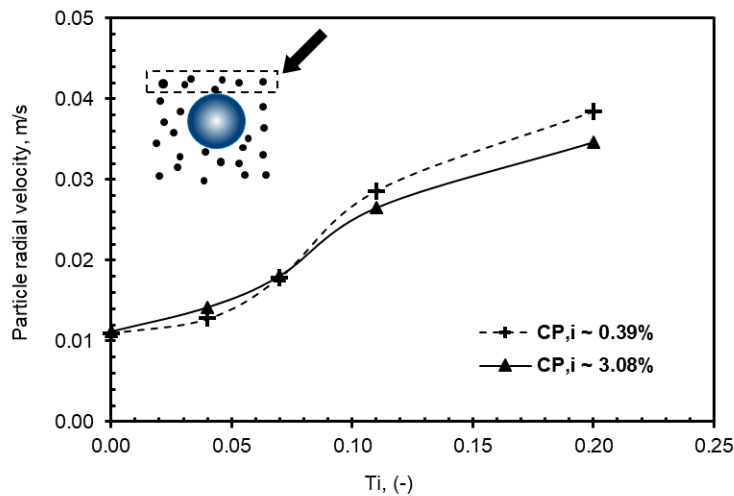


**Fig. 4.5.** Particle radial velocity as a function of turbulence intensity at  $Re_B \sim 230$  for different injecting solid concentration at 0.0112 s after the first injection.

radial velocity decreased with solid concentration. Such velocity reduction can be explained by the turbulence attenuation, namely the reduction in turbulence intensity in the presence of particles. Gore and Crowe (1989) reported that turbulence attenuation occurs when the ratio of particle diameter to the integral length scale of the flow,  $d_P/l$  is less than the critical value of 0.1. **Table 4.2** illustrates the CFD-predicted ratio  $d_P/l$  for turbulence intensities  $Ti \sim 4\%$  to 20%

wherein the method of determining the integral length scale is provided in Appendix A. Apparently, at  $Ti \geq 7\%$  the ratio  $d_p/l$  is below 0.1, indicating the presence of turbulence attenuation at higher turbulence intensity. As a result of turbulence attenuation, the energy passed from the turbulent eddies to the particles decreases with increased solid concentration, resulting in lower particle radial velocity.

**Table 4.2.** Summary of the ratio of particle diameter to the integral length scale of the flow for turbulence intensity 4% - 20%.

	Ti ~ 4%	Ti ~ 7%	Ti ~ 11%	Ti ~ 20%
Integral length scale, $l$ , mm	0.294	0.312	0.356	0.448
$d_p/l$ , -	0.102	0.096	0.084	0.067

The CFD model predicted temporal evolution of particles movement in turbulent flow field for  $Ti \sim 4\%$  and 20% is shown in **Fig. 4.6a-b**. At lower turbulence level ( $Ti \sim 4\%$ ), the flow field around the bubble appears to be symmetric except at the rear surface where attached vortices alter periodically, and the downstream flow field loses symmetry to some extent. As  $Ti$  is increased ( $Ti \sim 20\%$ ), the flow field apparently becomes highly distorted around the bubble in both axial and lateral direction.

At low turbulence intensity ( $Ti \sim 4\%$ ), particles somewhat follow the fluid streamlines and their trajectories remain ordered. For illustration purpose, trajectories of only four randomly selected particles are presented. Noticeably at higher  $Ti$  ( $Ti \sim 20\%$ ), due to higher fluctuating momentum transport from fluid to particles, particle motion becomes substantially chaotic which apparently causes lateral changes in the particle trajectory forcing them to follow different streamlines.

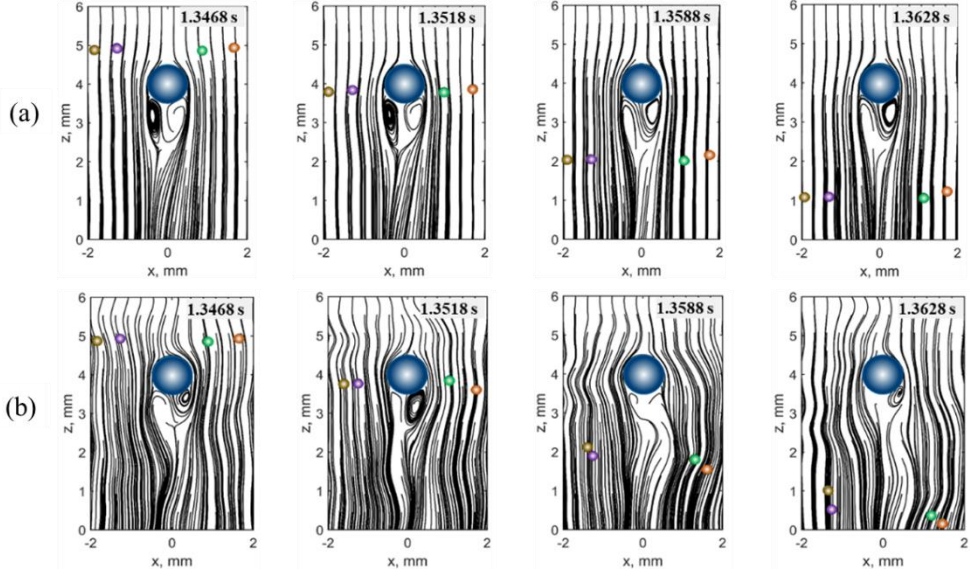


**Fig. 4.6.** Interaction of particle with fluid at  $Re_B \sim 230$  for (a)  $Ti \sim 4\%$ ,  $C_{P,i} \sim 0.77$  vol%; (b)  $Ti \sim 20\%$ ,  $C_{P,i} \sim 0.77$  vol%. Flow field was marked by streamline, and for demonstration of the evolution of single particle trajectory, only the positions of 4 particles (size exaggerated for illustration purpose) from the particle swarm are shown.

#### 4.4.2. Particles collision number and local solid concentration

In the CFD model, particles were injected at different radial locations (see **Fig. 4.1**) to examine the effect of spatial locations of particles on collision interaction and determine an injection area which results in approximately identical collision rates (bubble-particles collisions/time). The collision rate for a given injecting radius was estimated based on the slope of the cumulative number of particles that made a physical contact with the bubble over a certain time duration. This ensures that the collision interaction was accounted in a quasi-steady regime.

As an illustration, **Fig. 4.7** shows the cumulative number of collided particles as a function of time (the initial time, 0 s, represents when the first injection of particles) at a particular injection location  $R_{i,cyl} = 3R_B$  for  $Ti \sim 4\%$  and  $C_{P,i} = 3.08$  vol%. It can be observed that the cumulative particles collision number increases with time up to  $t = 0.015$ s. Apparently, some non-linearity is present in the early stage of this cumulative curve up to  $t = 0.0036$  s. This non-linearity was neglected and only the relatively steady period ( $0.0036 \leq t \leq 0.0131$ ) was used to fit a linear curve ( $R^2 = 0.99$ ) to calculate the collision rate.

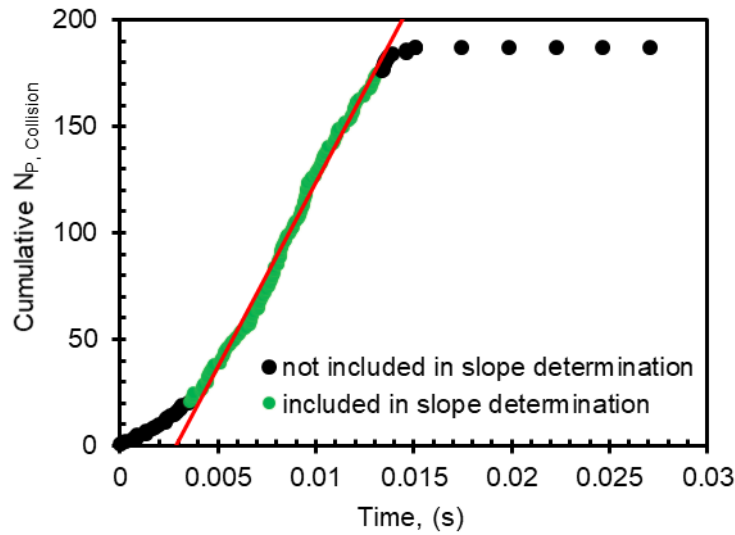


**Fig. 4.7.** The cumulative number of particle-bubble collisions vs time ( $R_{t,cyl} \sim 3R_B$ ;  $Ti \sim 4\%$  and  $C_{P,i} \sim 3.08$  vol%).

**Fig. 4.8a-b** shows the collision rate as a function of  $R_i/R_B$  for three different solid concentrations ( $C_{P,i} = 0.77, 1.54$  and  $3.08\%$ ) at  $Ti = 4\%$  and  $20\%$ , respectively. It can be observed that the collision rate does not follow any specific trend with respect to  $R_i/R_B$  which indicates this parameter to be independent of the particle injection location. However, for both  $Ti$  values, the collision rate at every injection location increases with increasing solid concentration.

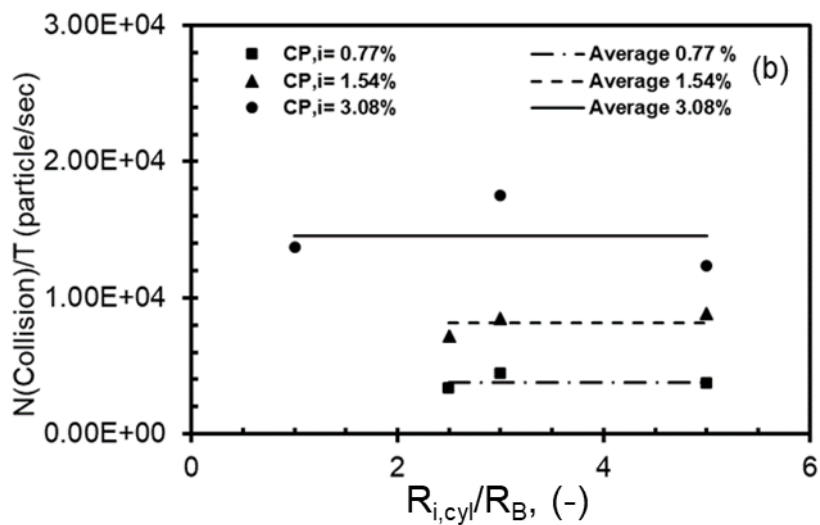
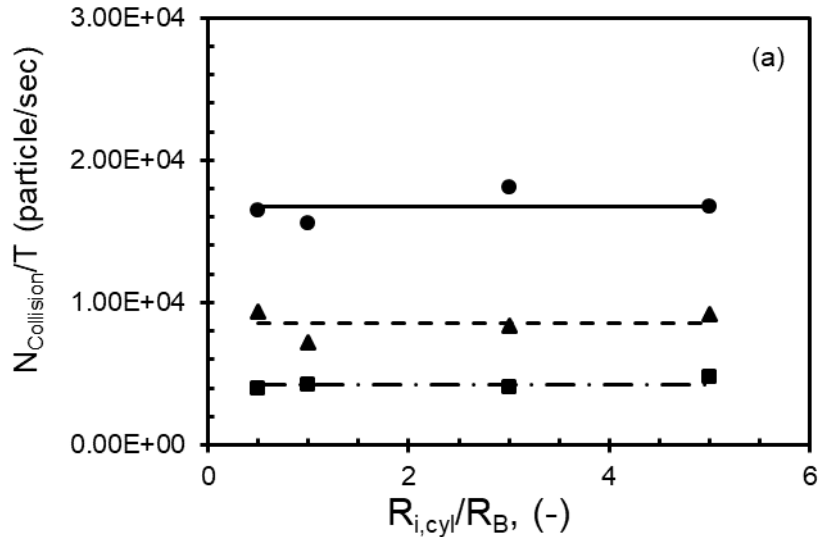


**Fig. 4.8.** The number of particles that collide against the bubble per time unit vs  $R_{i,cyl}/R_B$  ratio for three different solid concentrations  $C_{P,i}$ : a)  $Ti \sim 4\%$ ; b)  $Ti \sim 20\%$ .

It was shown in **Fig. 4.6** that particle trajectory becomes increasingly chaotic in the presence of turbulence. It is therefore intuitive to hypothesise that the local solid concentration ( $C_{P,sB,j}$ ) around the bubble will change with turbulence intensity for a given injection condition.

**Fig. 4.9** shows the solid concentration (particles volumetric concentration in a virtual shell volume) distribution around the bubble as a function of the ratio of the radius of a virtual shell to the bubble radius ( $R_{s,j}/R_B$ ) for a range of  $R_{i,cyl}$  varying from  $2.5R_B$  to  $5.0R_B$ . The results are shown for two turbulence intensities –  $Ti \sim 4\%$  (**Fig. 4.9a-c**) and  $Ti \sim 20\%$  (**Fig. 4.9d-f**). It can be observed that in all cases, the local solid concentration is zero at the bubble surface

$(R_{s,j}/R_B = 1.00)$  due to zero virtual shell volume, however, in the finite volume virtual shells away from bubble surface, concentration increases and exhibits a relatively flat profile in  $R_{s,j}/R_B$  ranging from  $\sim 1.4$  to  $2.8$ .

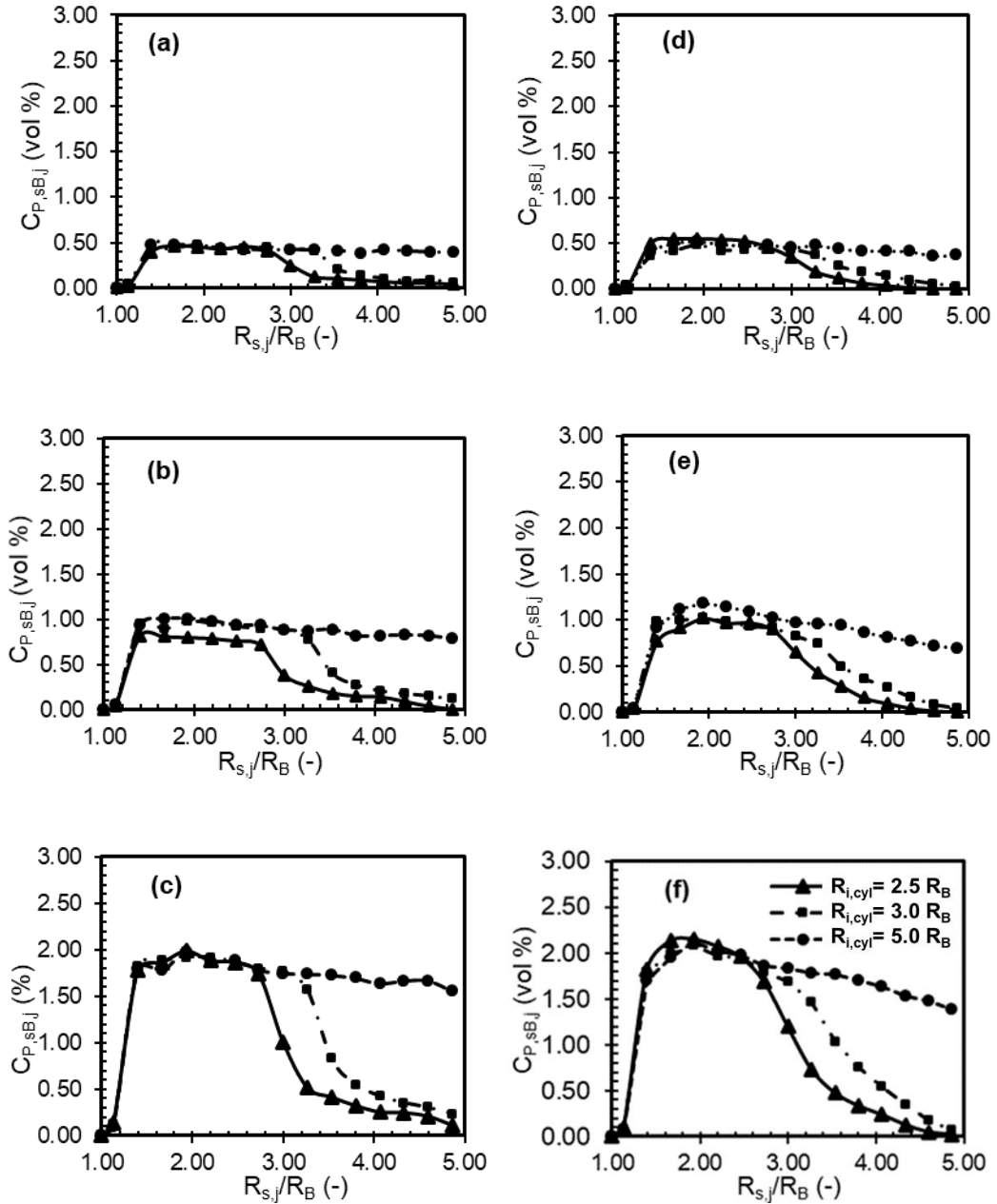


**Fig. 4.9.** Solid concentration vs  $R_{s,j}/R_B$  ratio at  $0.0132$  s after the first injection of particles: (a)  $Ti \sim 4\%$ ,  $C_{P,i} \sim 0.77$  vol%; (b)  $Ti \sim 4\%$ ,  $C_{P,i} \sim 1.54$  vol%; (c)  $Ti \sim 4\%$ ,  $C_{P,i} \sim 3.08$  vol%; (d)  $Ti \sim 20\%$ ,  $C_{P,i} \sim 0.77$  vol%; (e)  $Ti \sim 20\%$ ,  $C_{P,i} \sim 1.54$  vol%; (f)  $Ti \sim 20\%$ ,  $C_{P,i} \sim 3.08$  vol%.

It is apparent that the average local concentration around the bubble increases with increasing initial injecting solid concentration for both turbulence intensity cases. The average

values of the local concentration in the virtual shells of radius  $R_{s,j} \sim 1.4R_B$  to  $2.8R_B$  for the examined turbulence intensities  $Ti \sim 4\% - 20\%$  cases are summarised in **Table 4.3**.

**Table 4.3.** Average local concentration in the virtual shell of radius  $R_{s,j} \sim 1.4R_B$  to  $2.8R_B$ .

$C_{P,i}$ , vol%	$C_{P,sB,j}$ , vol%			
	$Ti \sim 4\%$	$Ti \sim 7\%$	$Ti \sim 11\%$	$Ti \sim 20\%$
0.385	0.22	0.22	0.23	0.24
0.770	0.44	0.47	0.47	0.47
1.540	0.89	0.95	0.97	0.99
3.080	1.85	1.82	1.85	1.94
6.160	3.68	3.65	3.67	3.94

It is noted that the average  $C_{P,sB,j}$  value for each case is lower than the initial injecting concentration which could be attributed to particle dispersion in a turbulent flow medium. In addition, for all initial injecting concentration  $C_{P,i}$  cases, the average  $C_{P,sB,j}$  values only slightly increased with turbulence intensity level. For example, the average  $C_{P,sB,j}$  increased by 9% as  $Ti$  increased from 4% to 20% at  $C_{P,i} \sim 0.385\%$ . It can be concluded that the turbulence intensity has insignificant effect on local solid concentration.

#### 4.4.3. Turbulent collision efficiency

Numerically, collision efficiency is defined as the ratio of the number of particles that made a physical contact with the bubble to the total number of particles injected. Based on this definition, it is quite apparent that the collision efficiency would follow a probability distribution depending on the solid concentration and flow field profile in the vicinity of bubble. **Fig. 4.10** illustrates an example of the distribution of total particles injected from each releasing bin (**Fig. 4.2**) and number of particles that collided against the bubble in the bin at low turbulence intensity  $Ti \sim 4\%$  and  $C_{P,i} \sim 3.08$  vol%. Based on the bubble-particle collision detection algorithm (Eqs. (4.3) - (4.7)), no particle collision with the bubble was detected beyond the bin radius  $0.6R_B$ . The collision efficiency was therefore quantified within bin range from 0 to  $0.6R_B$ . This collision favourable zone was then split into 7 bins based on a physical requirement such that each bin could accommodate at least one particle (selected bin width 43

$\mu\text{m} > \text{particle diameter}$ ). It can be noticed that except for the bin located close to the bubble surface ( $R_{bin,i}/R_B = 0.043$ ), only a small fraction of the particles contained in other bins located away from bubble surface contributed to a collision outcome. For instance, in the 2<sup>nd</sup> bin, 82 particles out of a total 110 injected particles collided with the bubble, however, no particles from the farthest bin (7<sup>th</sup> bin,  $R_{bin,i}/R_B = 0.557$ ), resulted in a collision.

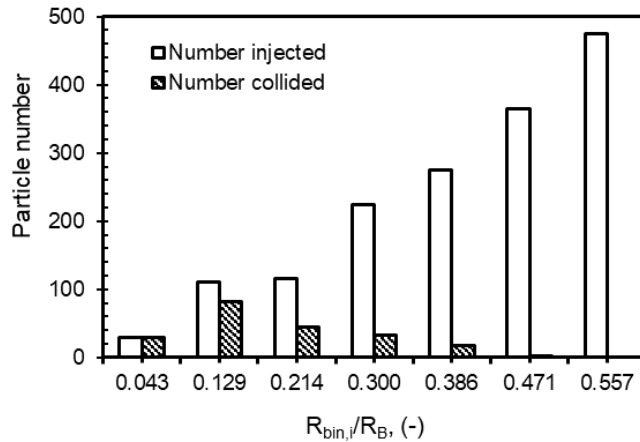


**Fig. 4.10.** The injected and collided particle number vs  $R_{bin,i}/R_B$  ratio. ( $Ti \sim 4\%$ ;  $C_{P,i} \sim 3.08$  vol% and  $R_{i,cyl}/R_B \sim 5.0$ ).

The collision efficiency for each bin  $E_{ct,i}$  was calculated using Eq. (4.7) based on the method of examining the total injection and collision number in **Fig. 4.10**. **Fig. 4.11** presents  $E_{ct,i}$  for different turbulence intensities and solid concentrations. It can be observed that in both **Fig. 4.11a** and **Fig. 4.11b**, the collision efficiency  $E_{ct,i}$  clearly follows a probability distribution with the 1<sup>st</sup> bin having the highest value of 0.967, and the 7<sup>th</sup> bin having a zero-collision efficiency value for  $C_{P,i} \sim 3.08$  vol%. The probabilistic nature of the collision efficiency parameter is similar to that in the single-particle injection cases in Chapter 3. This nature indicates that in a turbulent environment defining a grazing radius  $R_c$  within which the collision efficiency of particles is always 1, is not straightforward. In an idealised steady flow field (Stokes flow or potential flow), streamlines remain ordered and only a particle located on the streamline closest to the bubble is able make a physical contact. In contrast, turbulent flow motion is inherently unsteady which causes significant deviation in a particle trajectory depending on the intensity level (see **Fig. 4.6**). Therefore, it is possible that a collision event occurs even when a particle is located at a distant streamline away from the bubble surface.

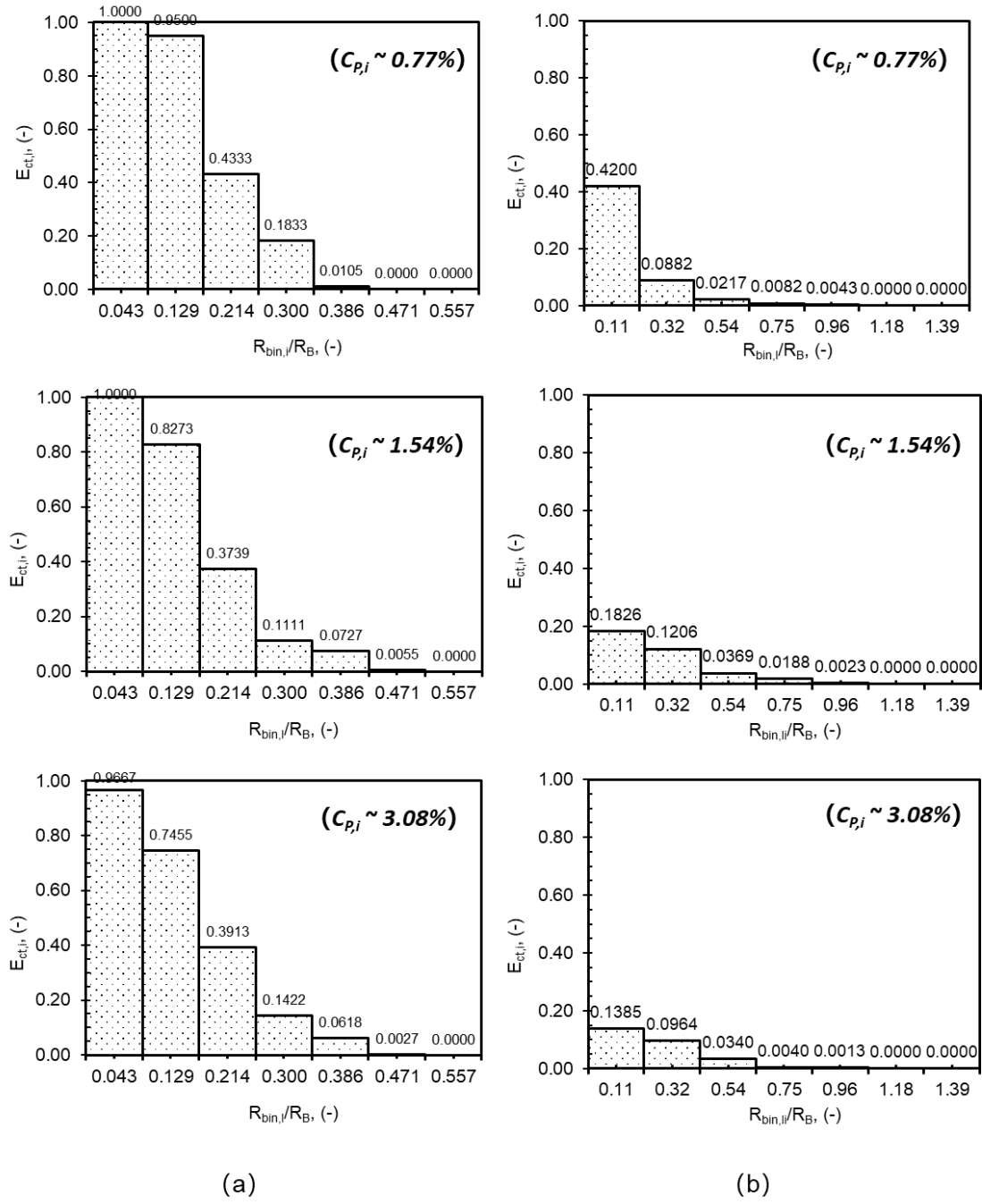


**Fig. 4.11.** Collision efficiency vs  $R_{bin,i}/R_B$  ratio for  $C_{P,i} \sim 0.77\% - 3.08$  vol% at (a)  $Ti \sim 4\%$ ; (b)  $Ti \sim 20\%$ .

The maximum collision efficiency along bin radius  $E_{ct,i}$  occurred in the bin above the bubble centre and was observed to decrease with the increase of solid concentration in both  $Ti \sim 4\%$  and  $\sim 20\%$  cases. This is because more particles are dispersed away from the bubble centre in higher solid concentrations. It can also be observed that from  $C_{P,i} \sim 0.77\%$  to 3.08 vol%, the reduction of maximum  $E_{ct,i}$  in  $Ti \sim 20\%$  cases was more obvious with the decreasing rate being

$\sim 66.7\%$ , compared to  $\sim 3.3\%$  at  $Ti \sim 4\%$ . Considering that particles movements in turbulent flow were more chaotic with the increase of  $Ti$  (see **Fig. 4.6**), the increase in solid concentration may impact the particle dispersion in higher  $Ti$  cases more than that in lower  $Ti$  cases. As a result, the collision efficiency was more sensitive to the solid concentration at higher  $Ti$ .

The collision efficiency distribution obtained in **Fig. 4.11** was used to calculate the overall collision efficiency  $E_{ct}$  using Eqs. (4.8) - (4.10). **Fig. 4.12** illustrates the variation of the overall collision efficiency for different turbulence intensity levels  $Ti$  ( $\sim 4\%$  to  $20\%$ ), against the average local solid concentration around the bubble,  $C_{P,sB,j}$  (as shown in **Table 4.3**). For comparative purposes,  $E_{ct}$  under the condition of  $Ti \sim 0\%$  was also calculated using the same method described in Section 4.2. In all  $Ti$  cases, the overall collision efficiency  $E_{ct}$  generally decreased with the concentration  $C_{P,sB,j}$ . For example, as  $C_{P,sB,j}$  increased from  $0.22\%$  to  $3.65\%$ ,  $E_{ct}$  decreased by  $\sim 112\%$  at  $Ti \sim 0\%$  and by  $\sim 156\%$  at  $Ti \sim 20\%$  respectively. Such a reduction trend agreed well with the numerical studies of Ge et al. (2020). The agreement suggests that, while Ge et al. (2020) attributed the reduction trend in higher solid concentration to the increased lateral dispersion of particle swarm which draws particles away from the bubble in laminar flow, such dispersion also holds true in turbulent flow.

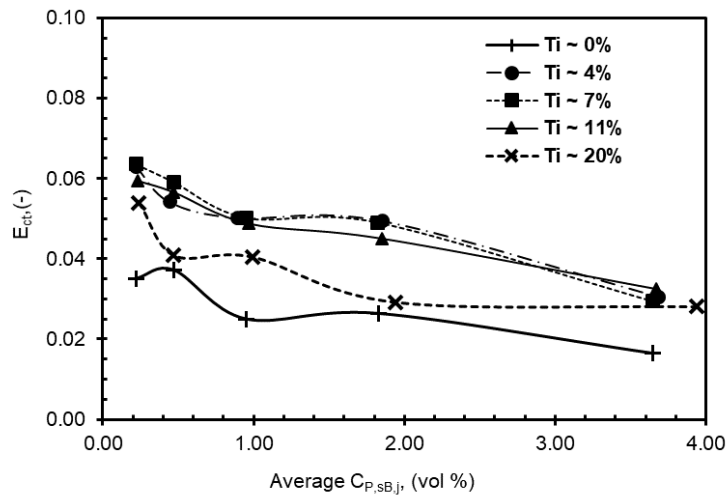


**Fig. 4.12.** Change of turbulent collision efficiency vs solid concentration around the bubble for different turbulence intensity values.

As the turbulence intensity increased from  $\sim 0\%$  to  $\sim 4\%$ , it was observed that the overall collision efficiency  $E_{ct}$  significantly increased with the minimum increase rate  $\sim 46\%$  occurring at  $C_{P,sB,j} \sim 0.47\%$  and the maximum rate  $\sim 100\%$  occurring at  $C_{P,sB,j} \sim 0.95\%$ . As

the  $Ti$  further increased from  $\sim 4\%$  to  $\sim 7\%$ , slight increase in  $E_{ct}$  was noted at lower average solid concentration  $C_{P,sB,j}$  in the range of  $\sim 0.22\%$  to  $0.95\%$ . After the turbulence intensity exceeded than the optimal turbulence intensity of  $\sim 7\%$ , the overall collision efficiency  $E_{ct}$  reduced with  $Ti$ , with low reduction rate  $\sim 2.8\%$  to  $\sim 10.7\%$  as  $Ti$  increased from  $7\%$  to  $11\%$  and significant reduction rate  $\sim 9.4\%$  to  $\sim 27.9\%$  as  $Ti$  increased from  $11\%$  to  $20\%$ .

The optimal  $Ti \sim 7\%$  can be attributed to the interaction between particles and the surrounding turbulent eddies. In the lower turbulence intensity case ( $Ti \sim 4\%$ ) as illustrated in **Fig. 3.14**, particles still loosely follow the flow streamlines. Such dispersion behaviour makes it difficult for particles which are initially released outside of the volume enclosed by the grazing trajectories to obtain enough kinetic energy from eddies to migrate laterally towards the bubble surface. In  $Ti \sim 7\%$  case however, the collision efficiency along the bubble radial direction for particles released outside of this enclosed volume, as shown in **Fig. 3.10**, is higher than  $Ti \sim 4\%$  case. As the turbulence intensity increases further ( $Ti \sim 11\%$  and  $20\%$ ), particles initially released inside this enclosed volume are significantly diverted away from the bubble surface, with the maximum collision efficiency in the radial direction decreasing from 0.8 in  $Ti \sim 7\%$  to approximately 0.32 and 0.17 in  $Ti \sim 11\%$  and  $Ti \sim 20\%$  cases.

Although in the current system (single bubble-multiparticle system) a reduction in the overall collision efficiency  $E_{ct}$  from  $Ti \sim 7\%$  to  $Ti \sim 20\%$  is predicted, it may not be necessarily so if multiple bubbles are considered to exist in the computational domain as multiple bubbles may be available for further collisions. In addition, in the presence of multiple bubbles the turbulent flow field can significantly differ from that of single bubble cases, therefore affecting the trend of overall collision with turbulence intensity.

#### 4.5. Conclusion

In this chapter, the effect of solid concentrations on bubble-particle collision efficiency under different levels of turbulence intensity ( $Ti \sim 4\%$  to  $20\%$ ) was examined numerically.

Particles in lower solid concentration cases accumulated on the edge of vortices due to the inertia, suggesting that the local solid concentration may be different from that of the injecting concentration. In addition, turbulence attenuation which caused the decrease of particle radial velocity with solid concentration, occurred for turbulence intensities above 7%.

Besides this, at higher  $Ti$  levels the flow field became highly distorted and particle trajectories were substantially chaotic with particles apparently switching between different streamlines.

The average solid concentration in the vicinity of bubble was lower than the initial injecting concentration which could be attributed to particle dispersion in a turbulent flow medium. Turbulence intensity was found to have insignificant effect on local solid concentration.

Collision efficiency was found to follow a probability distribution in the vicinity of the bubble wherein particles injected close to the bubble had a higher collision efficiency than particles injected far from the bubble surface. The maximum collision efficiency along the bin radius decreased with the increase of solid concentration because more particles are dispersed away from the bubble centre in higher solid concentration. The overall collision efficiency  $E_c$  generally decreased with the solid concentration due to the increased lateral dispersion of particles. The optimal turbulence intensity was 7% where the maximum overall collision efficiency occurs in the current single-bubble flotation domain.

# **Chapter 5. Effect of bubble surface loading on bubble rising velocity**

---

## **5.1. Introduction**

In-depth understanding of particle-laden bubble motion in a liquid medium is critical to the recovery of valuable minerals from flotation (Bradshaw and Connor, 1996; Uribe-Salas et al., 2003; Moys et al., 2010). Loading of particles on bubble surface is outcome of successful collision, attachment and balanced forces between particles and bubble. Depending on the flow conditions, the bubble surface loading (defined as the ratio of the bubble surface area occupied by loaded particles to the interfacial area of the bubble) may be loaded up to 0.14 in a flotation cell (Bradshaw and Connor, 1996), a value which was close to 0.2 found by Koh and Schwarz (2008). It is noted that a bubble may be fully loaded in quiescent liquid (Vinke et al., 1991a, b). The bubble surface loading level directly affects the recovery by influencing the rising behaviour of the bubbles which serve as the particle carrier.

When compared to the “clean” bubble (zero bubble surface loading), a particle-laden bubble exhibits behave differently which includes resistance to shape deformation by becoming more spherical (Wang, et al. 2019a); and decrease in rise velocity due to increased resisting forces (drag and gravitational force) arising from the loaded particles (Huang, et al. 2011). More specifically, if the buoyancy force of a particle-laden bubble is subdued by these resisting forces at a high surface loading level, it may even descend (Uribe-Salas et al., 2003). Despite of the importance of bubble surface loading (BSL), quantifying influence of BSL on bubble rising behaviour is rather difficult due to flow field effect, opaqueness of gas-solid-liquid slurry system and difficulty in coating a flotation-sized bubble ( $\leq 1$  mm) with a controllable BSL due to sensitiveness of its capillary force to the injecting air flow rate even in a quiescent system (Oguz and Prosperetti, 1993). Due to such difficulties, a constant bubble velocity has been commonly used in predicting the minerals recovery (Jameson et al., 1977; Yoon and Mao, 1996).

Relatively fewer studies are indeed reported on the effect of bubble surface loading on bubble rise velocity reduction (Huang et al., 2011; Wang et al., 2019a). Huang et al. (2011) examined the velocity reduction of  $\sim 1.00$  mm bubble with BSL being approximately 0.12 in absence of any surfactant. They found that only accounting for the additional weight of the loaded particles in the force balance analysis led to significant overestimation of bubble rise velocity and it is important to consider the effect of the increased drag force due to particles. Assuming an immobile bubble surface due to high packing ratio of particles ( $\sim 0.8$ ), Huang et al. (2011) applied the drag coefficient of Sadhal and Johnson (1983) based on the partially contaminated bubble in their force balance analysis and predicted a bubble velocity within 4% deviation from experimental measurements.

Huang et al. (2011) only examined the fixed level of bubble surface loading by letting a bubble rising through a solid-liquid slurry. Wang et al. (2019a) investigated the effect of bubble surface loading over a range (0.00 – 0.60) on reduction in the rise velocity. In their work, bubble surface loading was controlled by forming a stationary bubble at the tip of a capillary tube in a suspended slurry medium and then stopping stirring once the bubble was loaded to the desirable level. A correction factor was used in their work to modify the well-known Schiller-Nauman drag coefficient model to include the effect of bubble surface loading on drag coefficient.

This chapter aims at determining the dependency of bubble rise velocity on bubble surface loading both in the absence and presence of surfactant and modelled a correction factor of drag coefficient. This chapter is organized as follows: Section 2 illustrates the experimental methodology to achieve a controlled level of surface loading on a stationary bubble; and the algorithm of quantifying the bubble surface loading from high-speed image processing; Section 3 examines the rising behaviour of particles-laden bubble and the interaction of the bare bubble with the trailing vortices. Finally, the Schiller-Naumann drag coefficient was modified to account for the effect of bubble surface loading both in the presence and absence of surfactant.

## 5.2. Experimental methodology

### 5.2.1. Materials

Controlled experiments were performed to study the effect of different level of surface loading on the rise velocity of a single particle-laden bubble ( $d_B \sim 2.76$  to  $3.34$  mm) for a fixed size of glass ballotini particles ( $d_B \sim 114$   $\mu\text{m}$ ). A single bubble was generated at the tip of a nozzle (flat-cut hypodermic needle of different sizes). Bubble sizes (after releasing from the nozzle) for two different nozzle sizes are presented in **Table 5.1** in the absence and presence of surfactant (Sodium Dodecyl Sulfate (SDS) at 20% of critical micelle concentration (CMC) with the CMC being  $8.2 \times 10^{-3}$  mol/L as per Markarian, et al. (2005). Surface tension of water at this condition was estimated to be  $\sim 0.058$  N/m. It was very difficult to generate any smaller size bubbles ( $d_B < 2.76$  mm) at stationary state either by decreasing the needle diameter further or by increasing the concentration of SDS beyond 20% of CMC.

**Table 5.1.** A summary of bubble size and surface mobility in pure water / SDS solution

Case 1	18G needle, in pure water	$d_B \sim 3.34$ mm
Case 2	23G needle, in pure water	$d_B \sim 2.76$ mm
Case 3	18G needle, in 20% of CMC of SDS solution	$d_B \sim 2.76$ mm

Glass ballotini particles (Potter Mix, Australia) were hydrophobicised with up to 90% volumetric concentration of a commercial hydrophobic agent, NG1010 (Nanovations, Australia) to achieve varying degree of hydrophobicity. For hydrophobicisation purpose, 10 g of glass ballotini were kept immersed in 4 ml of hydrophobic solution (NG1010 in RO water) of different concentration for 12 hours. Soaked particles were then dried in a dehydration oven at 50 °C until a free-flowing state was obtained. In the current study, no experiments were conducted to check the retention of particle hydrophobicity with time. However, precautions were taken to avoid any loss in particle hydrophobicity. The glass ballotini particles were hydrophobized within only three days before the loading experiments. These particles were then subsequently stored in sealed glass vials to prevent any possible oxidation and moisture ingressions. Also, these vials were kept in a temperature

controlled laboratory room avoiding any direct exposure to sunlight. The narrow time window of usage and storage method arguably ensure the retention of hydrophobicity at the time when experiments were conducted. This can also be seen from the successfully loading of particles onto bubbles during the course of experiment.

To quantify the surface hydrophobicity, a sessile drop method was used on a microscopy glass slide coated with same concentration of hydrophobic solution. Static contact angle was measured by depositing a single drop of RO water on coated surface using a precision syringe pump. The experiments were performed at least three times and all the measured contact angles are presented in **Fig. 5.1**. It can be noted that the contact angle sharply increased from 25.77 deg at 0% hydrophobic agent to 83.28 deg at 5% and then gradually increased to the peak at  $\sim 101^\circ$  at 50% concentration before it decreased to 96° at 90% concentration.

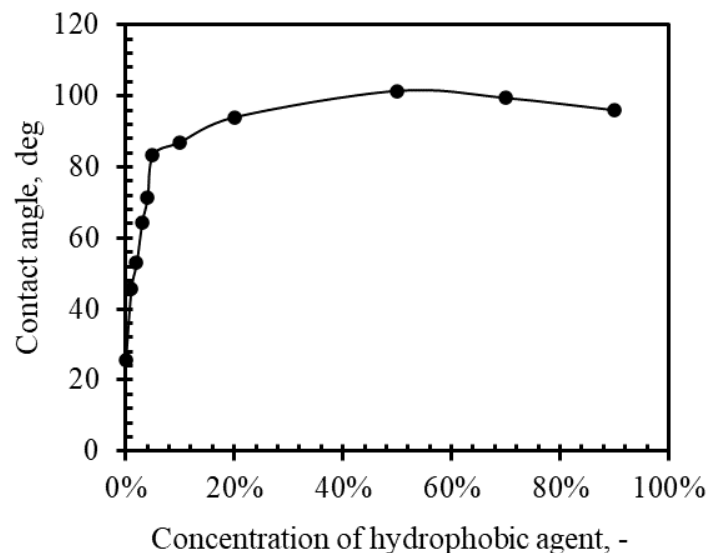


**Fig. 5.1.** Variation of contact angle with the concentration of hydrophobic agent

To determine the desired hydrophobicity level of particles for dosing into the liquid, a series of separate experiments was conducted. It was observed that particles coated with 2% hydrophobic solution (corresponding contact angle  $\sim 53^\circ$ ) was able to penetrate through the free gas-liquid surface and attach to the bubble. Any higher concentration of hydrophobic solution led to formation of particle agglomerates during feeding and lower concentration was not conducive for bubble-particle attachment. Subsequently, particles coated with 2% hydrophobic solution were used in all subsequent experimental runs.

### 5.2.2. Method

Using a precision syringe pump (Adelab Scientific), a single bubble was generated through the tip of a nozzle installed inside an acrylic tank (7 cm length × 7 cm width × 9.5 cm height) as shown in **Fig. 5.2**. To ensure bubble stability at the needle tip during the coating process, needles were bent to few different shapes to create additional pressure drop (**Fig. 5.2**). The distance between the needle tip and the free gas-liquid surface of the tank was 55 mm implying negligible effect of hydrostatic pressure on the bubble size.

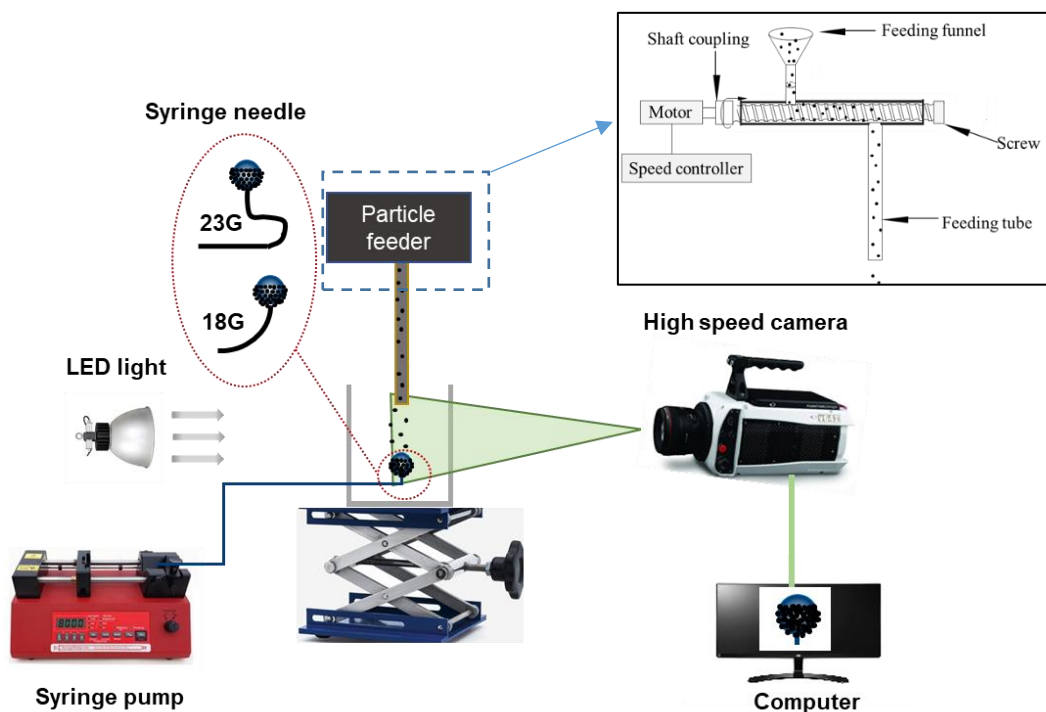


**Fig. 5.2.** Schematic diagram of the experimental setup for determining bubble rising behaviour

To generate a stationary bubble, air injection was initially kept at a rate of 0.1 ml/min and paused when the bubble grew up to a diameter of ~ 2.4 – 2.5 mm. After achieving a stable bubble at nozzle tip, glass ballotini particles were fed through an in-house developed miniature screw feeder system with variable speed control functionality to control particle dosing rate. The feeder was connected to a feeding tube for particle dosing directly into liquid and mounted on a 3D optical traverse with micrometric precision to facilitate perfect alignment. During the experiments, it was ensured that the tip of the feeding tube just touched the free gas-liquid surface of the tank to reduce the chance of blockage due to particle agglomeration. The screw

feeder was turned on for certain time to dose particles at the free surface which settle gently and coated the bubble below. After achieving the required surface loading level, the feeder was stopped and the air injection (at 0.1 ml/min) was resumed to dislodge the bubble-particles aggregate from the tip of the needle.

The rising dynamics of the particle-laden bubble were captured by a CMOS type high speed camera (Phantom v311, Vision Research Inc.) at 1000 frames per second and 65  $\mu$ s exposure time in a field of view (FOV) of  $512 \times 800$  pixels. A shadowgraphy imaging technique was adopted using proper backlighting by placing a diffuser screen in front of a bright halogen light source (12V, 50W) to obtain high contrast images. A 100 mm focal length lens (Tokina) was used together with a combination of three extension rings, 36mm, 20 mm and 12 mm (Tokina) to achieve a pixel resolution of  $\sim 17.5 \mu\text{m}/\text{pixel}$ .

A Particle Image Velocimetry (PIV) system as shown in **Fig. 5.3** was set up to investigate the vortex behind a rising bubble in the absence of Sodium Dodecyl Sulfate. The seeding particles - orange fluorescent polymer microspheres (diameter 15  $\mu\text{m}$  and density 1100  $\text{kg}/\text{m}^3$ ) - were uniformly mixed with R.O. water and transported into the tank. Inside the tank a bubble was generated by the syringe pump at a flow rate of 0.1 ml/min. The PIV system was then switched to Acquire mode to capture the movement of bubble and seeding particles. The PIV system consisted of a Nd-YLF laser generator, a Synchronizer, and a Phantom high-speed camera (V640) with a Tokina lens (macro F2.8D, 100 mm). Unlike single phase flow, when capturing bubbles in water overbrightness on the raw image may occur due to the reflection of bubble surface and the accumulation of seeding particles on the bubble surface. Such overbrightness is not only detrimental to the camera sensor, but also blur the bubble boundary. Therefore, an optical long wave pass filter was fitted to the camera to ensure just enough of the reflect light was received by the camera.

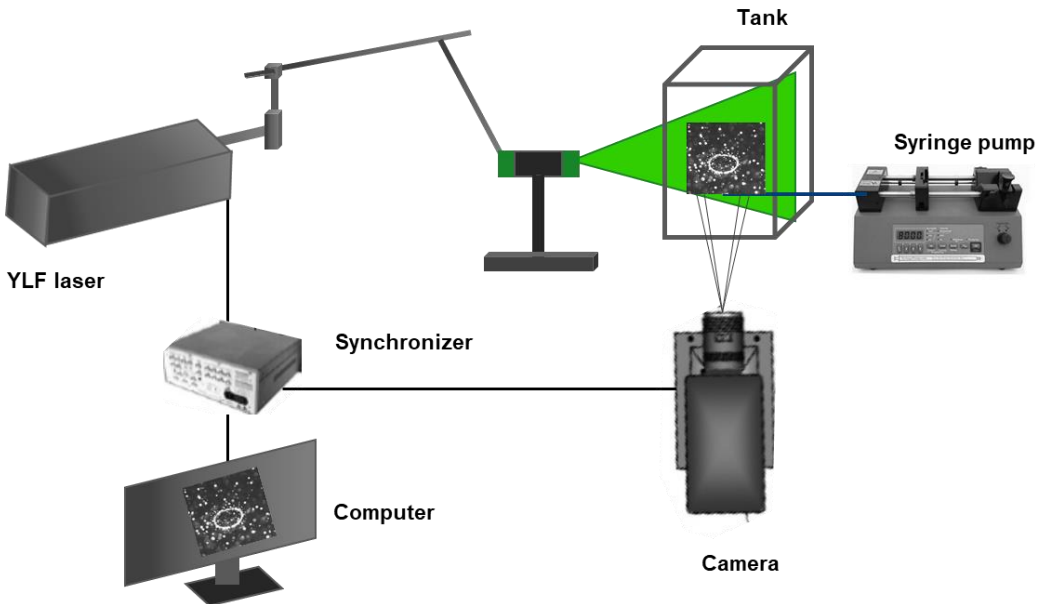


**Fig. 5.3.** Schematic of the experimental setup for vortex identification

The image recording frequency was kept at 400 Hz to ensure that the velocity field around the bubble can be resolved and bubble movement over the travelling distance of 30 mm can be recorded based on the limited storage space. The field of view (FOV) was kept at 20 mm x 30 mm. To ensure each interrogation window occupied a minimum of ~5 to 15 fluorescent particles, an integration area of 32 x 32 pixels with a 50% overlap was used to grid the recorded images. Based on the aforementioned FOV and interrogation window, a spatial resolution of ~ 0.34 mm/pixel can be achieved.

### 5.2.3. Data processing

The acquired shadowgraphy images were analysed by an in-house MATLAB (ver: R2018) code to determine the following parameters - (a) bubble diameter, (b) bubble surface loading, (c) bubble aspect ratio, and (d) bubble-particle (BP) aggregate rise velocity. First, the raw grayscale image obtained directly from high-speed camera were binarized using *im2bw* function with suitable threshold value in the range of 0.20 – 0.35 for determining the high contrast boundary of the BP aggregate as shown in **Fig. 5.4**.

Next, the black and white pixels were swapped using *imcomplement* function. The holes (black) inside the bubble region (white) caused by the light reflection, were repaired using *imfill* function. All suspended particles in the vicinity of a rising bubble in detached state were removed using *bwareaopen* function. Finally, the boundary points of the BP aggregates were traced using *bwboundaries* function. These boundary points were split into two groups – left half and right half based on the bubble symmetry axis. An illustration of the method to determine the loading point from the right half of the BP aggregate is presented in **Fig. 5.5**. For any arbitrary point  $P_l(x_i, y_i)$  on the boundary arc (**Fig. 5.5a**), the surface loading angle  $\theta_{li}$  between two position vectors  $\overrightarrow{PP_3}(x_{l,i-3} - x_{l,i}, y_{l,i-3} - y_{l,i})$  and  $\overrightarrow{PP_2}(x_{l,i+3} - x_{l,i}, y_{l,i+3} - y_{l,i})$  was determined applying vector dot product as follows:

$$\theta_{li} = \cos^{-1} \left( \frac{(x_{l,i-3} - x_{l,i})(x_{l,i+3} - x_{l,i}) + (y_{l,i-3} - y_{l,i})(y_{l,i+3} - y_{l,i})}{\sqrt{(x_{l,i-3} - x_{l,i})^2 + (y_{l,i-3} - y_{l,i})^2} \sqrt{(x_{l,i+3} - x_{l,i})^2 + (y_{l,i+3} - y_{l,i})^2}} \right) \quad (5.1)$$

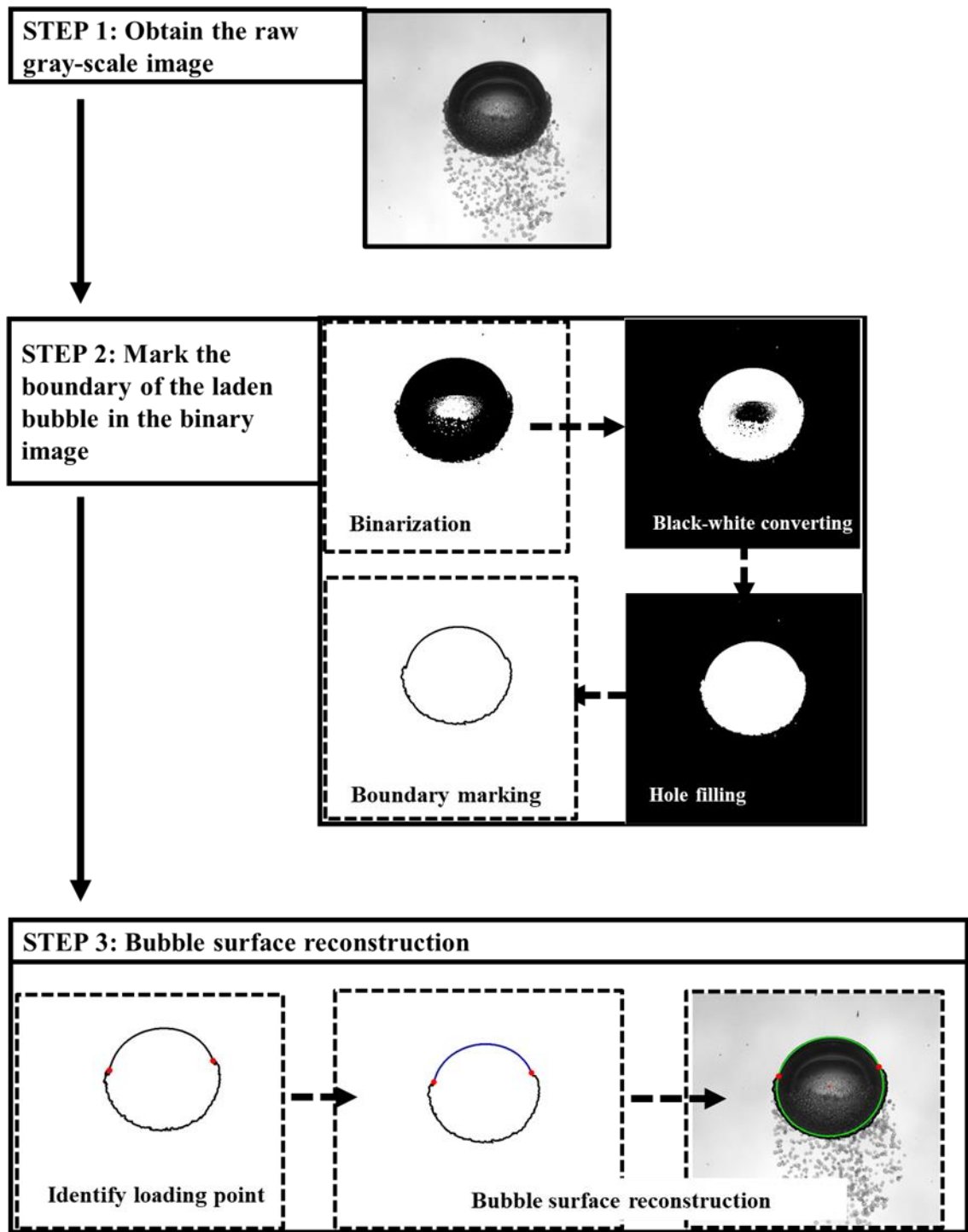


**Fig. 5.4.** Image processing algorithm applied to determine the bubble surface loading of a rising particle-laden bubble: (step 1) high-speed image; (step 2) Boundary marking; (step 3) Identification of the loading section and reconstruction of the bubble surface.

Variations in the seven-point-based angle  $\theta_i$  in the clockwise direction from point A to B are reported in **Fig. 5.5b** wherein the loading positions were determined according to **Fig. 5.5c** and Step 3 in **Fig. 5.4**. The loading start point on the left half of the BP aggregates can be determined

using the same method. The particle loading section between the two identified loading points was hence located.

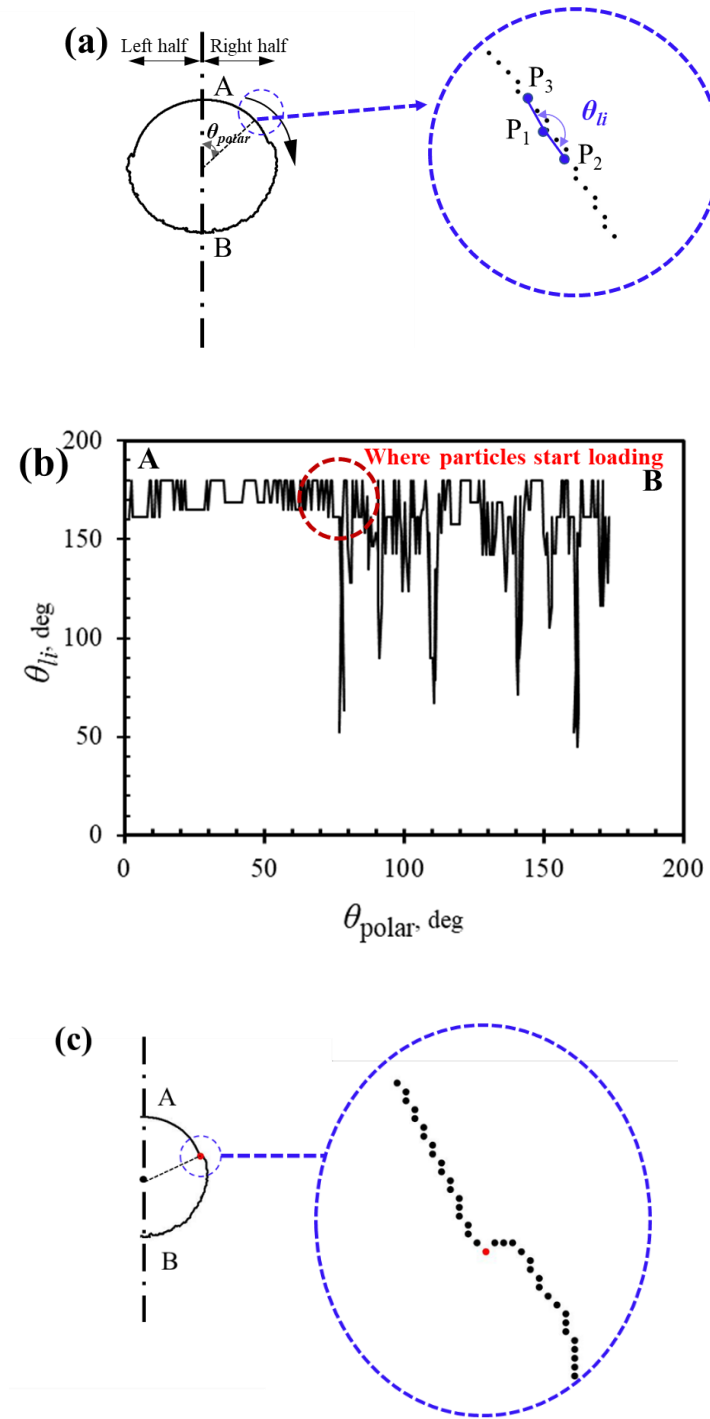


**Fig. 5.5.** Determining the two loading points: (a) two loading points marked on the bubble (b) enlarged zoom-in angle of the determined loading points; (c) the critical angle as a function of the distance in pixels.

For reconstructing the clean bubble surface from the BP aggregates, the boundary points marked by blue arc in **Fig. 5.4**, which connected the two loading points identified above, was fitted by an ellipse marked by green arc (step 3, **Fig. 5.4**). The best fitted semi-minor axis  $a$  and semi-major axis  $b$  can be then be obtained. Assuming the bubble shape as symmetric in the direction of rising, the bubble diameter can then be calculated as:

$$d_B = 2(ab^2)^{1/3} \quad (5.2)$$

Bubble surface loading (BSL) for the rising bubble is a ratio of the surface area of the loading ellipsoidal cap,  $S_{cap}$ , to the surface area of the ellipsoid bubble,  $S_{bubble}$ :

$$BSL = \frac{S_{cap}}{S_{bubble}} \quad (5.3)$$

where the surface area of the ellipsoid bubble,  $S_{bubble}$ , is calculated as:

$$S_{bubble} = 4\pi \left( \frac{2(ab)^{1.6} + (bb)^{1.6}}{3} \right)^{1/1.6} \quad (5.4)$$

The surface area for the ellipsoidal cap  $S_{cap}$ , which is a function of the cap height and the shape of the ellipsoidal bubble, can be derived as follows (please refer to Appendix C for detailed development of the Eq. (5.5)):

$$S_{cap} = ab \sum_{i=1}^n \frac{\pi}{n} f(\cos(\frac{2i-1}{2n}\pi)) \quad (5.5)$$

After marking the particle covered segment on the boundary, the clean interface (blue arc AB in **Fig. 5.6**) was fitted to the pendant drop model (Yang, et al., 2017, Wang. et al., 2019a). The area for the bubble pendant surface and the loading surface was calculated by numerically integrating the area enclosed by rotating the pendant curve AC and BC (**Fig. 5.6b**), respectively. The bubble surface loading for the bubble pendant can then be determined as the ratio of the loading surface area  $S_{Loading}$  to the whole bubble pendant surface area  $S_{Pendant}$  as follows,

$$BSL_{initial} = \frac{S_{Loading}}{S_{Pendant}}. \quad (5.6)$$

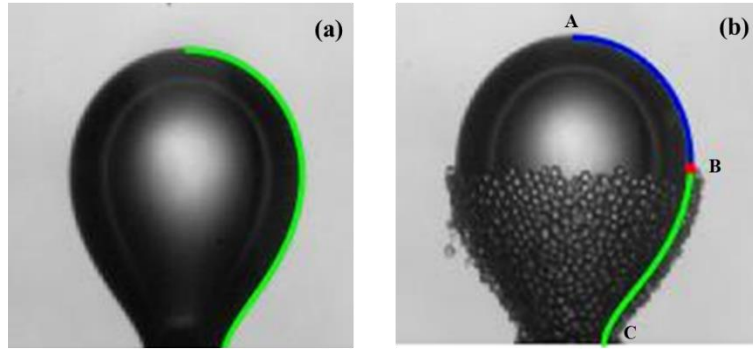


**Fig. 5.6.** Image processing algorithm applied to determine the bubble surface loading of the particle-laden bubble pendant: (a) Surface reconstruction of the clean pendant; (b) Loading section identification and surface reconstruction of the particle-laden pendant.

The bubble aspect ratio, AR, was determined by taking ratio of the semi-minor axis  $a$  to the semi-major axis  $b$  of the fitted ellipse to the reconstructed bubble surface at different time instances and given as

$$AR = \frac{a}{b}. \quad (5.7)$$

The bubble velocity,  $u_{BP}$ , was computed by computing the distance between the centroids of the fitted ellipse in the two successive images and the corresponding time difference from known image capturing frame rate as follows

$$u_{BP} = \frac{y_{B,i+1} - y_{B,i}}{\Delta t}. \quad (5.8)$$

The acquired PIV images were analysed by an in-house MATLAB code to determine the following parameters of the rising bubble – (a) bubble diameter; (b) velocity field of liquid; (c) vorticity field of liquid.

To determine the bubble diameter, it is essential to mark the bubble surface. For this purpose, the raw PIV images were binarized using *im2bw* function with a threshold of 0.5 – 0.6 as shown in **Fig. 5.7**(step 2). The binarized images were then denoised by removing small segments – the seeding particles – using *bwareaopen* function. To distinguish the bubble boundary from the seeding-particle segments (step 3, **Fig. 5.7**), the *regionprops* function was used to identify the coordinates and area of each segments. The *max* function was then used to locate the bubble boundary. The elliptic bubble surface then can be reconstructed (step 4, **Fig. 5.7**) using the properties identified by the *regionprops* function, namely the centre, major/minor

axis length and orientation of the bubble. Based on the reconstructed ellipse, Eq. (5.2) can be used to calculate the bubble diameter.

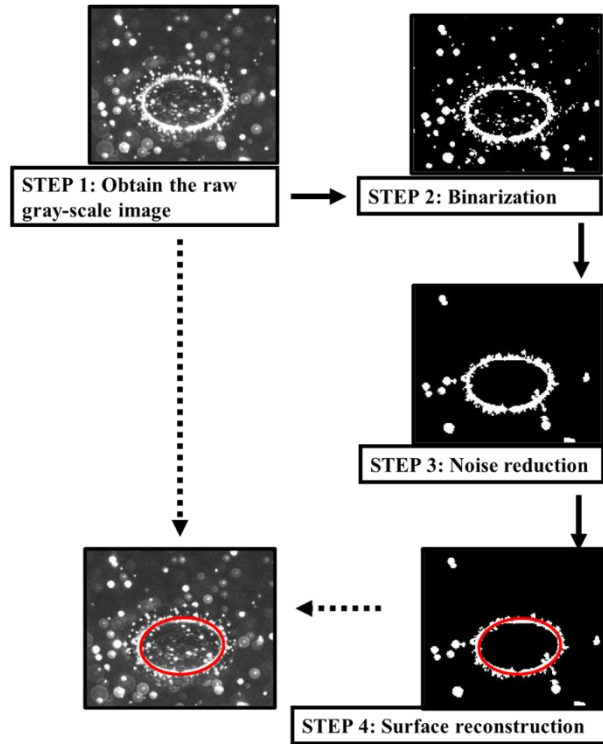


**Fig. 5.7.** Image processing algorithm to mark the bubble from the PIV raw images

To determine the velocity field of the liquid, the raw PIV images were analysed from Dantec Dynamic studio software (V3.4) using the adaptive PIV method.

The vorticity field  $w$  can be calculated from the above determined velocity field using the following equation:

$$w = \frac{\partial v_L}{\partial x} - \frac{\partial u_L}{\partial y} \quad (5.9)$$

where  $u$  and  $v$  are the  $x$  and  $y$  component of liquid velocity, respectively.

## 5.3. Results and discussion

### 5.3.1. Bubble rising behaviour

The time sequence of high-speed visualizations for particle-laden bubble with initial bubble surface loading in the range from 0.00 to 0.77 calculated using Eq.(5.6), is presented in **Fig. 5.8**. For the bare bubble case (BSL  $\sim$  0.00, **Fig. 5.8a**), following its detachment, bubble undergoes a shape transition from the pendant state ( $t = 0$  ms) to ellipsoidal state ( $t = 30$  ms) due to a competition between the inertia and surface tension force as the bubble detaches from the needle tip.

For a lower surface coverage case (BSL  $\sim$  0.14, **Fig. 5.8b**), the particle-laden bubble shows a similar shape transition behaviour in the early stage of rising ( $t = 0 \sim 30$  ms). During this transition period, some loosely attached particles are observed to detach from the bubble surface due to sudden change in bubble inertia following its detachment from the nozzle. At the end of the transition period ( $t \sim 30$  ms), the bubble attains an ellipsoidal state with a stable monolayer of tightly packed particles below its equator. As the bubble further ascends, particles within the rear ellipsoidal cap region are pushed above towards the bubble equator. This behaviour can be attributed to the formation of counter rotating trailing vortices behind a rising bubble. Consequently, instantaneous bubble surface loading exhibits an apparent increase as the loading region expands and particles remain sparsely packed on the bubble surface. Some detached particles could be observed to remain captured in the trailing vortices and move along with the rising bubble.

At intermediate to higher surface loading values cases (initial BSL  $\sim$  0.40 and  $\sim$ 0.77) in **Fig. 5.8c** and **Fig. 5.8d**, bubble shape becomes more spherical ( $t = 15$  ms) compared to the corresponding bubble state for zero initial BSL (**Fig. 5.8a**) during the same transition period. Such tendency of bubble shapes to become more spherical with increasing particle loading was also observed by Wang et al. (2019a). This is because the presence of a monolayer of particles on bubble surface increases the interface rigidity significantly hence reduces any deformation. As the bubble further ascends, unlike the lower bubble surface loading case (**Fig. 5.8a**) which shows only a small amount of particle detachment, a substantial number of particles were observed to detach from the bubble surface ( $t = 50$  ms in **Fig. 5.8c** and **Fig. 5.8d**). The detached particles were entrained and circulated in the wake of the bubble ( $t = 60$  ms in **Fig. 5.8c** and

**Fig. 5.8d).** An explanation of such detachment can be provided based on the interplay of particle kinetic energy imparted by the trailing vortices and bubble-particle adhesion to interface. Detachment occurs when the kinetic energy of the particles overcome the adhesion work.

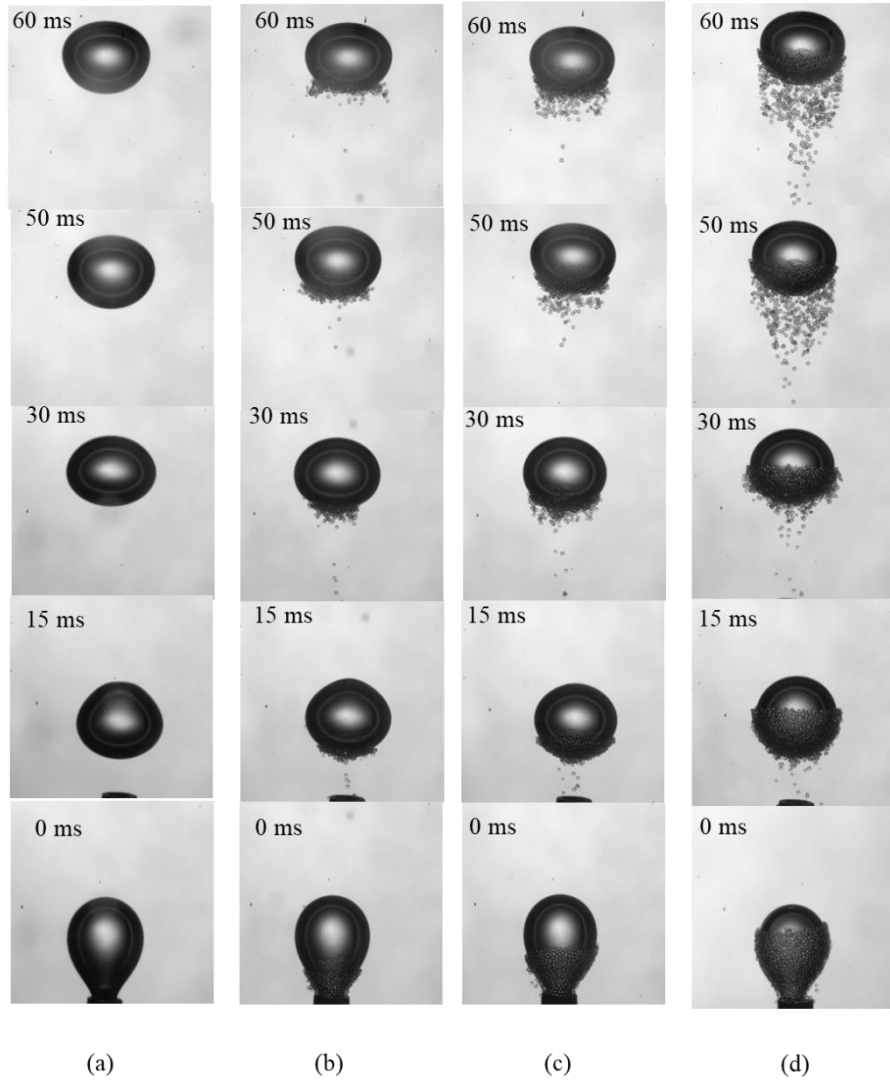


**Fig. 5.8.** High speed visualizations of particle-laden bubble ( $d_B \sim 2.76$  mm) in 20% of CMC of SDS solution for different initial surface loading level: (a) 0.00; (b) 0.14; (c) 0.40; (d) 0.77.

**Fig. 5.9** compares the trajectory of a particle-laden bubble with different initial bubble surface loadings (0.00 – 0.94) both in the presence (**Fig. 5.9a**) and absence (**Fig. 5.9b**) of surfactant. For both cases, a rectilinear trajectory was obtained however deviation from the nozzle centreline was very minimal (0.283 mm) in the presence of surfactant while some deviation (0.430 mm) was observed in absence of surfactant within the travelling height of 12 mm. The observed rectilinear trajectory can be attributed to the accumulation of surfactant and

loaded particles on the bubble surface which dampen out the bubble internal circulation and increases the rigidity of the interface.

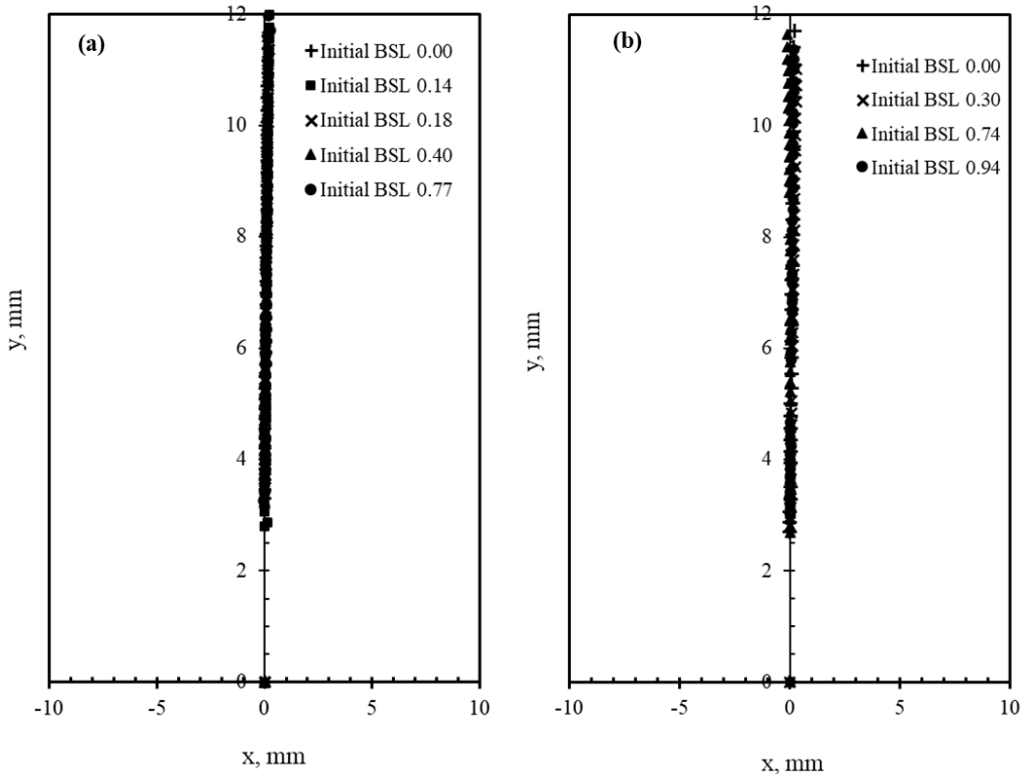


**Fig. 5.9.** Variation of trajectory for a particle-laden bubble in (a) 20% of CMC of SDS,  $d_B \sim 2.76$  mm; and (b) pure water,  $d_B \sim 2.76$  mm for a range of initial bubble surface loading 0.00 – 0.94.

Effect of both surfactant and bubble surface loading was examined using the aspect ratio parameter (**Fig. 5.10**) calculated from Eq. (5.7). In absence of surfactant (**Fig. 5.10b**), significant deviation from the spherical shape was observed in the bare bubble case where aspect ratio reduced to below 0.5 at 60 ms indicating an ellipsoidal state was reached. Aspect ratio values improved as the surface loading was increased however such changes were less pronounced in the presence of surfactant. For this case, an average aspect ratio  $\sim 0.80$  was obtained at  $t > 40$  ms. The aspect ratio profiles can be seen almost collapsing on the same line suggesting that the surfactant is the controlling factor for surface loading range from 0 to 0.77. However, in absence of surfactant, for initial BSL  $> 0.40$  cases, the aspect ratio significantly increased, indicating that the bubble rigidity is mainly controlled by the monolayer coverage of particles. At  $t > 0.05$  s, after a substantial number of particles detached from the bubble for

cases with an initial BSL > 0.40, the aspect ratio profile gradually decreases and overlap with other initial BSL profile.

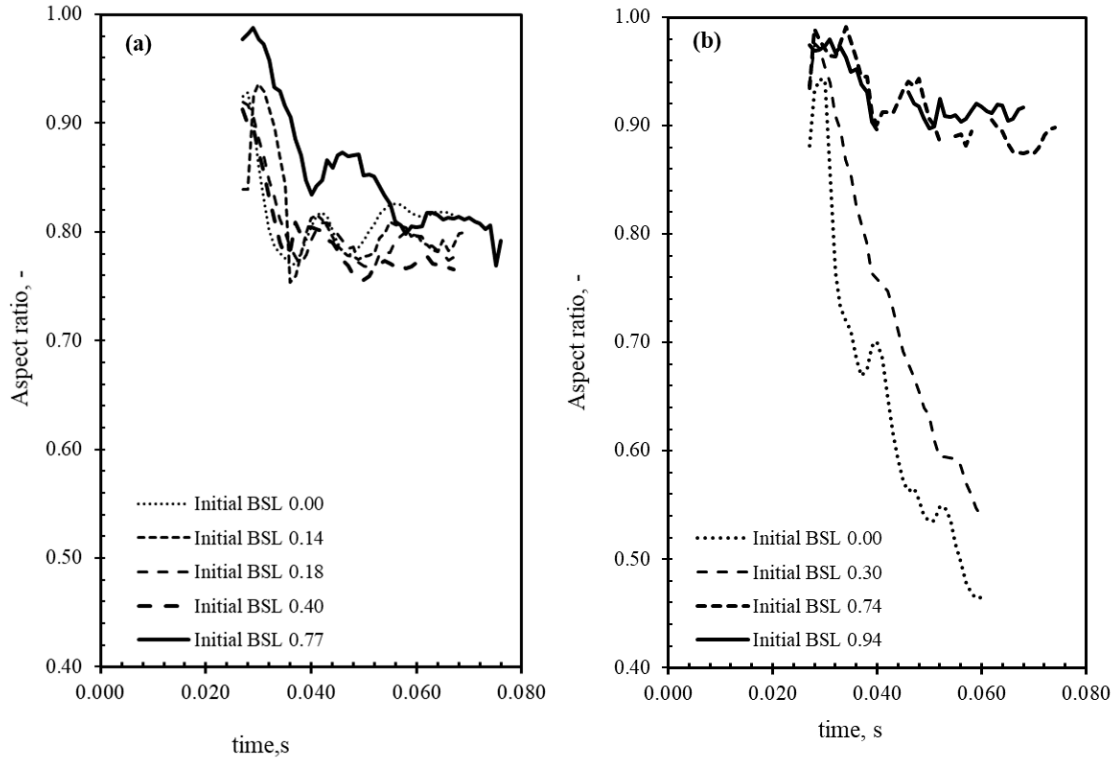


**Fig. 5.10.** Variation of aspect ratio for particle-laden bubble in (a) 20% of CMC of SDS,  $d_B \sim 2.76$  mm; and (b) pure water,  $d_B \sim 2.76$  mm for a range of initial bubble surface loading 0.00 – 0.94.

The temporal evolution of bubble surface loading during bubble rising in the presence of surfactant and in pure water is compared in **Fig. 5.11**. It can be observed that the instantaneous BSL exhibits three distinct regimes: R1 – bubble shape deformation; R2 – particle detachment; R3 - steady shape (for higher initial BSL) or expansion (for lower initial BSL). The instantaneous BSL during regime R1, (with the exception for the start and end of the regime R1), is not reported here due to the difficulty in estimating BSL based on irregular bubble shape (illustrated in **Fig. 5.8**).

Of the three regimes, regime R1 which involves shape deformation, not only features the shape transition as described in **Fig. 5.8**, but also involves some detachment of particles. Significant detachment of particles occurs as the bottom part of the bubble recoils and the equatorial part of the bubble expands to achieve the oblate ellipsoidal shape. Regime R2

features substantial particle detachment due to the strong interplay between the particle kinetic energy and adhesion work. The slope of regime R2 in pure water case (**Fig. 5.11b**), however, is steeper compared to the same initial BSL in the presence of surfactant (**Fig. 5.11a**). For example, the slope of regime R2 for initial BSL  $\sim 0.74$  is  $8.08 \text{ s}^{-1}$  (**Fig. 5.11b**), larger than the  $6.43 \text{ s}^{-1}$  in surfactant case for the same initial BSL  $\sim 0.77$  (**Fig. 5.11a**).

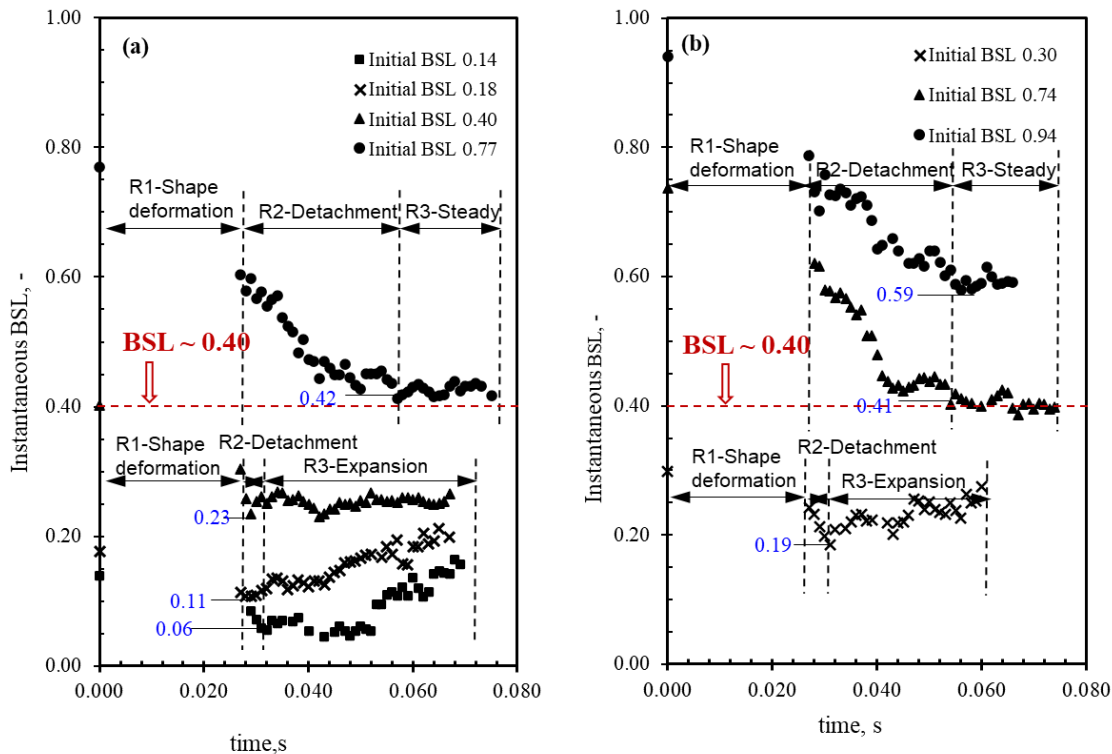


**Fig. 5.11.** Evolution of instantaneous bubble surface loading in (a) 20% of CMC of SDS,  $d_B \sim 2.76 \text{ mm}$ ; and (b) pure water,  $d_B \sim 2.76 \text{ mm}$  for a range of initial bubble surface loading  $0.00 - 0.94$ .

Depending on whether the loading particles can obtain enough kinetic energy to move towards the equator of the bubble, the instantaneous bubble surface loading in Regime R3 may expand or remain steady. It can be further observed from **Fig. 5.11** that the expansion occurs at lower initial BSL ( $\sim 0.14 - 0.40$  in **Fig. 5.11a** and  $\sim 0.30$  in **Fig. 5.11b**) cases while the steady state occurs at higher initial BSL ( $\sim 0.77$  in **Fig. 5.11a** and  $\sim 0.74 - 0.94$  in **Fig. 5.11b**) cases. Considering that the aspect ratio at both these lower and higher initial BSL cases (see **Fig. 5.10a**) were similar, such kinetic energy obtained by the loading particles is less likely to be imparted by the bubble deformation but more likely by the trailing vortex of the bubble, as schematically shown in **Fig. 5.12**. A separation point on the bubble surface exists where the

shear stress is zero (Jiang, 2020), and vortex was formed below this point. Therefore, it is reasonable to assume that only particles loaded below the separation point obtain kinetic energy from the counter-rotating vortex and move towards the bubble equator. Therefore, a critical bubble surface loading level ( $BSL_{cri}$ ) exists, below which the instantaneous BSL expands and above which remains steady, and the corresponding critical loading angle, as shown in **Fig. 5.12** is equal to the separation angle.

The separation angle is defined as the angle from the front stagnation point of the bubble to the separation point (see **Fig. 5.12**). The bubble Reynolds number is necessary to calculate the separation angle and can be calculated as follows:

$$Re_B = \frac{\rho_L d_B u_B}{\mu_L} \quad (5.10)$$

where  $\rho_L$  is water density  $1000 \text{ kg/m}^3$ ,  $\mu_L$  is the dynamic viscosity of water  $0.001 \text{ Pa.s}$  and  $u_B$  is the terminal velocity  $0.311 \text{ m/s}$  for a bare bubble diameter  $d_B$  of  $2.76 \text{ mm}$ . A bubble Reynolds number of 859 can be obtained from Eq. (5.10). The curve of the separation angle reported by Chadel (2021) for bubble Reynolds number in the range of  $\sim 115 - 550$  can be extrapolated to a separation angle of  $\sim 101^\circ$  when the bubble Reynolds number is equal to 859. The critical bubble surface loading ( $BSL_{cri}$ ) can easily be derived as a function of the critical loading angle ( $\theta_{crit}$ ) ( $\sim 101^\circ$ ) (Wimmers and Fortuin, 1988) as follows:

$$BSL_{cri} = \frac{\cos \theta_{crit} + 1}{2} \quad (5.11)$$

Using Eq. (5.11), a critical bubble surface loading value ( $BSL_{cri}$ ) of  $\sim 0.40$  was obtained which was then compared with the observations shown in **Fig. 5.11**. It can be noted that expansion of the loading region in Regime R3 consistently occurred around an instantaneous  $BSL$  threshold  $\sim 0.40$ .

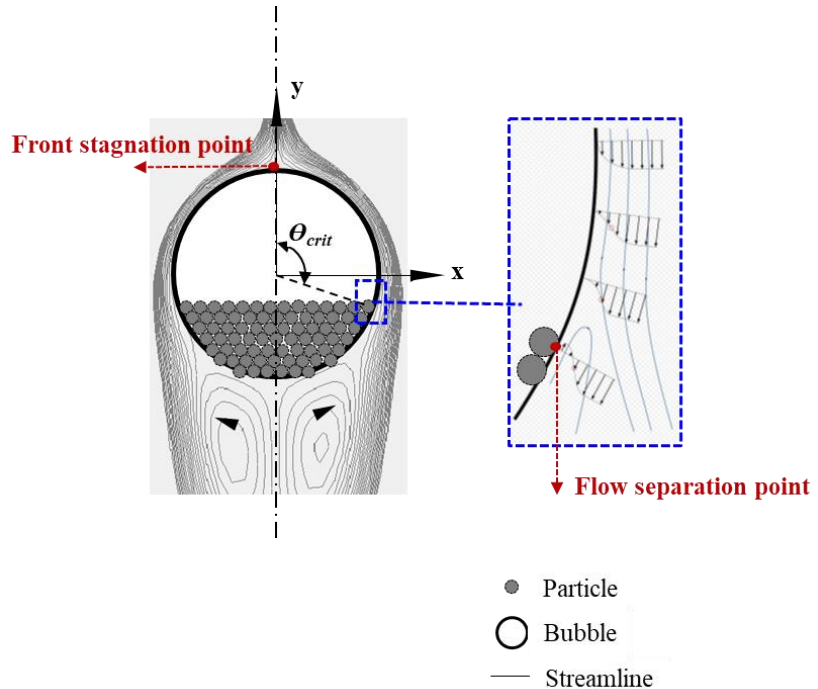


**Fig. 5.12.** Schematic of the critical loading angle.

In **Fig. 5.11b**, it can also be observed that a periodic oscillation of instantaneous bubble surface loading exists for the initial BSL  $\sim 0.30$  case in pure water. Such oscillation – expanding and contracting – of the loading region on the rear bubble surface can be attributed to the shedding of vortices in the vicinity of the rear of the bubble. Although the vortex shedding of a particle-laden bubble in this study cannot be experimentally observed by the shadowgraph method, we however can prove such shedding based on the bubble Reynolds number, 836, in this case (initial BSL  $\sim 0.30$ ). This is because the bubble Reynolds number 836 is well above 700, at which Magnaudet and Mougin (2007) numerically reported the shedding of vortices for a bubble rising in pure water. The theoretical period of vortex shedding, according to Clift et al. (1978), can be calculated as follows:

$$T_{wakeshed} = \sqrt{\frac{\pi^2 d_B^3 \rho_L (2 + 3\gamma)}{48\sigma}} \quad (5.12)$$

where  $\gamma$  is the Euler–Mascheroni constant, 0.58.

Using Eq. (5.12), the period of oscillation is estimated to be 0.0147 s which agrees well ( $\sim 11\%$  deviation) with the experimental value of 0.0130 s obtained in the present study. Such close agreement indicates that the origins of the oscillation of instantaneous BSL may be caused by the vortex shedding. Such oscillation, however, is damped in higher BSL cases in

pure water ( $Re_B \sim 530 - 596$ ) and in all cases in the presence of surfactant ( $Re_B \sim 563 - 604$ ) because the vortex shedding is damped for Reynolds number lower than 686 (Wimmers and Fortuin, 1988).

In view of the importance of vortex in affecting the behaviour of the particle-laden bubble as described above, the separate PIV experiment was conducted to determine the vortex structure behind the bare bubble (zero initial BSL). **Fig. 5.13** illustrates the vorticity distribution around a rising bubble at different time instances for bubble of diameter  $\sim 2.70$  mm, bubble Reynolds number  $\sim 775$ . After the bubble detaches from the needle, at  $t = 25$  ms the vorticity behind the bubble is as high as  $0.04 \text{ s}^{-1}$ , with vortices remain attached to the bubble surface. The vortices develop as the bare bubble further ascends. At  $t = 50$  ms, behind the bubble the trailing counter-rotating vortex pairs, marked by the positive and negative signs of vorticity, are formed which indicates that flow separation, as schematically shown in **Fig. 5.12** occurs. Besides, at  $t = 50$  ms, vortex loops around the bubble are shed from alternate sides of the bubble within a short distance.

The observed vortex shedding is consistent with the numerical results of Magnaudet and Mougin (2007) showing that vortex shedding occurs for a rising bubble in pure water with  $Re_B$  greater than 700. At  $t = 63$  ms and  $t = 75$  ms, the shedding of vortex loops become more apparent. The shed vortices progressively lose their structures before dissipating in the downstream. These shed vortices are likely to cause periodic velocity fluctuations at the rear end of the bubble. In a particle-laden bubble case, such velocity fluctuations on the bubble surface would cause the periodic oscillation of loaded particles as shown in the initial BSL  $\sim 0.30$  case in **Fig. 5.11b**.

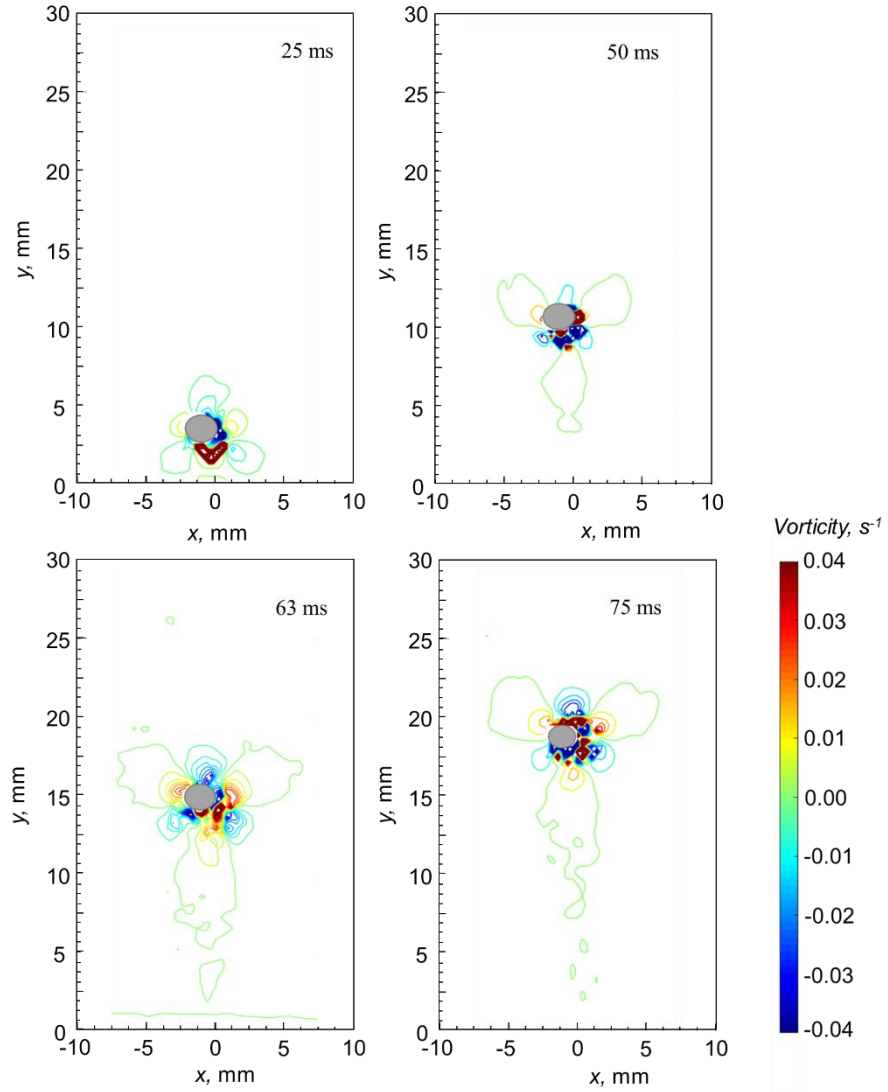


**Fig. 5.13.** Contours of vorticity around the rising bubble ( $d_B \sim 2.70$  mm,  $Re_B \sim 775$ ) in pure water at different time instances after the bubble detach from the needle at  $t = 0$  ms. Filled circle represents the marked bubble. Colour bar represents the vorticity value.

### 5.3.2. Bubble rise velocity and drag coefficient

To investigate the relationship between the terminal velocity of particle-laden bubble and the bubble surface loading, it was necessary to quantify the steady bubble surface loading. Based on the time-varying properties of the instantaneous BSL as described in **Fig. 5.11**, for higher initial bubble surface loading cases (instantaneous BSL  $\geq 0.40$  in Regime R3), the steady BSL was determined to be the average of the instantaneous BSL in Regime R3 – the steady state. For lower initial bubble surface loading cases (instantaneous BSL  $< 0.40$  in

Regime R3), the steady BSL was determined (marked in **Fig. 5.11**) as the instantaneous BSL at the end of particle detachment state (regime R2).

The instantaneous velocity of the particle-laden bubble for  $d_B \sim 2.76$  mm at different steady BSL values is presented in **Fig. 5.14**. For the steady BSL larger than the critical BSL value (0.40), the bubble velocity reached a steady value over regime R3 (steady regime) both in pure water and 20% of CMC cases. However, for the steady BSL values smaller than this critical value, bubble velocity was still noted to increase at the early stage of R3 and only reached a steady state at a late stage of R3 (expansion regime). The bubble terminal velocity was calculated by averaging over the steady velocity regime denoted by the bidirectional arrows shown in **Fig. 5.14**.

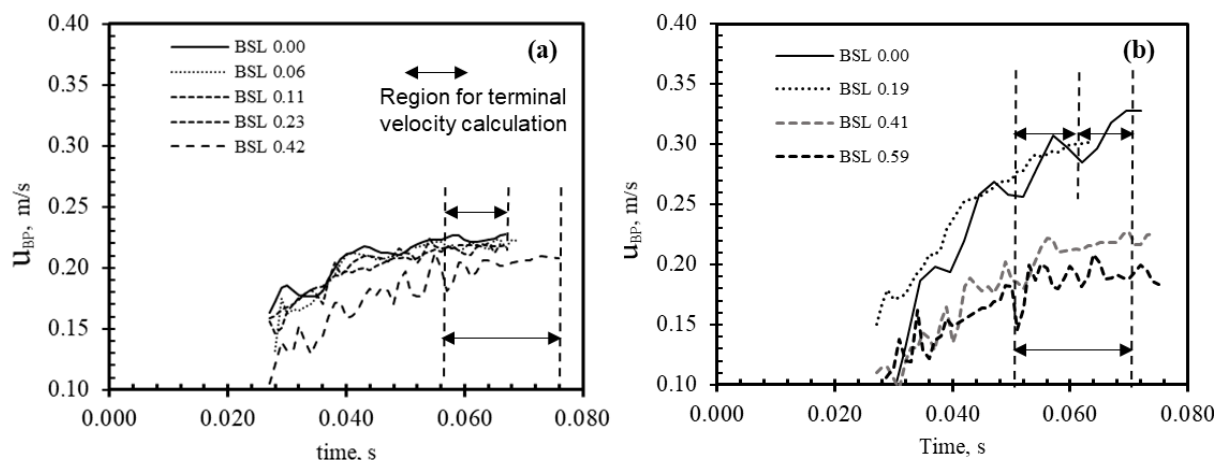


**Fig. 5.14.** Instantaneous velocity of particle-laden bubble vs different bubble surface levels in (a) 20% of CMC of SDS,  $d_B \sim 2.76$  mm; (b) pure water,  $d_B \sim 2.76$  mm.

The terminal velocity for each bubble size was compared against the reported data in literature (Clift et al., 1978) and a reasonable agreement was achieved with deviation less than 10% in all cases.

Bubbles ( $d_B \sim 2.76$  mm) examined in this Chapter reach steady terminal velocity within time period  $\sim 0.05$  s, corresponding to a distance of 0.007 m, after they are released from the needle. Such distance and time period are significantly shorter than the height of a mechanical flotation cell and its bubble residence time. This indicates that the bubble transient time in a flotation cell is negligible and bubbles quickly reach terminal velocity. It can therefore be concluded that the steady component of the terminal velocity of bubbles contributes more to

the cell performance. It however should be noted that in this Chapter the bubbles were loaded with particles before they rise from the needles. In a real flotation system, bare bubbles are injected into the cell which start loading particles as they ascend. Consequently, the bubble rise velocity still changes due to the surface loading level. Such changes in bubble velocity have been considered in modelling recovery in Chapter 6.

The trends between the steady BSLs and the terminal rise velocity of bubbles are presented in **Fig. 5.15**. It should be noted that for  $BSL \sim 0$ , the terminal rise velocity of 3.34 mm bubble is smaller than the 2.76 mm bubble in pure water. Such trend agrees with the reported data in available literature (Clift et al., 1978). This behaviour is exhibited due to increased drag. Larger bubble with diameter of 3.34 mm in pure water is in disk shape (aspect ratio  $\sim 0.3$ ), more flattened than the smaller bubble with diameter of 2.76 mm in ellipsoidal shape (aspect ratio  $\sim 0.5$ ). Disk-shape bubbles are reported to subject to larger drag coefficient (Clift et al., 1978) as is also confirmed later in this Chapter.

In general, terminal rise velocity decreases with increasing BSL in all cases. For the same bubble size case ( $d_B \sim 2.76$  mm), rise velocity is significantly lower in the presence of surfactant implying face immobility hence a no-slip condition. Interestingly, however, in this case, reduction in the rise velocity in pure water (reduction rate: 0.25 m/s/%BSL) reduced 5.4 times higher than that of the surfactant case (0.046 m/s/%BSL). Such significant difference in the reduction of velocity for the same-size bubble indicates that the bubble surface characteristics is primarily governed by adsorption of surfactant and particles have relatively smaller effect. However, as the level of bubble surface loading increases, the terminal velocity of the particle-laden bubble ( $d_B \sim 2.76$  mm) in pure water approaches to that surfactant case. The velocity profiles shown in **Fig. 5.15** can be described by a generic second order polynomial fit as follows:

$$u_{BP} = a_1 BSL^2 + b_1 BSL + c_1 \quad (5.13)$$

where the parameters  $a_1$ ,  $b_1$  and  $c_1$  are fitted constants summarized in **Table 5.2**.

Using the fitted curves, the terminal velocity for the particle-laden bubble ( $d_B \sim 2.76$  mm) intersects at  $BSL \sim 0.55$  which represents the threshold below which surfactant is the controlling factor for the terminal velocity, and above which bubble surface loading is the controlling factor.

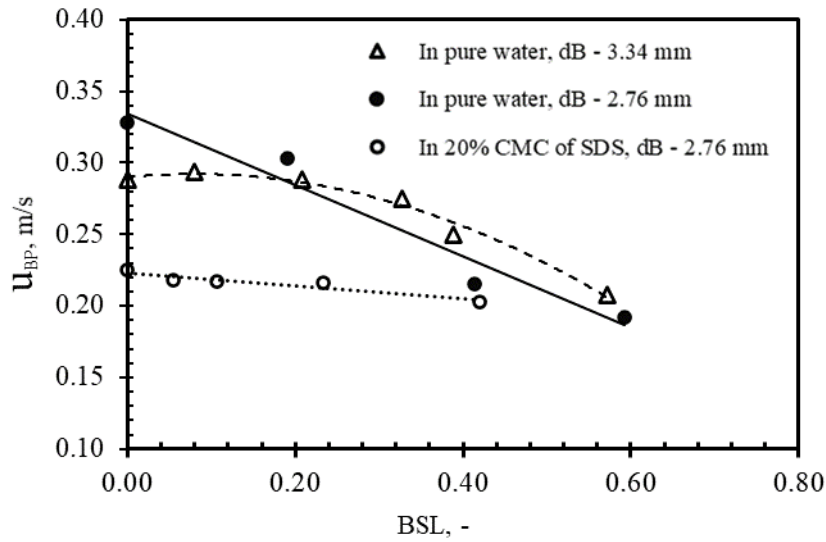


**Fig. 5.15.** Terminal velocity of particle-laden bubble as a function of bubble surface level for two bubble size in different solutions.

In contrast to the linear decline in the terminal rise velocity in the lower bubble size cases, the larger bubble size case ( $d_B \sim 3.34\text{ mm}$ ) in **Fig. 5.15** shows as a non-linear dependency on the bubble surface loading. This behaviour can be attributed to significant deformation in bubble shape due to dominance of inertia over surface tension force in large diameter cases and leading to variation in the resisting drag force. Complex interaction of trailing vortices with the monolayer of particles at bubble interface is also expected to contribute to this observed non-linearity.

**Table 5.2.** Fitting parameters in the bubble rise velocity correlation

Cases	$a_1$	$b_1$	$c_1$	$R^2$
In pure water, $d_B \sim 3.34\text{ mm}$	-0.35	0.06	0.29	0.98
In pure water, $d_B \sim 2.76\text{ mm}$	0	-0.25	0.33	0.96
In 20% of CMC of SDS, $d_B \sim 2.76\text{ mm}$	0	-0.05	0.22	0.91

The difference in the terminal rise velocity trend - polynomial for larger bubble and linear for smaller bubble can be attributed to variation in bubble shape and interaction with the trailing wakes. It is known that wake volume behind a disc shaped bubble is greater than a

spherical bubble (Clift et al., 1978) and expected to have a greater influence on the rise velocity of larger size bubbles. As shown in **Fig. 5.16a**, the bare bubble of larger diameter ( $d_B \sim 3.34$  mm) in pure water takes shape of a disc shaped or squeezed ellipsoid (aspect ratio  $\sim 0.3$ ), however, when BSL was increased to  $\sim 0.40$ , its aspect ratio increased to  $\sim 0.7$ . In contrast to the larger bubble case, smaller bubble ( $d_B \sim 2.76$  mm) exhibited relatively moderate shape modification (**Fig. 5.16b-c**) in the BSL range from 0.00 to  $\sim 0.40$  wherein aspect ratio increased from  $\sim 0.5$  to 0.9 in pure water and being steady  $\sim 0.80$  in the presence of surfactant.

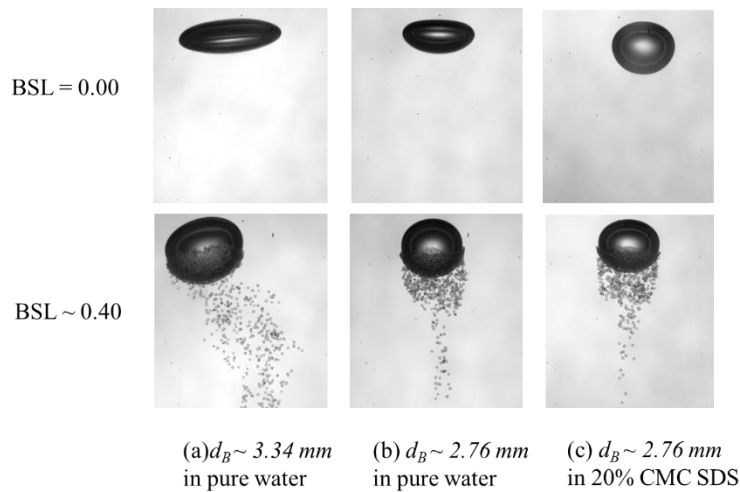


**Fig. 5.16.** Bubble shape vs surface loading in pure water and 20% of CMC of SDS surfactant

The observed reduction in the rise velocity trends presented in **Fig. 5.15** inevitably brings focus to drag coefficient and its dependency on the bubble surface loading. A force balance approach was used to determine the drag coefficient for particle-laden bubble system ( $C_{D,BP}$ ) as follows:

$$\frac{1}{6}\pi d_B^3 \rho_L g + N_p \frac{1}{6}\pi d_p^3 \rho_L g - N_p \frac{1}{6}\pi d_p^3 \rho_p g - \frac{1}{8}C_{D,BP}\rho_L u_{BP}^2 \pi d_B^2 = 0 \quad (5.14)$$

where  $\rho_L$  and  $\rho_p$  are the liquid and particle density respectively.

The bubble mass was ignored due to the significantly smaller density compared to liquid medium. In Eq. (5.14), the first term  $1/6\pi d_B^3 \rho_L g$  and the second term  $1/6N_p\pi d_p^3 \rho_L g$  denote the bubble and particle buoyancy forces respectively. The number of particles loaded to bubble,  $N_p$ , is related to the corresponding steady bubble surface loading by the following equation:

$$N_p = \frac{4\pi d_B^2 (\phi BSL)}{\pi d_p^2} \quad (5.15)$$

The packing factor  $\phi$  in Eq. (5.15) denotes the ratio of the bubble surface occupied by attached particles to the total bubble surface area, and  $\phi$  was experimentally found to be 0.8 (Gallegos-Acevedo et al., 2006; Huang et al., 2011). The third term  $1/6N_p\pi d_p^3\rho_p g$  in Eq. (5.14) denotes the particle gravity; the fourth term  $1/8C_{D,BP}\rho_L u_{BP}^2 \pi d_B^2$  denotes the drag force on the particle-laden bubble, where the terminal velocity  $u_{BP}$  from **Fig. 5.15** was used.

The resultant drag coefficient of the particle-laden bubble in Eq. (5.14) is presented in **Fig. 5.17**. It can be noted that the drag coefficient for the bubble in the presence of surfactant ( $d_B \sim 2.76$  mm) is larger than that for the bubble of similar size in pure water. Similar to the aforementioned velocity trends, the difference in drag coefficient for  $d_B \sim 2.76$  mm in both liquid conditions decreases as bubble surface loading increases. This decrease in difference is due to the increasing bubble surface rigidity caused by the loaded particles. It is also noteworthy to mention that for the drag coefficient of the two bubble sizes  $d_B \sim 2.76$  mm and  $d_B \sim 3.34$  mm in pure water, the initial difference, although being as high as  $\sim 0.20$  at zero BSL, gradually decreases until  $C_{D,BP}$  collapses onto a single line. Overall, the decreasing difference of  $C_{D,BP}$  in all three cases suggests that the bubble surface loading becomes the dominant factor in determining the drag coefficient.

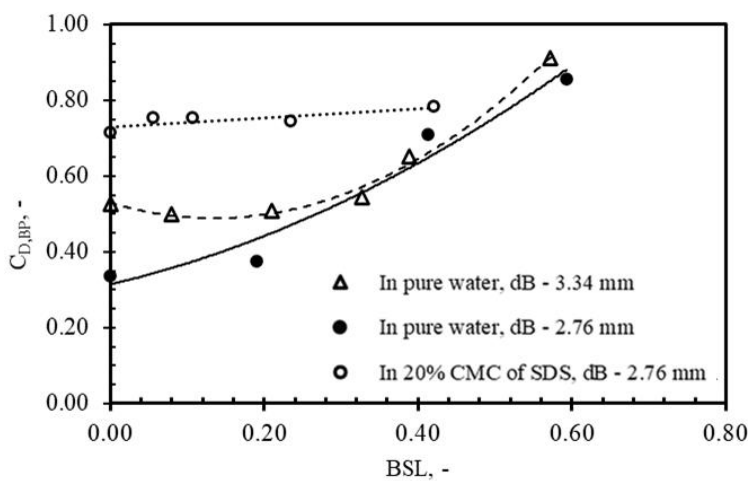


**Fig. 5.17.** The drag coefficient of particle-laden bubble as a function of bubble surface level for two bubble size in different solutions.

A correction factor  $\alpha_p$  was introduced to modify the drag coefficient in order to include the effect of bubble surface loading. With the increasing surface loading, the behaviour of a particle-laden bubble is expected approach to that of a rigid sphere. Hence, the Schiller-Naumann drag coefficient (Schiller and Naumann, 1935), originally developed for a rigid sphere, was used as the targeted drag coefficient model to be modified. This correction factor  $\alpha_p$  can be calculated as the ratio of the experimentally determined drag coefficient,  $C_{D,BP}$  (**Fig. 5.17**) to the Schiller-Naumann drag coefficient model, as shown in the following equation:

$$C_{D,BP} = \alpha_p \frac{24}{Re_{BP}} (1 + 0.15 Re_{BP}^{0.687}) \quad (5.16)$$

where the Reynolds number  $Re_{BP}$  was calculated using the diameter of bubble determined using Eq. (5.2)

$$Re_{BP} = \frac{\rho_L d_B u_{BP}}{\mu_L} \quad (5.17)$$

and the terminal velocity of the particle-laden bubble was obtained from **Fig. 5.15**.

**Fig. 5.18a** presents the correction factor  $\alpha_p$  as a function of bubble surface loading in the presence of surfactant. The bare bubble in this case, even when coated by surfactant, was still deformable with aspect ratio  $\sim 0.8$  suggesting its drag coefficient larger than that for a sphere with the same projected area. This is confirmed in **Fig. 5.18a** by showing that drag coefficient  $\alpha_p$  at zero BSL was larger than unity. Besides, the correction factor  $\alpha_p$  was found to be a constant value 1.42 (standard deviation = 2.40% of mean value), suggesting that  $\alpha_p$  is insensitive to BSL. Such invariance can be attributed to the fact that particles accumulated at interface hardly alter the immobility of the bubble surface in the presence of surfactant, hence it has limited influence on the drag force.

**Fig. 5.18b** presents the correction factor  $\alpha_p$  for the mobile surface bubble in pure water together with that reported in the available literature (Huang et, al., 2011 and Wang, et al., 2019a). The correction factor  $\alpha_p$  extrapolated at BSL  $\sim 0$  in pure water, unlike that in the presence of surfactant (**Fig. 5.18a**), was smaller than unity due to the mobile bubble surface. In addition, the correction factor in BSL  $< 0.3$  cases for larger bubble size ( $d_B \sim 3.34$  mm) in this study was not included in **Fig. 5.18b** as their low aspect ratio (AR  $\sim 0.3$ ) is not in the scope of this study. In contrast, the correction factor in BSL  $< 0.3$  cases for different millimetric size

bubbles,  $d_B \sim 1.00$  mm (Huang et al., 2011),  $d_B \sim 2.90$  mm (Wang et al., 2019a) and  $d_B \sim 2.76$  mm in this study, were included as the aspect ratio AR in these cases were larger than 0.5. In **Fig. 5.18b**, it can be seen that in all cases  $\alpha_p$  parameter collapsed onto a single linear trendline ( $R^2 \sim 0.93$ ) as follows:

$$\alpha_p = 2.41BSL + 0.29 \quad (5.18)$$

for  $d_B \leq 3.34$  mm and  $AR \geq 0.5$ .

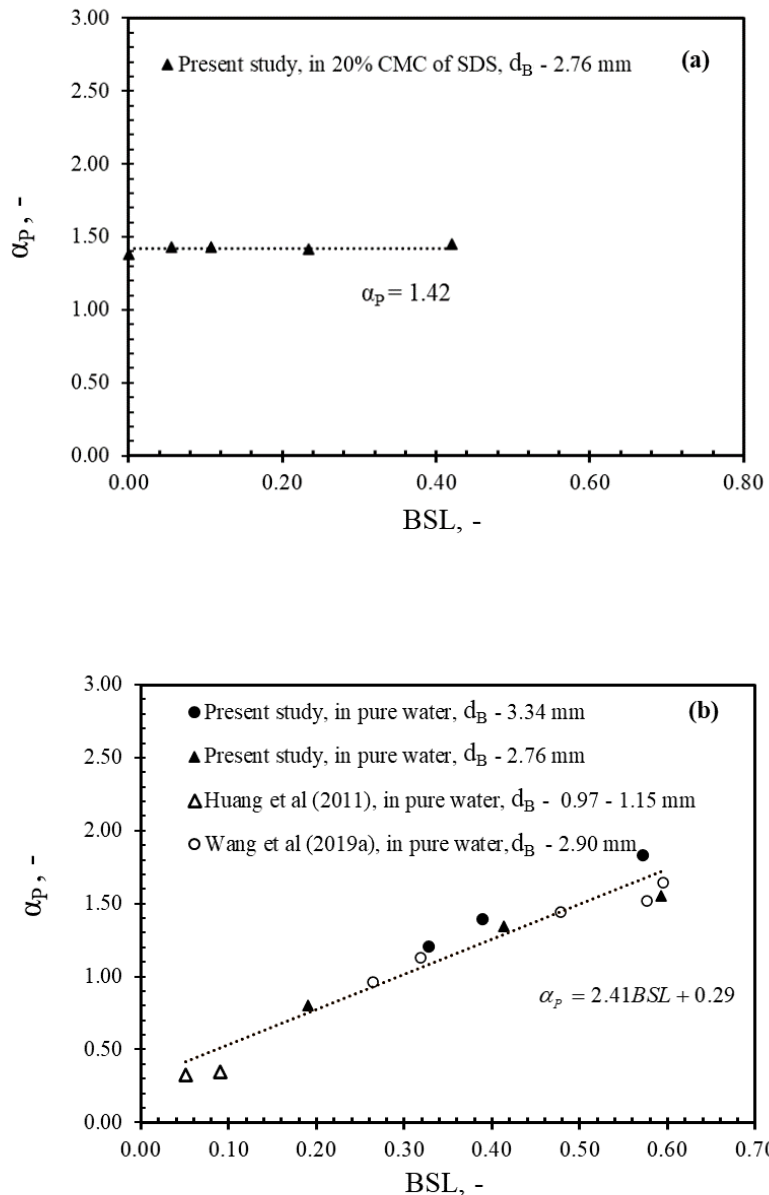


**Fig. 5.18.** The correction factor as a function of bubble surface loading level in (a) 20% of CMC of SDS,  $d_B \sim 2.76$  mm; and (b) pure water,  $d_B \sim 2.76$  mm for a range of initial bubble surface loading 0.00 – 0.94.

Unlike the insensitiveness of the correction factor  $\alpha_p$  with BSL in the presence of surfactant (**Fig. 5.18a**), the  $\alpha_p$  parameter in pure water case features a steeper slope (2.41) due to the significant improvement of bubble rigidity from the loaded particles. It can also be noted that the correction factor  $\alpha_p$  at BSL  $\sim 0.6$  in pure water is  $\sim 1.74$ , indicating that the corresponding drag coefficient of the particle-laden bubble is  $\sim 1.74$  times that of a same-sized sphere. Considering the aspect ratio is  $\sim 0.9$  for a BSL value  $\sim 0.6$  in pure water (**Fig. 5.10**), such increase in the drag coefficient value for the particle-laden bubble is attributed to the rougher surface due to the loaded particles compared to the smooth surface of a sphere.

## 5.4. Conclusion

In this chapter, rising behaviour of particle-laden bubbles with different levels of bubble surface loading (BSL) in the presence and absence of surfactant was examined experimentally.

With the increase of BSL, particle-laden bubbles became more spherical in absence of surfactant, suggesting bubble surface rigidity is governed by the monolayer coverage of particles. As the particle-laden bubble ascended, the loading region expanded towards the bubble equator due to kinetic energy from the trailing vortices. Such expansion however ceased once the bubble surface loading level exceeded the flow separation point of the bubble, which was equivalent to BSL  $\sim 0.40$ . Periodic oscillation of the instantaneous BSL in initial BSL  $\sim 0.30$  cases occurred due to the vortex shedding at high bubble Reynolds number ( $Re_B \sim 836$ ).

Terminal velocity of particle-laden bubbles of larger size ( $d_B \sim 3.34$  mm) followed a non-linear trend with BSL due to the complex shape change of bubble. Terminal velocity of particle-laden bubbles of smaller size ( $d_B \sim 2.76$  mm) however followed a linear trend and monotonously decreased with the increasing BSL. The velocity reduction was attributed to the increased drag force. In the presence of surfactant, the correction factor to drag coefficient was noted to be almost independent of BSL. It implies that particles at interface is less effective in altering the immobility of the bubble surface compared to surfactant. This was verified by the results obtained from pure water scenario wherein the correction factor from this study and literature was found to collapse onto a single curve with a slope of 2.41.

The developed correlation of the correction factor to the Schiller-Naumann drag coefficient is a step further to the reported velocity reduction by Wang et al. (2019a). In real

flotation systems, the quiescent liquid environment is a rarity, and some level of turbulence is always present. The rise velocity and bubble surface loading of a bubble-particle aggregate is affected by turbulence due to interaction with eddies and corresponding change in the assumed drag coefficient. The eddies are characterised by their respective length and time scale (Doroodchi et al., 2008; Jafari et al., 2018) which need to be determined by appropriate technique such as particle image velocimetry (PIV). Future work will examine the rise velocity and drag coefficient of particle-laden bubbles in presence of a well characterised background turbulence.

# Chapter 6. Development of a flotation recovery model

---

## 6.1. Introduction

Recovery models play an important role in assessing the flotation performance of an ore or a separation equipment. Previous studies focused on the development of empirical models by fitting the relationship between input parameters and recovery (Nguyen and Schulze, 2004; Amini et al., 2017). Amini et al. (2017) developed an empirical recovery model by incorporating the ore- or bubble-related parameters and cell-related parameters based on dimensional analysis. The model agreed well with the experimental data under a variety of hydrodynamic conditions. However, empirical models are only suitable for a particular flotation system and are limited in their general application.

Although the recovery of particles is a function of the operation condition and ore properties, the governing factors are the three sub-processes of bubble-particle interaction – collision, attachment, and detachment in flotation. Recovery is determined by the product of the individual efficiency of the three interaction sub-processes (Nguyen and Schulze, 2004). Analytical models are extensively applied in flotation systems to optimize the recovery (Jameson et al., 1977; Yoon and Mao, 1996; Bloom and Heindel, 2002, 2003; Koh and Schwarz, 2006; Koh and Smith, 2011). Koh and Schwarz (2006) embedded the analytical first-order recovery model into the 3D numerical simulation of a flotation cell. The prediction showed a fast attachment rate of particles onto bubbles and therefore identified the bubble surface area flux as the limiting factor of the recovery. Applying a similar method, Karimi et al (2014b) found that the recovery significantly increased for more hydrophobic particles. The accuracy level of these analytical recovery model predictions, however, depends on whether the models of the sub-processes can reflect on the practical flotation system.

Numerical investigations in the single-bubble flotation domain in Chapter 3 and Chapter 4 has included the effect of turbulence dispersion and solid concentration on bubble-particle collision efficiency. In reality, to overcome the limiting factor - bubble surface area flux, gas is broken into millimetric size bubbles by the turbulent shear force. In the presence of these multiple bubbles, the flow field around a bubble can be changed in the presence of

bubbles around it (Choi and Park, 2018). Furthermore, the collision behaviour between bubbles and particles may be different from that in the presence of single bubble, particularly in high gas volumetric fraction cases where multiple bubbles may be available for further collisions. Despite that multi-bubble collision behaviour provide more realistic estimation of collision efficiency, the studies in this field are rather limited.

Another important parameter in the recovery model is the bubble velocity which is affected by bubble surface loading (Bloom and Heindel, 2003; Ngo-Cong et al., 2018; Wang, et al. 2019a). Earlier studies considered the bubble velocity as the superficial gas velocity and neglected both the actual gas holdup and the bubble rise velocity (Jameson et al., 1977; Yoon and Mao, 1996). Bloom and Heindel (2003) included gas holdup into the first-order kinetic model to solve the transportation of particles between pulp and bubble surface. A general approach observed in the recovery modelling is the assumption that the slip velocity between bubble and particle remains constant based on their individual terminal settling velocity (Ngo-Cong et al., 2018). However, quantification of the terminal rising velocity of a particle-laden bubble in Chapter 5 reveals that the rising velocity decreases with the increase of bubble surface loading. It is necessary to include the velocity of particle-laden bubbles in recovery models.

Bubble loading capacity can be exhausted once the maximum surface loading is reached, as experimentally observed by Wimmers and Fortuin (1988). Heiskanen (2013) demonstrated that upon the exhausting loading level, the first-order kinetics of the recovery of particles becomes “zero-order”. Therefore, the existing recovery models do not fully capture the complexities of flotation and it is necessary to develop a recovery model which considered the temporal evolution of the rising behaviour of particle – laden bubbles in flotation.

This chapter aims at developing a novel flotation recovery model which includes a) the effect of turbulence intensity and solid concentration on collision efficiency, and b) the bubble surface loading in the recovery. This chapter is organized as follows: Section 2 presents the numerical investigation of collision efficiency in multi-bubble system; Section 3 illustrates the development of the flotation recovery model which incorporates the CFD-predicted collision efficiency in Chapter 4 and the correction factor of drag coefficient in Chapter 5. Section 4 investigates the effect of turbulence, solid concentration and bubble surface loading on recovery.

## 6.2. Multi-bubble flotation system

### 6.2.1. Modelling method

Simulations of bubble-particle interactions were performed using the finite volume CFD model comprising continuity, momentum, large eddy simulation (LES) turbulence model and discrete phase method (DPM) in Ansys Fluent (version 19.2). The relevant governing equations are summarized in **Table 3.1** in Chapter 3. **Fig. 6.1** presents the dimensions of the 3D computational domain ( $10\text{ mm} \times 10\text{ mm} \times 6\text{ mm}$ ).

The 7 bubbles configuration on an equilateral triangular plane taking benefit of symmetry would not maintain equal distance of all neighbouring bubbles from the central bubble. If the central bubble is placed on the centroid/area centre of an equilateral triangular plane, the three neighbouring bubbles located on the midpoint of adjacent sides will be equidistant, but the neighbouring bubbles at the vertex will be at a different equal distance from the central bubble. Due to this mismatch, from flow and collision perspective, there will be a bias between the inner and outer neighbours. For this reason, a 9 bubbles configuration (**Fig. 6.1b**) was adopted which keeps all the neighbouring bubbles equidistant from the central bubble eliminating any possible bias.

It should be noted that in a real mechanical flotation cell, bubbles are dispersed in turbulent flow caused by an impeller. The turbulent flow environment may result in a variety of multi-bubble configurations. This nine-bubble configuration is a preliminary step in understanding the complex collision mechanism and in obtaining a more realistic estimation of collision efficiency in a real flotation system. The configuration was chosen here to simulate the scenario in which one bubble is uniformly surrounded by other bubbles in its vicinity.

Nine spherical bubbles of radius 0.5 mm (**Fig. 6.1b**) were held stationary with their apexes 1.5 mm away from the inlet boundary. The central bubble was surrounded by a circle of eight bubbles, with each bubble separated from the neighbouring bubble by 45 degrees and from the central bubble by 2.5 mm (see **Fig. 6.1**). The circle radius, 2.5 mm, was set as the distance between the bubble centre and the wall in Chapter 3 to examine the possibility of particles colliding with the neighbouring bubble.

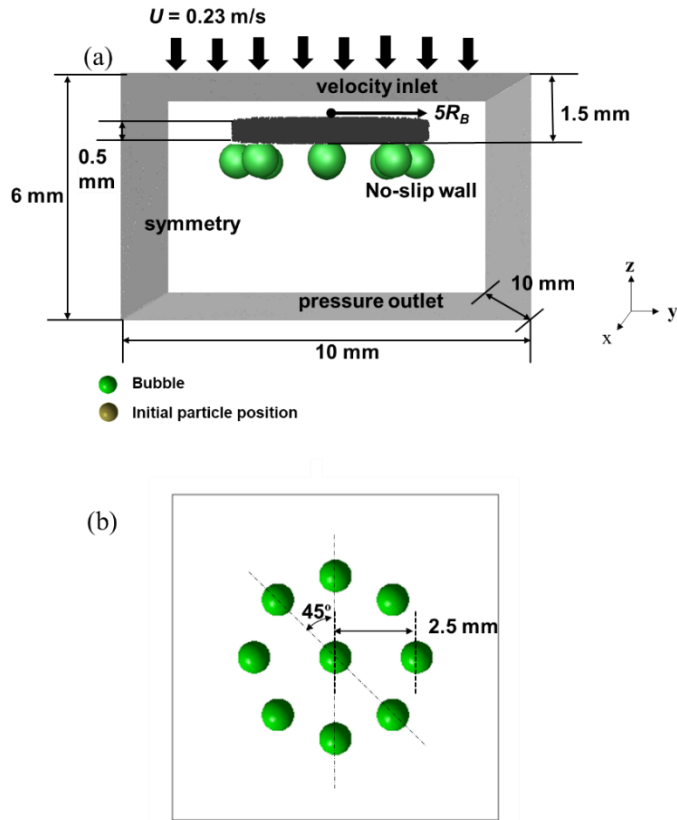


**Fig. 6.1.** (a) 3D computational domain and boundary conditions and (b) the top view of nine - bubble arrangement.

Despite of the capacity of ICEM to generate the structured mesh in single-bubble domain, it is unsuitable for the complicated circular-distribution domain of the surrounding bubbles (**Fig. 6.1**). The Mosaic poly-hexacore meshing method (Zore et al., 2019) was applied to build the 3D mesh in multi-bubble domain based on the platform Ansys Fluent Meshing (version 19.2). This meshing method generated pure hexahedral mesh in the bulk domain and layered polyhedral mesh in the boundary layer with the generalized polyhedral mesh as the transitional mesh between the two mesh types. Such combination of polyhedral and hexahedral mesh allowed the refinement of mesh around the nine bubbles to gain more accurate velocity distribution while maintaining favourable mesh quality. **Fig. 6.2** presents the sectional view of the poly-hexacore mesh at the bubble centre plane through the  $z \sim 4\text{mm}$  plane (**Fig. 6.2a**) and the  $y \sim 0 \text{ mm}$  plane (**Fig. 6.2b**) respectively. The first cell layer around each bubble was set as  $30 \mu\text{m}$  to meet the  $y^+ = 1$  requirement of the LES model and the meshing size in the bulk domain was kept at  $83 \mu\text{m}$ . The total mesh count was 1.11 million, with the maximum skewness

being 0.38, the minimum orthogonal quality 0.62, and the maximum aspect ratio 5.55 which suggested desirable mesh quality.

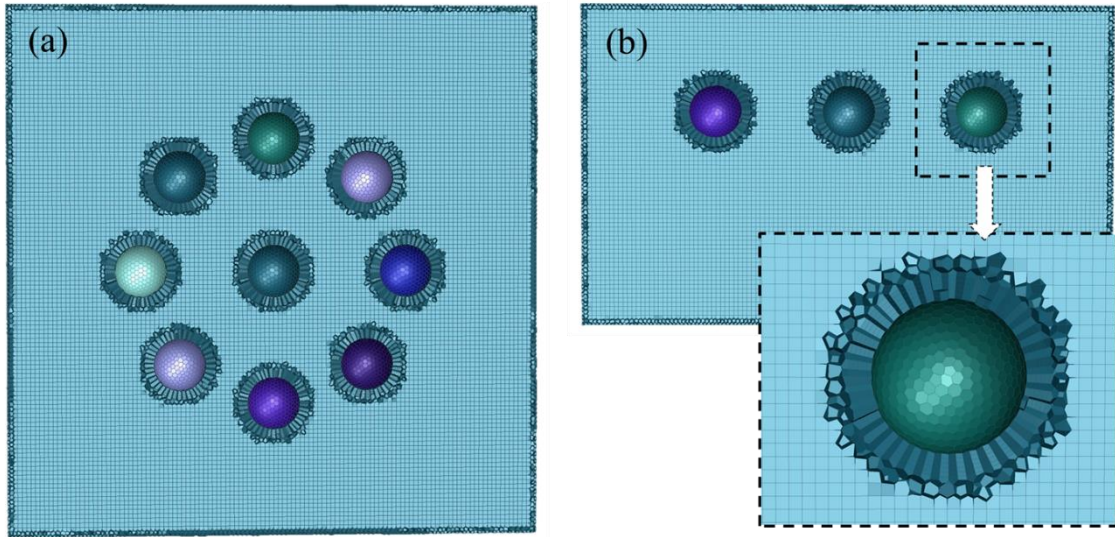


**Fig. 6.2.** Sectional view of the poly-hexacore meshing in the plane of (a)  $z \sim 4\text{mm}$  and (b) middle plane  $y \sim 0\text{ mm}$ .

The scheme of particle swarm injection in Chapter 4 was applied in the multi-bubble domain and the summary of phase parameters along with boundary conditions are listed in **Table 4.1**.

### 6.2.2. Data analysis

The bubble-particle collision efficiency in the presence of multiple bubbles is determined in this section. The method of classifying particles at  $t \sim 0\text{ s}$  described in Section 4.2 was applied to determine the total number of particles initially injected in each bin  $N_{\text{injected},i}$  ( $i = 1$  to  $N$ ,  $N = 7$ ). The collision criterion and particle tracking method in Section 4.2 was used to determine the total number of injected particles that finally collided with the bubble. The total number of collision with the central bubble  $N_{\text{collision},i,0}$ , however, was differentiated from that with the surrounding bubbles  $N_{\text{collision},i,j}$  ( $j = 1$  to  $N'$ ,  $N' = 8$ ) to examine the possibility of particles which missed the collision with the central bubble but collided with the surrounding bubbles.

As an illustration of determining  $N_{\text{collision},i,j}$ , let us consider the vertical plane through the centre of the central bubble No. 0 and the two surrounding bubbles No. 3 and No. 7, as shown in **Fig. 6.3a**. **Fig. 6.3b** presents the schematic of collision behaviour of two particles *a* and *b* which were initially injected in bin  $i^{\text{th}}$ . Particle *a* which collided with the central bubble (No. 0) is counted in the collision number  $N_{\text{collision},i,0}$ . Correspondingly, particle *b* which collided with the surrounding bubble (No. 3) is counted in the collision number  $N_{\text{collision},i,3}$ .

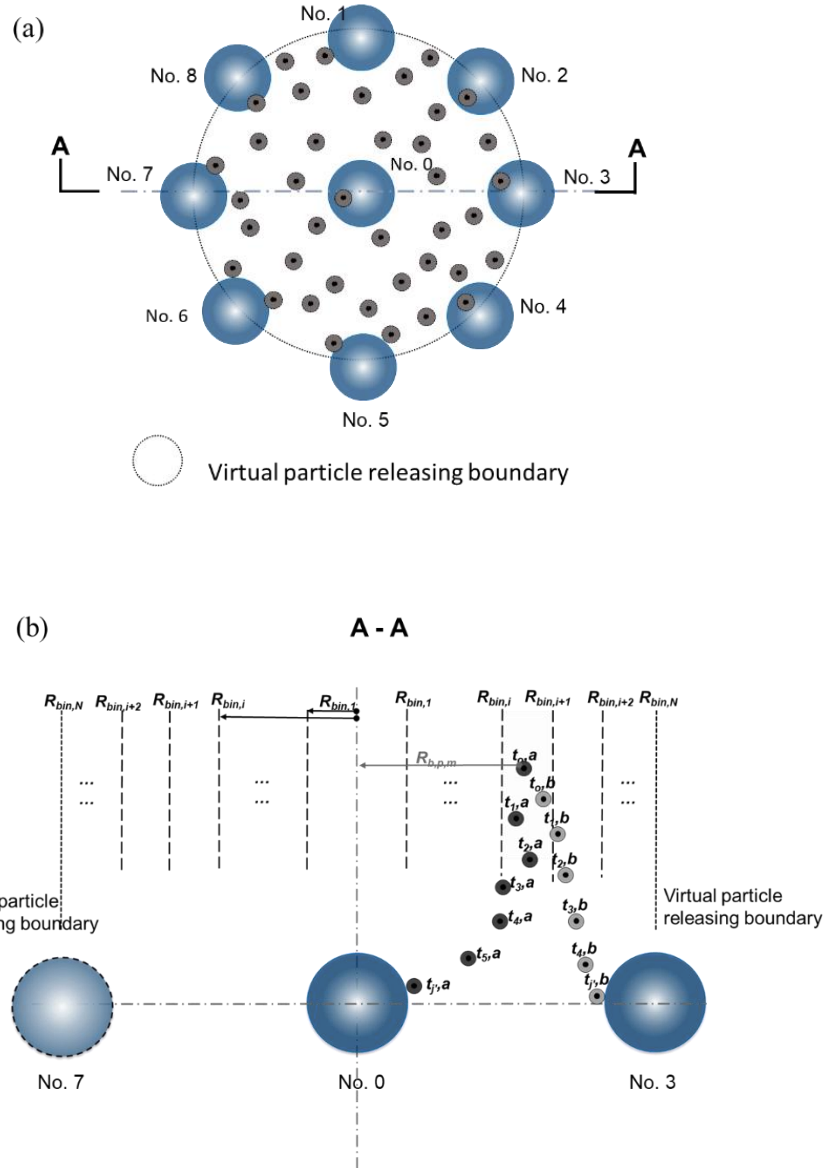


**Fig. 6.3.** Schematic of tracking individual particles from releasing bins in the presence of multiple bubbles: (a) top view; (b) side view of Plane A-A.

After the total collision number in each bin was determined, the bubble-particle collision efficiency with the central bubble in  $i^{\text{th}}$  bin was obtained as follows:

$$E_{ct,i} = \frac{N_{\text{collision},i,0}}{N_{\text{injected},i}} \quad (\text{for central bubble}) \quad (6.1)$$

The collision efficiency with the surrounding bubbles in  $i^{\text{th}}$  bin was calculated as the ratio of the total number of collided particles in this bin with the eight surrounding bubbles to the number of injected particles in this bin, using the following expression:

$$E_{ct,i} = \frac{\sum_{j=1}^{N'} N_{\text{collision},i,j}}{N_{\text{injected},i}} \quad (\text{for surrounding bubbles}) \quad (6.2)$$

### 6.2.3. Modelling results

The collision efficiency for each bin calculated using Eqs. (6.1) - (6.2) in different turbulence intensity cases ( $Ti \sim 0\%$  to  $20\%$ ) in multi-bubble domain is presented in **Fig. 6.4**. Similar to the single-bubble domain reported in Chapter 4, the collision efficiency along each bin  $E_{ct,i}$  here showed a probability distribution in all  $Ti$  cases. The maximum  $E_{ct,i}$  occurred above the centre of the central bubble and decreased with the increase of turbulence intensity. Furthermore, the normalized bin radius  $R_{bin,i} / R_B$  where the collision efficiency is zero increased from 0.39 to 0.47 as  $Ti$  increased from 4% to 20%, suggesting the horizontal dispersion of particles is strengthened in high turbulence intensities. Moreover, it is apparent in **Fig. 6.4** that in all  $Ti$  cases the particles injected in the same bin collide only with the central bubble or the surrounding bubbles. Such collision behaviour indicated that for  $Ti \leq 20\%$ , the particles released at a height of  $R_B$  above a bubble still loosely follows the mean flow around the bubble and cannot obtain enough kinetic energy from the surrounding eddies to migrate to the surface of a neighbouring bubble.

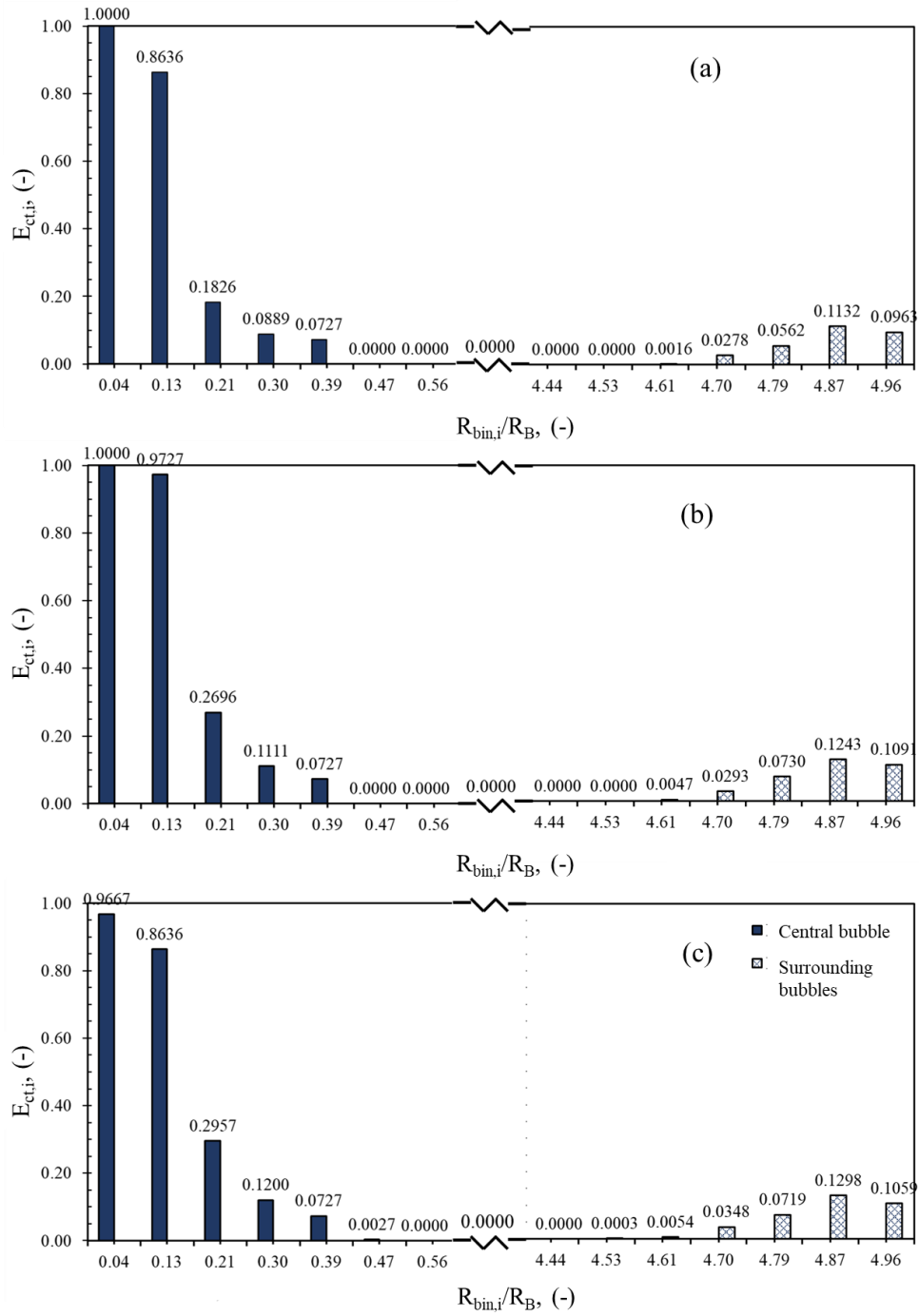


**Fig. 6.4.** Collision efficiency with the central bubble and the surrounding bubbles vs  $R_{bin,i}/R_B$  ratio for particle injecting concentration  $C_{P,i} \sim 3.08\%$  at (a)  $Ti \sim 0\%$ ; (b)  $Ti \sim 4\%$ ; (c)  $Ti \sim 20\%$ .

It is of interest to compare the overall collision efficiency of particles and the central bubble  $E_{ct}$  in the presence of single and multiple bubbles. The  $E_{ct}$  in the presence of multiple bubbles can be calculated by applying the “normalized equivalent critical radius”  $K_1$  proposed in Chapter 4, as shown in the following equation:

$$E_{ct} \equiv K_1^2 \quad (6.3)$$

where the parameter  $K_1$  was calculated by equating the number of possible collisions in the grazing volume above the central bubble to the sum of the number of actual collisions occurred due to release of particles from the virtual bins as follows:

$$R_B \pi (K_1 R_B)^2 E_{co} = \sum_{i=2}^N (R_B \pi R_{bin,i}^2 E_{ct,i} + R_B \pi (R_{bin,i}^2 - R_{bin,i-1}^2) E_{ct,i}) \quad (i > 1) \quad (6.4)$$

where the collision efficiency along the bin radius  $E_{ct,i}$  was calculated using Eq. (6.1).

The overall collision efficiency  $E_{ct}$  calculated in Eq. (6.3) under different turbulence intensities and solid concentrations in multi-bubble domain is presented in **Fig. 6.5** together with that in single-bubble domain. It can be noted that in both cases, the overall collision efficiency  $E_{ct,i}$  decreased with solid concentration due to the increased particle lateral dispersion, resulting in more particles diverted from the bubble. However, as bubble numbers increased, two different phenomena can be observed. Firstly,  $E_{ct,i}$  in multi-bubble cases (**Fig. 6.5b**) generally followed a monotonically increasing trend with the turbulence intensity  $Ti$ , indicating that the optimal  $Ti$  level for collision efficiency occurs at  $Ti \sim 20\%$ . Such optimal  $Ti$  level contradicted in single-bubble domain which occurs at  $Ti \sim 7\%$  (**Fig. 6.5a**). Secondly, the overall collision efficiency  $E_{ct,i}$  for the central bubble increased with the number of bubbles surrounding it. For example, in the case of injecting concentration  $C_{P,i} \sim 3.08\%$  in  $Ti \sim 20\%$ ,  $E_{ct,i}$  increased by  $\sim 63\%$  in the multi-bubble cases compared to that the single bubble case.

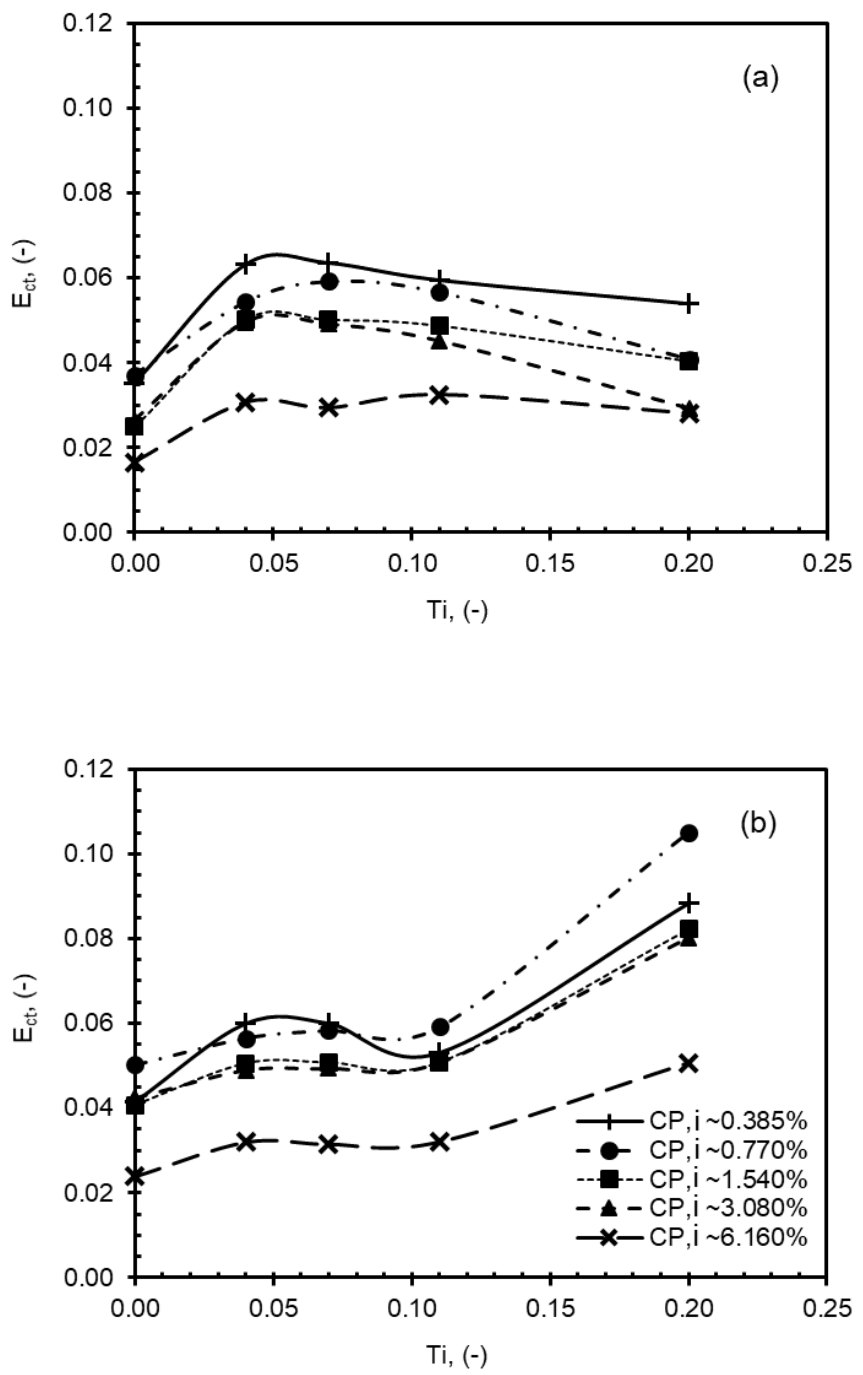


**Fig. 6.5.** Comparison of collision efficiency in (a) single-bubble system and (b) multi-bubble system for different turbulence intensities and solid concentration.

With the increase of surrounding bubble numbers, these two differences in overall collision efficiency can be attributed to the attenuated fluctuating flow around the central bubble, as shown in **Fig. 6.6** at  $Ti \sim 20\%$ . In multi-bubble domain, the instantaneous velocity

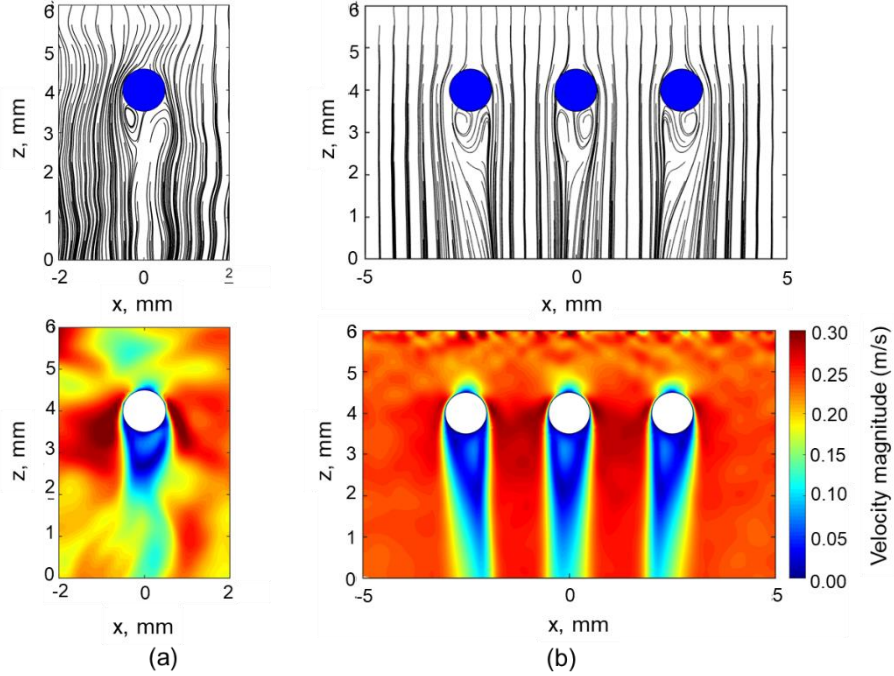


**Fig. 6.6.** Comparison of flow field in (a) single-bubble domain and (b) multi-bubble domain at  $Ti \sim 20\%$  (Up: instantaneous velocity field; Down: flow streamline).

field in the upstream of the bubbles was more evenly distributed than that in single-bubble domain which caused less chaotic flow streamline above the central bubble. Consequently, the chaotic lateral dispersion of particles above the central bubble observed in single-bubble case at high turbulence intensity ( $Ti \sim 20\%$ ) reduced in muti-bubble case, suggesting less particles were diverted away from the central bubble which resulted in higher collision efficiency.

### 6.3. Flotation recovery model

Recovery parameter is defined as a ratio of the recovered number of particles to the initial number of particles present in the system. For a semi-batch flotation cell, this parameter is calculated as the ratio of the number of particles  $N_p$  at a time instant  $t$  to the initial number of particles present in the flotation cell. Following a first-order kinetics, removal rate of particles from a flotation system can be written as:

$$\frac{dN_p}{dt} = -kN_p \quad (6.5)$$

where  $k$  is the flotation rate constant, which is a function of individual efficiency of the three interaction sub-processes, gas holdup and bubble velocity.

Admittedly, in real flotation system, a rising bubble encounters different solid concentrations at different locations. However, for the sake of simplifying this complex interaction process, it was assumed that solid and gas volume concentrations in the flotation system are uniformly distributed and all bubbles interact with the surrounding particles in a similar manner. i.e. at any instant bubbles are in contact with the same pulp phase concentration and they have the same collision efficiency,  $E_C$ .

In a real system, a bubble continuously moves through the pulp phase as it rises to the froth zone at the cell top implying that a bubble is constantly in contact with the new pulp material. It is therefore assumed that a virtual “volume” of pulp is associated with every bubble during its residence time in the system. Within this pulp volume, solid concentration changes with time as particles are attached onto the surface of the bubble. **Fig. 6.7** presents a schematic of the bubble-pulp interaction process.

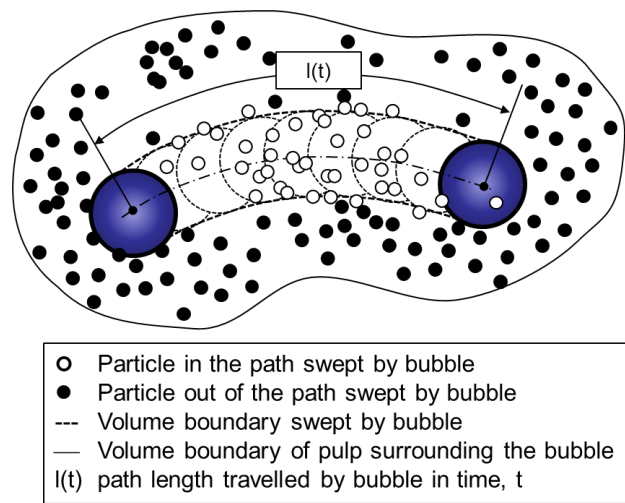


**Fig. 6.7.** Schematic of bubble-particle interaction process in the pulp phase.

For each gas bubble with radius,  $R_B$ , the total volume,  $V_T$ , occupied by the gas bubble,  $V_G$ , and associated pulp,  $V_{pulp}$ , is given by:

$$V_T = V_G + V_{pulp} \quad (6.6)$$

For a given gas volume fraction,  $\epsilon_G$ , then:

$$V_G = \epsilon_G V_T \quad (6.7)$$

$$V_{pulp} = \epsilon_{pulp} V_T = (1 - \epsilon_G) V_T \quad (6.8)$$

where:

$$\epsilon_G + \epsilon_{pulp} = 1 \quad (6.9)$$

For a single bubble, the gas volume is:

$$V_{sB,G} = (4/3)\pi R_B^3 \quad (6.10)$$

and the corresponding pulp volume surrounding (associated with) that bubble is:

$$V_{sB,pulp} = V_{sB,G} ((1 - \epsilon_G)/\epsilon_G) \quad (6.11)$$

Within the pulp volume, the following relationships apply:

$$V_{sB,pulp} = V_S + V_L \quad (6.12)$$

$$V_L = \epsilon_L V_{sB,pulp} \quad (6.13)$$

$$V_S = \epsilon_S V_{sB,pulp} = (1 - \epsilon_L) V_{sB,pulp} \quad (6.14)$$

where:

$$\epsilon_L + \epsilon_S = 1 \quad (6.15)$$

where  $\epsilon_S$  and  $\epsilon_L$  are the volume fractions of the solids and liquid, respectively, within the pulp phase.

Within the pulp volume associated with the single bubble, the volume of solids,  $V_{sB,S}$ , is given as:

$$V_{sB,S} = V_{sB,pulp} \in_s = V_{sB,G} \left( \in_{pulp} / \in_G \right) \in_s \quad (6.16)$$

The corresponding number of particles,  $n_{sB,S}$ , with radius,  $R_P$ , and volume,  $V_{sP}$ , in the pulp is:

$$n_{sB,S} = V_{sB,S} / V_{sP} \quad (6.17)$$

where

$$V_{sP} = (4/3)\pi R_P^3 \quad (6.18)$$

As the bubble moves within the pulp, it makes physical contacts with the particles leading to attachment. The recovery of particles,  $R(T)$ , after time,  $T$ , is given by:

$$R(T) = N_{P,recovered}(T) / N_P(0) \quad (6.19)$$

where  $N_{P,recovered}(T)$  is the total number of particles recovered after time,  $T$ , and  $N_P(0)$  is the initial number of particles in the pulp volume associated with each (single) bubble.

The number of recovered particles at any given time step,  $\Delta t$ , is equal to the number of particles encountered by the bubble during that time,  $N_{P,encountered}$ , multiplied by the collision efficiency,  $E_C$ , attachment efficiency,  $E_A$ , and detachment efficiency,  $E_D$  i.e.:

$$N_{P,recovered}(\Delta t) = N_{P,encountered}(\Delta t) E_C E_A (1 - E_D) \quad (6.20)$$

The particles encountered by the bubble during time interval,  $\Delta t$ , are those within the swept volume,  $A_{cross,B}(\Delta t)$ , of the moving bubble as it travels with (slip) velocity relative to the pulp,  $U_B(\Delta t)$ . If the pulp has an average number concentration of particles,  $C_P(\Delta t)$ , then:

$$N_{P,encountered}(\Delta t) = V_{cross,B}(\Delta t) C_P(\Delta t) = A_{cross,B} U_B(\Delta t) \Delta t C_P(\Delta t) \quad (6.21)$$

where  $A_{cross,B}$  is the cross-sectional area of the moving bubble, given by:

$$A_{cross,B} = \pi R_B^2 \quad (6.22)$$

Eqs. (6.19) - (6.22) can be combined and integrated with respect to time to obtain the cumulative recovery of particles for a bubble-pulp contact time,  $T$  as:

$$R(T) = \int_0^T \left( \frac{A_{cross,B} U_B(t) C_P(t) E_C E_A (1-E_D)}{N_P(0)} \right) dt \quad (6.23)$$

The average number concentration of particles remaining at time,  $t$ , is equal to:

$$C_P(t) = \frac{N_P(0)}{V_{sB,pulp}} [1 - R(t)] \quad (6.24)$$

Hence:

$$R(T) = \frac{A_{cross,B}}{V_{sB,pulp}} \int_0^T (U_B(t) E_C E_A (1-E_D)) [1 - R(t)] dt \quad (6.25)$$

Substituting for  $A_{cross,B}$  (Eq. (6.22)) and  $V_{sB,pulp}$  (Eqs. (6.10) - (6.11)), gives:

$$R(T) = \int_0^T \left( \frac{3U_B(t) E_C E_A (1-E_D)}{4R_B(t)} \right) \left( \frac{\epsilon_G}{1-\epsilon_G} \right) [1 - R(t)] dt \quad (6.26)$$

Eq. (6.26) can be integrated to obtain the cumulative particle recovery for a given time,  $T$ . All operating variables, such as  $R_B$ ,  $U_B$ ,  $E_C$ , etc., are shown within the integral as each of these terms can possibly change with time. For example, the bubble radius,  $R_B$ , will change due to the change in hydrostatic pressure as it rises through the pulp. This will also cause a change in the bubble velocity. Similarly, collision and detachment efficiencies might change with time due to changes in local turbulence levels (energy dissipation rates) within the pulp. For a simplified scenario, however, if all these terms are assumed to remain constant throughout the recovery time period, Eq. (6.26) can be re-written as:

$$R(T) = k \int_0^T [1 - R(t)] dt \quad (6.27)$$

The analytical solution to Eq. (6.27) is:

$$R(t) = 1 - e^{-kt} \quad (6.28)$$

where  $k$  is given by:

$$k = \left( \frac{3U_B}{4R_B} \right) \left( \frac{\epsilon_G}{1-\epsilon_G} \right) E_C E_A (1-E_D) \quad (6.29)$$

which is equivalent to the first order rate constant in Eq. (6.5).

Eq. (6.26) can be solved numerically to obtain flotation recovery,  $R(T)$  for a given gas volume fraction,  $\epsilon_G$ , pulp solids (number) concentration,  $N_P(0)$ , and bubble-pulp contact time,  $T$ ; provided suitable expressions for collision,  $E_C$ , attachment,  $E_A$ , and detachment,  $E_D$ , efficiencies, and bubble-pulp slip velocity,  $U_B$ , are known. Suitable expressions for each of these terms are described below.

### Bubble rise velocity

In chapter 5, the reduction in terminal velocity of particle-laden bubble due to the increased drag force was observed and a correction factor to Schiller-Naumann drag coefficient model was proposed accounting for the bubble surface loading in pure water. The correction factor  $\alpha_P$  can be calculated by the following expression:

$$C_{D,BP} = \alpha_P \frac{24}{Re_{BP}} (1 + 0.15 Re_{BP}^{0.687}) \quad (6.30)$$

In pure water, the  $\alpha_P$  parameter can be calculated as follows:

$$\alpha_P = 2.41BSL + 0.29 \quad (6.31)$$

for bubble diameter  $d_B \leq 3.34$  mm and aspect ratio  $AR \geq 0.5$ . The bubble surface loading (BSL) in Eq. (6.31) takes the following form (Huang et al., 2011):

$$BSL = \frac{N_{P,recovered}(T) \pi R_p^2}{4\pi R_B^2 \phi} \quad (6.32)$$

The rise velocity of a bubble with a given surface loading can be determined from the following expression:

$$U_B(t) = \left( \frac{8R_B g}{3C_{D,BP}} \left( 1 - \frac{\rho_{BP}}{\rho_{pulp}} \right) \right)^{1/2} \quad (6.33)$$

where  $\rho_{BP}$  is the density of the particle-laden bubble and  $\rho_{pulp}$  is the density of the pulp.

It is noteworthy to mention that the bubble surface cannot be fully covered by particles (Bradshaw and O'Connor, 1996; Koh and Schwarz, 2008). Hence, a maximum bubble surface loading  $BSL_{max}$  was considered which set the upper limit for  $BSL$  in Eq. (6.31). Once  $BSL_{max}$  is reached, bubble would not collect anymore particles which leads to a constant bubble velocity and  $N_{P,recovered}(T)$  in Eq. (6.32) remains unchanged. Due to lack of a physical model for  $BSL_{max}$  (Eskanlou et al., 2019), its value in this study was determined by validating bubble velocity against the experimental data reported by Huang et al. (2011).

### Attachment efficiency

According to Yoon and Luttrell (1989), particle attachment (adhesion) efficiency is given as:

$$E_A = \sin^2 \left( 2 \tan^{-1} \left[ \exp \left( \frac{-\left( 45 + 8 \text{Re}_B^{0.72} \right) U_B t_{ind}}{30 R_B (R_B / R_P + 1)} \right) \right] \right) \quad (6.34)$$

where the induction time,  $t_{ind}$ , is a function of the particle radius and contact angle,  $\theta_{con}$  (Koh and Schwarz, 2006) is given as i.e.:

$$t_{ind} = \frac{75}{\theta_{con}} (2R_P)^{0.6} \quad (6.35)$$

### Detachment efficiency

According to Wang et al. (2016), the following expression for particle detachment efficiency can be applied:

$$E_D = \exp \left( 1 - \left[ \frac{3\sigma(1-\cos\theta)}{4R_P^2(g+b_m)(\rho_p - \rho_L)} \right] \right) \quad (6.36)$$

where  $b_m$  is the “machine acceleration”, and according to Schulze (1982) related to the specific energy dissipation rate,  $\varepsilon$ , by the following relationship:

$$b_m = 1.9\varepsilon^{2/3} / 1.26(R_B + R_P)^{1/3} \quad (6.37)$$

### Collision efficiency

The turbulent collision efficiency investigated in single-bubble flotation system in Chapter 4 and in multi-bubble flotation system in this chapter using Eqs. (6.3) - (6.4) were used in predicting the recovery in the following sections.

## 6.4. Results and discussion

### 6.4.1. Bubble surface loading and predicted recovery in a batch flotation cell

The maximum bubble surface loading  $BSL_{max}$  was determined by validating the bubble velocity against the experimental data of Huang et al. (2011) involving a single bubble rising in a quiescent liquid. The operating conditions used in the validating procedure are presented in **Table 6.1** where the normalized equivalent critical radius  $K_l$  was determined in Chapter 4. In the absence of any reported energy dissipation rate  $\varepsilon$ , the CFD model predicted  $\varepsilon$  was used for the zero-turbulence intensity case. The bubble density  $\rho_B$  was initially set to  $1.18 \text{ kg/m}^3$  which then increased with time as particles attached to a bubble, thus forming an aggregate. The simulations were carried out for a total time of  $1.27\text{s}$  using a time step equal to  $dt = 0.01 \text{ s}$ . Upon completion of each time step, the physical properties i.e. the density of the bubble-particle aggregate, the pulp dynamic viscosity and density were updated.

**Table 6.1.** Physical properties and operating conditions used in the model prediction

Operating parameters	Values
Particle radius $R_P$ ( $\mu\text{m}$ )	12.5
Particle density $\rho_p$ ( $\text{kg}/\text{m}^3$ )	2363
Contact angle $\theta_{\text{con}}$ (degree)	47
Bubble radius $R_B$ (mm)	0.535
Bubble density $\rho_B$ ( $\text{kg}/\text{m}^3$ )	1.18
Liquid density $\rho_L$ ( $\text{kg}/\text{m}^3$ )	1000
Surface tension $\sigma$ (N/m)	0.072
Solid volume concentration $\epsilon_s$	0.69%
Normalized equivalent critical radius $K_l$	0.27
Energy dissipation rate $\varepsilon$ ( $\text{m}^2\text{s}^{-3}$ )	0.0225

The bubble velocity  $U_B$  can be calculated as follows. Initially at  $t = t(0)$ , the number of particle recovered  $N_{P,\text{recovered}}(0)$  was set to 0, hence both the recovery  $R(0)$  and the bubble surface loading  $BSL(0)$  were zero. Bubble velocity  $U_B(0)$  was then calculated from the zero-BSL. It is noted that here the bubble velocity was related to the BSL through the Sadhal and Johnson (1983) model of drag coefficient that Huang et al. (2011) applied to find the maximum BSL in Huang's study. Using Eq. (6.26), the flotation rate constant  $k(0)$  was calculated from bubble velocity  $U_B(0)$ . On finishing a time step, the recovery  $R(t)$  was updated to  $R(0) + k(0)[1 - R(0)]dt$ . The number of particles recovered  $N_{P,\text{recovered}}(dt)$  was calculated using  $R(dt)$  according to Eq. (6.19). Next, bubble surface loading  $BSL(dt)$  in Eq. (6.32) was updated using  $N_{P,\text{recovered}}(dt)$ . Bubble velocity  $U_B(dt)$  was then recomputed from the  $BSL(dt)$  using Eq. (6.33).

The bubble surface loading,  $BSL$  was monitored after each time step and compared with an assumed  $BSL_{\max}$ . Once the computed BSL reached this  $BSL_{\max}$  limit, no further bubble loading was permitted hence the recovery  $R(t)$  also reached a plateau. A range of  $BSL_{\max}$  was

explored to fit the predicted bubble velocity  $U_B$  to the experimental data of Huang et al. (2011). The best fit resulted in  $BSL_{max} \sim 0.142$  (root-mean-square deviation, RMSD  $\sim 0.037$ ) which reasonably agreed with the experimentally determined maximum bubble surface loading of 0.137 (Bradshaw and O'Connor, 1996) and computationally determined value of 0.20 (Koh and Schwarz, 2008).

**Fig. 6.8** compares the predicted bubble rise velocity  $U_B$ , bubble surface loading,  $BSL$  and distance travelled by bubble  $H_{B,trav}$  with experimental data of Huang et al. (2011). According to the predicted temporal evolution of bubble surface loading, two distinct regimes were observed – a loading regime in early period (0 to 0.1 s) during which  $BSL_{max}$  was reached and a saturated regime wherein the surface loading remained unchanged at  $BSL_{max}$ . It was noted that the predicted loading regime was slightly longer than the experimental observation (0 to 0.04 s). The observed discrepancy in the reported period duration may be attributed to an obvious difficulty of keeping the bubble surface clean of particles in the experiment before a rising bubble makes a contact with the pulp phase (Huang et al. 2011).

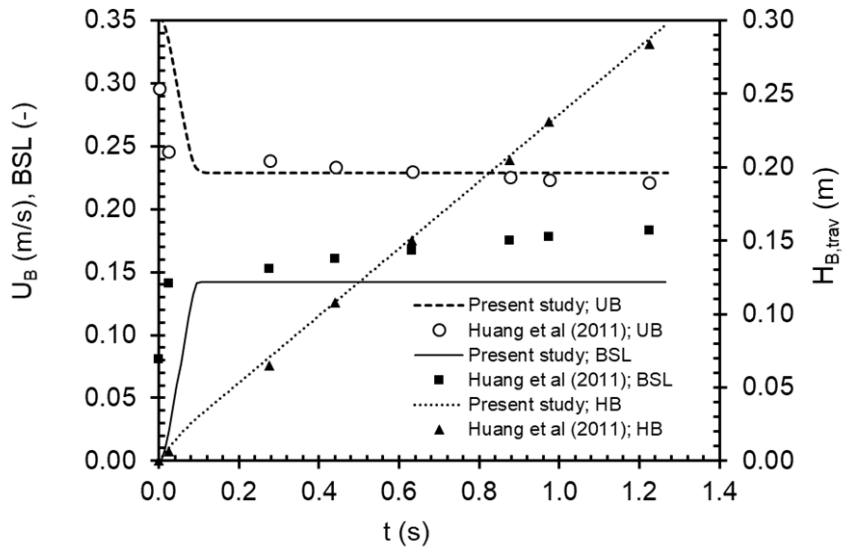


**Fig. 6.8.** Comparison of bubble solid loading,  $BSL$  and bubble rise velocity,  $U_B$  with Huang et al (2011) for solid concentration  $\epsilon_s \sim 0.69\%$ . Here  $H_{B,trav}$  represents the distance travelled by the bubble over time.

It was of interest to investigate the effect of solid concentration in pulp phase on the bubble surface loading which is essential to predict recovery (Chegeni et al., 2016; Sarkar et al., 2011). This effect was studied in the solid concentration range from 0.22% to 1.83% in the

absence of any turbulence ( $Ti \sim 0\%$ ). Phase properties used in the simulations are summarized in **Table 6.2**. The overall collision efficiency determined in **Fig. 6.5a** for single-bubble domain and **Fig. 6.5b** for multi-bubble domain were used in the recovery model Eqs. (6.5) - (6.37) respectively to determine the effect of surrounding bubbles on the bubble loading behaviour. Assuming a negligible effect of the bubble surface loading on collision behaviour,  $K_l$  was assumed to remain constant irrespective of the bubble surface loading.

**Table 6.2.** Input phase parameters of the recovery model

Phase	Properties	Value
Liquid	Density $\rho_L$ (kg/m <sup>3</sup> )	1000
	Dynamic viscosity $\mu_L$ (Pa.s)	0.00089
	Surface tension $\sigma$ (N/m)	0.065
	Turbulent energy dissipation rate $\varepsilon$ (m <sup>2</sup> /s <sup>3</sup> )	0.0225 ( $\varepsilon$ calculated from simulation)
Gas	Bubble radius $R_B$ (mm)	0.5
	Bubble density $\rho_B$ (kg/m <sup>3</sup> )	1.18
	Gas volume fraction $\epsilon_G$ (-)	0.1 (Araya et al., 2014; Azgomi et al., 2007)
Solid	Particle radius $R_P$ (μm)	15
	Particle density $\rho_P$ (kg/m <sup>3</sup> )	1200
	Particle contact angle $\theta_{con}$ (degree)	80 (Yang et al., 2018)

**Fig. 6.9a** illustrates the temporal evolution of the predicted bubble surface loading in conjunction with the bubble velocity for different solid concentrations. In single-bubble (SB) cases, the loading regime for the  $\epsilon_s \sim 1.83\%$  case had a steeper slope compared with the loading behaviour for the other two solid concentration cases ( $\epsilon_s \sim 0.22\%$  and  $0.44\%$ ), resulting in a much shorter time span ( $t \sim 0.0$  to  $0.1$ s). The steeper slope is attributed to the occurrence of a larger number of bubble-particle collisions leading to a faster collection of particles. As a result, the bubble velocity reduced to  $\sim 0.15$  m/s at a rate of approximately  $1.0$  m/s<sup>2</sup> and the maximum loading was achieved  $\sim 1.05$  s earlier than in the most dilute pulp system ( $\epsilon_s \sim 0.22\%$ ). It was noted that for a given number of bubbles (i.e. a fixed air flow rate), recovery in a dense pulp system was predicted to be less compared to a relatively dilute pulp system.

A further analysis of recovery for different solid concentrations is presented in **Fig. 6.9b**. The predicted recovery in the saturated regime decreased from  $\sim 0.70$  to  $0.10$  as the solid concentration increased from  $0.22\%$  to  $1.83\%$ . This inverse correlation indicates that for a dense pulp system, flotation cells should be operated at higher air flow rate to compensate for quick exhaustion of the loading capability of bubbles. This result agrees with the earlier

observation of Sarkar et al. (2011) which showed that an increase in the air flow rate led to declined surface loading and hence improved recovery.

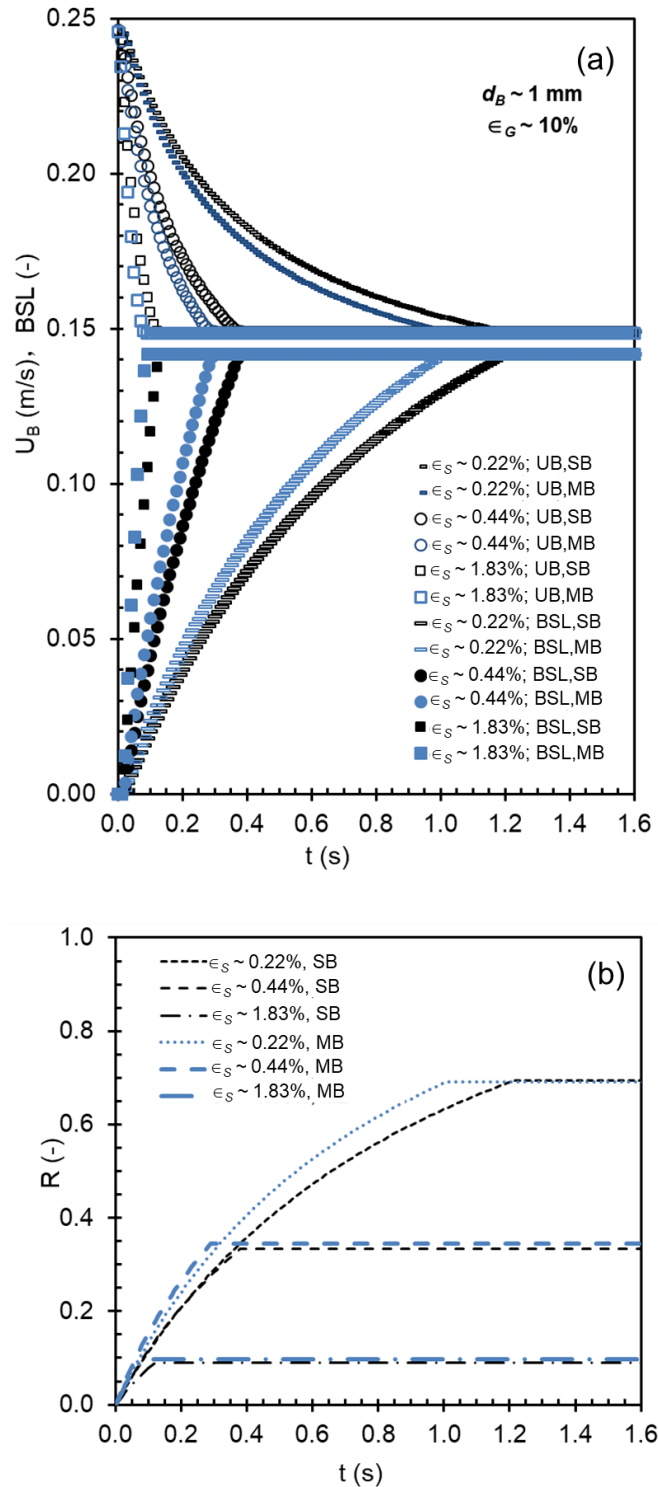


**Fig. 6.9.** Temporal evolution of a) Bubble velocity  $U_B$  and bubble surface loading  $BSL$ ; and b) Recovery  $R$ , calculated from the collision efficiency in both single-bubble (SB) and multi-bubble (MB) domain, for three different solid concentrations (at  $\epsilon_G \sim 10\%$ ,  $Ti \sim 0\%$ ).

In multi-bubble (MB) case, it is apparent that as bubble were loaded with more particles over time the reduction of bubble velocity was larger than that in single-bubble case for all concentration cases. This larger reduction rate can be attributed to more quickly exhausted bubble surface loading (**Fig. 6.9a**) which resulted from larger collision efficiency (see **Fig. 6.5b**). For example, for the  $\epsilon_s \sim 1.83\%$  case, the bubble surface loading reached  $BSL_{max}$  approximately 0.15 s faster than the SB case. However, the difference in the period of the loading regime between the single- and multi-bubble cases, decreased with the increase of solid concentration. This indicates that in MB case recovery prediction in dilute flotation system is more sensitive to the collision efficiency. Indeed, **Fig. 6.9b** showed that compared with  $\epsilon_s \sim 1.83\%$ , the recovery for the lowest  $\epsilon_s \sim 0.22\%$  case for the multi-bubble case was significantly higher than the single-bubble case.

The effect of turbulence intensity on temporal evolution of bubble rising velocity and bubble surface loading for multi-bubble cases ( $\epsilon_s \sim 0.44\%$ ,  $Ti \sim 0\%$  to 20%) is presented in **Fig. 6.10a**. It is apparent that the loading period was longest in  $Ti \sim 0\%$  case ( $\sim 0.30$  s) and shortest in  $Ti \sim 20\%$  case ( $\sim 0.15$  s), indicating that particles can be loaded onto bubble faster in flow of higher turbulence intensity level. **Fig. 6.10b** also reveals the increasing trend of recovery with turbulence intensity which can be attributed to increasing collision efficiency with  $Ti$  as shown in **Fig. 6.5b**.

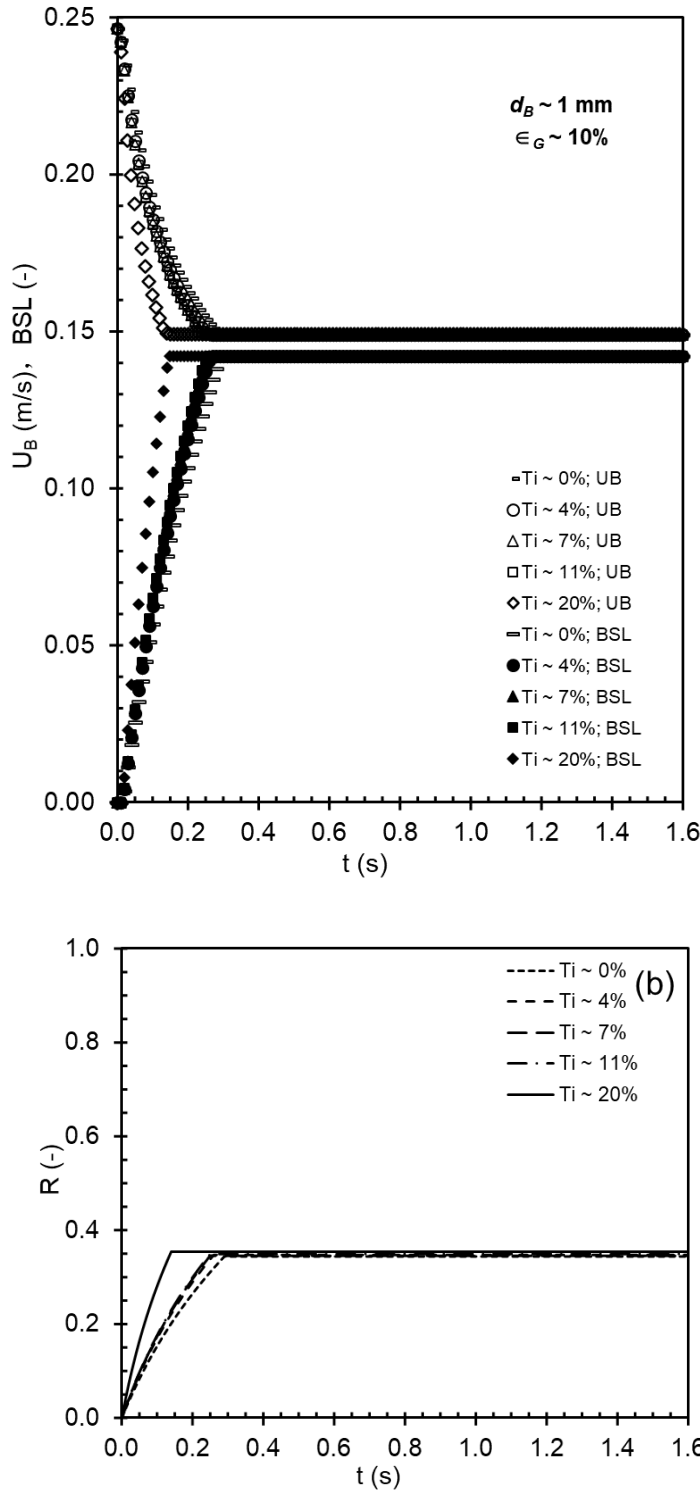


**Fig. 6.10.** Temporal evolution of a) Bubble velocity  $U_B$  and bubble surface loading  $BSL$ ; and b) Recovery  $R$ , at  $\epsilon_G \sim 10\%$  and  $\epsilon_S \sim 0.44\%$  for three different solid concentrations.  $U_B$ ,  $BSL$  and  $R$  were calculated from the collision efficiency in multi-bubble (MB) domain.

It is worth mentioning that **Fig. 6.8 – Fig. 6.10** were based on a pure batch flotation process which assumed a finite number of bubbles and particles existed initially in the system.

However, lab scale flotation cells are often operated in a semi-batch mode with fresh bubbles (zero surface loading) injected continuously into the system. For this reason, the recovery model was modified to simulate a semi-batch system which is described in the next section.

#### 6.4.2. Recovery in a semi-batch flotation cell

To adapt the proposed model to a semi-batch system, the following modifications were made: a) within one bubble residence time, if the maximum bubble surface loading  $BSL_{max}$  was reached, the bubble surface loading was reset to zero at the end of the one bubble residence time to represent injection of fresh bubbles; b) the pulp concentration at the end of the present time period was used as the initial pulp concentration for the next time period. In this sense, the pulp was aerated by discrete bubble injections. Pulp height here was assumed to be 0.10 m typical in a lab scale flotation cell with bubble residence time of 0.4 s. Strong hydrophobic particles with a contact angle of  $80^\circ$  were used in the flotation system. Detailed operating parameters are presented in **Table 6.2**. A plot of the recovery calculated by the modified semi-batch model is shown in **Fig. 6.11** for solid concentration cases in the absence of turbulence ( $Ti \sim 0\%$ ) accounting for collision efficiency determined in single-bubble (SB) and multi-bubble (MB) cases respectively.

Similar to the batch flotation (**Fig. 6.9**), recovery in **Fig. 6.11** for multi-bubble cases is higher than that for single-bubble cases. An interesting recovery pattern is exhibited in the semi-batch flotation process for both SB and MB cases. Compared to the smooth profiles of recovery observed in  $\epsilon_s \sim 0.22\%$  to  $0.44\%$  cases, the presence of remarkable jumps with magnitudes of  $\Delta R \sim 0.10$  and  $\sim 0.05$  was observed in the  $\epsilon_s \sim 1.83\%$  and  $3.58\%$  cases respectively in the early flotation period ( $t \sim 0$  to  $2.0$  s). The discrete jumps observed at the highest solid concentration are attributed to the existence of a saturated regime where the bubble loading ability is exhausted after injection of bubbles. The magnitudes of the staircase jumps decreased over time for  $\epsilon_s = 1.84\%$  case until the recovery profile became smooth after  $t \sim 3.3$  s. The transition from the jump pattern to the smooth pattern is attributed to the removal of particles from pulp phase by fresh bubbles to the extent that the bubble surface loading cannot reach  $BSL_{max}$  within the bubble residence time.

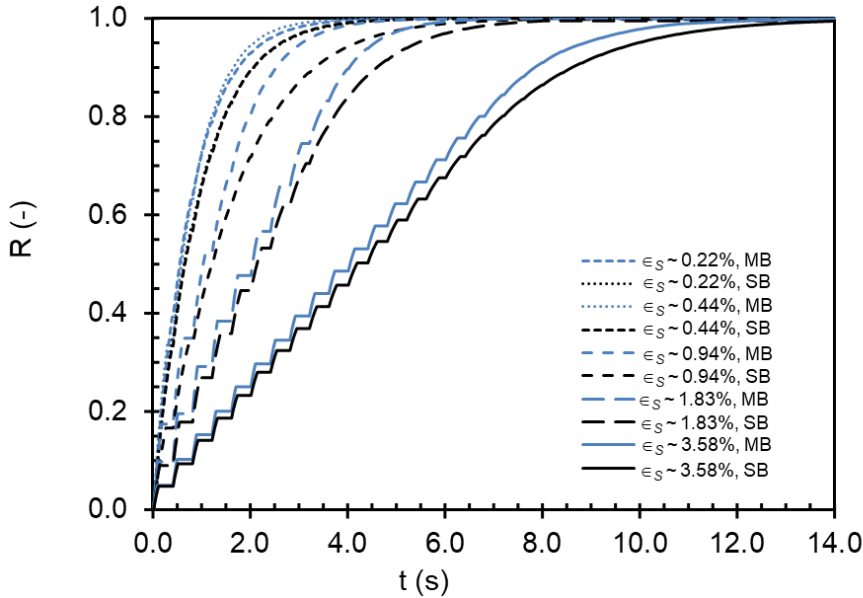


**Fig. 6.11.** Recovery profile for five different solid concentrations at  $Ti \sim 0\%$  in a semi-batch flotation process.  $R$  was calculated from the collision efficiency in both single-bubble (SB) and multi-bubble (MB) domain.

**Fig. 6.12** compares the effect of the turbulence intensity on the recovery at high solid concentration ( $\epsilon_s \sim 1.83\%$ ) under five turbulence conditions ( $Ti \sim 0\%$  to  $20\%$ ) with collision efficiency determined for single-bubble (SB) cases (**Fig. 6.12a**) and multi-bubble (MB) cases (**Fig. 6.12b**) respectively. The staircase jumps type recovery pattern occurs in all five cases for the examined solid concentration. However, the optimal recovery for SB cases occurred at  $Ti \sim 7\%$  wherein the recovery was slightly larger than at  $Ti \sim 4\%$ . In comparison, the optimal recovery for MB cases occurred at  $Ti \sim 20\%$ , almost three times of the optimal turbulence intensity for SB cases. The difference in optimal recovery can be attributed to the different optimal  $Ti$  for collision efficiency for SB and MB cases given the invariance of the efficiency of the other two governing sub-processes: attachment efficiency ( $E_A = 0.91$ ) and detachment efficiency ( $E_D = 0$ ) computed from standard expressions (Eqs. (6.34)- (6.37)) and not numerically simulated.

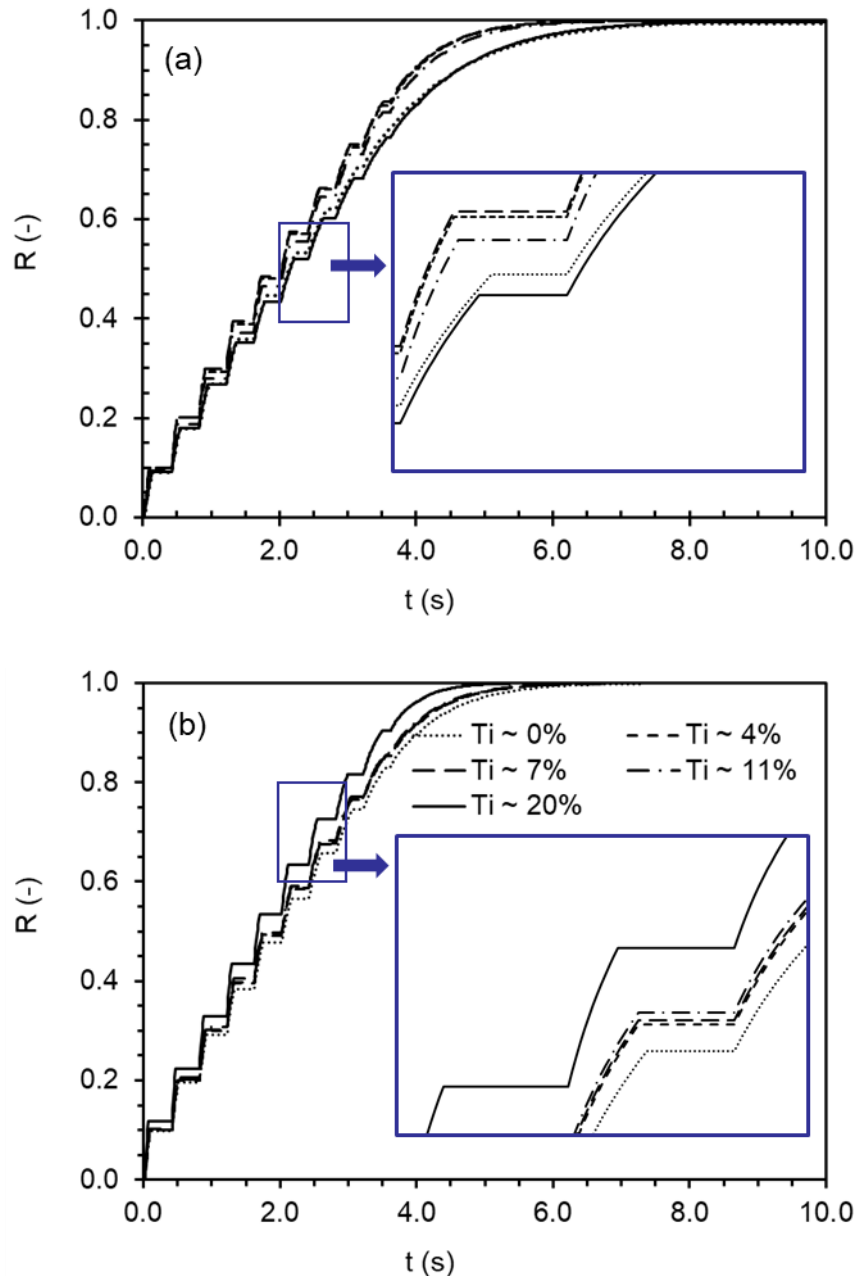


**Fig. 6.12.** Model predicted recovery calculated using collision efficiency determined for a) single-bubble cases and b) multi-bubble cases, under different turbulence for  $\epsilon_s \sim 1.83\%$  in a semi-batch flotation process for different turbulence intensities.

The particle recovery predicted by the model was validated against the experimental data reported in Yang et al. (2018). The operating conditions for this case are summarized in **Table 6.3**. In the simulation, the average gas volume fraction was set to 2.10% according to the experimental observation of Kourunen et al. (2011) and Dahlke et al. (2005), and a gas superficial velocity 0.42 cm/s was used as per Yang's flotation test. The solid volume concentration  $\epsilon_s$  was set to 6.90% which was calculated from Yang's experimental data (100

g coal with density  $1200 \text{ kg/m}^3$ , added in 1.2 L water). The time step used in the simulation was set to 0.1 s.

**Table 6.3.** Input phase parameters for the model prediction

Operating parameters	Values
Particle radius $R_P (\mu\text{m})$	15
Particle density $\rho_p (\text{kg/m}^3)$	1200
Contact angle $\theta_{\text{con}}$ (degree)	86
Bubble radius $R_B (\text{mm})$	0.5
Bubble density $\rho_B (\text{kg/m}^3)$	1.18
Liquid density $\rho_L (\text{kg/m}^3)$	1000
Surface tension $\sigma (\text{N/m})$	0.065
Solid volume concentration $\epsilon_s$	6.90%
Normalized equivalent critical radius $K_I$	0.18
Energy dissipation rate $\varepsilon (\text{m}^2\text{s}^{-3})$	0.05425

**Fig. 6.13** presents the comparison between the predicted and experimental recovery trend. Overall the prediction was in agreement with the experiment ( $\text{RMSD} \sim 0.12$ ) with the experimental recovery at  $\sim 5$  mins being  $\sim 0.78$  times of the predicted recovery. It can be noted that recovery was more accurately predicted ( $\text{RMSD} \sim 0.078$ ) for time period of  $t = 0-1$

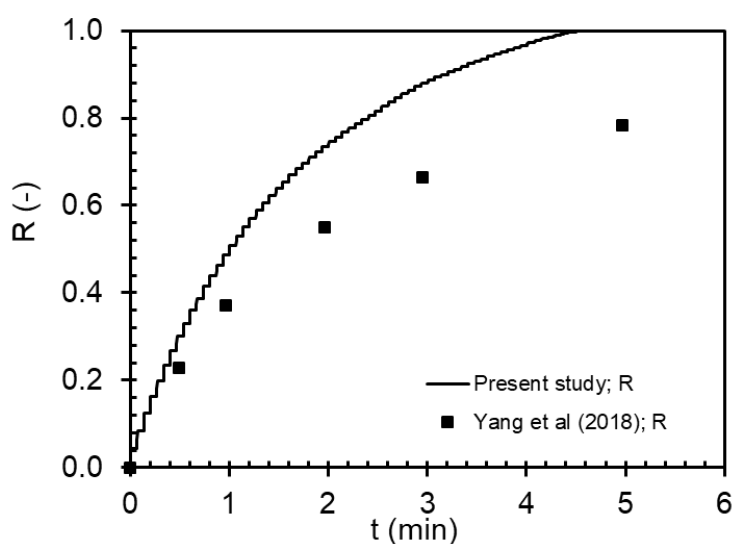


**Fig. 6.13.** Comparison of model predicted recovery with Yang et al (2018), solid concentration  $\epsilon_s \sim 6.90\%$ , gas volume fraction  $\epsilon_G \sim 2.10\%$ .

mins. The discrepancy occurred for  $t = 1$  to 5 min duration wherein the predicted recovery was overestimated ( $\text{RMSD} \sim 0.151$ ). Such discrepancy may be attributed to the assumption of the mobile bubble surface in the model and the fact that bubble surface becomes fully or partially immobile in experiment after surfactant is added (Liu and Schwarz, 2009a). Mobile bubble surface can cause the increase of the critical thickness for rupture of the film between particle and bubbles, leading to the enhancement of collision efficiency (Schulze, 1992). Such enhancement was quantified by Legendre et al. (2009) and they concluded that collision efficiency for a contaminated bubble (immobile) is much smaller than that for a clean bubble (mobile) when  $R_p \ll R_b$ . More accurate prediction of recovery may be achieved if the effect of bubble surface mobility (completely mobile, partially mobile, completely immobile), extent of bubble surface loading and different multi-bubble configurations on collision efficiency in turbulent flow are included in the recovery model.

## 6.5. Conclusion

In this study, collision efficiency in the presence of multi-bubbles was examined numerically and a theoretical flotation recovery model was developed accounting for the effect of turbulence on bubble-particle collision efficiency and the change in bubble rise velocity due to surface loading.

In the domain of the one-central-eight-surrounding-bubbles arrangement, for all  $Ti$  cases the particles only collided with either the central bubble or the surrounding bubbles. This was because for  $Ti \leq 20\%$  particle still loosely followed the mean flow around the bubble and cannot obtain enough kinetic energy from the surrounding eddies to migrate to the surface of a neighbouring bubble. The overall collision efficiency for the multi-bubble case, however, was higher than that for the single-bubble case due to the attenuated fluctuating flow around the central bubble which resulted in less particles diverted away from the central bubble. This attenuated fluctuating flow also explains that the optimal turbulence intensity for collision efficiency increased from  $\sim 7\%$  in single-bubble cases to  $Ti \sim 20\%$  in multi-bubble cases.

Using the developed recovery model, a maximum bubble surface loading ( $BSL_{max} \sim 0.142$ ) was determined by validating the model-predicted bubble velocity against the experimental data reported by Huang et al. (2011). Two regimes were noted – loading regime

in the early flotation period and the saturated regime when the bubble loading ability was exhausted. The prediction for a batch flotation system suggested that the bubble surface loading in the loading regime was apparently affected by solid concentration. Compared to a dilute pulp system, bubble loading ability in a dense pulp system was exhausted earlier due to the larger number of bubble-particle collision events. The apparent loss in loading capacity manifests in an inverse correlation between the recovery and the solid concentration in the saturated regime. Besides, due to the quicker exhausted bubble surface loading, the reduction rate of bubble velocity predicted based on the collision efficiency in multi-bubble cases were higher than that in single-bubble case. In the multi-bubble case, for a fixed solid concentration, the recovery increased with turbulence intensity which can be attributed to the increased collision efficiency with turbulence intensity.

The model prediction of a semi-batch flotation system revealed that recovery based on collision efficiency predicted in multi-bubble cases was higher than that in single-bubble cases. In both the single-bubble and multi-bubble predicted cases, the recovery showed a transition from the staircase jumps to the smooth recovery pattern with time in the dense pulp system ( $\epsilon_s \geq 1.83\%$ ) in the absence of turbulence. This transition was attributed to the gradually shrinking saturated regime with the decreasing solid concentration. Similar to the collision efficiency, the recovery was found to be optimal at  $Ti \sim 7\%$  for single-bubble cases, but increased to a higher value  $Ti \sim 20\%$  for multi-bubble case. The model prediction was overall in reasonable agreement with the experimental data with some discrepancy at later stage of flotation which was attributed to a possible decrease in the collision efficiency due to immobile bubble surface in experiment but not accounted in the model.

# Chapter 7. Conclusions and recommendations

---

## 7.1. Summary of the work

This study was aimed to improve the fundamental understandings of the effect of turbulence on bubble-particle interaction in flotation. A comprehensive literature review in Chapter 2 shows that whilst there are extensive experimental and numerical studies reported on the bubble-particle collision in laminar flow, there are relatively fewer studies that have investigated the effect of turbulence on bubble-particle collision. Also, the effect of bubble surface loading level on the rising velocity of a particle-laden bubble, critical to predict the recovery of particles, has been limitedly studied, even in the laminar flow case.

In the present study, a combination of numerical and experimental methods were applied to examine the effect of turbulence dispersion (Chapter 3) and solid concentration (Chapter 4) on bubble-particle collision in turbulent flow in the presence of single bubble; drag coefficient model for a particle-laden bubble in stationary liquid condition(Chapter 5); the collision efficiency in the presence of multiple bubbles and the effect of turbulence dispersion, solid concentration and bubble surface loading on the recovery of particles (Chapter 6). The conclusions of the specific studies are presented at the end of each chapter which are summarized below.

In Chapter 3, the effect of turbulence dispersion on bubble-particle collision efficiency in single-bubble flotation system ( $d_B \sim 1$  mm,  $Re_B \sim 230$ ) for different turbulence intensities ( $Ti \sim 4\% - 20\%$ ) and various particle size ( $d_P \sim 30$  to  $100$   $\mu\text{m}$ ) were theoretically and numerically studied. The critical distance for the onset of streamline distortion above the bubble followed a power law dependency on the bubble Reynolds number. This dependency indicated that the streamline distortion occurs closer to the bubble for larger bubble Reynolds number due to the increased inertia of fluid particles. A value of  $\sim 4.0$  for the critical distance normalized by bubble radius was found suitable to avoid the streamline distortion at the inlet over the typical range of bubble Reynolds number (20 - 300) in flotation. This critical distance was used in the subsequent theoretical and numerical models of collision efficiency.

A theoretical turbulence dispersion (TD) model based on the assumption of homogeneous and isotropic turbulence was developed to predict the collision efficiency between bubble and particles. The effect of turbulence dispersion was included in the model by relating the particle root-mean-square (RMS) fluctuating velocity to the flow RMS fluctuating velocity. To assess the capability of the developed turbulence dispersion model, a 3D Eulerian–Lagrangian CFD model which applied random walk momentum exchange model was also developed. In the absence of turbulence, good agreement of the two theoretical and numerical model against the literature was obtained. In turbulent flow, in lower turbulence intensity cases ( $Ti \leq 7\%$ ), the turbulence dispersion model agreed well with the prediction of the developed CFD model. However, in higher turbulence intensity cases ( $Ti > 7\%$ ), the turbulence dispersion model was found to overestimate the collision efficiency. This bias in prediction by the TD model can be attributed to the simplified correlation of momentum exchange between particles and eddies. The random walk model method applied in CFD model accounted for the localized momentum exchange for the particle dispersion by including turbulence dissipation rate and eddy integral time scale and therefore is preferable to the theoretical TD model. Subsequent numerical investigations were conducted using the CFD with the random walk model to capture the effect of turbulence dispersion on bubble-particle collision behaviour.

Unlike the 0 – 1 distribution in laminar flow, the CFD-predicted collision efficiency along the radius of particle injecting circle in turbulent flow showed a probability distribution due to the chaotic and random particle movement. Besides, the standard deviation of the probability distribution increased with the increase of turbulence intensity because the effect of mean flow velocity on the collision efficiency was subdued by the effect of random fluctuating flow velocity. The CFD model revealed that for particles released at same positions, the trajectories of these particles showed stochastic pattern. This pattern became more chaotic with the increase of turbulence intensity as the fluctuating flow gradually dominated the mean flow. Force analysis showed that when approaching the bubble, larger particle in higher turbulence intensity was subject to larger inertia leading to higher particle horizontal velocity.

In Chapter 4, the CFD model developed in Chapter 3 was used to predict the combined effect of turbulence and solid concentration on bubble-particle collision efficiency in single-bubble flotation system ( $Ti \sim 4\%$  to  $20\%$ ,  $d_B \sim 1$  mm,  $Re_B \sim 230$ ,  $d_P \sim 30$   $\mu\text{m}$ ). In lower solid concentration cases, preferential concentration occurred with the increase of turbulence

intensity because particles accumulated on the edge of vortex due to the inertia. However, in higher solid concentration cases, the preferential concentration was not obvious due to the large number of particles. A threshold for turbulence attenuation was found to occur at turbulence intensity  $\sim 7\%$ , above which particle radial velocity decreased with the increase of solid concentration. Temporal evolution of particle movement showed that at higher turbulence intensity  $\sim 20\%$ , particle motion became substantially chaotic which apparently caused lateral changes in the particle trajectory. Due to high fluctuating momentum transport from fluid to particles at  $Ti \sim 20\%$ , particles were forced to follow different streamlines. These visualization of the interaction between the particle swarm and the turbulent flow in the vicinity of bubble indicated that solid concentration and turbulence dispersion have an important role in the collision efficiency.

The cumulative particle collision number was found to be non-linear in the early stage of simulation and became linear over time with a constant slope irrespective of injection locations. Turbulence intensity was found to have insignificant effect on local solid concentration. An algorithm of particle-tracking and bin division was developed for quantifying collision efficiency  $E_c$  along the radius of the injecting virtual bin within the bubble swarm. Similar to the single-particle injection in Chapter 3, the collision efficiency here was also found to follow a probability distribution in the vicinity of the bubble wherein particles injected close to the bubble had a higher collision efficiency compared to particles injected away from the bubble surface. With the increase of solid concentration, the maximum collision efficiency along bin radius decreased because more particles were dispersed away from the bubble centre in higher solid concentration cases.

The overall collision efficiency in turbulent flow was calculated from collision efficiency along the bin radius by equating the number of possible collisions in the particle grazing volume above the bubble to the sum of actual collisions due to the release of particles from the virtual bins. The overall collision efficiency  $E_c$  generally decreased with the solid concentration due to the increased lateral dispersion of particles. The optimal turbulence intensity was 7% where the maximum overall collision efficiency occurred in the current single-bubble flotation domain.

In Chapter 5, the rising behaviour of the millimetric size particle-laden bubbles (particle diameter  $d_p \sim 114 \mu\text{m}$ , bubble diameter  $d_B \sim 2.76 \text{ mm}$  and  $3.34 \text{ mm}$ ) in the range of bubble surface loading (BSL)  $\sim 0$  to  $0.6$  both in the absence and presence of surfactant was

experimentally explored. An image processing methodology was developed to quantify the bubble surface loading. Aspect ratio values improved as the bubble surface loading increased however such changes were pronounced in absence of surfactant, suggesting bubble surface loading contributed significantly to surface rigidity in absence of surfactant. Upon the bubble ascending, three different regimes were observed - bubble shape transition (nearly spherical to ellipsoidal), particle detachment (at bubble rear end), and steady (for high BSL) or expansion (for low BSL) of the particle loading zone. Based on the theory of interaction between particles and the trailing vortex of the bubble, a threshold for bubble surface loading ( $BSL \sim 0.40$ ) was determined, below which the expansion of particle loading zone on the bubble surface ceased. Periodic oscillation of the instantaneous BSL in initial  $BSL \sim 0.30$  case occurred due to the vortex shedding occurring at the corresponding high bubble Reynolds number  $Re_B \sim 836$ . The trailing vortex in the vicinity of the rear bubble and the vortex shedding for a bare bubble ( $BSL \sim 0.00$ ,  $d_B \sim 2.70$  mm) in pure water were confirmed using Particle Image Velocimetry (PIV).

The velocity of particle-laden bubbles of larger size ( $d_B \sim 3.34$  mm) followed a non-linear trend with BSL due to the complicated dynamics of the wake as the bubble transitioned from disk-like to sphere-like shape with the increase of BSL. Terminal velocities of particle-laden bubbles of smaller size ( $d_B \sim 2.76$  mm) however followed a linear trend and monotonously decreased with the increase of BSL. In addition, the bubble terminal rise velocity was observed to decrease with bubble surface loading but this trend was less steep in the presence of surfactant, suggesting that the drag force of particle-laden bubble was more sensitive to BSL in absence of surfactant. A correction factor to Schiller-Naumann drag coefficient model was proposed accounting for the bubble surface loading both in the presence and absence of surfactant. In the presence of surfactant, the correction factor to include the effect of BSL on the drag coefficient of the particle-laden bubble was found to be insensitive to the BSL because the loaded particles hardly alter the immobility of the bubble surface. In contrast, in pure water, the correction factor in this study and in literature was found to collapse onto a single curve with a slope of  $\sim 2.41$ , indicating the significant influence of the loading particles on the bubble rigidity and therefore the drag force.

In Chapter 6, the effect of turbulence dispersion, solid concentration on bubble-particle collision efficiency in the presence of multiple bubbles was numerically examined up to turbulence intensity  $\sim 20\%$  using the CFD model in Chapter 4. The hypothesis proposed in Chapter 4 that the surrounding bubbles may allow further collisions of particles was tested.

Simulation results showed that with the increase in the number of surrounding bubbles, the instantaneous velocity field in the upstream of the bubbles became more evenly distributed than that in single-bubble domain which caused less chaotic flow streamline above the central bubble. As a result, in multi-bubble domain, particle still loosely followed the mean flow around the bubble and cannot obtain enough kinetic energy from the surrounding eddies to migrate to the surface of a neighbouring bubble. The overall collision efficiency for the multi-bubble cases, however, was higher than that for the single-bubble cases due to the attenuated fluctuating flow around the central bubble which resulted in less particles diverted away from the central bubble. This optimal turbulence intensity increased from  $\sim 7\%$  for single-bubble cases to  $Ti \sim 20\%$  for multi-bubble cases.

The effect of turbulence dispersion, solid concentration and bubble surface loading on flotation recovery was investigated. A novel flotation recovery model based on a first-order kinetics was proposed. A maximum bubble surface loading ( $BSL_{max} \sim 0.142$ ) was determined by validating the model-predicted bubble velocity against the reported experimental data. The determined  $BSL_{max}$  was applied in the recovery model wherein once this maximum level was reached, the bubble stopped loading more particles. Temporal evolution of bubble velocity and recovery in batch flotation system revealed two regimes – a loading regime in the early flotation period and a saturated regime when the bubble loading ability was exhausted. Specifically, bubble loading ability was exhausted earlier with the increase of solid concentration due to the larger number of bubble-particle collision events. Besides, bubble loading ability which was calculated based on the CFD-predicted collision efficiency was exhausted more quickly in multi-bubble cases than that in single-bubble cases. For a fixed solid concentration, the recovery increased with the turbulence intensity in multi-bubble cases which can be attributed to the increased collision efficiency.

The recovery model was modified to predict semi-batch flotation systems by incorporating the bubble residence time and updating pulp concentration after bubble residence time to simulate the scenario that the pulp was aerated by injecting discrete bubble injections over time. The semi-batch recovery model revealed that recovery based on collision efficiency predicted in multi-bubble cases was higher than that in single-bubble case because of the higher collision efficiency. In both cases, the recovery showed a transition from the staircase jumps to the smooth recovery pattern with time in the dense pulp system ( $\epsilon_s \geq 1.83\%$ ) in the absence of turbulence. This transition was attributed to the gradually shrinking saturated regime with

the decreasing solid concentration. The recovery of strong hydrophobic particles (contact angle  $\sim 80^\circ$ , attachment efficiency  $\sim 0.91$ ) and detachment efficiency  $\sim 1.00$ ) was found to be optimal at  $Ti \sim 7\%$  for single-bubble cases, but increased to a higher value  $Ti \sim 20\%$  for multi-bubble case. The semi-batch recovery model was validated against the reported data from flotation test and reasonable agreement was obtained.

## 7.2. Recommended future work

### 1. Quantifying particle trajectory in turbulent flow field

In Chapter 3, 4 and 6, numerical modelling was conducted to determine particle trajectory in the presence of a turbulent flow field. It is noted that experimental studies reporting fluctuating trajectory of particles are very limited. Previous experimental studies of particle trajectory have been conducted only in laminar flow (Nguyen and Schulze, 2004; Li et al., 2020). Sommer et al. (2020) applied a layer of radioactive material onto the particle surface, based on which they observed the trajectories of particles passing a stationary bubble under various levels of turbulence intensity. Future work in this area is required to experimentally determine the particle dispersion behaviour in the presence of turbulence which can be then utilised to validate the numerical modelling.

### 2. Bubble-particle collision efficiency in the presence of multiple bubbles

A simple configuration of multi-bubble system comprising one-central-eight-surrounding bubbles was adopted in Chapter 6 to examine the effect of multiple-bubbles on collision efficiency at various turbulence intensity levels. However, in flotation system bubbles are randomly distributed and a more comprehensive numerical modelling framework such as coupled CFD-DEM (discrete element method) framework can be utilised to determine collision efficiency. Other sub-processes of bubble-particle interaction i.e. particle attachment and detachment can also be simulated by incorporating the extended DLVO force models which consider the Electrical double layer force, the van der Waals force and the hydrophobic forces. Also can be examined in this framework is the evolution of bubble surface loading in different flow conditions and particle recovery.

### 3. Examine the vortex dynamics of a rising particle-laden bubble

In Chapter 5, vortex structure behind a rising bubble with zero surface loading was experimentally quantified to explain the movement of particles on the bubble surface in

quiescent liquid. Such explanation may hold true for low surface loading wherein the particles may have negligible influence on the vortex. However, for high surface loading, the vortex structure changes significantly which explains the corresponding significant increase of drag coefficient. Particle Image Velocimetry (PIV) can be used to quantify the velocity field behind the particle-laden bubble and the corresponding vortex structure can be constructed. This approach would strengthen the physical understanding behind the increased drag coefficient of particle laden bubble.

#### **4. Rising behaviour of particle-laden bubble in turbulent flow**

A knowledge gap pertaining to quantifying rise velocity of a particle laden bubble has been addressed in this research work. To add another layer of complexity, a future study needs to quantify the rising behaviour of a particle-laden bubble in a turbulent flow field. A well characterised nearly homogeneous turbulent flow field can be considered for this purpose which can be created in an oscillating grid system (Hoque et al., 2018). High speed imaging can be applied to quantify the bubble surface loading based on the methodology presented in Chapter 5 and particle image velocimetry can be applied to quantify the turbulence intensity. Both surface loading and turbulence intensity level can then be correlated to bubble rise velocity which will aid in improving the prediction of particle recovery model presented in Chapter 6.

# References

---

- Abrahamson, J., 1975. Collision rates of small particles in a vigorously turbulent fluid. *Chem. Eng. Sci.* 30(11), 1371-1379.
- Ahmed, N., Jameson, G.J., 1985. The effect of bubble size on the rate of flotation of fine particle. *Int. J. Miner. Process.* 14(3), 195-215.
- Amini, E., Bradshaw, D. J., Xie, W., 2017. Influence of flotation cell hydrodynamics on the flotation kinetics and scale up, Part 2: Introducing turbulence parameters to improve predictions. *Miner. Eng.* 100: 31-39.
- Anfruns, J.F., Kitchener, J.A., 1977. Rate of capture of small particles in solution. *Trans. Inst. Min. Metall.* 86, C9-C15.
- ANSYS, Inc., ANSYS Fluent theory guide, Release 19.2.
- Azgomi, F., Gomez, C.O., Finch, J.A., 2007. Correspondence of gas holdup and bubble size in presence of different frothers. *Int. J. Miner. Process.* 83(1-2), 1-11.
- Behin, J., Bahrami, S., 2012. Modeling an industrial dissolved air flotation tank used for separating oil from wastewater. *Chem. Eng. Process.* 59, 1-8.
- Bhutani, G., Brito-Parada, P.R., Cilliers, J. J., 2016. Polydispersed flow modelling using population balances in an adaptive mesh finite element framework. *Comput. Chem. Eng.* 87, 208-225.
- Bhutani, G., Brito-Parada, P.R., 2020. A framework for polydisperse pulp phase modelling in flotation. *Sep. Purif. Technol.* 236, 116252.
- Bloom, F., Heindel, T.J. 2002. On the structure of collision and detachment frequencies in flotation models. *Chem. Eng. Sci.* 57, 2467–2473.

Bloom, F., Heindel, T.J., 2003. Modelling flotation separation in a semi-batch. *Chem. Eng. Sci.* 58(2), 353–365.

Bloor, M. S., 1964. The transition to turbulence in the wake of a circular cylinder, *J. Fluid Mech.* 19, 290.

Bradshaw, D.J., Connor, C.T., 1996. Measurement of the sub-process of bubble loading in flotation. *Miner. Eng.* 9(4), 443-448.

Brady, M.R., Telionis, D.P., Vlachos, P.P., Yoon, R.H. 2006. Evaluation of multiphase flotation models in grid turbulence via Particle Image Velocimetry. *Int. J. Miner. Process.* 80(2-4), 133-143.

Chandel, A., Das, S.P., 2021. Wake of transversely rotating and translating sphere in quiescent water at low Reynolds number. *Acta Mechanica.* 232, 949–966.

Chegeni, M.H., Abdollahy, M., Khalesi, M.R., 2016. Bubble loading measurement in a continuous flotation column. *Miner. Eng.* 85, 49-54.

Choi, D., Park, H., 2018. Flow around in-line sphere array at moderate Reynolds number. *Phys. Fluids.* 30, 097104.

Clift, R., Grace, J.R., Weber, M.E., 1978. Bubbles, drops, and particles. Academic Press New York.

Cole, K., Brito-Parada, P.R., Hadler, K., Mesa, D., Neethling, S.J., Norori-McCormac, A., M., Cilliers, J.J., 2022. Characterisation of solid hydrodynamics in a three-phase stirred tank reactor with positron emission particle tracking (PEPT). *Chem. Eng. J.* 433, 133819.

Dahlke, R., Gomez, C., Finch, J.A., 2005. Operating range of a flotation cell determined from gas holdup vs. gas rate. *Miner. Eng.* 18(9), 977-980.

Dai, Z.F., Dukhin, S., Fornasiero, D., Ralston, J., 1998. The inertial hydrodynamic interaction of particles and rising bubbles with mobile surfaces. *J. Colloid Interf. Sci.* 197(2), 275-292.

Dai, Z.F., Fornasiero, D., Ralston, J., 2000. Particle-bubble collision models - a review. *Adv. Colloid Interface Sci.* 85(2-3), 231-256.

Dančová, P., Kysela, B., Konfršt, J., Chára, Z., Novontý, P., 2013. LDA measurements and turbulence spectral analysis in an agitated vessel. *EPJ Web of Conferences*, 45, 01055.

Darabi, H., Koleini, S.M., Deglon, D., Rezai, B., Abdollahy, M., 2019. Investigation of bubble-particle interactions in a mechanical flotation cell, part 1: Collision frequencies and efficiencies. *Miner. Eng.* 134, 54-64.

Dobby, G.S., Finch, J.A., 1987. Particle size dependence in flotation derived from a fundamental model of the capture process. *Int. J. Miner. Process.* 21, 241-260.

Doroodchi, E., Evans, G.M., Schwarz, M.P., Lane, G.L., Shah, N., Nguyen, A., 2008. Influence of turbulence intensity on particle drag coefficients. *Chem. Eng. J.* 135, 129-134.

Duan, J., Fornasiero, D., Ralston, J., 2003. Calculation of the flotation rate constant of chalcopyrite particles in an ore. *Int. J. Miner. Process.* 72(1-4), 227-237.

Eaton, J. K., Fessle, J. R., 1994. Preferential concentration of particles by turbulence. *Int. J. Multiphase Flow.* 20, 169-209.

Eskanlou, A., Khalesi, M.R., Mirmogaddam, M., Hemmati Chegeni, M., Vaziri Hassas, B., 2018a. Investigation of trajectory and rise velocity of loaded and bare single bubbles in flotation process using video processing technique. *Sep. Purif. Technol.* 54(11), 1795-1802.

Eskanlou, A., Khalesi, M.R., Abdollahy, M., 2018b. Bubble loading profiles in a flotation column. *Physicochem. Probl. Miner. Process.* 54(2), 355-362.

Eskanlou, A., Chegeni, M.H., Khalesi, M.R., Abdollahy, M., Huang, Q., 2019. Modeling the bubble loading based on force balance on the particles attached to the bubble. *Colloids Surfaces A*. 582, 123892.

Falutsu, M., Dobby, G.S., 1992. Froth performance in commercial sized flotation columns. *Miner. Eng.* 5, 1207-1223.

Firouzi, M., Nguyen, A.V., Hashemabadi, S.H., 2011. The effect of microhydrodynamics on bubble-particle collision interaction. *Miner. Eng.* 24(9), 973-986.

Flint, L .R., Howarth, W. J., 1971. The collision efficiency of small particles with spherical air bubbles. *Chem. Eng. Sci.* 26, 1155-1168.

Gallegos-Acevedo, P.M., Pérez-Garibay, R., Uribe-Salas, A., 2006. Maximum bubble loads: Experimental measurement vs. analytical estimation. *Miner. Eng.* 19(1), 12-18.

Gao, Y., Evans, G.M., Wanless, E.J., Moreno-Atanasio, R., 2017. DEM modelling of particle-bubble capture through extended DLVO theory. *Colloids Surfaces A*. 529, 876-885.

Gaudin, A.M., 1957. Flotation, 2nd edition. McGraw-Hill, New York.

Ge, L., Evans, G., Moreno-Atanasio, R., 2020. CFD-DEM investigation of the interaction between a particle swarm and a stationary bubble: Particle-bubble collision efficiency. *Powder Technol.* 366, 641-652.

Gharai, M., Venugopal, R., 2015. Modeling of flotation process – an overview of different approaches. *Miner. Ext. Met. Rev.* 37(2), 120-133.

Gorain, B. K., Franzidis, J. P., Manlapig, E.V., 1995. Studies on impeller type, impeller speed and air flow rate in an industrial scale flotation cell, part 2: effect on gas holdup. *Miner. Eng.* 8(12), 1557-1570.

Gore, R.A., Crowe, C.T., 1989. Effect of particle size on modulating turbulent intensity. *Internal. J. Multiphase Flow.* 15, 279-285.

Hassanzadeh, A., Firouzi, M., Albijanic, B., Celik, M.S., 2018. A review on determination of particle–bubble encounter using analytical, experimental and numerical methods. Miner. Eng. 122, 296-311.

Hassas, B.V., Caliskan, H., Guven, O., Karakas, F., Cinar, M., Celik, M., S., 2016. Effect of roughness and shape factor on flotation characteristics of glass beads. Colloids Surfaces A. 492, 88-99.

Heiskanen, K., 2013. Flotation research, does advancement require a paradigm shift? Flotation 13. Cape Town, South Africa.

Hoque, M.M., Mitra, S., Evans, G.M., Sathe, M.J., Joshi, J.B., 2018. Modulation of turbulent flow field in an oscillating grid system owing to single bubble rise. Chem. Eng. Sci. 185, 26-49.

Huang, Z., Legendre, D., Guiraud, P., 2011. A new experimental method for determining particle capture efficiency in flotation. Chem. Eng. Sci. 66(5), 982-997.

Huang, Z., Legendre, D., Guiraud, P., 2012. Effect of interface contamination on particle–bubble collision. Chem. Eng. Sci. 68(1), 1-18.

Islam, M.T., Nguyen, A.V., 2020. Effect of microturbulence on bubble-particle collision during the bubble rise in a flotation cell. Miner. Eng. 155, 106418.

Jafari, A., Ghanadi, F., Emes, M.J., Arjomandi, M., Cazzolato, B.S., 2018. Effect of free-stream turbulence on the drag force on a flat plate. 21st Australasian Fluid Mechanics Conference Adelaide, Australia.

Jameson, G.J., Nam, S., Young, M.M., 1977. Physical factors affecting recovery rates in flotation. Miner. Sci. Eng. 9, 103 - 118.

Jameson, G.J., 2010. New directions in flotation machine design. Miner. Eng. 23(11-13), 835-841.

Jeong, J., Hussain, F., 2006. On the identification of a vortex. *J. Fluid Mech.* 285(1).

Jiang, H. 2020. Separation angle for flow past a circular cylinder in the subcritical regime. *Phys. Fluids*. 32, 014106.

Karimi, M., Akdogan, G., Bradshaw, S.M., 2014a. A computational fluid dynamics model for the flotation rate constant, Part I: Model development. *Miner. Eng.* 69, 214-222.

Karimi, M., Akdogan, G., Bradshaw, S.M., 2014b. A CFD-kinetic model for the flotation rate constant, Part II: Model validation. *Miner. Eng.* 69, 205-213.

Kostoglou, M., Karapantsios, T.D., Matis, K.A., 2006. Modeling local flotation frequency in a turbulent flow field. *Adv. Colloid Interface Sci.* 122(1-3), 79-91.

Kostoglou, M., Karapantsios, T.D., Matis, K.A., 2007. CFD model for the design of large scale flotation tanks for water and wastewater treatment. *Ind. Eng. Chem. Res.* 46, 6590-6599.

Kostoglou, M., Karapantsios, T.D., Oikonomidou, O., 2020. A critical review on turbulent collision frequency/efficiency models in flotation: Unravelling the path from general coagulation to flotation. *Adv. Colloid Interface Sci.* 279, 102158.

Koh, P.T.L., Schwarz, M.P., 2003. CFD modelling of bubble-particle collision rates and efficiencies in a flotation cell. *Miner. Eng.* 16(11), 1055-1059.

Koh, P.T.L., Schwarz, M.P., 2006. CFD modelling of bubble-particle attachments in flotation cells. *Miner. Eng.* 19(6-8), 619-626.

Koh, P.T.L., Schwarz, M.P., 2007. CFD model of a self-aerating flotation cell. *Int. J. Miner. Process.* 85(1-3), 16-24.

Koh, P.T.L., Schwarz, M.P., 2008. Modelling attachment rates of multi-sized bubbles with particles in a flotation cell. *Miner. Eng.* 21(12-14), 989-993.

Koh, P.T.L., Hao, F.P., Smith, L.K., Chau, T.T., Bruckard, W.J., 2009. The effect of particle shape and hydrophobicity in flotation. *Int. J. Miner. Process.* 93(2), 128-134.

Koh, P.T.L., Smith, L.K., 2011. The effect of stirring speed and induction time on flotation. *Miner. Eng.* 24(5), 442-448.

Kourunen, J., Niitti T., Heikkinen, L.M., 2011. Application of three-dimensional electrical resistance tomography to characterize gas holdup distribution in laboratory flotation cell. *Miner. Eng.* 24(15), 1677-1686.

Langmuir, I., Blodgett, K. 1946. Mathematical investigation of water droplet trajectories. *Gen. Elec. Comp. Rep.*

Lee, A. F. 1969. New bubble pick-up technique as a rapid flotation test method. *J. S. Afr. Inst. Mining Met.* 77-80.

Lee, C.A., Erickson, L.E., 1987. Bubble breakup and coalescence in turbulent gas–liquid dispersions. *Chem. Eng. Commun.* 59 (1–6), 65–84.

Legendre, D., Sarrot, V., Guiraud, P., 2009. On the particle inertia-free collision with a partially contaminated spherical bubble. *Int. J. Multiph.* 35(2), 163-170.

Leipe, F., Mockel, O.H., 1976. Untersuchungen zum stoffvereinigen in flüssiger phase. *Chem. Technol.* 30, 205–209.

Levich, V.G., 1962. Physicochemical Hydrodynamics, Prentice-Hall, Englewood Cliffs, New Jersey.

Levin L.I., 1961. Research into the physics of coarsely dispersed aerosols. Isd. Akad. Nauk SSR, Moscow, 267.

Levins, B.E., Glastonbury, J.R., 1972. Transactions of the Institution of Chemical Engineers 50 (32), 132.

Li, S., Schwarz, M.P., Feng, Y., Witt, P., Sun, C., 2019. A CFD study of particle–bubble collision efficiency in froth flotation. Miner. Eng. 141, 105855.

Li, S., Schwarz, M. P., Yang, W., Feng, Y., Witt, P., Sun, C., 2020. Experimental observations of bubble–particle collisional interaction relevant to froth flotation, and calculation of the associated forces. Miner. Eng. 151, 106335.

Li, S., Schwarz, M. P., Feng, Y., Witt, P., Sun, C., 2021. Numerical investigations into the effect of turbulence on collision efficiency in flotation. Miner. Eng. 163, 106744.

Liu, T.Y., Schwarz, M.P., 2009a. CFD-based multiscale modelling of bubble–particle collision efficiency in a turbulent flotation cell. Chem. Eng. Sci. 64(24), 5287-5301.

Liu, T.Y., Schwarz, M.P., 2009b. CFD-based modelling of bubble-particle collision efficiency with mobile bubble surface in a turbulent environment. Int. J. Miner. Process. 90(1-4), 45-55.

Lysenko, D. A., Ertesvag, I.S., Rian, K.E., 2012. Large-Eddy Simulation of the Flow Over a Circular Cylinder at Reynolds Number 3900 Using the OpenFOAM Toolbox. Flow Turbul. Combust. 89(4), 491-518.

Magnaudet, J., Mougin, G. 2007. Wake instability of a fixed spheroidal bubble. J. Fluid Mech. 572, 311-337.

Markarian, S.A., Harutyunyan, L.R., Harutyunyan, R.S., 2005. The properties of mixtures of sodium dodecylsulfate and diethylsulfoxide in water. J. Solution Chem. 34(3), 361-368.

Mehta, S.M., Ityokumbul, M.T., 2003. Particle size and frother effects in column flotation. Miner. Metall. Proc. 20 (1), 26-30.

Meng, J., Xie, W., Brennan, M., Runge, K., Bradshaw, D., 2014. Measuring turbulence in a flotation cell using the piezoelectric sensor. Miner. Eng. 66-68, 84-93.

Meng, J., Tabosa, E., Xie, W., Runge, K., Bradshaw, D., Manlapig, E., 2016. A review of turbulence measurement techniques for flotation. Miner. Eng. 95, 79-95.

Mirgaux, O., Ablitzer, D., Waz, E., Bellot, J.P., 2009. Mathematical modeling and computer simulation of molten aluminum purification by flotation in stirred reactor. *Metall. Mater. Trans. B*, 40 (3), 363–375

Montorfano, A., Piscaglia, F., Ferrari, G., 2013. Inlet boundary conditions for incompressible LES: A comparative study. *Math. Comput. Model.* 57(7-8), 1640-1647.

Moreno-Atanasio, R., Gao, Y., Neville, F., Evans, G.M., Wanless, E.J., 2016. Computational analysis of the selective capture of binary mixtures of particles by a bubble in quiescent and fluid flow. *Chem. Eng. Res. Des.* 109, 354-365.

Morsi, S.A., Alexander, A. J. 1972. An investigation of particle trajectories in two-phase flow systems. *J. Fluid Mech.* 55(02), 193-208.

Moys, M.H., Yianatos, J., Larenas, J., 2010. Measurement of particle loading on bubbles in the flotation process. *Miner. Eng.* 23(2), 131-136.

Nadeem, M., Ahmed, J., Chughtai, I. R., 2006. CFD-based estimation of collision probabilities between fine particles and bubbles having intermediate Reynolds number. Fifth International Conference on CFD in the Process Industries, Melbourne, Australia.

Ngo-Cong, D., Nguyen, A.V., Tran-Cong, T.T, 2018. Isotropic turbulence surpasses gravity in affecting bubble-particle collision interaction in flotation. *Miner. Eng.* 122, 165-175.

Nguyen, V.A., Kmet, S., 1992. Collision efficiency for fine mineral particles with single bubble in a countercurrent flow regime. *Int. J. Miner. Process.* 35(3), 205-223.

Nguyen, V.A., Schulze, H.J., 2004. Colloidal science of flotation. Marcel Dekker, New York.

Nguyen, A.V., Evans, G.M., 2004a. Movement of fine particles on an air bubble surface studied using high-speed video microscopy. *J. Colloid Interface Sci.* 273(1), 271-277.

Nguyen, A.V., Evans, G.M. 2004b. Exact and global rational approximate expressions for resistance coefficients for a colloidal solid sphere moving in a quiescent liquid parallel to a slip gas-liquid interface. *J. Colloid Interface Sci.* 273(1), 262-270.

Nguyen, C.M., Nguyen, A.V., Miller, J.D., 2006. Computational validation of the Generalized Sutherland Equation for bubble-particle encounter efficiency in flotation. *Int. J. Miner. Process.* 81(3), 141-148.

Nguyen, A.V., An-Vo, D.A., Tran-Cong, T., Evans, G.M., 2016. A review of stochastic description of the turbulence effect on bubble-particle interactions in flotation. *Int. J. Miner. Process.* 156, 75-86.

Nitsche, J.M., Batchelor, G.K., 1997. Break-up of a falling drop containing dispersed particles. *J. Fluid Mech.* 340, 161-175.

Oguz, H. N., Prosperetti, A. 1993. Dynamics of bubble growth and detachment from a needle. *J. Fluid Mech.* 257, 111-145.

Omota, F., Dimian, A.C., Bliek, A., 2006a. Adhesion of solid particles to gas bubbles. Part 1: Modelling. *Chem. Eng. Sci.* 61(2), 823-834.

Omota, F., Dimian, A.C., Bliek, A., 2006b. Adhesion of solid particles to gas bubbles. Part 2: Experimental. *Chem. Eng. Sci.* 61(2), 835-844.

Ostadrahimi, M., Gharibi, K., Dehghani, A., Farrokhpay, S., 2019. Estimating bubble loading in industrial flotation cells. *Minerals.* 9(4), 222.

Pope, S.B. 2000. *Turbulent flows*. Cambridge University Press, UK.

Ramsey, A.S. 1935. *A treatise of hydrodynamics, Part II. Hydrodynamics*. G. Bell and Sons, London. 160.

Reay, D., Ratcliff, G.A., 1973. Removal of fine particles from water by dispersed air flotation: Effects of bubble size and particle size on collection efficiency. *Can. J. Chem. Eng.* 41, 178-185.

Sadhal, S.S., Johnson, R.E., 1983. Stokes flow past bubbles and drops partially coated with thin films. Part 1. Stagnant cap of surfactant film – exact solution. *J. Fluid Mech.* 126, 237-250.

Saffman, P.G., Turner, J.S., 1956. On the collision of drops in turbulent clouds. *J. Fluid Mech.* 1(1), 16-30.

Sahbaz, O., Ercetin, U., Oteyaka, B., 2012. Determination of turbulence and upper size limit in Jameson flotation cell by the use of computational fluid dynamic modelling. *Physicochem. Probl. Miner. Process.* 48(2), 533-544.

Sarhan, A. R., Naser, J., Brooks, G., 2018. Effects of particle size and concentration on bubble coalescence and froth formation in a slurry bubble column. *Particuology*. 36, 82-95.

Sarkar, M.S.K.A., Donne, S.W., Evans, G.M., 2011. Utilization of hydrogen in electroflotation of silica. *Adv. Powder Technol.* 22(4), 482-492.

Sarrot, V., Guiraud, P., Legendre, D., 2005. Determination of the collision frequency between bubbles and particles in flotation. *Chem. Eng. Sci.* 60(22), 6107-6117.

Schiller, L., Naumann, Z., 1935. A drag coefficient correlation. *Z.Ver. Deutsch. Ing.*, 77-318.

Schlichting, H., 1979. *Boundary layer theory*, McGraw-Hill, New York

Schulze, H.J., 1977. New theoretical and experimental investigations on stability of bubble/particle aggregates in flotation: a theory of the upper particle size of floatability. *Int. J. Miner. Process.* 4, 241-259.

Schulze, H.J., 1982. Dimensionless number and approximate calculation of the upper particle size of floatability in flotation machines. *Int. J. Miner. Process.* 9, 321-328.

Schulze, H.J., 1989. Hydrodynamics of bubble-mineral particle collisions. Miner. Process. Extr. Metall. Rev. 5, 43-76.

Schulze, H. J., 1992. Probability of particle attachment on gas bubbles by sliding. Adv. Colloid Interface Sci. 40, 283-305.

Seaman, D.R., Franzidis, J.P., Manlapig, E.V., 2004. Bubble load measurement in the pulp zone of industrial flotation machines—a new device for determining the froth recovery of attached particles. Int. J. Miner. Process. 74(1-4), 1-13.

Shahbazi, B., Rezai, B., Koleini, S. M. J., 2010. Bubble-particle collision and attachment probability on fine particles flotation. Chem. Eng. Process. 49(6), 622-627.

Sherrell, I.M., 2004. Development of a flotation rate equation from first principles under turbulent flow conditions. Ph. D. Thesis. Virginia Polytechnic Institute and State University.

Sommer, A. E., Ortmann, K., Heerden, M. V., Richter, T., Leadbeater, T., Cole, K., Heitkam, S., Brito-Parada, P. R., Eckert, K., 2020. Application of Positron Emission Particle Tracking (PEPT) to measure the bubble-particle interaction in a turbulent and dense flow. Miner. Eng. 156, 106410.

Sokovnin, O.M., Zagorskina, N.V., Zagorskin, S.N., 2014. Determination of the collision probability between bubbles and nonspherical particles in Flotation. Chem. Eng. Technol. 37(11), 1964-1974.

Spencer, S.J., Bruniges, R., Roberts, G., Sharp, V., Catanzano, A., Bruckard, W.J., Davey, K.J., Zhang, W., 2012. An acoustic technique for measurement of bubble solids mass loading: (b) Monitoring of Jameson cell flotation performance by passive acoustic emissions. Miner. Eng. 36-38, 21-30.

Sutherland, K.L., 1948. Physcal chemistry of flotation. XI: Kinetics of the flotation process. J. Phys. Chem. 46(52), 394.

Thompson, M. C., Hourigan, K., 2005. The shear-layer instability of a circular cylinder wake. *Phys. Fluids* 17, 021702.

Troshko, A.A., Zdravistch, F., 2009. CFD modeling of slurry bubble column reactors for Fisher-Tropsch synthesis. *Chem. Eng. Sci.* 64 (5), 892-903.

Uribe-Salas, A., de Lira-Gómez, P., Pérez-Garibay, R., Nava-Alonso, F., Magallanes-Hernández, L., Lara-Valenzuela, C., 2003. Overloading of gas bubbles in column flotation of coarse particles and effect upon recovery. *Int. J. Miner. Process.* 71(1-4), 167-178.

Vallée, R., Henry, C., Hachem, E., Bec, J., 2018. Inelastic accretion of inertial particles by a towed sphere. *Phys. Rev. Fluids.* 3(2), 024303.

Verrelli, D.I., Koh, P.T.L., Nguyen, A. V., 2011. Particle-bubble interaction and attachment in flotation. *Chem. Eng. Sci.* 66(23), 5910-5921.

Vinke, H., Hamersma, P.J., Fortuin, J.M.H., 1991a. Particle-to-bubble adhesion in Gas-Liquid-Solid Slurries. *AIChEJ* 37(12), 1801-1809.

Vinke, H., Hamersma, P.J., Fortuin, J.M.H., 1991b. adhesion of small particles to gas bubbles: determination of small effective solid-liquid-gas contact angles. *Chem. Eng. Sci.* 46(10), 2497-2506.

Vinke, H., Hamersma, P.J., Fortuin, J.M.H., 1993. Enhancement of the gas-absorption rate in agitated slurry reactors by gas-adsorbing particles adhering to gas bubbles. *Chem. Eng. Sci.* 48(12), 2197-2210.

Wan, D., Yi, X., Wang, L., Sun, X., Chen, S., Wang, G., 2020. Study of collisions between particles and unloaded bubbles with point-particle model embedded in the direct numerical simulation of turbulent flows. *Miner. Eng.* 146, 106137.

Wang, A., Yan, X., Wang, L., Cao, Y., Liu, J., 2015. Effect of cone angles on single-phase flow of a laboratory cyclonic-static micro-bubble flotation column: PIV measurement and CFD simulations. *Sep. Purif. Technol.* 149, 308-314.

Wang, G., Nguyen, A.V., Mitra, S., Joshi, J.B., Jameson, G.J., Evans, G.M., 2016. A review of the mechanisms and models of bubble-particle detachment in froth flotation. *Sep. Purif. Technol.* 170, 155-172.

Wang, G., Evans, G.M., Jameson, G.J., 2017a. Bubble-particle detachment in a turbulent vortex II—Computational methods. *Miner. Eng.* 102, 58-67.

Wang, L., Wang, Y., Yan, X., Wang, A., Cao, Y., 2017b. A numerical study on efficient recovery of fine-grained minerals with vortex generators in pipe flow unit of a cyclonic-static micro bubble flotation column. *Chem. Eng. Sci.* 158, 304-313.

Wang, P., Cilliers, J.J., Neethling, S.J., Brito-Parada, P.R., 2019a. The behavior of rising bubbles covered by particles. *Chem. Eng. J.* 365, 111-120.

Wang, P., Cilliers, J.J., Neethling, S.J., Brito-Parada, P.R., 2019b. Effect of particle size on the rising behavior of particle-laden bubbles. *Langmuir*. 35(10), 3680-3687.

Weber, M.E., Paddock, D., 1983. Interceptional and gravitational collision efficiencies for single collectors at intermediate Reynolds-numbers. *J. Colloid Interf. Sci.* 94(2), 328-335.

Wierink, G. A., 2012. A computational framework for coupled modelling of three-phase systems with soluble surfactants. Ph. D. Thesis, Aalto University.

Wimmers, O. J., Fortuin, J. M. H., 1988. The use of adhesion of catalyst particles to gas bubbles to achieve enhancement – I. investigation of particle-to-bubble adhesion using the bubble pick-up method. *Chem. Eng. Sci.* 43, 303-312.

Woo, S.W., 1971. Simulateous free and forced convection around submerged cylinders and spheres. Phd thesis.

Xia, W., Ma, G., Bu, X., Peng, Y., 2018. Effect of particle shape on bubble-particle attachment angle and flotation behavior of glass beads and fragments. *Powder Technol.* 338, 168-172.

Yang, Z., 2015. Large-eddy simulation: Past, present and the future. Chinese J. Aeronaut. 28(1), 11-24.

Yang, J., Yu, K., Zuo, Y.Y., 2017. Accuracy of axisymmetric drop shape analysis in determining surface and interfacial tensions. Langmuir. 33(36), 8914-8923.

Yang, H., Cai, Y., Wu, L., 2018. Flotation behavior of raw and oxidized fine coal when mixed with coarse particles. Fuel. 232, 225-232.

Yao, N., Liu, J., Sun, X., Liu, Y., Chen, S., Wang, G., 2021. A Rational Interpretation of the Role of Turbulence in Particle-Bubble Interactions. Minerals. 11(9), 1006.

Yasmin, D., Mitra, S., Evans, G. M., 2019. Analysis of dynamic interactions in a bubble-particle system in presence of an acoustic field. Miner. Eng. 131, 111-123.

Yoon, R.H., Luttrell, G.H., 1989. The Effect of bubble size on fine particle flotation. Miner. Process Extr. M. 5(1-4), 101-122.

Yoon, R.H., Mao, L.Q., 1996. Application of extended DLVO Theory, IV: derivation of flotation rate equation from first principles. J. Colloid Interf. Sci. 181(2), 613-626.

Yuu, S. 1984. Collision rate of small particles in a homogeneous and isotropic turbulence. AIChE J. 30(5), 802-807.

Zhang, W., Spencer, S.J., Coghill, P., 2012. An acoustic technique for measurement of bubble solids mass loading – (a) Fundamental study of single bubble. Miner. Eng. 36-38, 45-52.

Ziff, R.M., Majumdar, S.N., Comtet, A., 2009. Capture of particles undergoing discrete random walks. J Chem. Phys. 130(20), 204104.

Zore, K., Sasanapuri, B., Parkhi, G., Varghese, A., 2019. Ansys Mosaic Poly-Hexcore mesh for high-lift aircraft configuration. 21st Annual CFD Symposium, Bangalore.

Zuniga, H.G., 1935. Bol. Minero Soc. Nacl. Mineria (Chile) 47-83.

# Appendix A – Turbulent eddy sizes

As turbulent flow consists of a series of eddy size, in this appendix we summarised three important eddy sizes: integral length scale, Taylor microscale and Kolmogorov scale in the single-bubble domain described in Chapter 3. The integral length scale,  $l$ , can be quantified by integrating the autocorrelation function  $C(r_{auto})$  with position as follows:

$$l = \int_0^{\infty} C(r_{auto}) dr_{auto} \quad (\text{A.1})$$

where the  $C(r_{auto})$  can be calculated by the following expression (Hoque et al., 2018):

$$C(r_{auto}) = \frac{\langle u'(x)u'(x+r_{auto}) \rangle}{\langle u'(x)^2 \rangle} \quad (\text{A.2})$$

where  $u'(x)$  denotes fluctuating velocity at position  $x$  and  $u'(x+r_{auto})$  denotes the fluctuating velocity at a distance  $r$  from position  $x$ . **Fig. A.1** shows the autocorrelation function plotted at the middle plane  $y = 0$  for  $Ti \sim 4\%$  to  $20\%$ .

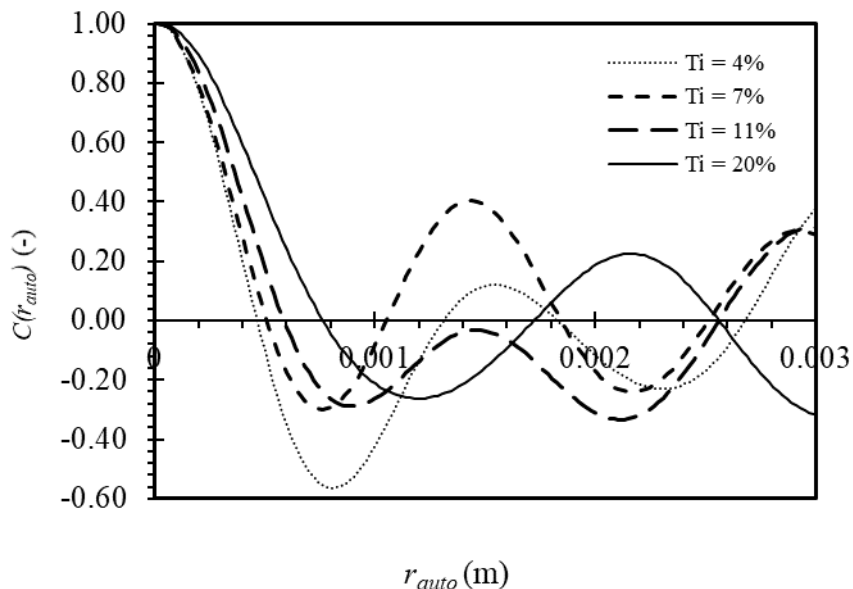


**Fig. A.1.** Autocorrelation function at plane  $y = 0$  for different turbulence intensity

The Taylor length scale,  $\lambda$ , is the intermediate length scale at which the fluid viscosity significantly affects the dynamics of turbulent eddies. This length scale is calculated as follows:

$$\lambda = \left( \frac{15\nu u_{rms}^2}{\varepsilon} \right)^{0.5} \quad (\text{A.3})$$

where  $\nu$  is kinematic viscosity. The Kolmogorov length scale,  $\eta$ , is the smallest length scale in turbulent flow.  $\eta$  can be calculated by:

$$\eta = \left( \frac{\nu^3}{\varepsilon} \right)^{0.25} \quad (\text{A.4})$$

These three eddy-length scales calculated based on the centre plane of the bubble (plane  $y = 0$ ) are presented in **Table A.1**.

**Table A.1** Summary of length scales for different turbulent intensity

Turbulence intensity	RMS velocity	Kinematic viscosity	Energy dissipation rate	Integral length scale	Taylor length scale	Kolmogorov length scale
$Ti$ (-)	$u_{f,rms}$ (m/s)	$\nu$ (m <sup>2</sup> /s)	$\varepsilon$ (m <sup>2</sup> s <sup>-3</sup> )	$l$ (mm)	$\lambda$ (mm)	$\eta$ (mm)
4%	0.0064	0.000001	0.02251	0.294	0.165	0.082
7%	0.0113	0.000001	0.02792	0.312	0.262	0.077
11%	0.0188	0.000001	0.05425	0.356	0.313	0.066
20%	0.0315	0.000001	0.11020	0.448	0.368	0.055

It can be noted that bulk mesh size of 83  $\mu\text{m}$  was smaller than the Taylor length scale, 165  $\mu\text{m}$  in  $Ti = 4\%$  case and 368  $\mu\text{m}$  in  $Ti = 20\%$  case. Hence Taylor length scale was resolved in this study.

## Appendix B – Inlet turbulence intensity levels in single-bubble domain

This section aims to confirm that the turbulence intensity  $Ti$  generated by the CFD model at the inlet is consistent with the pre-set  $Ti$ . Turbulence intensity can be calculated by the temporal-spatial-averaged RMS velocity from the instantaneous velocity generated on the inlet. For this purpose, at each time step the spatial-averaged RMS velocity on the inlet was first calculated using Eq. (B.1) (Hoque et al., 2018).

$$u_{rms,s} = \sqrt{\frac{\sum_{i=1}^M (u_i - \bar{u}_s)^2}{M}} \quad (M = 3680) \quad (\text{B.1})$$

where  $u_{rms,s}$  is the spatial-averaged RMS velocity,  $\bar{u}_s$  is the mean velocity on the inlet. M is the number of cells on the inlet.

**Fig. B.1** shows the time history of the spatial-averaged RMS velocity  $u_{rms\_s}$  for turbulence intensity  $Ti \sim 4\% - 20\%$ . It can be noted that the spatial-averaged RMS velocity  $u_{rms\_s}$  also fluctuated over time. Taking the average of the  $u_{rms,s}$  over time gave 0.047, 0.025, 0.016 and 0.009 m/s which corresponded to ratios 3.78%, 6.83%, 11.04% and 20.48% of the mean flow velocity 0.23 m/s for each  $Ti$  case. These four ratios were close to the pre-set turbulent intensity 4%, 7%, 11% and 20% on the inlet with slight deviations between 0.4% and 5.5%. Such small discrepancy demonstrated that the CFD method is capable of generating fluctuating velocity for a predefined turbulence intensity.

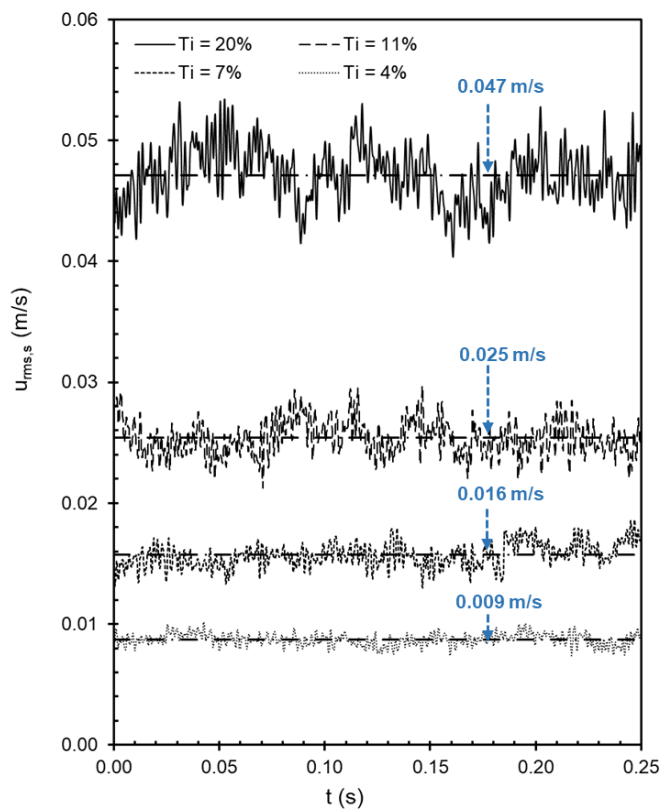


**Fig. B.1.** Temporal evolution of spatial-averaged RMS velocity on the inlet for different turbulence intensity levels.

# Appendix C - Surface area of an ellipsoidal cap

This section illustrated the calculation of the surface area of the ellipsoidal cap, as shown in **Fig. C.1**. The ellipsoid can be defined by the parametric function:

$$\vec{r} = a \sin \theta \cos \varphi \hat{i} + b \sin \theta \sin \varphi \hat{j} + c \cos \theta \hat{k} \quad (\text{C.1})$$

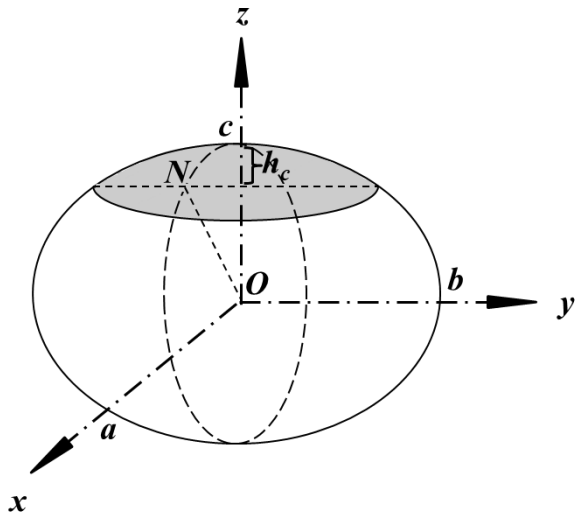


**Fig. C.1.** Schematic of the ellipsoidal cap

where  $a$ ,  $b$  and  $c$  are the three semi-axes,  $\theta$  is the polar angle, and  $\varphi$  is the azimuth angle. Differentiating Eq. (C.1) leads to the surface unit:

$$d\vec{s} = \frac{\partial \vec{r}}{\partial \theta} d\theta \times \frac{\partial \vec{r}}{\partial \varphi} d\varphi \quad (\text{C.2})$$

where the two differentials on the right side of Eq. (C.2) are expressed as:

$$\frac{\partial \vec{r}}{\partial \theta} = a \cos \theta \cos \varphi \hat{i} + b \cos \theta \sin \varphi \hat{j} - c \sin \theta \hat{k} \quad (\text{C.3})$$

$$\frac{\partial \vec{r}}{\partial \varphi} = -a \sin \theta \sin \varphi \hat{i} + b \sin \theta \cos \varphi \hat{j} \quad (\text{C.4})$$

The norm of the unit surface,  $ds$ , can be calculated by substitute Eq. (C.3)- (C.4) into Eq. (C.2).

$$ds = \left| d\vec{s} \right| = \sqrt{(bc \sin \theta \cos \varphi)^2 + (ac \sin \theta \sin \varphi)^2 + (ab \cos \theta)^2} \sin \theta d\theta d\varphi \quad (\text{C.5})$$

Integrating Eq. (C.5) leads to the surface area of the ellipsoidal cap,  $S_{cap}$ :

$$S_{cap} = \int_{\theta=0}^{\theta_1} \int_{\varphi=0}^{2\pi} \sqrt{(bc \sin \theta \cos \varphi)^2 + (ac \sin \theta \sin \varphi)^2 + (ab \cos \theta)^2} \sin \theta d\theta d\varphi \quad (\text{C.6})$$

where the boundary angle  $\theta_1$  denotes the polar angle at the base of the ellipsoidal cap. To calculate  $\theta_1$ , the ellipsoid reduces to an ellipse at  $y = 0$  as shown in **Fig. C.2**. On this ellipse, the polar angle  $\theta$  in Eq. (C.1) is the angle between the axis z and the vector ON' where the N' is intersect of the circle with a radius  $c$  and the bottom boundary of the ellipsoidal cap NM.

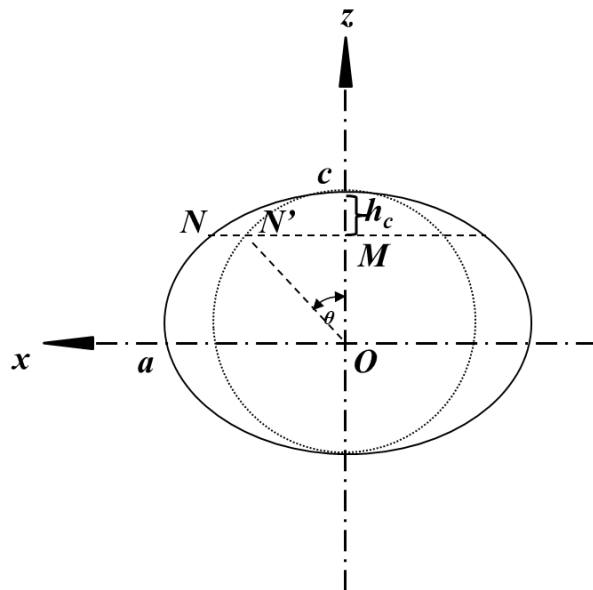


**Fig. C.2.** X-Z plane of the ellipsoid

Considering the triangle MON', the boundary angle  $\theta_1$  can be calculated by the following equation:

$$\theta_1 = \cos^{-1} \left( \frac{|OM|}{|ON'|} \right) = \cos^{-1} \left( \frac{c - h_c}{c} \right) \quad (\text{C.7})$$

The resultant value  $\theta_1$  from Eq. (C.7) is then used to solve Eq. (C.6). After manipulation, Eq. (C.6) can be expressed as:

$$s_{cap} = 4bc \int_{\theta=0}^{\theta} \int_{\varphi=0}^{\pi/2} \sqrt{(1-\cos^2 \theta)[(1-\cos^2 \varphi) + \frac{a^2}{b^2} \sin \varphi^2] + \frac{a^2}{c^2} \cos^2 \theta} \sin \theta d\theta d\varphi \quad (\text{C.8})$$

Let:

$$u = \cos \theta \quad (\text{C.9})$$

And

$$B = (1 - \cos^2 \varphi) + \frac{a^2}{b^2} \sin \varphi^2 \quad (\text{C.10})$$

Eq. (C.9) and (C.10) can be combined to simplify Eq. (C.8) as:

$$s_{cap} = 4bc \int_{u=\cos \theta_l}^1 \int_{\varphi=0}^{\pi/2} \sqrt{(1-u^2)B + \frac{a^2}{c^2} u^2} du d\varphi \quad (\text{C.11})$$

After manipulation, Eq. (C.11) becomes:

$$s_{cap} = 4bc \int_{u=\cos \theta_l}^1 \int_{\varphi=0}^{\pi/2} \sqrt{B} \sqrt{1 + (\frac{a^2}{c^2 B} - 1)u^2} du d\varphi \quad (\text{C.12})$$

Let

$$F = \frac{a^2}{c^2 B} - 1 \quad (\text{C.13})$$

and Eq. (C.12) becomes:

$$s_{cap} = 4bc \int_{\varphi=0}^{\pi/2} \sqrt{B} d\varphi \int_{u=\cos \theta_l}^1 \sqrt{1 + F u^2} du \quad (\text{C.14})$$

Eq. (C.14) can then be reorganized as:

$$s_{cap} = 4bc \int_{\varphi=0}^{\pi/2} \left| \frac{u}{2} \sqrt{1 + F u^2} + \frac{1}{2\sqrt{F}} \sinh^{-1}(\sqrt{F}u) \right|_{\cos \theta_l}^1 \sqrt{B} d\varphi \quad (\text{C.15})$$

After manipulation, Eq. (C.15) can be represented by the following expression:

$$s_{cap} = 2bc \int_{\varphi=0}^{\pi/2} \left\{ \underbrace{\sqrt{B}(\sqrt{1+F} - h\sqrt{1+Fh^2})}_{\text{first}} + \underbrace{\sqrt{\frac{B}{F}} a \sinh(\sqrt{F(1+Fh^2)} - h\sqrt{F(1+F)})}_{\text{second}} \right\} d\varphi \quad (\text{C.16})$$

Let

$$t = \sin \varphi \quad (\text{C.17})$$

Applying Eq. (C.17), the  $d\varphi$ , B - Eq. (C.10) - and F - (Eq. (C.13) - become:

$$d\varphi = \frac{1}{\sqrt{1-t^2}} dt \quad (\text{C.18})$$

$$B = 1 - \left(1 - \frac{a^2}{b^2}\right)t^2 \quad (\text{C.19})$$

$$F = \frac{a^2}{c^2 B} - 1 \quad (\text{C.20})$$

Combining Eq. (C.18) - (C.20), the first term in Eq. (C.16) becomes:

$$\sqrt{B}(\sqrt{1+F} - h\sqrt{1+Fh^2}) = \sqrt{B}\left(\sqrt{\frac{a^2}{c^2 B}} - h\sqrt{1+\left(\frac{a^2}{c^2 B}-1\right)h^2}\right) \quad (\text{C.21})$$

which can be further manipulated as:

$$\sqrt{B}(\sqrt{1+F} - h\sqrt{1+Fh^2}) = \frac{a}{c}(1 - h\sqrt{h^2 + \frac{c^2}{a^2} B(1-h^2)}) \quad (\text{C.22})$$

Let

$$G(t) = \sqrt{h^2 + \frac{c^2}{a^2} B(1-h^2)} \quad (\text{C.23})$$

Substituting of G(t) into Eq. (C.22) leads to:

$$\sqrt{B}(\sqrt{1+F} - h\sqrt{1+Fh^2}) = \frac{a}{c}(1 - hG(t)) \quad (\text{C.24})$$

The second term in Eq. (C.16) can be manipulated as:

$$\sqrt{\frac{B}{F}} a \sinh(\sqrt{F(1+Fh^2)} - h\sqrt{F(1+F)}) = \sqrt{\frac{B}{F}} a \sinh\left(\frac{a}{c} \sqrt{\frac{F}{B}(G(t)-h)}\right) \quad (\text{C.25})$$

Substitute Eq. (C.24) and Eq. (C.25) into Eq. (C.16), the following expression is obtained:

$$s_{cap} = 2bc \int_0^1 \left\{ \frac{\frac{a}{c}(1-hG(t)) + \sqrt{\frac{B}{F}} a \sinh\left(\frac{a}{c} \sqrt{\frac{F}{B}(G(t)-h)}\right)}{\sqrt{1-t^2}} \right\} dt \quad (\text{C.26})$$

It can be noted that the surface area of the ellipsoidal cap,  $S_{cap}$ , in Eq. (C.26) is an even function and can be changed into

$$S_{cap} = bc \int_{-1}^1 \left\{ \frac{\frac{a}{c}(1-hG(t)) + \sqrt{\frac{B}{F}}a \sinh(\frac{a}{c}\sqrt{\frac{F}{B}}(G(t)-h))}{\sqrt{1-t^2}} \right\} dt \quad (\text{C.27})$$

In order to calculate Eq. (C.27) using Gauss-Chebyshev Integration method, define the function  $f(t)$  as:

$$f(t) = (1-hG(t)) + \frac{c}{a} \sqrt{\frac{B}{F}} a \sinh\left(\frac{a}{c} \sqrt{\frac{F}{B}} (G(t)-h)\right) \quad (\text{C.28})$$

Hence Eq. (C.27) becomes:

$$S_{cap} = ab \int_{-1}^1 \left\{ \frac{f(t)}{\sqrt{1-t^2}} \right\} dt \quad (\text{C.29})$$

Utilizing the Gauss-Chebyshev Integration, Eq. (C.29) can be calculated using the following expression:

$$S_{cap} = ab \sum_{i=1}^n \frac{\pi}{n} f\left(\cos\left(\frac{2i-1}{2n}\pi\right)\right) \quad (\text{C.30})$$